Advances in Gas-Phase Electron Diffraction

Robert Scott Fender

A thesis submitted in fulfilment of the requirements
for the degree of Doctor of Philosophy
to the
University of Edinburgh
1996

In Memory of
Gail Marie Fender

"I was happy in the haze of a drunken hour
but heaven knows I'm miserable now"

(Taken from "Heaven Knows I'm Miserable Now" by The Smiths)

Abstract

A new gas-phase electron diffraction apparatus is reported in this thesis. The machine complements the existing electron diffraction set-up at Edinburgh University. The new apparatus utilises an electron counting device consisting of a pair of stacked microchannel plates and a novel, position-sensitive anode counter rather than the photographic plate-rotating sector method more commonly used in electron diffraction studies. The work carried out with this detector is discussed. The molecular target source was provided by a Campargue-type molecular beam and the electron beam was produced by a telefocus electron gun. Both of these beams have been fully characterised and the results are presented in this work. A short review is given of the current developments in gas-phase electron diffraction. Finally, the structural refinements of two molecules studied using the photographic method are reported. These are 1,2-di-*tert*-butyldisilane and 1,2-dicarbapentaborane(7).

Declaration

This thesis has been composed by myself and it has not been submitted in any previous application for a degree. The work reported within was executed by myself, unless otherwise stated.

Contents

Chapter 1

Introduction

For over 60 years electron diffraction has been the major source of structural information for gas-phase molecules. The first gas-phase electron diffraction investigation of a molecular structure, that of carbon tetrachloride, was reported by Mark and Wierl [1] in 1930. Up to that point X-ray diffraction had been the main technique used to determine gas-phase molecular structures. It remained so until the end of the 1930's. A new technique then appeared, known as microwave spectroscopy.

Today electron diffraction and microwave spectroscopy are the two principal experimental techniques for the determination of molecular geometry in the vapour phase. Microwave spectroscopy is most useful and accurate for molecules containing relatively few atoms. In fact results for diatomic molecules can have a very high order of precision. In this technique the rotational constants of a molecule are measured. These yield the moments of inertia which in turn lead to the bond lengths within the molecule. An asymmetric rotor has three different rotational constants. More symmetrical molecules, for example prolate or oblate symmetric rotors, linear molecules, and spherical rotors, have one or more special restrictions on the magnitudes of the rotational constants. Thus microwave spectroscopy gives limited information about molecular structure as there are at best three moments of inertia giving three geometrical parameters. To overcome this drawback isotopic substitution can be used to increase the amount of data for a particular molecule. However for complex molecules this necessitates tedious and perhaps expensive isotopic syntheses, if the required isotopically substituted molecules cannot be observed in natural abundance.

For a molecule containing N atoms there are N(N-1)/2 internuclear distances which, if well resolved, would provide more than enough information to establish the (3N-6) atomic co-ordinates describing the structure. Only in an ideal molecule could all of these distances be determined accurately but in molecules with some symmetry the number of distinct distances is reduced. In such cases electron diffraction can give precise structural data on systems containing many (tens of) atoms.

These two methods have become increasingly complemented by a theoretical technique; quantum mechanical calculations. Indeed many structure refinements begin with *ab initio* calculations to establish reasonable values for bond lengths. In fact, most electron diffraction studies today incorporate data from microwave spectroscopy and quantum mechanical calculations. In the determination of the structures of free, isolated molecules other techniques used include vibrational spectroscopy, EXAFS and although less common, neutron diffraction.

A new apparatus has been designed and built using state-of-the-art technology to extend the range of molecules that can be studied using gas-phase electron diffraction. The main advantage of this apparatus is that a better S:N ratio can be achieved with a lower density of sample than is currently used in electron diffraction. The S:N ratio is the total accumulated signal divided by the noise in an experiment. This is helpful in that many species of interest to the chemist are available only in small amounts or at low densities.

Typically, the electron diffraction set-up consists of an electron beam that crosses a beam of gaseous molecules perpendicularly. The resulting scattered electron image is then collected by a suitable detector, usually a photographic plate, but in a few cases electron counting devices [2,3,4] are used.

The electron diffraction technique has evolved in three distinct stages. The first gas-phase experiment was performed by Mark and Wierl [1] in the

1930's. During this decade the so-called "visual" electron diffraction technique was used. The positions of maxima and minima of a molecular interference pattern could be determined surprisingly well against the steeply falling background of atomic scattering intensity, due to the exaggerating ability of the human eye. The relative intensities could only be roughly estimated but interatomic distances were determined by measuring the positions of the maxima and minima on the interference pattern [5]. No information was available from this method on the vibrational frequencies. In 1935 Pauling and Brockway [6] introduced a more direct method for determining interatomic distances. By Fourier transforming the estimated intensity data they produced the radial distribution curve which was related to the probability distribution of interatomic distances.

In the late 1930's Debye [7] and Finbak [8] independently suggested the use of a rotating sector to compensate for the steeply falling background. This was simply a metallic disk of special shape that increased the relative exposure time of the photographic plate toward large scattering angles. This allowed elucidation of the intensity distribution over a wide range of scattering angles. The invention of photometers capable of measuring the optical density distribution of the interference pattern on the photographic plate led eventually in the early 1950's to the second stage of gas-phase electron diffraction known as the "sector-microphotometer" method. Jerome and Isabella Karle [9,10,11] did much to develop this technique and were able to treat the recorded data quantitatively in order to obtain accurate geometrical and vibrational parameters. Since the mid-1950's the technique has blossomed with the advent of experimental apparatus of higher precision. Faster, more powerful computers have also made the task of refining structures much easier. In fact the basis of this technique is the one still used today by most laboratories involved in structure determination.

In 1970 Fink and Bonham [2] reported a new electron diffraction apparatus which used counting techniques. This machine did away with the photographic plate and rotating sector as the means of recording the interference pattern in the electron diffraction experiment. They used instead a detector composed of a scintillator mounted on top of a photomultiplier. Two of these detectors were employed. One detector on a scanning arm was used to record the scattered intensity as a function of scattering angle. The other unit acted as a monitor for fluctuations in the atomic or molecular beam. It was on another scanning arm and was locked into a fixed angular position. The count rates from both detectors were corrected for variations in the incident electron beam by monitoring the current of the unscattered electrons. These improvements led to count rates of up to 1 MHz.

This new apparatus began the third age of gas-phase electron diffraction. The counting technique used by Bonham and Fink provided much information about low-angle scattering but was also used for more conventional structural work including the determination of the structures of alkali halides, Cr_2 acetates and some phthalocyanine complexes. They used their apparatus to investigate the breakdown of the independent atom model (IAM) for electron scattering at low angles due to chemical binding and electron correlation effects. An apparatus based on this arrangement was reported by Konaka [12] in 1972 for the same type of studies. An estimate of the chemical binding energy of the electrons in water molecules was obtained from the differences between the observed and theoretical intensities based on the IAM. In 1982 Stein [13] introduced an electron diffraction apparatus based on a similar detection system to study the electron scattering produced by small clusters. At around the same time groups led by Monot and Schäfer developed machines incorporating electronic techniques to study a wider range of molecular species. Monot's apparatus utilises electron counting whereas Schäfer's apparatus is an analogue device.

By utilising two 1-D charge-coupled device (CCD) imagers Monot [14-22] studied the structure of polyatomic metallic clusters, in particular those of silver. Ewbank, Schäfer and Ischenko [23-34] developed the "stroboscopic" electron diffraction method. Through use of a pulsed electron beam and a photo-diode array (PDA), combined in some cases with laser excitation of the molecular species, they have looked at photodissociation of CS_2 [35], the structures of SF_6 [36] and SeF_6 [37] and the laser-induced interconversion between cis- and trans-1,2-dichloroethylene [38,39,40].

More recently Zewail and co-workers [41-45] have built an apparatus which incorporates a 2-D CCD camera and a pulsed electron beam source. With the use of a femtosecond laser system they hope to look at chemical phenomena that occur on this timescale including bond cleavage. Ultimately it may be possible to determine the structures of transition states. These developments in electron diffraction are discussed in greater detail in **Chapter 6.** A comparison is made between our detection system and those mentioned above.

The new Edinburgh apparatus incorporates an electron source known as a telefocus electron gun [46-51] which is capable of producing stable, high current electron beams. The target molecules are projected in front of the electron beam using a skimmed free-jet molecular beam [52,53]. The reasons for using this molecular source, instead of the effusive source more commonly used in electron diffraction, are twofold: firstly, the free-jet source produces much higher target densities. Secondly, it allows vibrational and rotational cooling of the target molecules that can be used in state-specific experiments.

Both of these pieces of equipment have been used independently before in the area of electron diffraction. However, the electron detector that has been designed for our apparatus is a novel, position-sensitive detector [54,55]. This consists of a set of electron sensing electrodes together with a corresponding set of amplifiers, discriminators and 8-bit counters integrated onto four microchips. The whole detector is mounted behind a set of HOT (high optical technology) Chevron microchannel plates (MCPs) [56] which permit the detection of single electrons.

This new detector should allow us to overcome the shortfalls in existing photographic plates, whilst utilising instruments which already use single electron counting. The detector can cope with count rates of up to 4 MHz at small scattering angles. It is hoped that the detector will facilitate an increased sensitivity in electron detection, evaluation of a true background count rate (from extraneous electron scattering) and time resolved electron images on the 10^{-9}-10^{-8} s timescale.

Unfortunately the anode device has proved to be very problematic. Initially the detector suffered static damage that caused the chips of the anode to latch every time the device was operated. Work was then carried out by the company who built the detector to make it more static resistant. This proved successful to a certain extent and then another problem arose. In order to see if the device was counting we would turn on the detector and ramp up the MCP voltage. The idea was that as the MCPs warmed up any charged particles released would cause counting events on the anode plate. No counting was ever seen under these conditions and the next step taken was to see if there was any scattering from background gas along the electron beam path. With the anode and MCPs turned on an electron beam of around 2 μA was projected toward the centre of the detector. The anode device appeared to count for a short period and then stopped. Some individual elements on the anode plate suffered permanent static damage. This was attributed to spiking. The anode and MCPs shared a common power supply and when charge was drawn from the MCPs the voltage on the anode dropped causing damage. The next step taken was to run the anode and the MCPs from separate power supplies. However the anode stopped working before any proper work could be carried out.

Many of the problems of the anode device were attributed to the Xilinx chip [57,58] that controlled the operations of the counting elements. This device seemed to be the main weakness of the detector and overall the detection system used was not robust enough for the particular apparatus it was used in.

Work with the anode device has ceased and a detection system comprised of a scintillator and a commercially available 2-D CCD camera has been installed. Although the anode device can cope with higher counting rates this detector has been abandoned in favour of the CCD.

As mentioned previously, the operating characteristics of this machine should enable the study of a whole new range of compounds as yet not studied by electron diffraction. Due to the increased target densities, together with the cooling effect of the molecular beam, compounds with low vapour pressures and unstable molecules can be investigated.

With the aid of jet-cooling, research can be carried out on so-called floppy molecules such as C_3O_2 [59,60,61]; these are molecules which exist as a mixture of excited states at room temperature or above. They have very large amplitude motions leading to a shrinkage effect [62] in some internuclear distances. It is hoped to look at these compounds in their ground vibrational states and in doing so establish the nature of their geometry.

Under certain conditions, the free-jet source is capable of producing clusters [63] containing two or more gaseous molecules or atoms, or van der Waals molecules. The three operational parameters that influence the molecular beam are the stagnation or pushing pressure P_0, the source temperature T_0 and the diameter of the nozzle source d. By reducing the source temperature or increasing the stagnation pressure these clusters or van der Waals molecules can be created. Normally only a small percentage of the parent molecules or atoms form clusters such as dimers or trimers. It will be possible with the increased sensitivity of the new detector to study the geometry of these structures.

The clustering effect in supersonic molecular beams has been adopted in some electron diffraction studies. Stein and co-workers have done studies on clusters of SF_6 [64], H_2O and CO_2 [65]. They have also developed a system for studying metal clusters as previously mentioned which uses electron counting [13,66]. Farges [67] has also used supersonic beams to create clusters. He has investigated the crystalline and non-crystalline effects in argon clusters [68,69]. However, Bartell has done more than any other to research the nucleation and growth of clusters using electron diffraction [70,71,72]. He has looked at many different species and has carried out extensive work on the phase changes in going from the gas-phase to the liquid-phase. This work has been done using photographic recording of the diffraction patterns.

The use of laser excitation could also open up new areas as yet virtually unexplored using electron diffraction. The operation of the molecular beam results in the rotational and vibrational modes of the target molecule becoming cooled, so that ideally, the target molecules exist in a small range of rotational and vibrational states within the electronic ground state. Upon excitation using a laser pulse of known energy individual vibrational levels in an upper electronic state can be populated. In doing so it will be possible to probe such potential surfaces over a wide region and also to map out a time averaged probability distribution of the nuclear wavefunction in a given vibrational state.

A simpler option entails the study of the molecular geometries of isolated polyatomic ions; using resonance enhanced multiphoton ionisation (REMPI) [73-76], ion densities have been achieved that are large enough to allow the use of electron diffraction to see the effect of electron ejection on molecular structure.

Finally, time-dependent phenomena may be investigated. It should be possible to study processes such as pseudorotation. Excited states decaying by internal conversion rather than radiation exhibit geometry changes in the 10^{-14} to 10^{-6} s timescale range. Corresponding changes in the electron scattering can be observed with a resolution of 10^{-9} to 10^{-8} s, opening the possibility of detailed studies of internal energy transfer in favourable systems.

The principal reason for building this machine was to extend the range of systems and molecular phenomena that can be studied by gas-phase electron diffraction. The classes of molecule mentioned above could potentially be investigated by the apparatus. However, some work on exotic species, in particular radicals, has been carried out. Anderson has studied the structure of several radical species by electron diffraction [77-82]. The structures of the NF_2 radicals and N_2F_4 have been studied by Bauer [83] and the structure of N_2F_4 was reinvestigated by Hedberg [84]. Schäfer has studied the structure of indenyl [85,86,87]. Kohl and co-workers undertook several interesting studies of reaction intermediates and radicals. They have looked at the structures of the products of the thermal decomposition of $BrCCl_3$ [88]. Studies of the dibromoethylene radical [89] and of the reaction intermediate in the gas-phase bromination of ethylene [90] were also undertaken. In 1984 Rood and Milledge [91] reported an apparatus designed to observe the electron diffraction pattern from short-lived species in the gas-phase generated by the technique of flash photolysis. They looked at the flash photolysis products of chlorine dioxide and biacetyl. Ischenko [23] has also done studies on excited-states created by a tuneable carbon dioxide laser.

Including this introductory chapter, this thesis consists of eight chapters. **Chapter Two** covers the basic theory of gas-phase electron diffraction, outlining the most important concepts and equations. Also included is an indication as to how molecular structures are derived from electron scattering.

A description of the experimental apparatus is given in **Chapter Three**. An overview of the new machine is presented including the vacuum system, details of instrumentation and computer control. The three main components of the apparatus; the molecular beam assembly, the telefocus electron gun and the novel position-sensitive electron detector are introduced.

Chapter Four deals in depth with the molecular beam assembly. The characteristics of the skimmed Campargue source have been investigated and the results are displayed here.

The performance of the telefocus electron gun is presented in **Chapter Five**. The operation of the high voltage power supply is described together with cross-sectional data and profiles of the electron beam. The focussing properties of the telefocus electron gun have been studied and displayed.

A discussion of the position-sensitive electron detector is given in **Chapter Six**. A short review of the uses of this class of detector and details of the operation of our particular detector are covered here. An account of the problems that were encountered with this detector are reported along with the subsequent improvements that were made over the course of three years.

Chapter Seven gives details of two actual molecular structures derived from data obtained using the existing electron diffraction machine in Edinburgh University. The molecules studied were 1,2-di-*tert*-butyldisilane [92] and 1,2-dicarbapentaborane(7).

The concluding chapter, **Chapter Eight**, is a report on the current state of the project. A CCD based system has been designed and is currently being tested.

Bibliography

1 H. Mark and R. Wierl, Z. Phys., 60 (1930) 741

2 M. Fink and R.A. Bonham, Rev. Sci. Instrum., 41 (1970) 389

3 H. Schmoranzer, H.F. Wellenstein, and R.A. Bonham, Rev. Sci. Instrum., 46 (1975) 89

4 M. Fink, P.G. Moore, and D. Gregory, J. Chem. Phys., 71 (1979) 5227

5 R. Wierl, in: Electroneninterferenzen, Ed., P. Debye, (Hirzel, Leipzig, 1930)

6 L. Pauling and L.O. Brockway, J. Am. Chem. Soc., 57 (1935), 2684

7 P.P. Deybe, Phys. Z., 80 (1939) 404

8 C. Finbak, Avh. Norsk Vidensk.-Akad. Oslo (1937) 13

9 I.L. Karle and J. Karle, J. Chem. Phys., 17 (1949) 1052

10 I.L. Karle and J. Karle, J. Chem. Phys., 18 (1950), 957

11 I.L. Karle and J. Karle, J. Chem. Phys., 18 (1950) 963

12 S. Konaka, Jpn. J. Appl. Phys., 11 (1972) 1199

13 S.S. Kim and G.D. Stein, Rev. Sci. Instrum., 53 (1982) 838

14 B.D. Hall, M. Flüeli, R. Monot, and J.-P. Borel, Helvetica Phys. Acta, 61 (1988) 193

15 B.D. Hall, M. Flüeli, R. Monot, and J.-P. Borel, Z. Phys. D, 12 (1989) 97

16 B.D. Hall, M. Flüeli, D. Reinhard, J.-P. Borel, and R. Monot, Rev. Sci. Instrum., 62 (1991) 1481

17 B.D. Hall, D. Reinhard, and R. Monot, Rev. Sci. Instrum., 62 (1991) 2486

18 B.D. Hall, and R. Monot, Helvetica Phys. Acta, 64 (1991) 193

19 B.D. Hall, D. Reinhard, J.-P. Borel, and R. Monot, Z. Phys. D, 20 (1991) 457

20 B.D. Hall, M. Flüeli, R. Monot, and J.-P. Borel, Phys. Rev. B, 43 (1991) 3906

21 D. Reinhard, B.D. Hall, D. Ugarte, and R. Monot, Z. Phys. D, 26 (1993) 576

22 B.D. Hall, D. Reinhard, and R. Monot, Rev. Sci. Instrum., 66 (1995) 2668

23 A.A. Ischenko, V.V. Golubkov, V.P. Spiridonov, A.V. Zgurskii, A.S. Akhmanov, M.G. Vabischevich, and V.N. Bagratashvili, Appl. Phys. B32 (1983) 161

24 J.D. Ewbank, L. Schäfer, D.W. Paul, O.J. Benston, and J.C. Lennox, Rev. Sci. Instrum., 55 (1984) 1598

25 J.D. Ewbank, L. Schäfer, D.W. Paul, and D.L. Monts, Rev. Sci. Instrum., 57 (1986) 967

26 L. Schäfer and J.D. Ewbank, Acta Chem. Scand. A42 (1988) 358

27 J.D. Ewbank, D.W. Paul, L. Schäfer, and R Bakhtiar, Appl. Spectrosc., 43 (1989) 415

28 J.D. Ewbank, W.L. Faust, D.L. Monts, D.W. Paul, L. Schäfer, R Bakhtiar, and Q. Dou, Mol. Cryst. Liq. Cryst., 187 (1990) 351

29 J.D. Ewbank, W.L. Faust, J.Y. Luo, J.T. English, D.L Monts, D.W. Paul, Q. Dou, and L. Schäfer, Rev. Sci. Instrum., 63 (1992) 3352

30 A.A. Ischenko, V.P. Spiridonov, L. Schäfer, and J.D. Ewbank, J. Mol. Struct., 300 (1993) 115

31 A.A. Ischenko, J.D. Ewbank, and L. Schäfer, J. Mol. Struct., 320 (1994) 147

32 J.D. Ewbank, L. Schäfer, and A.A. Ischenko, J. Mol. Struct., 321 (1994) 265

33 A.A. Ischenko, J.D. Ewbank, and L. Schäfer, J. Phys. Chem., 99 (1995) 15790

34 A.A. Ischenko, L. Schäfer, and J.D. Ewbank, J. Mol. Struct., 376 (1996) 157

35 A.A. Ischenko, L. Schäfer, J.Y. Luo, and J.D. Ewbank, J. Phys. Chem., 98 (1994) 8763

36 A.A. Ischenko, J.D. Ewbank, and L. Schäfer, J. Phys. Chem., 98 (1994) 4287

37 P. Maggard, V.A. Lobarstov, L. Schäfer, J.D. Ewbank, and A.A. Ischenko, J. Phys. Chem., 99 (1995) 13115

38 L. Schäfer, J.D. Ewbank, K. Siam, D.W. Paul , and D.L. Monts, J. Mol. Struct., 145 (1986) 135

39 D.W. Monts, J.D. Ewbank, K. Siam, W.L. Faust, D.W. Paul, and L. Schäfer, Appl. Spectrosc., 41 (1987) 631

40 J.D. Ewbank, J.Y. Luo, J.T. English, R. Lui, W.L. Faust, and L. Schäfer, J. Phys. Chem., 97 (1993) 8745

41 J.C. Williamson and A.H. Zewail, Proc. Natl. Acad. Sci. USA, 88 (1991) 5021

42 J.C. Williamson, M. Dantus, S.B. Kim, and A.H. Zewail, Chem. Phys. Lett., 196 (1992) 529

43 J.C. Williamson and A.H. Zewail, Chem. Phys. Lett., 209 (1993) 10

44 J.C. Williamson and A.H. Zewail, J. Phys. Chem., 98 (1994) 2766

45 M. Dantus, S.B. Kim, J.C. Williamson, and A.H. Zewail, J. Phys. Chem., 98 (1994) 2782

46 K.H. Steigerwald, Optik, 5 (1949) 469

47 F.W. Braucks, Optik, 14 (1958) 242

48 E.B. Bas and F. Gaydou, Z. Angew. Phys., 11 (1959) 370

49 H. Schmoranzer, H.F. Wellenstein, and R.A. Bonham, Rev. Sci. Instrum., 46 (1975) 89

50 B. Schiewe, H. Schmoranzer, and P. Wollenweber, Rev. Sci. Instrum., 48 (1977) 893

51 High energy electron scattering, Eds.: R.A. Bonham and M. Fink, (Van Nostrand Reinhold Co., New York, 1974), ACS Monograph 169

52 D.R. Miller in: Atomic and molecular beam methods, Ed.: G. Scoles, (Oxford University Press, Oxford/New York, 1988) Ch.2, 14

53 R. Campargue, J. Phys. Chem., 88 (1984) 4466

54 J.V. Hatfield, S.A. Burke, J. Comer, J. Goldfinch, T.A. York, and P. J. Hicks, Rev. Sci. Instrum., 63 (1992) 235

55 J.V. Hatfield, J. Comer, T.A. York, and P. J. Hicks, Rev. Sci. Instrum., 63 (1992) 792

56 J. Wiza, Nucl. Instrum. and Meth., 162 (1979) 587

57 B.C. Cole, Electronics, (Sept. 1987) 61

58 J. Mcleod, Electronics, 65 (1992) 7

59 A.H. Clark and H.M. Seip, Chem. Phys. Lett., 6 (1970) 452

60 M. Tanimoto, K. Kuchitsu, and Y. Marino, Bull. Chem. Soc. Japan, 43 (1970) 2776

61 M. Sugie and K. Kuchitsu, Acta. Cryst. A., 31 (1975) 5271

62 Molecular vibrations and mean square amplitudes, Ed.: S.J. Cyvin (Universitets Forgalet, Oslo, Elsevier, Amsterdam, 1968)

63 M. Kappes and S. Leutwyler in: Atomic and molecular beam methods, Ed.: G. Scoles, (Oxford University Press, Oxford/New York, 1988), Ch.15, 380

64 O. Abraham, S.S. Kim, and G.D. Stein, J. Chem. Phys., 75 (1981) 402

65 G.D. Stein and J.A. Armstrong, J. Chem. Phys., 58 (1973) 1999

66 A. Yokozeki and G.D. Stein, J. Appl. Phys., 49 (1978) 2224

67 B. Raoult and J. Farges, Rev. Sci. Instrum., 44 (1973) 430

68 J. Farges, B. Raoult, and G. Torchet, J. Chem. Phys., 59 (1973) 3454

69 J. Farges, M.F. de Feraudy, B. Raoult, and G. Torchet, J. Chem. Phys., 78 (1983) 5067

70 L.S. Bartell, Chem. Rev., 86 (1986) 491

71 L.S. Bartell and R.J. French, Rev. Sci. Instrum., 60 (1989) 1223

72 L.S. Bartell and R.J. French, Z. Phys. D., 12 (1989) 7

73 H.J. Neusser, Int. J. Mass Spec. Ion Proc., 79 (1987) 41

74 J.M. Hayes, Chem. Rev., 87 (1987) 745

75 P.M. Johnson and C.E. Otis, Ann. Rev. Phys. Chem., 32 (1981) 139

76 D.H. Levy, Ann. Rev. Phys. Chem., 31 (1980) 197

77 P. Anderson, Acta Chem. Scand., 19 (1965) 622

78 P. Anderson, Acta Chem. Scand., 19 (1965) 629

79 B. Anderson and P. Anderson, Acta Chem. Scand., 20 (1966) 2728

80 P. Anderson, E.E. Astrup, and A. Borgan, Acta Chem. Scand., A28 (1974) 239

81 P. Anderson, E.E. Astrup, P.S. Frederickson, and K.F. Nakken, Acta Chem. Scand., A28

82 P. Anderson, E.E. Astrup, P.S. Frederickson, and K.F. Nakken, Acta Chem. Scand., A28 (1974) 675

83 R.K. Bohn and S.H. Bauer, Inorg. Chem., 6 (1967) 304

84 M.M. Gilbert, G. Gunderson, and K. Hedberg, J. Chem. Phys., 56 (1972) 1691

85 L. Schäfer, J. Am. Chem. Soc., 90 (1968) 3919

86 L. Schäfer and H.H. Jensen, Acta Chem. Scand., 24 (1970) 1125

87 J.F. Southern, L. Schäfer, K. Brendhaugen, and H.M. Seip, J. Chem. Phys., 55 (1973) 2418

88 T.L. Leggett and D.A. Kohl, J. Chem. Phys., 59 (1973) 611

89 T.L. Leggett, R.E. Kennerly, and D.A. Kohl, J. Chem. Phys., 60 (1974) 3264

90 R.C. Ivey, P.D. Schulze, T.L. Leggett, and D.A. Kohl, J. Chem. Phys., 60 (1974) 3174

91 A.P. Rood and J. Milledge, J. Chem. Soc., Faraday Trans. 2, 80 (1984) 1145

92 D. Hynk, R.S. Fender, H.E. Robertson, D.W.H. Rankin, M. Bühl, K. Hassler, and K. Schenzel, J. Mol. Struct., 346 (1995) 215

Chapter 2

Theory Of Electron Scattering

2.1 Introduction

As a technique for structure determination gas-phase electron diffraction is essentially very simple. A beam of high-energy electrons (~40 keV) crosses a molecular jet and some of these incident electrons are deflected by the electric field gradient at the edges of the nuclei of the chosen target molecule (see **Fig. 2.1**). At some distance from this scattering centre the resulting pattern is recorded by a suitable detector, either a photographic plate, electron counting device or other electronic device.

The scattered electron image consists of a series of diffuse concentric rings of varying intensities (see **Figs. 2.2a** and **2.2b**). This intensity distribution is a function of the structure of the scattering molecules and by studying this interference pattern information on the molecular geometry, specifically interatomic distances and intramolecular motion, can be obtained.

Molecular geometry - that is the relative positions of the atomic nuclei in the molecule - is one of the three constituents of molecular structure. The other two are electronic structure and intramolecular motion. Molecular geometry can be characterised by nuclear co-ordinates if the molecule is affixed in a co-ordinate system or by so-called internal co-ordinates comprising bond lengths, bond angles, and angles of internal rotation.

The most important piece of structural information obtained from the technique is molecular geometry. However, data on intramolecular motion are also available, including vibrational amplitudes and occasionally barriers to internal rotation. Energy differences between conformers, other data related to molecular energetics, and even vibrational frequencies are

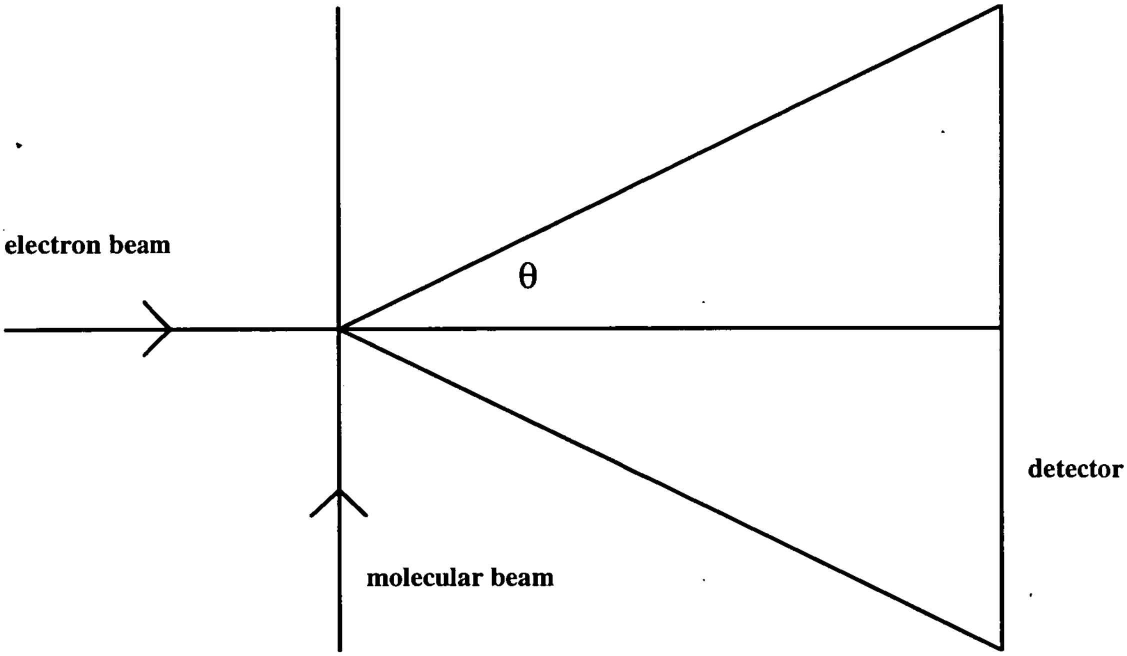

Figure 2.1 Schematic of electron diffraction set-up.

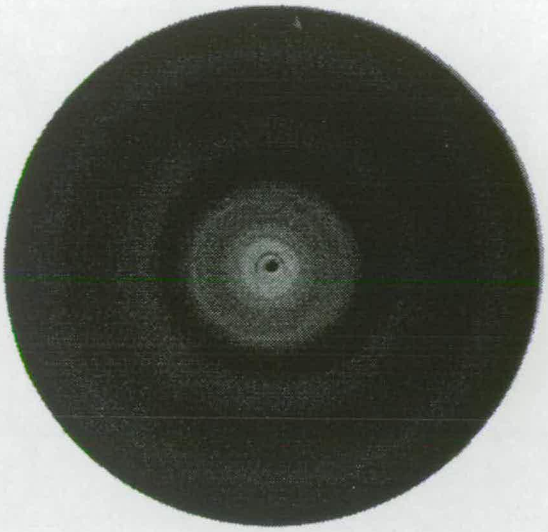

Figure 2.2a) Electron diffraction pattern (benzene).

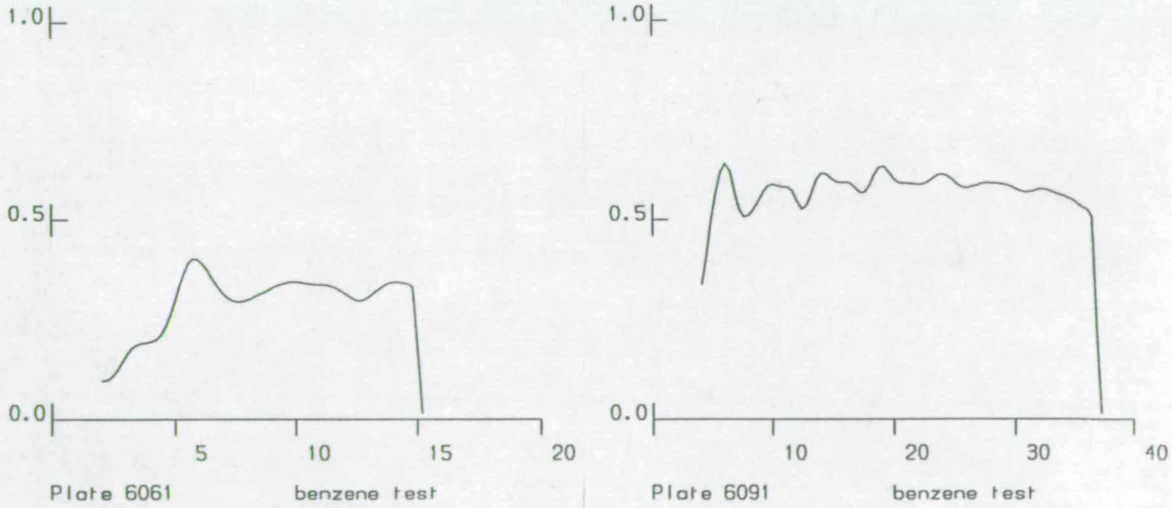

Figure 2.2b) Densitometer traces (multiplied by $1/s^4$) of two overlapping electron diffraction photographs.

potentially available through this method. In principle, at least, information on electron density distribution is also present in the electron scattering pattern. As the total charge distribution of the molecule produces the electron scattering a great deal of structural information as yet unstudied lies within the reach of this technique.

The theoretical framework required to carry out a fairly accurate electron diffraction investigation was developed many years ago. The bases of the theory are to be found in papers by Rutherford [1], Debye [2,3] and Ehrenfest [4]. The first electron diffraction experiments were performed by Davisson and Germer [5] and G.P. Thomson [6,7] using crystalline material, while the first gas electron diffraction experiments were conducted by Mark and Wierl [8]. These studies verified de Broglie's relation thus confirming the wave nature of the electron.

Many textbooks on quantum mechanics and on scattering theory [9,10] give details of the technique. However, several books relating directly to structure determination by gas-phase electron diffraction have been published [11,12]. The following outline of the theoretical basis follows that given by Schäfer [13] in an excellent review of this area of research published in 1976.

2.2 Theory

When a beam of electrons encounters a molecular beam some of the incident electrons, approximately 1% at 40 keV, are deflected from their direction of motion. The scattered electrons can undergo two types of collision with the molecular target. The first is inelastic scattering; a process in which the energy of the incident electrons is changed. For any molecular species there are many possible inelastic channels including electronic transitions. The second type involves no energy change and is known as elastic scattering.

Elastic scattering itself takes two forms. The first is simply scattering from single atoms within the molecule and contains no structural information in the high energy regime used in conventional electron diffraction studies. However, the interference pattern arising from electrons elastically scattered by atom pairs within a molecule can reveal molecular structure.

This scattering from atom pairs can be understood in terms of the familiar double-slit interference experiment. If a wavefront encounters two fixed scattering sites, the waves are diffracted in all directions by each site. When scattered wavelets from the sites are combined at, say, a photographic plate (see **Fig. 2.3**), they will be out of step with each other by an amount (d_j-d_i) corresponding to the path length difference. As the scattering angle θ increases, this path difference also increases; it is $r_{ij}\sin\theta$ in the plane of **Figure 2.3**.

Constructive (or destructive) interference occurs when the path difference is an integral (or half integral) number of waves and the resultant interference fringes can be recorded and measured. Constructive interference fringes occur, then, at

$$r_{ij}\sin\theta_n = n\lambda \quad (2.1)$$

where n is an integer. From the known wavelength and measured angles θ_n the distance r_{ij} between the scattering centres can be calculated.

This elementary construction illustrates the situation when a monochromatic electron beam is scattered by a stream of randomly oriented molecules. For a beam of energy E the wavelength of the electrons including the relativistic correction can be written

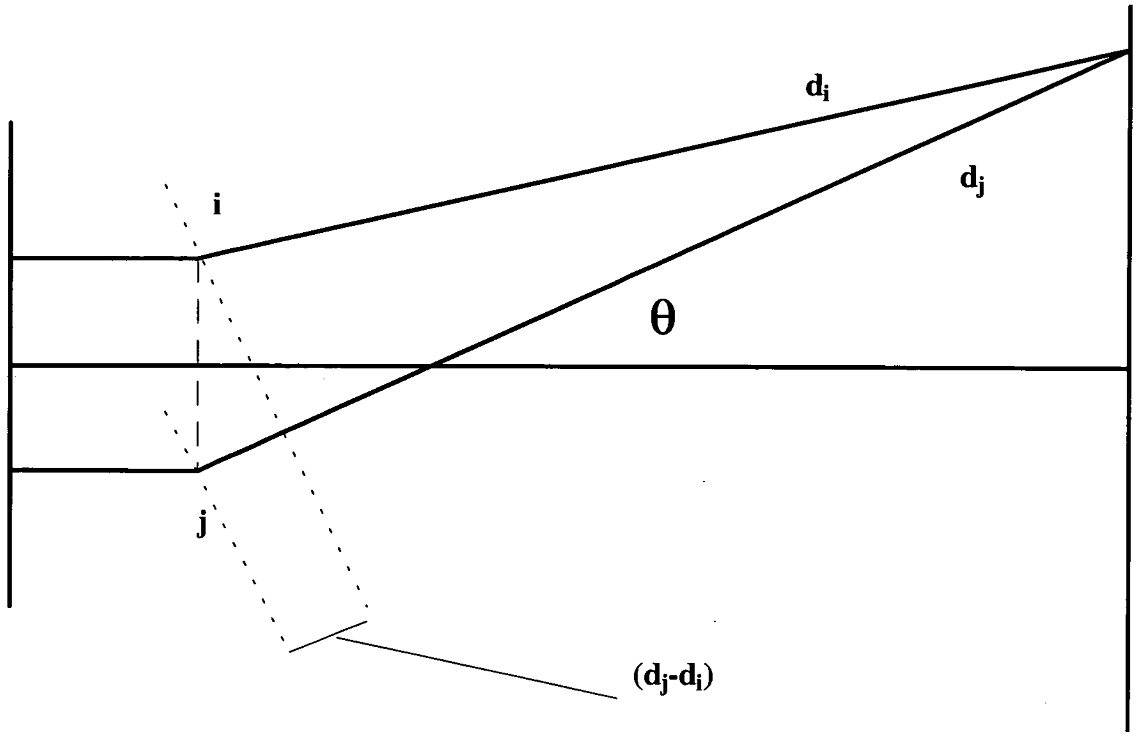

Figure 2.3 Scattering centres separated by r_{ij}.

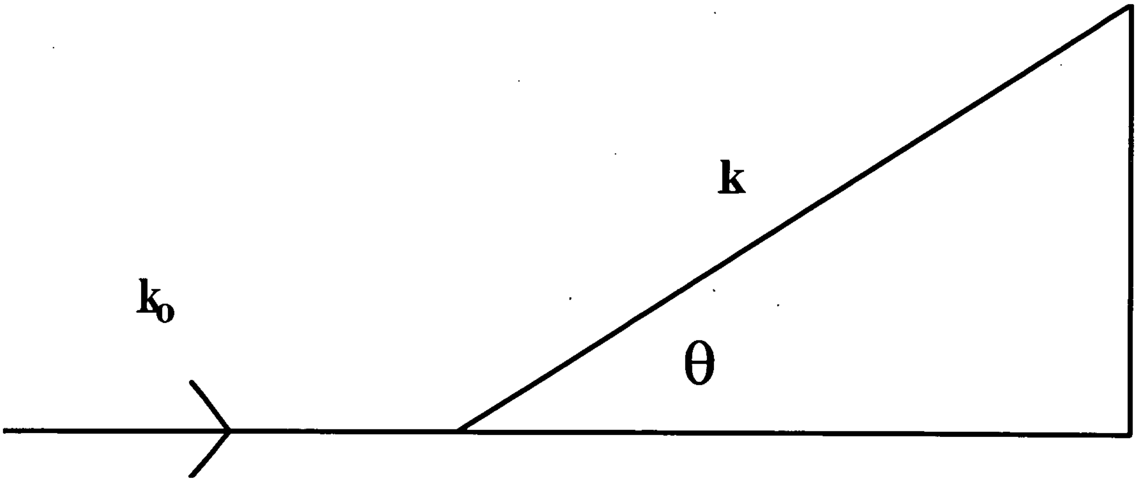

Figure 2.4 Schematic of wavevectors, $|\underline{k}_o| = |\underline{k}|$, $s = 2k \sin(\theta/2)$.

$$\lambda = \frac{h}{\sqrt{2mE}} \frac{1}{\sqrt{1 + E / 2mc^2}} \qquad (2.2)$$

For electrons at 40 keV, λ is about 0.06 Å. This wavelength is around 20-30 times smaller than common bonded intramolecular distances.

If the set of fringes corresponding to any given pair of atoms in a molecule are considered they would gyrate in synchrony with the tumbling of the molecule in the gas-phase. Importantly, a well-defined interference pattern survives this tumbling though, of course, in somewhat washed out form. As no orientation is preferred, the pattern is circularly symmetric about the axis of the electron beam (see **Fig. 2.2a**).

In a molecule each pair of atoms produces a set of interference fringes with a period related to that intermolecular distance. Widely spaced atoms lead to closely spaced fringes and covalently bonded atoms produce relatively widely spaced fringes. Analysis of the total molecular interference intensities produces internuclear distances and also vibrational amplitudes for atom pairs.

2.2.1 Atomic Scattering: Scattering Factors

Electron scattering by atoms and molecules originates in the wave nature of electrons. A stationary parallel beam of electrons with velocity v and kinetic energy E advancing in direction z can be described as a planar wave

$$\psi_o = Ae^{2\pi i z/\lambda} = Ae^{i k_o z} \qquad (2.3)$$

with wavelength $\lambda = 2\pi/k_o$. When this electron beam hits an atom or molecule, the electrons acquire a potential energy different from zero. The resulting wave ψ, after the scattering event, is then the sum of ψ_o, the incident planar wave, and ψ′, the scattered spherical wave. The scattered wave ψ′ can be expressed by

$$\psi' = A\frac{1}{R}f(\theta)e^{ik_oR} \qquad (2.4)$$

where f(θ) is the scattering factor and R is the distance from the scattering centre to the point of detection. The asymptotic form is therefore

$$\psi^{(\infty)} = \psi_o + \psi' = A\left[e^{ik_oz} + \frac{1}{R}f(\theta)e^{ik_oR}\right] \qquad (2.5)$$

The scattering factors, f(θ), are the main functions used to describe the scattering process. The scattering factors represent the power of an atom to scatter electrons, at a given incident energy, to an angle θ known as the scattering angle.

For an incident electron beam of intensity I_o the scattering factors act as proportionality functions with the scattered electron intensities I(θ) by the following relationship

$$I(\theta) = \frac{I_o}{R^2}\left|f(\theta)\right|^2 \qquad (2.6)$$

In **equation (2.6)** R is the distance from the scattering centre to the point of registration. In the electron diffraction experiment it is the so-called scattering cross-section, $[\ I(\theta)/I_o\ ]R^2$, which is determined so it is important to know the form of the scattering factors as accurately as possible in order to carry out meaningful structural work.

The relationship in **equation (2.6)** can be arrived at by solving the Schrödinger equation which is usually set up for one electron scattering by a spherically symmetric force field

$$\nabla^2\psi(\underline{R})+\left[k^2-U(R)\right]\psi(\underline{R})=0 \qquad (2.7)$$

In **equation (2.7)** $k^2=2mE/\hbar^2$ ($k=p/\hbar=2\pi/\lambda$, and λ is the electron wavelength); $U(R)=\left(2m/\hbar^2\right)V(R)$; V is the potential energy for the electron in the field representing the atom; R is the distance from the scattering centre; and $\underline{\mathrm{R}}$ is the corresponding vector.

The scattering factors, f(θ), are also often called scattering amplitudes and like many other quantum mechanical wave amplitudes they are complex quantities. They have magnitude, f(θ), and phase, η(θ)

$$f(\theta)=|f(\theta)|e^{i\eta(\theta)} \qquad (2.8)$$

It is in this form that the atomic scattering factors are used in electron diffraction.

The scattering amplitudes, f(θ), can be determined by the partial wave method [14] and expressed in terms of Legendre polynomials P_l

$$f(\theta)=\sum_{l=0}^{\infty}\frac{(2l+1)}{2ik}P_l(\cos\theta)\left(e^{2i\delta_l}-1\right) \qquad (2.9)$$

In elastic scattering the wavevector of the incident electrons, $k_0 = 2\pi/\lambda$, where λ is the wavelength of the electrons, remains unchanged in magnitude but not in direction (see **Fig. 2.4**). Instead of the scattering angle θ the parameter s, the scattering vector, is used to express the scattered intensities. The scattering angle θ and the scattering vector s are related by

$$s = |\underline{s}| = |k_o - k| = 2k\sin(\theta / 2) = 4\pi / \lambda \ \sin(\theta / 2) \quad (2.10)$$

This involves transforming from real space to scattering space which has units of Å^{-1}.

The scattering amplitudes f(s) of atoms and their respective phase shifts η(s) are well defined functions of s. The scattering amplitudes and phase shifts for a few elements are displayed in **Figures 2.5a** and **2.5b** respectively. Scattering amplitudes increase roughly in proportion to the atomic number of the scattering atom and as $1/s^2$. This is a description of a Coulombic scattering potential. However if a screening factor F(s) arising from electron screening is taken into account the electron scattering amplitude for the ith atom in a molecular assembly can be expressed in the following manner

$$f_i(s) = \frac{Z_i - F_i(s)}{s^2} \quad (2.11)$$

From **equation (2.11)** it is seen that heavy atoms scatter much more than light atoms and the scattering intensities fall off very steeply with increasing scattering angle. This rapid decline in scattering, even at moderate angles, has led to the use of the so-called rotating sector in electron diffraction set-ups incorporating the photographic technique.

Atomic and molecular scattering fall off as $1/s^4$. This leads to photographic plates becoming overexposed at small s values before a reasonable signal is collected at higher s values if a rotating sector is not used (see **Fig. 2.6a**). The sector is simply a piece of metallic sheet cut in such a way as to increase the relative exposure time of the photographic plate toward the

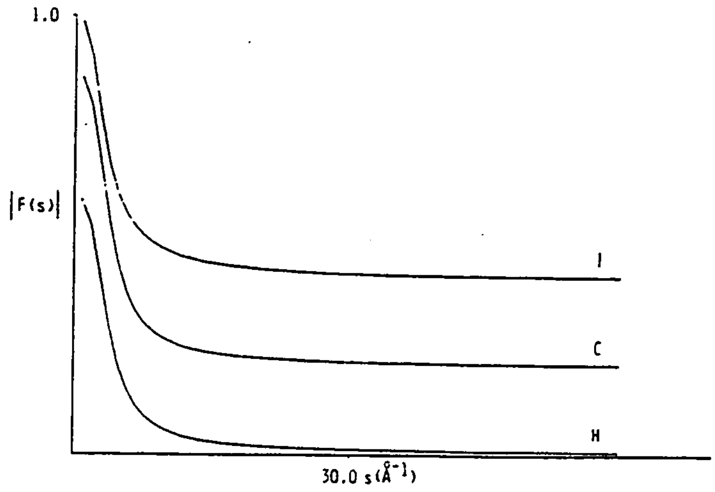

Figure 2.5a) Scattering factors, | f(s) |, for iodine, carbon, and hydrogen at 40 keV, from s = 0.0 to s = 60.0 Å^{-1}. Taken from [13].

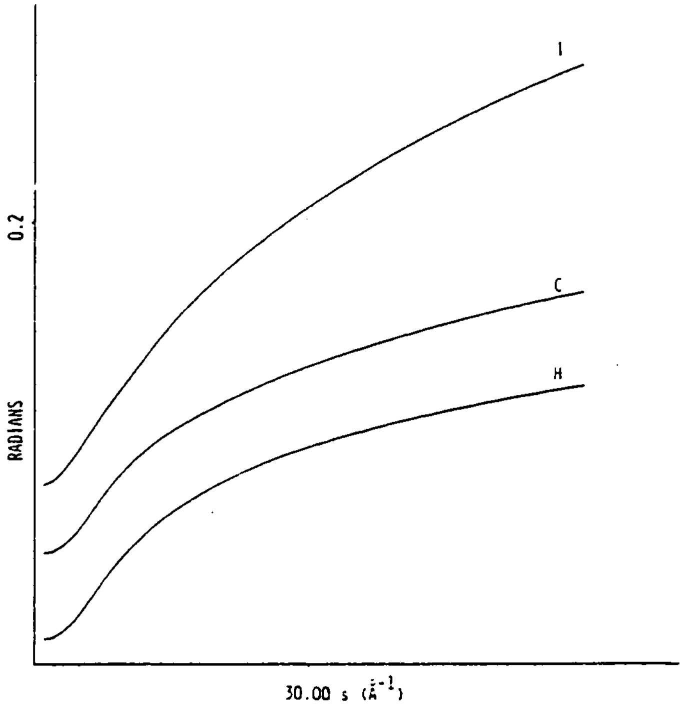

Figure 2.5b) Scattering factor phases, $\eta(s)$, for iodine, carbon, and hydrogen at 40 keV from s = 0.0 to s = 60.0 Å^{-1}. Taken from [13].

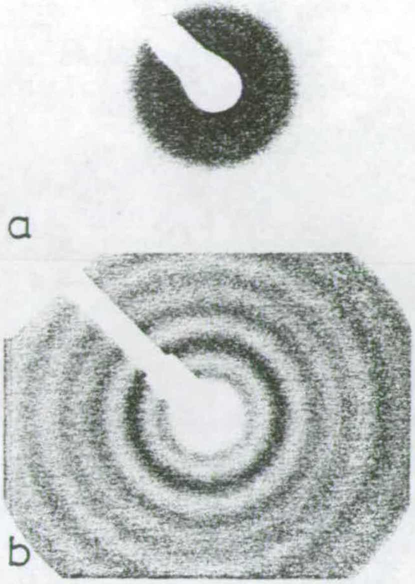

Figure 2.6 Diffraction photographs: (a) recorded without a rotating sector and (b) recorded with a rotating sector. Taken from [12].

large scattering angles, according to well-defined functions. An example of a diffraction photograph taken with a rotating sector is shown in **Figure 2.6b** and **Figure 2.7** displays two examples of rotating sectors.

The major difference between the new apparatus built in Edinburgh and existing gas-phase electron diffraction machines using photographic plates is that it possesses no rotating sector. This is possible because the electron counting device comprised of microchannel plates (MCPs) and a position-sensitive detector has a greater dynamic range (around $10^6 : 1$) compared to photographic plates ($10^2 : 1$). The dynamic range is the ratio of the largest signal that can be recorded to the smallest recordable signal.

The phase shifts $\eta(s)$ for atoms can be described by monotonically increasing functions of s [15] but are not proportional to s. They can be described as

$$\eta\,(s) = -2\alpha \frac{1+s^2a^2}{sa\left(4+s^2a^2\right)^{1/2}} \tanh^{-1} \frac{sa}{\left(4+s^2a^2\right)^{1/2}} \qquad (2.12)$$

where a is the atomic radius and $\alpha = Ze^2 / \hbar v$ (v is the velocity of the particle). The phase shift can be thought as a time delay suffered by the electrons, represented as waves, as they are scattered by atoms.

However, in structural analyses the structural information arises from scattering by pairs of atoms. In early electron diffraction studies the use of non-complex scattering amplitudes in the first Born approximation [16] led to some surprising and famous inaccurate structure determinations. These arose from the phase difference that results from scattering by pairs of unlike atoms in particular where one atom is much heavier than the other.

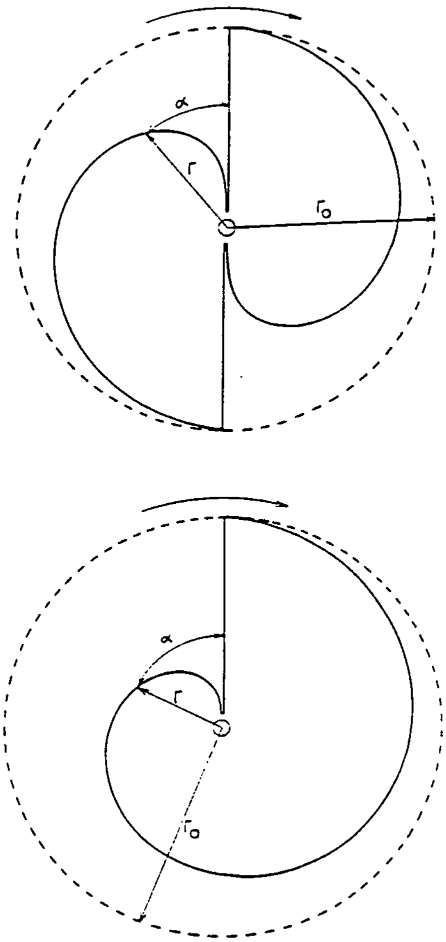

Figure 2.7 Shapes of cubic sectors. Taken from [12].

The phase shifts are proportional to atomic number as stated above in **equation (2.12)**. Glauber and Schomaker [15,16] were the first to demonstrate this failure in scattering theory and modified their scattering amplitudes to include phase shifts. A more detailed description of the limits of scattering theory as it relates to electron diffraction, including the first Born approximation, is given in **section 2.3**.

2.2.2 Scattering By Molecules: Molecular Intensities

Previously it was mentioned that the interaction of an electron beam with a molecular target leads to two types of scattering. Firstly, there is purely atomic scattering of intensity $I_{\text{atomic}}(s)$. Then there is molecular scattering of intensity $I_{\text{molecular}}(s)$ and the sum of the two scattering processes, $I_{\text{total}}(s)$, can be written

$$I_{total}(s) = I_{atomic}(s) + I_{molecular}(s) \qquad (2.13)$$

The atomic scattering takes two forms; elastic and inelastic scattering. Elastic scattering is a coherent process whereas inelastic scattering is assumed to be incoherent. They depend on the elastic and inelastic scattering factors for the atoms f(s) and S(s) respectively. For a system of N atoms the total atomic scattering $I_{\text{atomic}}(s)$ is written

$$I_{atomic}(s) = \frac{I_o}{R^2}\sum_{i=1}^{N}\left[\left|f_i(s)\right|^2 + 4/a_o{}^2 s^4 S_i(s)\right] \qquad (2.14)$$

where the first term is elastic scattering and the second is inelastic scattering. In **equation (2.14)** a_0 is the Bohr radius. The atomic scattering takes the form of a smooth decreasing function with respect to s. It can be calculated exactly using tabulated values of f(s) [17] and S(s) [18]. There is no structural information in the high-energy regime and it is removed during data analysis to produce molecular intensities. It is commonly known as the theoretical background.

The molecular intensities $I_{molecular}(s)$ result from elastic scattering by atom pairs, both bonded and non-bonded. It is a coherent process and scattering from groups of three atoms and higher order scattering terms are ignored. The intensities reflect the intramolecular structure of interatomic distances, bond angles, torsional angles and vibrational amplitudes. By averaging over all vibrational and rotational states of the target molecule the molecular intensities $I_{molecular}(s)$ for a system of N atoms can be expressed as

$$I_{molecular}(s) = \frac{I_o}{R^2} \sum_{i=1}^{N} \sum_{\substack{j=1 \\ i \neq j}}^{N} \frac{1}{r_{ij} s} |f_i||f_j| \cos(\eta_i - \eta_j) \exp\left(-\frac{1}{2} l_{ij}^2 s^2\right) \sin(r_{ij} s) \qquad (2.15)$$

In **equation (2.15)** the r_{ij} terms are the mean internuclear distances between two atoms i and j; the l_{ij}^2 terms are the corresponding mean square amplitudes of vibration. The physical meaning of these will be explained in **section 2.2.3.**

It is evident that as the scattering amplitudes are dependent on atomic number in **equation (2.11)** the scattering from a heavy atom like Br is much greater than that for an H atom. The phase shift is also greater for a heavier atom and this can cause problems in structure determinations. The molecular scattering arises from atom pairs and for a given distance r_{ij} the contribution to this distance is weighted by the scattering factor product $|f_i||f_j|$. This leads to a larger contribution to the diffraction pattern from a pair of heavy atoms than, say, a heavy-light pair or two light atoms. The $(\eta_i-\eta_j)$ term in **equation (2.15)** is the phase difference for the scattered electron wave between two atoms i and j within a molecule. The difficulties arising from this term, in particular where one of the scattering pair is much heavier than the other, were mentioned in **section 2.2.1** and will be treated in greater depth in **section 2.3**.

The form of **equation (2.15)** leads to the fact that the molecular intensity data will consist of a sum of damped sine curves as in **Figure 2.8a**, one curve for each distance within the molecule. Each distance has a distinct frequency and by Fourier transforming a modified form of the molecular intensities the radial distribution curve is obtained. Parameters (distances) can be read from this curve, but are actually obtained by fitting theoretical intensity curves to the experimental one.

2.2.3 Effect Of Molecular Vibrations

An important piece of structural information provided by the electron diffraction method is the extent to which molecules are vibrating. Molecular structure is better described as concerted motion rather than as simply a fixed arrangement of atoms. This dynamic element leads to several types of average internuclear distance being used to characterise the distance between an atom pair. Great care must be taken to choose the correct type of average distance in order that any study of free molecules has physical significance. Molecular vibrations modify the scattered intensities by the exponential term involving the mean amplitude of vibration, l_{ij}^2, of a distance r_{ij}. This is defined as the mean of the square of the difference between the equilibrium distance $r_{e,ij}$ and actual distance, r_{ij}^a, between two atoms i and j at a particular time

$$l_{ij}^2 = \left\langle \left(r_{ij}^a - r_{e,ij} \right)^2 \right\rangle \quad (2.16)$$

The structure-dependent molecular scattering intensity for a rigid system $I^r_{molecular}(s)$ can be written

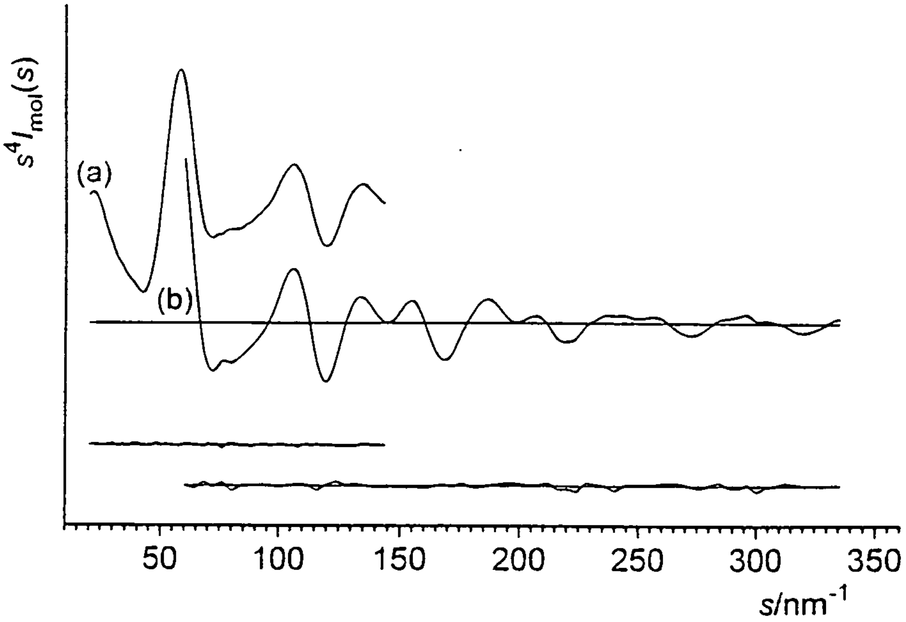

Figure 2.8a) Molecular intensity curves for benzene.

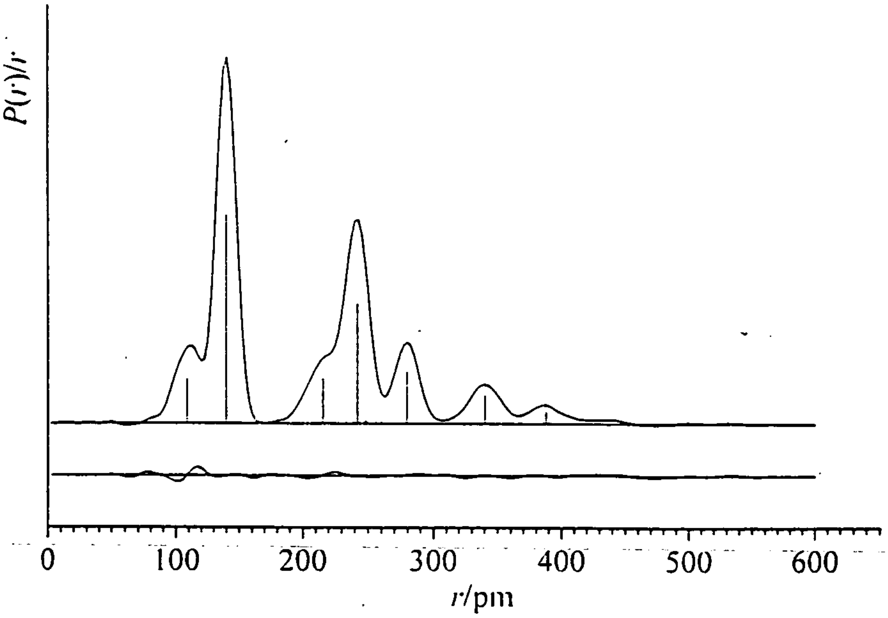

Figure 2.8b) Radial distribution curve for benzene.

$$I^{r}_{molecular} = \frac{I_o}{R^2}\sum_{i=1}^{N}\sum_{\substack{j=1\\ i\neq j}}^{N}|f_i||f_j|\cos(\eta_i - \eta_j)\frac{\sin(r_{ij}s)}{r_{ij}s} \quad (2.17)$$

During a vibration of an atom pair the atoms execute motion over a range of distances around some equilibrium separation. The amplitude of this motion is dependent on the temperature of the sample. In most electron diffraction experiments a distance averaged over all vibrational states for the potential between each atom pair is obtained. A good way to think of a vibrating molecule of N atoms is of a multidimensional potential surface comprised of N(N-1)/2 oscillating atom pairs each with its own potential well. If a distance distribution for r_{ij} is imposed of $P_{ij}(r)dr$ on **equation (2.17)**, where $P_{ij}(r)$ is the probability that the distance between atoms i and j is found between r and r+dr, then

$$I_{molecular}(s) = \frac{I_o}{R^2}\sum_{i=1}^{N}\sum_{\substack{j=1\\ i\neq j}}^{N}|f_i||f_j|\cos(\eta_i - \eta_j)\int_0^{\infty} P_{ij}(r)\frac{\sin(r_{ij}s)}{r_{ij}s}dr \quad (2.18)$$

$P_{ij}(r)$ for a given pair of atoms could in principle be calculated from a knowledge of the vibrational wavefunctions of the molecule and the population of each excited vibrational state, i.e. the Boltzmann factors for the excited vibrational states. The vibrational wavefunctions should (again in principle) be derived from a potential energy expression which includes anharmonic terms. Indeed this is one of the reasons for building this new apparatus. By using a laser to excite one particular vibrational mode in a chosen molecule it should be possible to populate one particular excited vibrational level within this mode highly. By analysing the electron scattering from this atom pair it may be possible to map out the vibrational wavefunction in this excited vibrational level.

If all molecular vibrations are assumed to be harmonic and of small amplitude, $P_{ij}(r)$ is a Gaussian function

$$P_{ij}(r) = \frac{1}{\sqrt{2\pi}\, u_{ij}} \exp\left[-\frac{(r - r_{ij})^2}{2u_{ij}^2} \right] \qquad (2.19)$$

where u_{ij} is the mean amplitude of vibration, and r_{ij} is the mean value of the distance between atoms i and j. Calculations of the harmonic force field of the molecule can lead to u_{ij}. For a general anharmonic force field $P_{ij}(r)$ is not Gaussian, but a somewhat distorted Gaussian, and its computation would be very laborious. There are two models used to treat the effect of anharmonic vibrations. For a large-amplitude mode where the energy level separations are small, a classical distribution may be used, i.e. for a potential energy function V(r)

$$P_{ij}(r) \propto \exp[-V(r)/RT] \qquad (2.20)$$

The other small-amplitude modes in the molecule are considered harmonic, and they contribute a broadening function which smears out the anharmonic $P_{ij}(r)$, as calculated by **equation (2.20)**. Where the effects of anharmonicity are small, the probability distribution of the ground vibrational state of a Morse oscillator is used

$$V(r) = D\{1 - \exp[-a(r - r_e)]\}^2 \qquad (2.21)$$

This function is a fairly good approximation to the true potential energy for diatomic molecules, so long as the deviation of r from r_e is not too large. The Morse function may also be reasonably used for the bond-stretching modes of polyatomic molecules. If a Morse-like anharmonic oscillator is assumed for the distance distribution, approximate evaluation of **equation (2.18)** leads to

$$I_{molecular}(s)=\frac{I_o}{R^2}\sum_{i=1}^{N}\sum_{\substack{j=1\\ i\neq j}}^{N}\frac{1}{r_{ij}s}|f_i||f_j|\cos(\eta_i-\eta_j)\exp\left(-\frac{1}{2}l_{ij}^2s^2\right)\sin\left[s\left(r_{ij}-\kappa_{ij}s^2\right)\right] \qquad (2.22)$$

the above expression is a slightly modified version of **equation (2.15)** with κ as an asymmetry parameter which is related to the Morse asymmetry constant and to the mean amplitude.

The vibrational motions of a molecule have two effects. First they damp out the molecular intensities; secondly they are also essential in defining different types of average internuclear distance exactly. In electron diffraction and spectroscopic studies of free, gas-phase molecules there are many ways of describing the internuclear distance between two atoms. They often differ in very subtle ways and are written with subscripted symbols, such as r_e, r_g, r_a and r_α, to distinguish between them. Detailed descriptions of the parameters currently used are given in references [13] and [19]. **Table 2.1** gives a brief review of the most important internuclear averages used in structural studies. The electron diffraction distances, r_{ij}, displayed in **equation (2.22)** are r_a. A good approximation useful for practical purposes is

$$r_a \cong r_g - l_{ij}^2 / r_a \qquad (2.23)$$

Table 2.1 Definitions of some distance parameters currently used in structural investigations of gas-phase molecules. The definitions in this table are taken from [13,19] and a full description of the link between electron diffraction and spectroscopy is given here also.

r_e	Distance between equilibrium positions
r_g	Average value of internuclear distance at thermal equilibrium; it can be defined as the centre of gravity of P(r) and can be related to r_e by $r_g=r_e+3al^2/2$, where a is the Morse function anharmonicity constant and l is the mean amplitude of vibration for the distance.
r_a	Distance obtained by least squares refinement of the molecular electron diffraction intensity curve. It is essentially related to r_g by $r_a=r_g-l^2/r_a$.
r_α	Distance between average nuclear positions at thermal equilibrium.

2.2.4 Radial Distribution Curves

In an electron diffraction experiment the total experimental scattering intensity $I_{total}(s)$ is composed of two parts

$$I_{total}(s) = I_{molecular}(s) + I_{background}(s) \qquad (2.24)$$

where $I_{molecular}(s)$ is the molecular scattering intensity containing all the information on the molecular geometry. The other term, $I_{background}(s)$, is the experimental background which can be written

$$I_{background}(s) = I_{atomic}(s) + I_{extraneous} \qquad (2.25)$$

where $I_{atomic}(s)$ is the total atomic scattering comprising the elastic and inelastic scattering. The $I_{atomic}(s)$ term can be evaluated exactly and is known as the theoretical background. If there was no extraneous scattering the total scattering could simply be divided by the theoretical background and this levelling would produce the molecular intensity data set. However in real electron diffraction experiments unwanted scattering arises from experimental imperfections such as reflections, aperture scattering and rest gas scattering. This extraneous scattering is a smooth function and has to be removed before structure refinement can take place. In data analysis a high-order polynomial is fitted to this extraneous background and it can be removed even though the exact contribution is not known. This can be improved as structure refinement proceeds. In structural analysis either $I_{molecular}(s) = I_{total}(s) - I_{background}$ or $I_{molecular} = (I_{total} - I_{background})/I_{background}$.

Once the molecular intensities have been separated from the other scattering that contributes to the total collected electron scattering, analysis of the molecular structure can proceed. In fact, if the modified molecular intensities, I′(s), are defined by

$$I'(s) = \frac{s\, I_{molecular}}{|f_k(s)||f_l(s)|} \qquad (2.26)$$

then it can be seen from **equation (2.26)** that for a homonuclear diatomic molecule (i=j=k=l) I′(s) is the Fourier transform of P(r)/r as follows

$$I'(s) = A\int_0^\infty P(r)\frac{\sin(rs)}{rs}dr \qquad (2.27)$$

where A is a constant. Consequently by inversion

$$P(r)/r = B\int_0^\infty I'(s)\sin(rs)ds \qquad (2.28)$$

where B is also a constant. Thus by Fourier transforming the modified molecular intensities the radial distribution curve (r.d.c.) is arrived at. The meaning of the r.d.c. is immediately clear if one recalls that, by definition, P_{ij}-(r)dr is the probability of an internuclear distance r_{ij} being found in the range r to r+dr.

To allow for the fact that experimental data are available in a certain s-range only, from s_{min} to s_{max}, a function similar to **equation (2.28)** is defined as

$$\sigma\ (r)/r = \int_{s_{min}}^{s_{max}} I'(s)\exp\left(-ks^2\right)\sin(rs)ds \qquad (2.29)$$

In the above expression the exponential damping reduces the effect of series termination errors. The term k is a constant which is chosen to make the quantity exp $(-ks^2_{max})$ equal to an empirically determined value. Data points are missing in the range $0 \leq s \leq s_{min}$ due to the beam stop for the incident electron beam. These missing points bend the zero line of the Fourier transform (adding a slope which is sometimes called the "envelope").

To overcome this lack of data at small scattering angles theoretical scattering intensities are used. A geometrical model constructed using bond lengths, bond angles and internal angles of rotation is created. This is used to produce a set of theoretical molecular scattering intensities and these are used in the refinement process. By fitting these theoretical intensities to the experimental intensities the molecular geometry is revealed. Data points in the range $0 \leq s \leq s_{min}$ from the best theoretical models rectify the problem of the lack of experimental data in this range. If experimental data start at around s = 2 or 3 $Å^{-1}$ the results of the data analysis are not influenced to too great a degree.

These approximations, together with the fact that, for polyatomic molecules, it is possible that $i \neq j \neq k \neq l$, lead to $\sigma(r)/r$ being only an approximation to the true radial distribution curve. Nevertheless it is referred to as the radial distribution curve by electron diffractionists. However, it presents a good physical representation of the atomic distribution within a molecule.

The radial distribution curve (see **Fig. 2.8b**) consists of a series of nearly Gaussian peaks corresponding to the internuclear distances r_{ij} within a molecule. The half-width of each peak depends on l_{ij}, with the area underneath following a relationship

$$area \approx \frac{n_{ij} Z_i Z_j}{r_{ij}} \qquad (2.30)$$

where Z_i and Z_j are the atomic numbers of the atoms making up the distance and n_{ij} is the multiplicity of that distance within the molecule. Structural information can be obtained directly from the r.d.c. for simple molecules but for larger, more complicated, molecules the distributions representing the distances may overlap and result in a loss of information.

As mentioned the experimental molecular intensities are compared with theoretical molecular intensities during routine electron diffraction. The geometrical model representing the molecule is constructed using estimates of the parameters that describe the molecule (bond distances, bond angles, torsional angles, vibrational amplitudes and occasionally relative amounts of conformers). By a least squares refinement process the parameters can be altered to fit the theoretical intensities to the experimental intensities. In this manner the structure of the molecule is worked out. It is thus important to have a good idea of the molecular structure before refinement and techniques such as microwave spectroscopy and increasingly quantum mechanical calculations are being used to support electron diffraction studies.

2.3 Limitations Of Scattering Theory

2.3.1 Introduction

In the theory used to describe the scattering of high-energy electrons by a molecular assembly several assumptions are made. Uncertainties are introduced into diffraction analyses by experimental imperfections but shortcomings in the theoretical expressions used must also be addressed. Obviously, it is futile for the accuracy of, say, experiment to exceed greatly that of the available theoretical framework. In favourable molecular examples, contemporary electron diffraction experiments could yield internuclear distances and amplitudes of vibration to the order of 10^{-4} Å if the theoretical model utilised was sufficiently accurate.

The main problem lies in applying quantum scattering theory to real target molecules. Virtually all electron diffraction studies of molecular structures are based on the independent atom model (IAM). In this model, the electron density is taken to be the sum of spherically averaged atomic densities. These atoms are further assumed to be undergoing small amplitude harmonic or nearly harmonic vibrations. A further assumption is that the scattering by each atom is small enough to allow the application of a kinematic or quasi-kinematic treatment. The three main sources of error are thus:

1. Atoms in molecules are not spherical

2. Atomic motions are not harmonic

3. Scattering potentials are not really weak.

2.3.2 Kinematic Theory

In the kinematic approximation, known as the "Born approximation" when applied to electron diffraction, it is assumed that the scattering is so weak that the electron wave encountering each volume element is the incident plane wave itself, unattenuated by the scattering from previous volume elements, unaugmented by wavelets arriving from other volume elements, and unshifted in phase as the electrons accelerate in the attractive fields of the atoms doing the scattering. It is readily seen that such an approximation does not even conserve electron flux. Nevertheless, it yields quite good results for the diffraction of 40 keV electrons by molecules composed of relatively light atoms.

The Born approximation is well known to predict exactly, in the nonrelativistic region, the intensity of electrons scattered by a Coulomb field. It is a perturbation method and there are several levels to which the theory can be invoked. Generally the 1st Born approximation is used in electron diffraction. The assumption is that the scattered wave is small compared to the incident wave and the wavefunction of the incident electron remains unaltered. The 1st Born approximation holds particularly well at small scattering angles. To undergo a small deflection an incident electron must approach the target nucleus with a relatively large impact parameter. This large distance between the electron and nucleus leads to a small perturbation of both the incident electron and atomic wavefunctions.

2.3.3 Independent Atom Model (IAM)

There are two assumptions made under the independent atom model. These are that atoms within a molecule are spherically symmetric isolated charge centres, i.e. point scatterers, and that the vibrational motion between pairs of these atoms is harmonic or nearly harmonic. This of course is contrary to the situation in real molecules.

There are two errors with this picture of atoms as point scatterers even in a kinematic framework. Firstly, even if bond formation did not polarise electron clouds, only atoms with filled or half-filled subshells would be (nominally) spherical. To participate maximally in normal covalent binding, atoms mutually align their asymmetric electron distributions to get overlap between participating orbitals. Secondly, once atoms have aligned themselves mutually there is a charge redistribution to minimise energy. Corrections to the IAM approximation from the second effect, the redistribution, are often modest compared with those from the first.

The effects of anharmonic vibrations manifest themselves in the scattering pattern. As molecules vibrate, the interference fringes they produce swell out and recede in synchrony. While this scarcely changes the innermost fringes, the oscillating displacements of the outer fringes exceed the natural fringe spacings, crests and troughs average out, and the interference is smeared out. This results in a loss of information in the diffraction pattern relative to the case in which the molecule was more rigid. A further problem arises in that because the potential energy surface on which the atoms oscillate has skewed rather than symmetric potential wells, and so the spacings of the fringes lose their periodicity. Outer fringe spacings relate approximately to the most probable internuclear distances, while inner spacings are determined by the centres of gravity of the distances. When the distribution of vibrational displacements is broad and highly skewed from anharmonicity, the discrepancy between mean and most probable can be substantial and confuse the very meaning of molecular structure.

Even with purely harmonic vibrations non-bonded distances suffer shrinkage effects that foreshorten them more than would be the case in a more rigid molecule with the same equilibrium bond angles. However, anharmonic vibrations have a more profound effect on non-bonded distances when bending amplitudes are large due to either the temperature of the molecule or its intrinsic flexibility.

This effect is known as "anharmonic shrinkage" and unlike the true shrinkage effect, where bending vibrations appear to shorten bond lengths in molecules, in particular linear molecules, it manifests itself in a slightly different manner. Anharmonic shrinkage has the effect of skewing the radial distribution peaks for non-bonded distances, shifting the maximum but leaving the centre of gravity untouched. The true shrinkage effect displaces both the maximum and the centre of gravity.

2.3.4 Breakdown Of Kinematic Theory

When an electron encounters an atom and undergoes a collision the incident electron wave suffers a phase shift as it traverses the atomic field, irrespective of the atomic number. As the electron approaches the nucleus it is attracted and the resulting acceleration decreases its de Broglie wavelength. While passing the nucleus and beyond, the electron decelerates to its original speed and wavelength if it has undergone an elastic collision. The resulting scattered wavelets are shifted in phase and electrons encountering heavier atoms experience a larger phase shift. The phase shift of the electron increases with increasing scattering angle as there is a semiclassical relation between closeness of approach to the nucleus and angle of scattering, and closeness of approach and depth of scattering potential.

In a molecule where some atoms are much heavier than others, thus having a deeper scattering potential, the resultant larger phase shifts can have a profound effect on the diffraction pattern produced. If one considers the form of **equation (2.18)** the important term for phase shifts is $\cos(\eta_i-\eta_j)$. Within the s ranges commonly used in electron diffraction the difference $\eta_i-\eta_j$ may pass through $\pi/2$, the point where $\cos(\eta_i-\eta_j)$ first changes sign and vanishes. Also as $\eta(s)$ increases monotonically with s, and increases faster the higher the atomic number, the envelope $\cos(\eta_i-\eta_j)$ resembles the envelope of two beating sine waves of slightly different frequencies.

Glauber and Schomaker [15,16] were the first to recognise that omission of the angle-dependent phase factor η in the scattering amplitude (see **eq. 2.8**) constituted a large error in the Born approximation. They noted that in molecules of the form MX_n, where M is a single heavy atom, the distances between the heavy atom and its neighbours were split into two equal groups differing by an amount roughly proportional to Z_M-Z_X. For equal atomic numbers as in the heavy molecule I_2, no splitting was observed. The splitting occurs because of the envelope of two beating sine waves that arise from the large difference in phase shifts between heavy and light atoms. Upon Fourier transformation two distinct distances are produced. The breakdown of the so-called kinematic approximation is sometimes ascribed to this intra-atomic multiple scattering.

Figure 2.9 illustrates the situation when an incident electron wave encounters an atom pair where one atom B is much heavier than the other atom A. The electrons incident on atom B experience a more substantial phase shift giving rise to the effect described above.

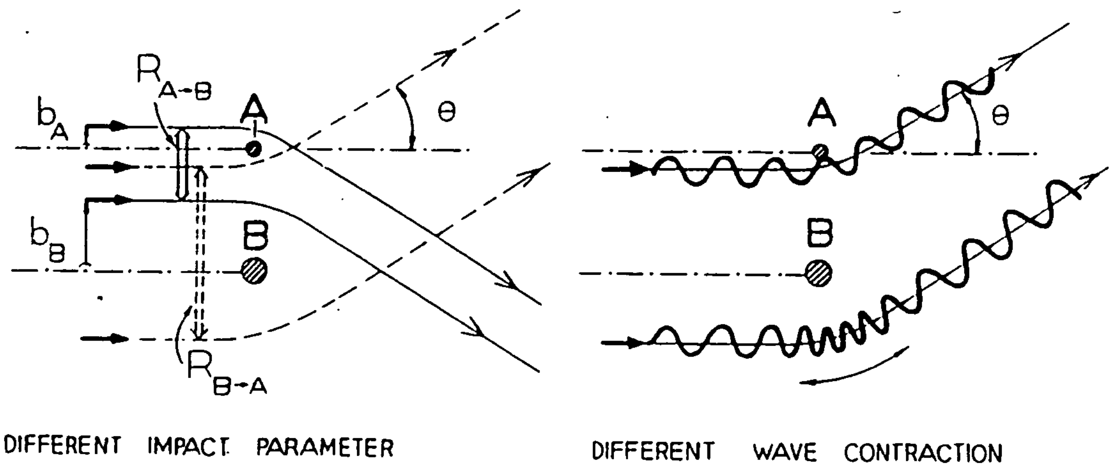

Figure 2.9 Semiclassical rationale of failure of kinematic scattering theory in case of an electron wave encountering a light atom (A) and a heavy atom (B). The phase retardations $\eta_A(s)$ and $\eta_B(s)$ neglected in kinematic theory are due partly to the real path length differences resulting from the different impact parameters b_A and b_B corresponding to a common scattering angle θ, and partly to different wave contractions in the atomic fields. Taken from [12].

By adopting complex scattering factors computed by the partial wave method structure analyses were improved. However, another effect which is not quite so well known, and less widely compensated for, is the interatomic, intramolecular multiple scattering. This effect occurs when one atom eclipses another. The scattered wave from the first atom is modified and the assumed incident plane wave is anything but planar as it encounters the second atom. When this double-scattered wave meets and interferes with another scattered wave the interference pattern becomes decidedly complicated.

The use of complex factors gives rise to the quasi-kinematic approximation. This still fails to conserve flux. To treat interatomic multiple scattering properly orientational averaging over the three Eulerian angles must be carried out. This makes computation difficult and time consuming but Kohl and Arvedson [20] did some excellent work on this topic based on a modified version of Glauber's theory. Their treatment is too demanding computationally to be practical for frequent application although a simpler analytical form of solution is available.

Interatomic, intramolecular multiple scattering effects show up in systems even where the atomic numbers are identical but they are more serious when atomic numbers are larger. They were first noticed by Seip [21] whilst looking at UF_6 but were properly investigated by Jacob and Bartell [22] when looking at ReF_6. The fact that this type of scattering occurs even when atomic numbers are identical is different from the quasi-kinematic result in which atomic numbers must be substantially different before its effects become apparent.

Bibliography

1 E. Rutherford, Phil. Mag., 21 (1911) 669

2 P. Debye, Ann. Physik, 46 (1915) 809

3 P. Debye, Phys. Z., 31 (1930) 419

4 P. Ehrenfest, Amsterdam Acad., 23 (1915) 1132

5 C. Davisson and L.H. Germer, Phys. Rev., 30 (1927) 705

6 G.P. Thomson, Proc. Roy. Soc. (London), A117 (1928) 600

7 G.P. Thomson, Proc. Roy. Soc. (London), A119 (1928) 651

8 H. Mark and R. Wierl, Naturiwiss., 18 (1930) 205

9 The theory of atomic collisions, 3rd ed., Eds.: N.F. Mott and H.S.W. Massey, (Clarendon Press, Oxford, 1965)

10 High energy electron scattering, Eds.: R.A. Bonham and M. Fink (Van Nostrand Reinhold Co., New York, 1974) ACS Monograph 169

11 H.M. Seip, in: Molecular structure by diffraction methods, Eds.: G.A. Sim and L.E. Sutton (Chemical Society, London, 1973) 7

12 J. Karle, H.F. Mark, and I. Hargittai in: Stereochemical applications of gas-phase electron diffraction, Eds.: I. Hargittai and M. Hargittai, (VCH, Deerfield Beach, 1988)

13 L. Schäfer, Appl. Spectrosc., 30 (1976) 123

14 H. Faxen and J. Holtsmark, Z. Physik, 45 (1927) 307

15 R. Glauber and V. Schomaker, Phys. Rev., 89 (1953) 667

16 V. Schomaker and R. Glauber, Nature, 170 (1952) 290

17 L. Schäfer, A.C. Yates, and R.A. Bonham, J. Chem. Phys., 55 (1971) 3055

18 D.T. Cromer, J. Chem. Phys., 50 (1969) 4857

19 A.G. Robiette in: Molecular structure by diffraction methods, Eds.: G.A. Sim and L.E. Sutton (Chemical Society, London, 1973) vol 1, 160

20 D.A. Kohl and M.M. Arvedson, J. Chem. Phys., 75 (1981) 2736

21 H.M. Seip, Acta Chem. Scand., 19 (1965) 1955

22 E.J. Jacob and L.S. Bartell, J. Chem. Phys., 56 (1972) 2364

Chapter 3

Experimental Apparatus

3.1 Introduction

This new apparatus was designed to study the structure of gas-phase molecules using high-energy electron diffraction. Using state-of-the-art technology it was hoped that this apparatus could complement the existing conventional electron diffraction apparatus at Edinburgh University and in time extend the range of molecules investigated to include ions and excited states.

The apparatus is shown schematically in **Figure 3.1** and in photograph form in **Figures 3.2** and **3.3**. It consists of three main components; a skimmed supersonic molecular beam source, a telefocus electron gun and a novel, position-sensitive electron detector. These are housed within a complex, high vacuum system.

Each of the three main components will be introduced briefly in this chapter as full descriptions will be given in subsequent chapters. Both the molecular beam and the electron beam have been well characterised. These results are presented in **Chapters Four** and **Five** respectively. The position-sensitive electron detector is also introduced with a full account given in **Chapter Six**.

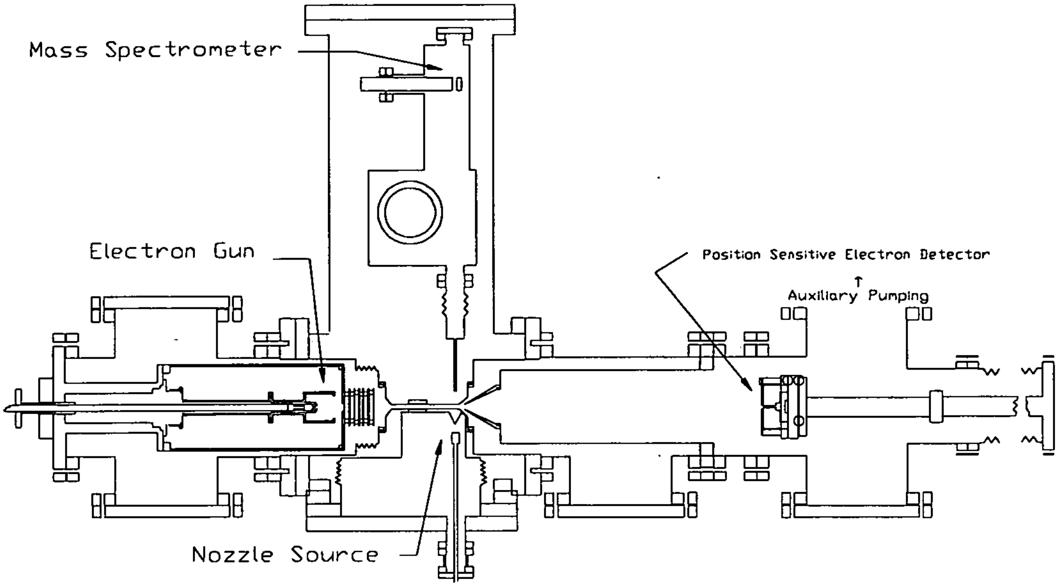

Figure 3.1 Overall schematic of Edinburgh electron diffraction apparatus. The apparatus measures aproximately 3.5 metres along the electron beam axis and 2.5 metres along the molecular beam axis.

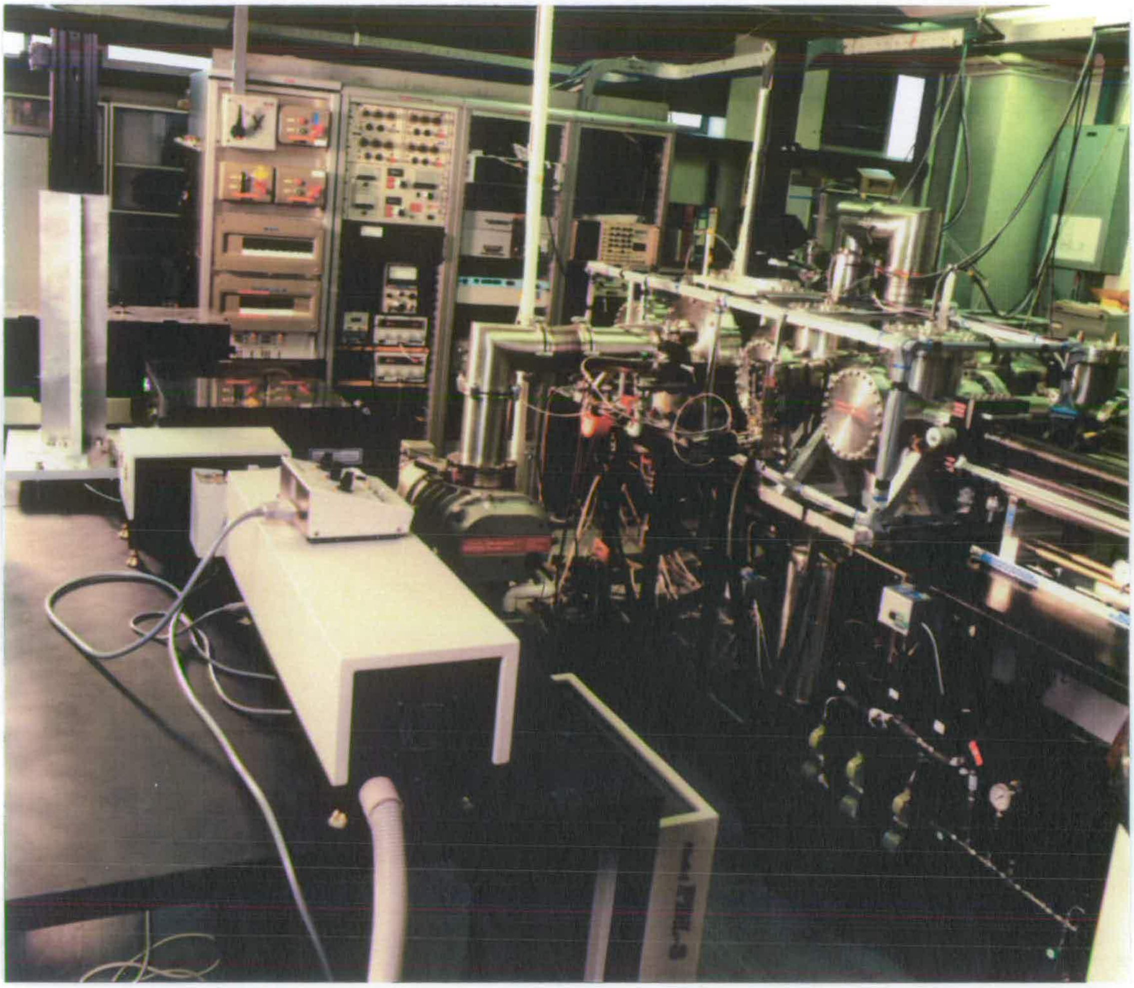

Figure 3.2 View of apparatus from molecular beam source side. The Roots blower combination that provides pumping for the nozzle chamber can be seen in the centre of the picture beneath the L-shaped metal tube. This tube is connected to the nozzle source flange, upon which is mounted an xyz translator to position the molecular beam, the nozzle power supply feedthrough and a Pirani gauge to measure the nozzle chamber pressure. The electron gun chamber is just above and to the left of the nozzle chamber in this picture. The detector xyz translator can be seen on the extreme right. The controls for the apparatus are at the top of the picture. The laser system pictured in the foreground was used to investigate the feasibility of creating ionised species in the molecular beam. It consisted of a Nd-YAG pumped dye laser with wavelength extender.

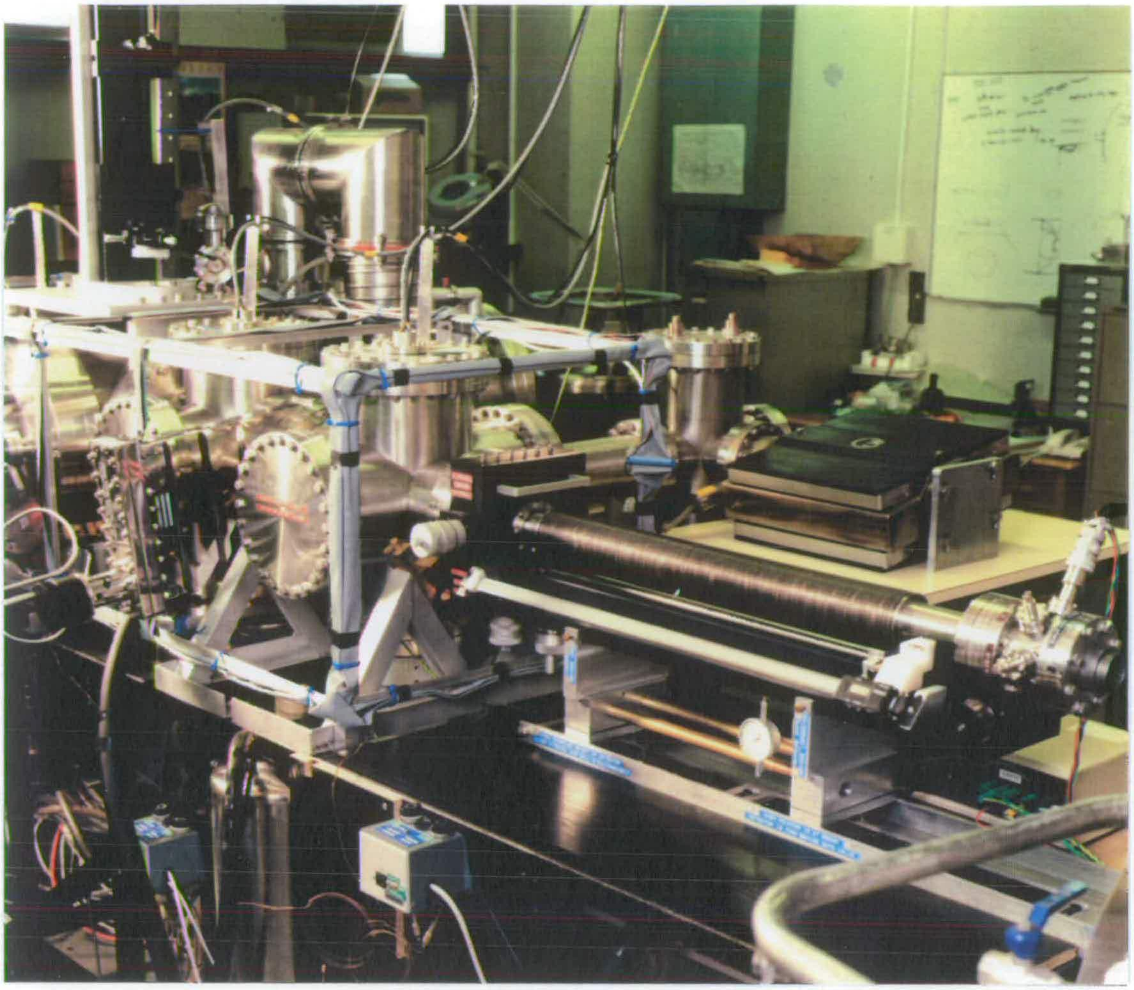

Figure 3.3 View of apparatus showing detector chamber and xyz translator for positioning detector. The gate valve which isolates the detector from the main part of the apparatus can be clearly seen on the left-hand side. The ion pump that provides an oil-free high vacuum environment for the detector is also pictured. On the extreme right hand side of the picture the vacuum feedthrough for the detector can be seen together with smaller feedthroughs for the microchannel plate connections and the electron beam monitor.

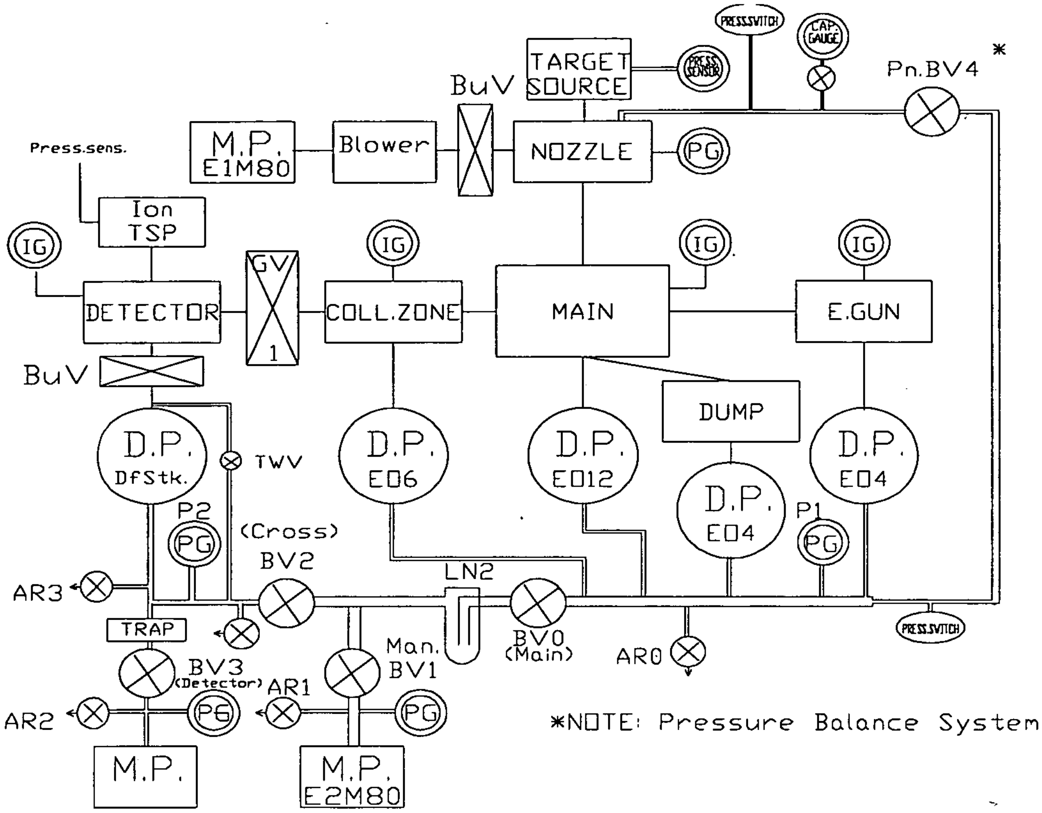

Figure 3.4 Vacuum schematic of the electron diffraction apparatus.

DP - Diffusion Pump
MP - Mechanical Pump
TSP - Titanium Sublimation Pump
PG - Pirani Gauge
IG - Ion Gauge
AR - Air Release
GV - Gate Valve
BV - Backing Valve
TWV - Three Way Valve
LN2 - Liquid Nitrogen
Pn. BV4 - Pneumatic Backing Valve
BuV - Butterfly Valve

3.2 Vacuum System

The apparatus comprises two sets of differentially pumped chambers arranged so that the high-energy electron beam interacts perpendicularly with the molecular beam in a fixed beam tube. A schematic of the vacuum system is shown in **Figure 3.4.**

The molecular beam-line consists of three differentially pumped chambers. The target gas molecules have entered the nozzle chamber at stagnation pressures of up to 40 bar (5% CO_2 in an He buffer). However, recently pressures of less than 10 bar have been used. An explanation of this is given in the next chapter. The pressure in the nozzle chamber is kept between 0.1 and 10 mbar (under a gas load) using an Edwards E1M80 mechanical pump combined with a mechanical booster pump (see **Fig. 3.2**). After passing through the skimmer and beam-tube assembly they travel into the dump tank via a flexible tube. This chamber is pumped by a small Edwards EO4 oil diffusion pump. This chamber sits inside the much larger main chamber which is pumped by an Edwards EO12 oil diffusion pump. The main chamber acts as an outlet for gas molecules that leave the centreline molecular beam. The typical operating pressure when the molecular beam is operating is $1x10^{-6}$ mbar.

There is differential pumping along the electron beam path also. The electron gun is housed in a chamber pumped by an Edwards EO4 oil diffusion pump with a liquid nitrogen cryogenic trap. This produces a pressure of around $7x10^{-7}$ mbar.

The scattering chamber is split into two by a retractable gate valve. When the detector is not in use an Edwards EO6 oil diffusion pump with a liquid nitrogen cryogenic trap maintains a pressure of about $2x10^{-7}$ mbar. A Leybold Heraeus ion-pump is used to provide an oil-free environment with a pressure of around $3x10^{-7}$ mbar in which the detector is stored, in particular the microchannel plates.

When the detector is to be operated a Diffstak cryopump is used to pump down the detector chamber. A butterfly valve can be used to isolate the chamber from the cryopump. With the gate valve open and both diffusion pumps operating a pressure of 2×10^{-7} mbar or lower can be maintained throughout the full scattering chamber.

The Diffstak cryopump is backed by a small mechanical rotary pump. The other four oil diffusion pumps are backed by an Edwards E2M80 mechanical pump. Both mechanical pumps are part of a roughing line that can be made continuous by opening an electrical solenoid valve (BV2). The backing line pressure is generally around 5×10^{-2} mbar.

A safety system comprised of two pressure sensors and a nitrogen operated solenoid valve is used to maintain a pressure difference of less than 20 Torr on either side of the skimmer wall during operation. The reason for using this safety system was because of the large difference in pumping speeds on either side of the skimmer wall. Initially the nozzle chamber was pumped down from atmospheric pressure by the single stage mechanical pump attached to the Roots blower. The rest of the apparatus, that is, the main chamber, the electron gun chamber and the collision zone were roughed by the two-stage mechanical pump via the backing line. The nozzle chamber is effectively sealed from the rest of the apparatus except for the small aperture of the skimmer which has a diameter of 0.18 mm. This led to the nozzle chamber being pumped down to say $5/6 \times 10^{-3}$ mbar whilst the other chambers were near atmospheric pressure. This pressure difference caused the flexible bellows inside the nozzle chamber (see **Fig. 3.1**) to buckle and twist the skimmer box. This resulted in damage to the skimmer box and subsequent welding caused permanent magnetism around this seal. In **section 3.4** the effects of this and other sources of magnetism are discussed.

A connection to the flange on the outside of the nozzle chamber which had supported a Pirani gauge was used instead as an extension of the main foreline of the machine. Thus all the chambers were roughed by the E2M80 mechanical pump. In **Figure 3.4** the pressure balance system is seen to consist of two pressure switches and a pneumatic valve (Pn. BV4). These three items are connected in such a way that if a pressure difference of greater than 20 Torr occurs on either side of the pneumatic valve a nitrogen cylinder connected provides a short burst of gas to open the valve. Once both sides of the roughing line are down to a good roughing pressure a burst of gas closes the valve. If the gas supply is disconnected the valve stays open continuously. Several ion gauges and Pirani gauges are used to monitor the vacuum system.

3.3 Molecular Beam Source

The molecular target species in this apparatus is provided by a Campargue source [1,2]. This is a skimmed, supersonic molecular beam source that produces a narrow, monoenergetic beam of gas-phase molecules. It can operate at stagnation pressures of up to 40 bar. At stagnation pressures above this the nozzle source can be pulsed.

In the apparatus the target species, typically 5% CO_2 by volume, in He carrier is introduced into the system via a General Valve nozzle operated by a General Valve pulsed valve driver. The resultant beam is then skimmed by a Beam Dynamics skimmer before the interaction region. The beam composition and intensity can then be monitored further downstream using a Leda Mass quadrupole mass spectrometer.

3.4 Telefocus Electron Gun

The high-energy electron beam in this apparatus is produced by a telefocus electron gun [3-7] powered by a high-voltage power supply. The gun was designed by Hermann Wellenstein of Brandeis University, Boston and was constructed by Chip Theusen at the University of Texas in Austin. The power supply is a commercial device purchased from Start Spellman.

The supply feeds a current of up to 2.50 Amperes (usually 2.30 Amps is used) to the gun filament. It also maintains the high voltage on the filament and the variable voltage between the filament and the gun optics. The supply can produce stable voltages of up to 50.00 kV with an accuracy of 0.01%. Practically the maximum voltage is around 49.00 kV, probably due to the gun optics being slightly dirty.

The telefocus electron gun is capable of producing high beam currents which are stable over a long period of time (several hours). The beam can be focused to a small spot size (around 0.5/6 mm) over a wide range of distances.

Initially the gun could produce beam currents on two current scales; 0-5 μA and 0-100 μA. Subsequent alterations to the power supply to improve E.H.T. stability led to these two scales being reduced a hundred-fold to 0-50 nA and 0-1000 nA. However the 0-50 nA current range is inoperable due to the large capacitance of the electron gun and the heavy duty cable that connects it to the power supply.

Creating a steady beam, however, is only half of the problem in electron diffraction. Any sources of magnetism, including the earth's magnetic field, can deflect a moving stream of charged particles from its trajectory.

A static homogeneous field within the instrument can be resolved into two components [8], one parallel (B_{parallel}) and one perpendicular ($B_{\text{perpendicular}}$) to the axis of the beam. In electron diffraction the perpendicular distance from the diffraction centre to the detector L, and R, the distance from the centre of the detector to the point of registration, are critical. If there is a magnetic field present any parallel component will have a tendency to modify the ring radii by an amount

$$\frac{\Delta R}{R} = \frac{1}{24}\left(\frac{eB_{parallel}}{mv}\right)\left(L^2 + R^2\right) \qquad (3.1)$$

leading to spreading of the concentric rings of the Deybe-Scherer pattern. A perpendicular component will tend to deflect the beam by an amount

$$\varepsilon = \frac{1}{2}\left(\frac{eB_{perpendicular}}{mv}\right)\left(L^2\right) \qquad (3.2)$$

For 40 keV electrons, fields of the order of a few tenths of a Gauss (typical values for terrestrial fields) have a negligible effect.

In this apparatus, to counteract the effect of the earth's magnetic field current carrying wires known as Helmholtz coils [9] form a three-dimensional lattice around the main chambers through which the electron beam passes. These coils can clearly seen in **Figures 3.2** and **3.3** as the grey strips held in place with blue cable grips. The result is that a volume inside the network of coils becomes virtually a field-free region. Coupled with this is the fact that most of the components are made of non-magnetic steel, brass and aluminium. Hence they contain no residual magnetism.

However, these measures have not been sufficient enough to allow the undeflected passage of the electron beam. An initial problem was that the base of the machine was made out of magnetic steel. Directly attached to this base were three solenoid valves that operated liquid nitrogen fillers as can be seen in the bottom left of **Figure 3.2**. Each time these were switched on they magnetised the frame. By placing a wooden board between the frame and the valves this problem was removed.

It was then found that the Roots blower combination pumps that operate the molecular beam caused the deflection of the electron beam. While trying to observe attenuation of the electron beam by the molecular beam a decaying and oscillating signal was detected in a collector downstream of the collision zone.

This was because the axis of rotation of the blades of the pumps was parallel to the axis of the molecular beam. This created a magnetic field with a component perpendicular to the electron beam direction. Thus it deflected the electron beam from its path. By moving the pumps by ninety degrees and slightly further away from the electron beam (see **Fig. 3.2**) this effect was diminished.

Magnetic effects were also experienced within the Helmholtz coil network. Initially the skimmer box was made out of two pieces of stainless steel that had been welded together. As mentioned in **section 3.2** this box had to be rewelded when it was twisted in the vacuum system. This further welding helped to create a localised magnetic field of up to 300 mG in places and had a catastrophic effect on the electron beam. Attempts were made at degaussing this box but these proved useless. The box was then remade in one piece out of aluminium.

The pulsed valve also produced an unwanted magnetic field contribution due to the solenoid valve that it uses in its operation. The method used to reduce this was to place a can made out of Mumetal [9] over the nozzle source.

Mumetal is a special alloy which has a high permeability. Thus it reduces the magnetic field inside any volume that it encloses to virtually zero. However if it is made into an open cylinder the magnetic field at the open ends is quite large. If small holes are put in any box or cylinder made out of

Mumetal a small magnetic field can extend out of the Mumetal to a distance equal to that of the diameter of the hole.

Mumetal was used in open and closed cylinder form inside the gun chamber and was made into a box that followed the contours of the skimmer box. It was found that the edges of such metal shields actually made the magnetic situation worse inside the nozzle chamber and collision zone. At present the only Mumetal sheeting used in the apparatus is an open cylinder covering the outside of the re-entrant tube which encloses the scattering chamber.

Less than 10 mG in any direction is a good Figure to aim at for the size of the magnetic field near the collision zone. Most of the Mumetal shielding was removed and the settings of the Helmholtz coils changed slightly to produce a virtually field-free region around the collision zone. Readings of the magnetic field were taken without the beam tube in position and the maximum field, at any point around the area where this tube normally sits, in each of the three dimensions, was found to be about 20-30 mG.

Initially the tube in which the two beams intersect was constructed out of brass. A tube made of a single piece of Mumetal was designed and built and is now in place in the machine.

Another method of changing the direction of travel of the electron beam is by using electrical deflector plates. At present a set of x and y deflector plates are used to ensure that the electron beam passes through the beam tube via the collision zone. The brass beam tube had two copper collars which were used as collectors to aid beam centring. One of these was placed at the entrance to the beam tube while the other sits just before the collision zone. The Mumetal beam tube has no collars for beam centring and the deflections required with the brass tube were assumed to be the same for the

Mumetal tube. A second set of deflector plates can be added to increase flexibility in beam positioning.

To aid beam centring there is a Faraday cup and four sectors positioned behind the 6 mm hole in the microchannel plates and the detector anode. At the moment there is an acceptable magnetic field in the apparatus. The deflector voltages required to centre the beam are currently 40 V horizontally and 80 V vertically. Voltages less than 100 V in each dimension are adequate.

To reduce extraneous scattering the inner surface of the aluminium cone at the left hand side of the scattering chamber is coated with Aerodag. This is a form of graphite paint and acts to absorb stray electrons which otherwise could collide with the chamber walls and create, for example, X-rays which could damage the detector, or reflect into the detector, causing a significant background signal. The reason for using aluminium for this aperture is that this material produces only negligible X-ray radiation at 40 keV.

3.5 Position-Sensitive Electron Detector

The electron detector used in this apparatus consists of two components. The diffracted electron image is collected by a set of stacked HOT (high optical technology) microchannnel plates (MCPs) [10] with an active area of diameter 75 mm and a central hole of diameter 6 mm. This device amplifies the electron image which is then counted by the novel position-sensitive detector [11,12]. This detector was designed and built by a company a called Integrated Sensors Limited (ISL) based at UMIST in Manchester. The detector was designed by J.V. Hatfield and J. Goldfinch.

The electron counter consists of a set of independent angularly and radially disposed electron sensing electrodes mounted onto a thin ceramic plate. In the present design there are 168 electrodes arranged in 83 concentric annular rings. Of these 168 electrodes only 128 are in use. The operations of these sensors are controlled by four microchips bonded to the rear of the ceramic plate. The anode detector is capable of counting rates of 4 MHz.

The whole detector is mounted on a translator assembly that permits three dimensional movement (see **Fig. 3.3**). This allows the distance from the scattering centre, or collision zone, to be changed quickly and accurately providing scattering data at a wide range of angles.

3.6 Computer Control And Data Collection

A sophisticated control program was written in QuickBasic by Dr. M.A.D. Fluendy to monitor the apparatus during operation and to aid data collection from the electron detector. This program incorporated a set of routines known as NIDAQDOS. This program was run by an RM VX486 P.C. and a data card was installed in the P.C. to monitor eight analogue inputs from the machine. These included five inputs from sensors used to centre the electron beam together with signals from the MCPs, the nozzle pressure gauge and the pressure gauges on the backing line. A separate card known as a frame-grabber was used to collect data from the detector.

The basic control philosophy is that all routine activities should be carried out under program control. This includes achieving appropriate vacuum conditions, establishing both electron and molecular target beams and their associated diagnostic monitors. The program also controls the normal operation of the electron detector, the collection of data and provides facilities to monitor the progress of the experiment.

Reliable self protection arrangements are provided to ensure that the apparatus is not damaged by possible failures. This is provided at the basic level by hardware which interlocks the vacuum system, the diffusion pumps and various power supplies for the electron beam and detector components. Two interlock channels each with two interlock stages are provided.

One channel controls the vacuum isolatable parts of the system known as main which comprises the electron gun, main, dump and collision zone chambers. The other channel controls the detector chamber and its associated hardware. The first stage interlock in each case monitors the water flow, temperature and foreline pressure backing the diffusion pumps used to evacuate the chambers. The backing pressure for the main part of the apparatus is monitored by the Pirani gauge P1 and the detector section backing pressure is monitored by P2 (see **Fig. 3.4**). This stage of the interlock controls the power to all the diffusion pumps. The set point for the diffusion pump backing pressure is 3×10^{-1} mbar.

The second stage of each interlock channel monitors the high vacuum pressure in the main and detector sections of the apparatus using the ion gauge set point (8×10^{-5} mbar) and the trip level set point in the ion pump power supply (around 1×10^{-5} mbar) respectively. This stage controls mains power to the electron gun supply, the gun deflector plate supplies and the MCP high voltage supply.

Additional protection is provided at the software level by monitoring the various water, temperature, foreline and high vacuum trips to generate a vacuum profile which is compared with a set acceptable pattern. The program also monitors analogue inputs from the detector ion pump and the scattering chamber ion gauge. Acceptable levels for these pressures are also set to provide early warning of vacuum difficulties and to turn off the electron gun and detector MCP supplies.

These functions are carried out by a slow autonomous analogue scan over the eight A>D channels which continuously updates a rolling 256 long data buffer. The data in this buffer are examined at intervals determined by the control program and if necessary sensitive components of the machine are shut down.

The two possible modes in which the program can be started are known as hot and cold. These correspond to the initial state of the apparatus and the cold start is when only the detector ion pump is on and the rest of the machine is in normal rest state. In this case all auto/manual switches must be at auto. Alternatively the apparatus may be fully or partially on and is said to be in the hot state. If a hot start is required all auto/manual switches must be set to manual. As much of the work carried out on the machine was developmental, provision was made to allow a choice between manual and computer control. Indeed, virtually all the work reported in this thesis was undertaken via manual control.

Bibliography

1 R. Campargue, J. Phys. Chem., 88 (1984) 4466

2 D.R. Miller in: Atomic and molecular beam methods, Ed.: G. Scoles, (Oxford University Press, Oxford/New York, 1988) Ch .2, 14

3 K.H. Steigerwald, Optik, 5 (1949) 469

4 F.W. Braucks, Optik, 14 (1958) 242

5 E.B. Bas and F. Gaydou, Z. Angew. Phys., 11 (1959) 370

6 H. Schmoranzer, H.F. Wellenstein, and R.A. Bonham, Rev. Sci. Instrum., 46 (1975) 89

7 B. Schiewe, H. Schmoranzer, and P. Wollenweber, Rev. Sci. Instrum., 48 (1977) 893

8 R.L. Hilderbrandt in: Molecular structure by diffraction methods, Eds.: G.A. Sim and L.E. Sutton, (The Chemical Society, London, 1975) Vol. 3, Ch. 2, 25

9 Building scientific apparatus, Eds.: J.H. Moore, C.C. Davis, M.A. Coplan, (Addison-Wesley Publishing Co., USA, 1989)

10 J.L. Wiza, Nucl. Instrum. and Meth., 162 (1979) 587

11 J.V. Hatfield, S.A. Burke, J. Comer, F. Curell, J. Goldfinch, and T.A. York, Rev. Sci. Instrum., 63 (1992) 235

12 J.V. Hatfield, J. Comer, T.A. York, and P.J. Hicks, Rev. Sci. Instrum., 63 (1992) 792

Chapter 4

Molecular Beam

4.1 Introduction

As the main reason for building this new apparatus was to extend the range of molecules and chemical systems studied by gas-phase electron diffraction a molecular beam source was chosen to accommodate this. Most electron diffraction instruments incorporate an effusive molecular beam source. However, in this new apparatus a Campargue-type free jet [1] was chosen to project the target molecules across the high-energy electron beam. There are three main advantages of this source over the more commonly used effusive source. Firstly, target densities of up to 1000 times that of the effusive source can be obtained for similar geometries. Secondly, the operation of the free-jet source leads to substantial cooling of the rotations and vibrational modes of the target molecules making it ideal for use in state-specific experiments. Through multiple molecular collisions the target molecules form a nearly monoenergetic beam characterised by very narrow distributions [2]. The velocity distribution parallel to the molecular flow is so narrow that essentially all molecules are travelling at the same speed. Using a laser pulse of known energy a single transition to a rovibrational level in an upper electronic state can be excited. This state-selectivity combined with the increased sensitivity of the new detector should allow the elucidation of the structures of the excited states, including ions, of many molecules. Finally, the cooling is also ideal for creating clusters and van der Waals molecules.

This new apparatus, together with this particular source, is capable of performing a wide range of novel experiments. Seven such classes of compounds and chemical systems are:

1. compounds with low vapour pressures

2. unstable molecules
3. floppy molecules in their ground states
4. clusters and van der Waals molecules
5. molecular excited states
6. molecular ions
7. time-dependent phenomena.

The final three classes of experiment listed above are only possible with laser excitation.

The study of compounds with low vapour pressures is a straightforward application. It will be possible to study compounds which decompose before their vapour pressure reaches 1 Torr (10^2 Pa) but can provide 10^{-3} Torr or more. This is an enormous category, including particularly large numbers of organic and organometallic compounds , for which gas-phase structures are increasingly needed for comparison with theoretical data. Almost any compound which can be sublimed can potentially be studied. Dissociation equilibria can also be investigated at lower temperatures. For example, important semi-conductor precursors such as $Me_3P.InMe_3$ are dissociated to a large extent at temperatures at which their vapour pressures reach 1 Torr. However, the cooling effect of the free-jet should allow the structure of the complex to be studied together with the thermodynamics of the dissociation process.

The ability to investigate compounds at lower vapour pressures than are necessary at present (10^2 Pa) should allow the determination of the structures of compounds of low thermal stability. Species such as phospha-ethene, $PH=CH_2$, sila-ethene, $SiH_2=CH_2$, together with other unstable compounds containing multiple bonds to second-row elements could be investigated. The study of S_2N_2, the precursor to the one-dimensional conductor 'polythiazyl', $[SN]_x$ could be undertaken. Other species worthy of study include PO_2Ph and PFS_2, which are the simplest known examples of phosphorus(V) in the rare 3-coordinated state, and can be cleanly generated by flash vapour pyrolysis, but only at pressures of up to ~10 Pa.

The cooling of the vibrational modes in the supersonic expansion will allow investigation of the ground vibrational states of so-called floppy molecules. These exist as a mixture of excited states at room temperature or above. The cooling effect will be most important for molecules with low frequency modes. One candidate for study is the linear molecule C_3O_2. It will also be possible to resolve long-standing uncertainties about the ground-state structures of compounds such as transition metal halides (linear or bent?) and trihalides (pyramidal or planar?).

A large amount of work has been carried out on clusters using photographic methods by Bartell [3]. The increased sensitivity of the new detector should allow the study of cluster formation at lower densities than are currently used. Investigations of nucleation in metal vapours, of the structures of dimers and of other small clusters are all possible.

With laser excitation, the structures of molecular excited states and molecular ions together some time-dependent phenomena can be looked at. As mentioned individual vibrational levels of an upper state in a molecule can be populated, so that the potential surface can be probed over a wide region. Using multiple-photon ionisation molecular ion densities high enough for study by electron diffraction can be created [4]. The structures of isolated polyatomic ions have hardly been studied, and molecular ions such as $C_6H_6^+$, $C_6H_5NH_2^+$ and CH_3I^+ would be suitable for investigation. Excited states decaying by internal conversion rather than radiation exhibit geometry changes in the 10^{-14} to 10^{-6} s range. Corresponding changes in the electron scattering can be observed with a resolution of 10^{-9} s, opening the possibility of detailed studies of internal energy transfer in favourable molecular systems.

In **section 4.2** the operation of the Campargue source is described together with the properties of molecules in such beams. **Section 4.3** outlines the actual experimental details of the source in the new apparatus. Plots of beam intensity versus the nozzle-skimmer distance at a range of stagnation pressures are displayed.

4.2 Theory

The Campargue-type free jet source is a molecular source where gases are introduced into an expansion chamber at pressures of up to 40 bar (and sometimes higher) through a small orifice, with an ambient pressure of around 0.1-10 mbar (depending on pushing pressure and pumping speed in the expansion chamber). As the expansion proceeds multiple collisions between atoms and/or molecules in the beam create a beam characterised by narrow velocity distributions (both parallel and perpendicular to the direction of flow). Generally, "heavy" target molecules are placed in a light carrier gas, usually He, which acts as a thermal bath to the molecules of interest. Although the target molecules are dilute within the stream (~1-10% by volume) much of the He is scattered away from the centreline of the molecular beam leading to a relative enrichment of the target molecule.

Free-jet expansion [5,6,7] converts random thermal motion into directed flow. The enthalpy of the atoms and/or molecules in the system reduces [8] as the gas expands resulting in an increase in the beam velocity and thus to extensive cooling of the gas in a very short time. The number density also drops quickly along the expansion direction. Relaxation of the translational degree of freedom via two-body collisions is the most efficient process in nozzle expansion, which results in very low local translational temperature. If polyatomic molecules are seeded into a lighter carrier gas their rotational and vibrational degrees of freedom communicate with this translationally cold bath through inelastic collisions and relax [9-12]. In the early part of the expansion the collision frequency and energy are high due to the high density and high translational temperature. In this regime energy is transferred from the internal modes to the translation mode. Further on in the expansion the beam density decreases and the translational velocity distribution becomes more uniform. As this happens the energy-transferring collisions become more infrequent. Finally the relaxation process ceases and populations of the internal modes are "frozen" at a certain value. The relaxation of vibrational, rotational and translational degrees of freedom being different, the freezing of these degrees of freedom occur successively along the flow direction.

In a free-jet expansion the gas begins with a low velocity in the stagnation state (P_o, T_o) where P_o is the source pressure and T_o is the source temperature. Thus the gas starts at a relatively small velocity. The source shown in **Figure 4.1** is a short converging nozzle [13] similar to the one used in our apparatus. If there is an imposed pressure difference (P_o-P_b) where P_b is the background pressure in the nozzle chamber, the gas accelerates as the area decreases, toward the source exit. For this class of nozzle the accelerating flow can be approximated as an isentropic flow, with negligible viscous and heat conduction effects. If the ratio of the two pressures, P_o/P_b is high enough the gas will exit the nozzle source at the local speed of sound or Mach number equal to 1.

To exit the source in this manner the pressure ratio must exceed a critical value $G \equiv ((\gamma+1)/2)^{\gamma/(\gamma-1)}$ (where $\gamma = C_p/C_v$), which is less than 2.1 for all gases. If the pressure ratio is less than this critical value, the flow will exit subsonically with a pressure nearly equal to P_b, without any further expansion. At pressure ratios above this critical value, the Mach number M equals 1 at the throat. At this point the exit pressure becomes independent of P_b and equal to P_o/G, i.e. approximately half of P_o. The pressure of the gas at the exit still exceeds P_b and the flow is said to be "underexpanded". The gas subsequently expands outwards downstream of the nozzle as the flow attempts to meet the boundary conditions imposed by the background pressure P_b.

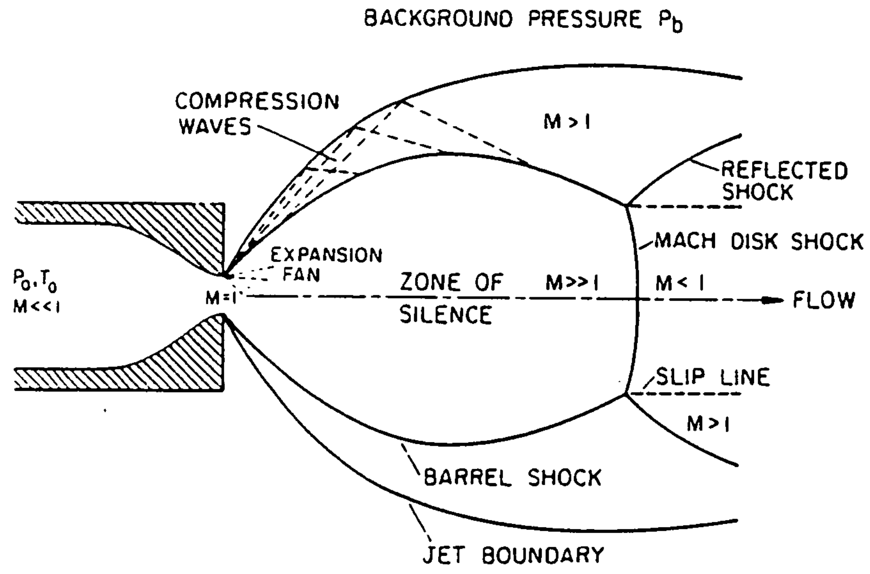

Figure 4.1 Continuum free-jet expansion. Taken from [7].

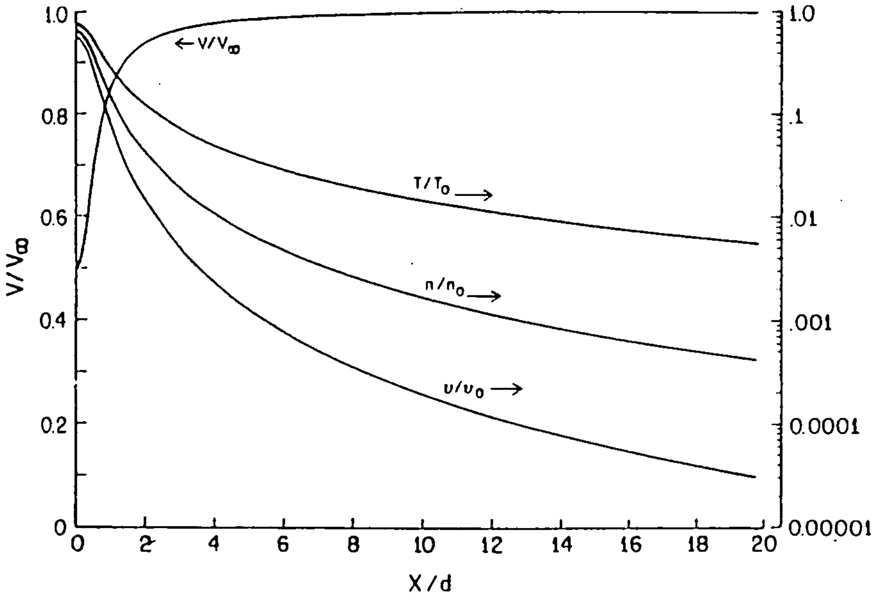

Figure 4.2 Free jet centreline properties versus distance in source diameters; $\gamma = 5/3$; temperature, T, density, n and binary hard sphere collision frequency, v, are normalised by source stagnation values T_o, n_o, v_o. Taken from [7].

There are two characteristics of supersonic flows that make such expansions interesting. Firstly, unlike subsonic flows, the velocity of the flow increases (M increases) as the flow area increases, resulting in M being greater than 1 beyond the exit. Secondly, a supersonic flow cannot "sense" downstream boundary conditions. This is due to the fact that information propagates at the speed of sound whereas the fluid is moving faster ($M>1$). Thus the flow does not know about the boundary conditions but it has to adjust to meet them somehow. It does so by a system of shock waves. These are very thin nonisentropic regions of large density, pressure, temperature and velocity gradients. At these points the flow becomes "aware" of the background molecules in the expansion chamber. The thickness of a shock wave is of the order of the local mean free path.

Figure 4.1 shows a gas flow initially expanding isentropically. The velocity M increases rapidly until the gas overexpands and has to be compressed by the system of shocks. There is a barrel shock at the sides and the Mach disk shock normal to the centreline flow. The position of this Mach disk shock is remarkably insensitive to the nature of the gas in the expansion and is given by

$$X_M / d = 0.67(P_o / P_b)^{1/2} \quad (4.1)$$

where X_M is the position of the disk and d is the nozzle source diameter. The core of the expansion is isentropic and the properties are independent of P_b as the supersonic flow in this region is not aware of any external conditions leading to the term *zone of silence*. The molecular beam is extracted from this region.

As the expansion proceeds, the gas cools and the enthalpy decreases. This leads to a rise in the mean velocity of the expanding gas. While the velocity rises, reaching a terminal velocity within a distance of about 10-20 nozzle diameters from the source (see **Fig. 4.2**), the temperature, density and collision frequency all fall rapidly as the gas expands.

By skimming off part of the centreline flow upstream of the Mach disk position (see **Fig. 4.3**) it is possible to attain highly accelerated gaseous atoms or molecules. In many systems seeded beams are used. An expansion consisting mainly of, for example, He atoms produces a gas stream with velocities in excess of 1700 m s^{-1}. By placing a small number of a heavier target molecules in this stream they too can become accelerated to high velocities.

During the expansion such polyatomic target molecules experience many two- and three-body collisions, mainly with the carrier gas, causing the translational, rotational and vibrational modes to become cooled. At some point in the expansion the number of collisions is so low that continuum flow can no longer be sustained. There is then a transition to free molecular flow (see **Fig. 4.4**). Beyond this point, in the absence of any further collisions, the properties of the molecules become frozen-in.

Another property of supersonic expansions is that the gases in the flow can condense and form clusters, or van der Waals molecules in mixed streams [14-19]. There are three experimental parameters that affect the molecular beam; P_o, T_o and d, the diameter of the nozzle source. By altering these, the conditions for clustering for different molecules or mixtures can be optimised. For dimers, the formation rate is proportional to P_o^2d, thus by increasing either P_o or the diameter d of the source such molecules can be created. This was one of the major reasons for using this particular molecular source. If one wants to avoid clustering for target molecules, the source temperature can be increased.

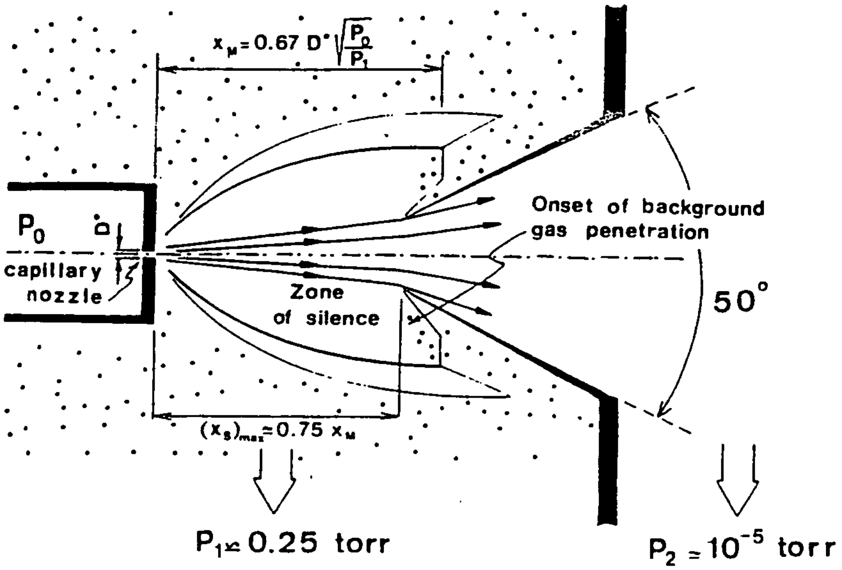

Figure 4.3 Schematic diagram of a nozzle beam source operated by skimming in the region of overexpansion of a free jet zone of silence (Campargue type). Taken from [1].

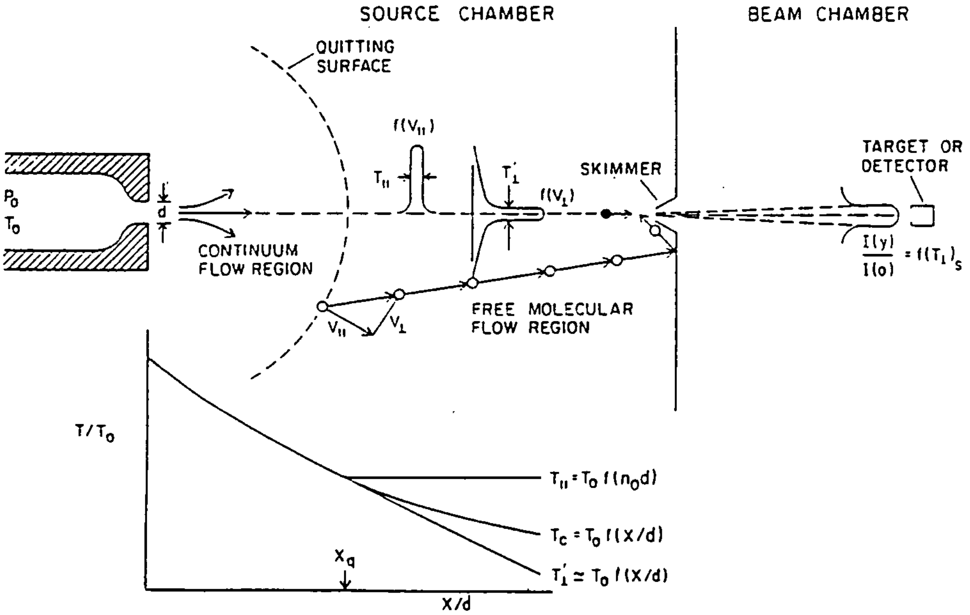

Figure 4.4 Free jet transition to free-molecular flow; the "quitting surface" model separates the flow into continuum and free-molecular regimens. $T_{parallel}$ characterises the spread in parallel velocities $f(V_{parallel})$; $T'_{perpendicular}$, the spread in the narrow centre gaussian of $f(V_{perpendicular})$; T_c is the continuum temperature. Taken from [7].

4.3 Experimental Details

In this apparatus gases at stagnation pressures of up to 40-45 bar (continuous beam) have been intoduced in to the expansion or nozzle chamber. The gases enter this chamber through a General Valve pulsed nozzle source of diameter 0.1 mm (100 μm). This nozzle source can be operated in continuous (one shot) or pulsed mode. The gases used have included mixtures of 5% CO_2 and 5% NO (both by volume) seeded in a stream of He, pure He and pure Ar. The nozzle source is mounted on an xyz translator to allow the distance between the nozzle and skimmer to be altered over the range 6-42 mm. It also allows exact alignment of these two components. **Figures 4.5-4.8** show the aluminium box upon which the skimmer is mounted. This box, seen in position within the apparatus in **Figures 4.6-4.8**, forms part of the nozzle chamber. A larger flange with a flexible bellows arrangement is attached to the screws on the skimmer box and via the bolt holes pictured completing the inner wall of this chamber. The flange upon which the xyz translator is mounted forms the outer wall of the nozzle chamber. This flange (see **Fig. 3.2**) has an attachment to the Roots blower and E1M80 mechanical pump combination, which pumps away excess gas from the chamber, together with a connection for a Pirani gauge to monitor pressure. The pressure in the nozzle chamber ranges from 0.1-10 mbar under a gas load (dependent on stagnation pressure) and with no gas load is usually around $5/6\text{x}10^{-3}$ mbar.

The expanded gas flow is then skimmed by a Beam Dynamics skimmer (pictured in **Figs. 4.6-4.8**). This skimmer has an aperture of diameter 0.18 mm (180 μm) and is 25 mm in length. The skimmed, cooled atoms and/or molecules then enter the beam tube, and intersect the electron beam, via a hole of diameter 1 mm. This beam tube has an inner diameter of 10 mm and an outer diameter of 14 mm. The collision zone, which lies at the centre of this tube, is 36 mm from the tip of the skimmer. The molecular beam leaves the beam tube by a hole of diameter 1.2 mm and travels a further 6 mm to

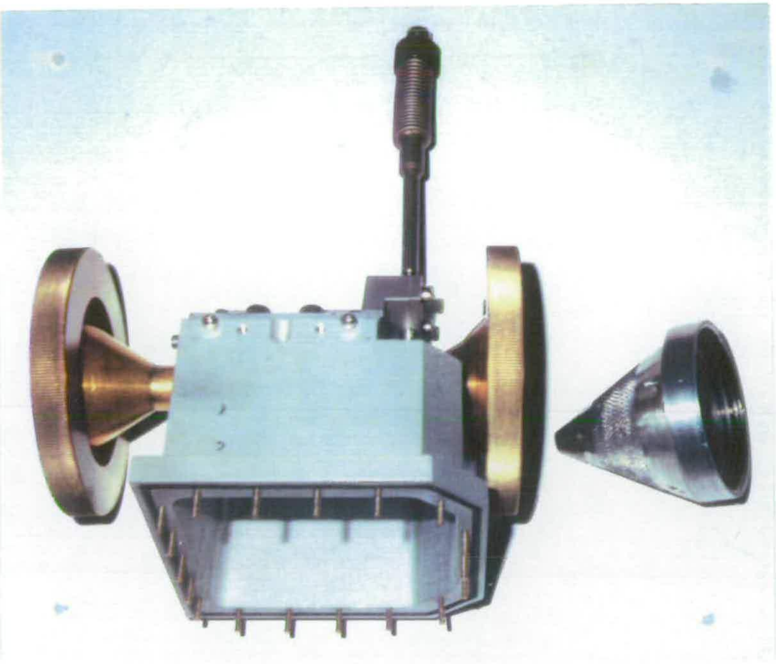

Figure 4.5 Skimmer box and brass beam tube assembly. On the right hand side of the picture is the aluminium cone through which scattered electrons enter the diffraction chamber. At the top of the picture is the flexible tube which guides the molecular beam into the dump tank chamber containing the mass spectrometer head.

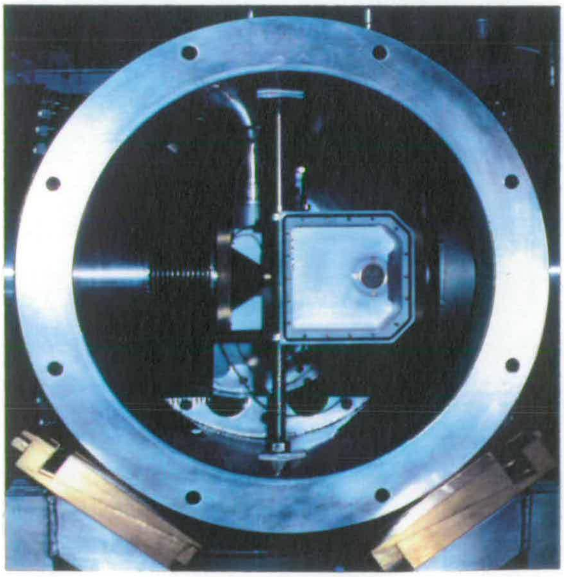

Figure 4.6 View of skimmer box and beam tube assembly in position within apparatus. Note the brass retaining rings which position the beam tube and the vertical clamp which orients the skimmer box.

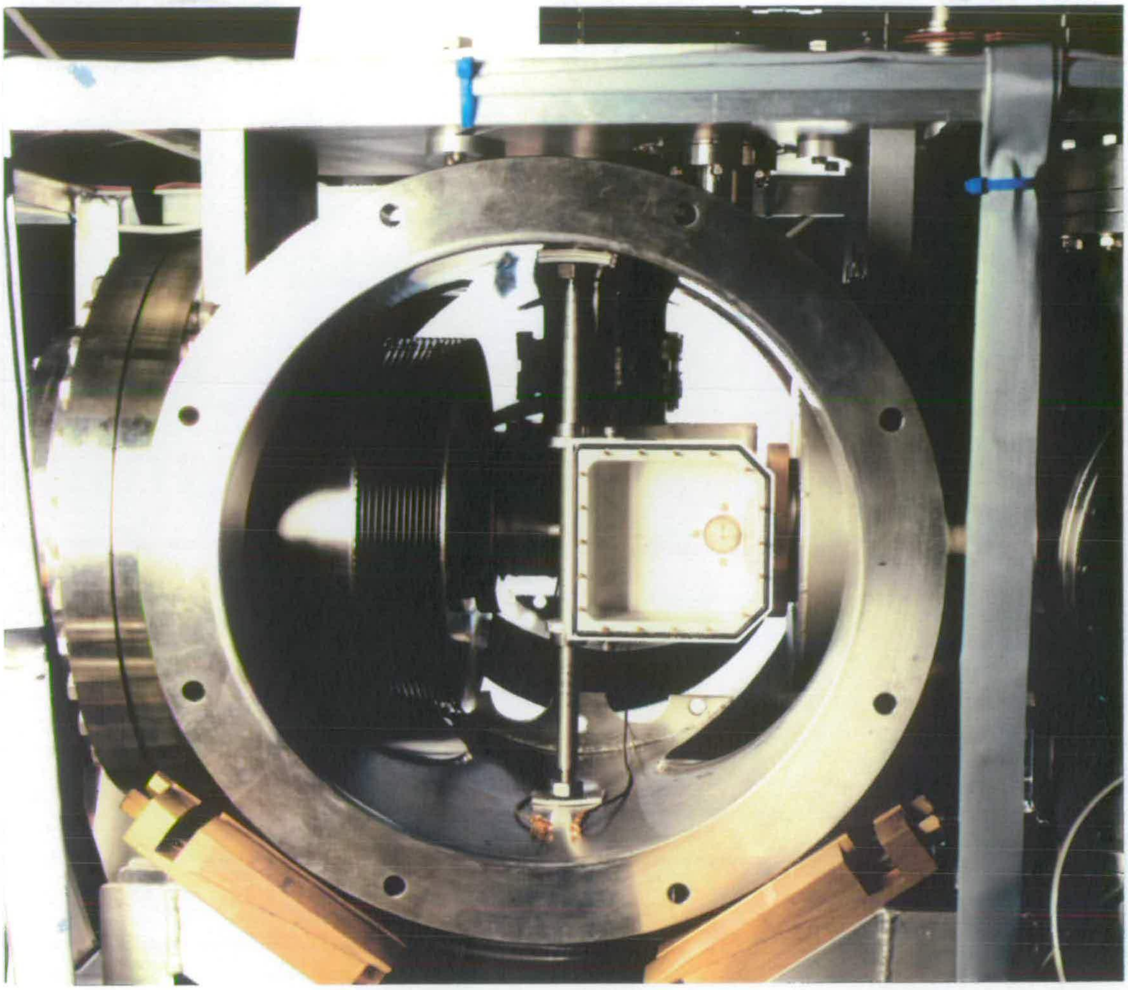

Figure 4.7 Detailed view of skimmer box within apparatus. Note the Mumetal beam tube.

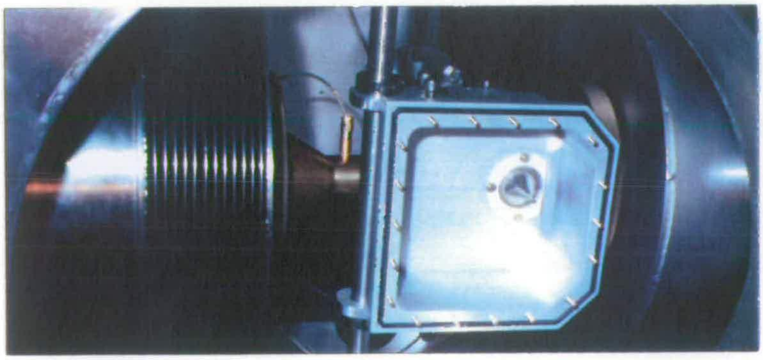

Figure 4.8 View of skimmer box showing the connection to the centring collar in the brass beam tube.

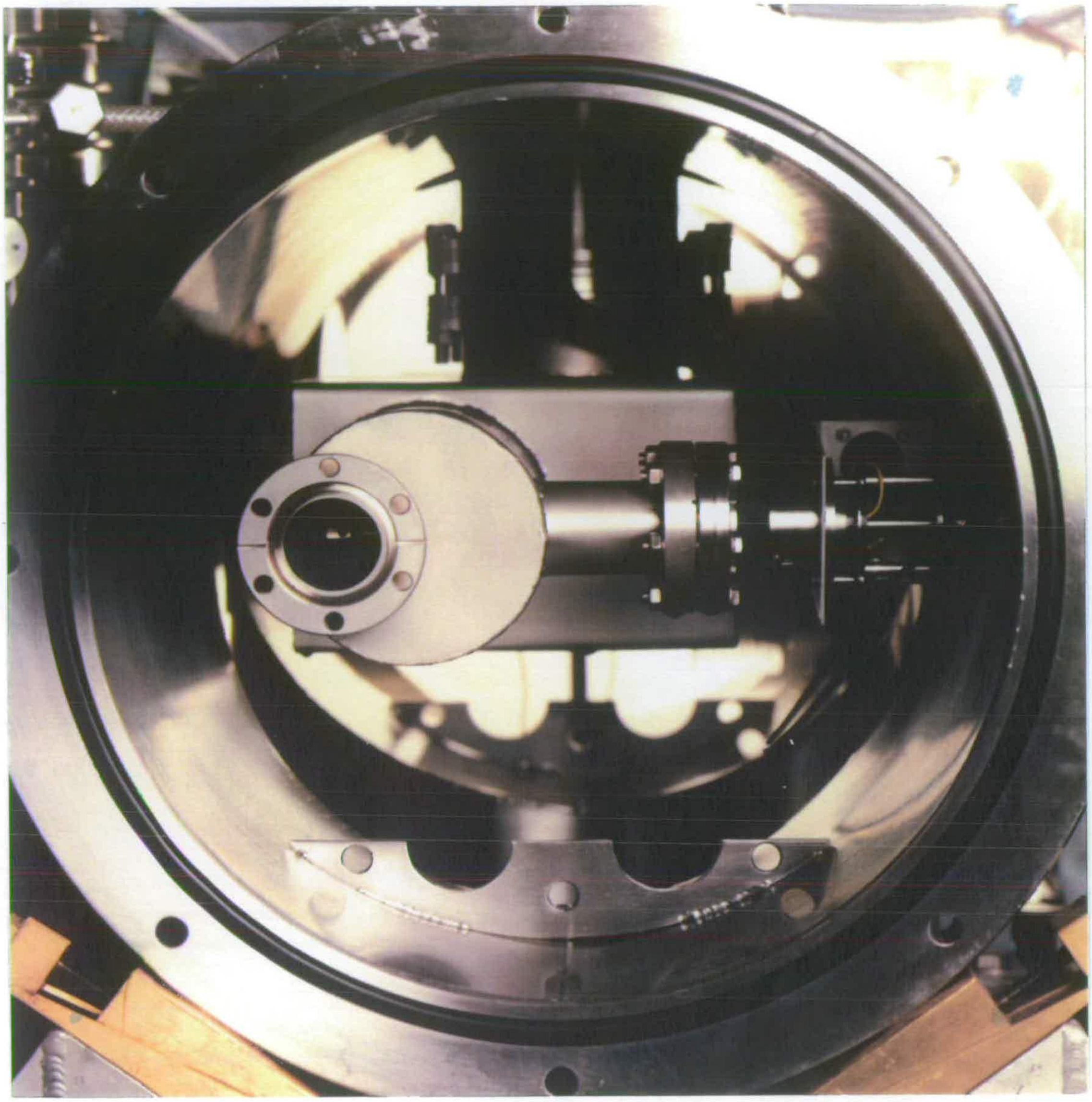

Figure 4.9 View of dump tank showing the mass spectrometer head. The ionisation region can be seen in the centre of the small flange.

enter a flexible tube (see **Fig. 4.5**) which opens into the dump tank. Excess gas in this chamber is pumped away by an Edwards EO4 oil diffusion pump whilst the centreline molecular beam travels to the ionisation region of a Leda Mass quadrupole (see **Figure 4.9**). This is used to monitor the molecular beam intensity. The ioniser lies 676 (± 5) mm from the tip of the skimmer. Alignment of the skimmer with the beam tube and ioniser is facilitated by a He-Ne laser.

Profiles of the beam intensity for several gases versus nozzle skimmer distance were obtained by monitoring the pressures of selected gases in the mass spectrometer. Initially it was thought that corrections to these pressures had to be made for ionisation sensitivity and mass transmission. The mass spectrometer was calibrated using a pulsed beam of 5% CO_2 in He and it was observed that the unit allowed for mass transmission. However, the recorded pressures had to be corrected to take into account the fact that the spectrometer has different sensitivities to different atoms and molecules. This stems from the fact that they have different ionisation cross-sections. A standard sensitivity of 1 is applied for N_2 (mass 28). The sensitivity for the required mass species X is defined as

$$\text{Ionisation sensitivity} = \frac{\text{Relative intensity of X}}{\text{Relative intensity of } N_2} \qquad (4.2)$$

Measured pressures, $P_{measured}$, are converted to true pressures, P_{true}, by the following expression

$$P_{true} = P_{measured} \times \frac{1}{\textit{Ionisation sensitivity}} \qquad (4.3)$$

The ionisation sensitivities of the gases reported in this section are listed in **Table 4.1**.

Table 4.1 Ionisation sensitivities relative to a nitrogen standard (=1)

Gas	Ionisation Sensitivity
He	0.14
CO_2	1.4
NO	1.2
Ar	1.2

Although the pressures in the mass spectrometer give an indication of the relative intensity of the molecular beam it is important to have an idea of the number density of the target molecules at the collision zone. A correction factor based on a solid angle argument was calculated to translate pressures at the ionisation region of the mass spectrometer to those at the collision zone. As the collision zone lies 36 mm from the tip of the skimmer and the ioniser is a further 640 mm from the collision zone the correction factor was defined as

$$Correction\ factor = \frac{(36+640)^2}{(36)^2} = 353 \qquad (4.4)$$

With this correction factor number densities for CO_2 of up to $3.5\text{x}10^{19}$ m^{-3} have been estimated/measured at the collision zone.

Initial measurements using a molecular beam of 5% CO_2 in He proved to be very promising. **Figure 4.10** shows the intensities of CO_2 (corrected) at the mass spectrometer versus the nozzle-skimmer distance for four stagnation pressures; 15, 20, 25 and 30 bar. At 30 bar He/CO_2 the maximum pressure recorded was $1.93\text{x}10^{-6}$ Torr at a distance of 9-11 mm which corresponds to a number density for CO_2 at the collision zone of $2.41\text{x}10^{19}$ m^{-3}. The profiles obtained in **Figure 4.10** have the expected shape as displayed in **Figure 4.11a**. In a supersonic expansion there is a maximum known as the *maximum maximorum* (MM) and as the nozzle-skimmer distance increases the centreline intensity falls off. The minimum (M) pictured in **Figure 4.11a** was

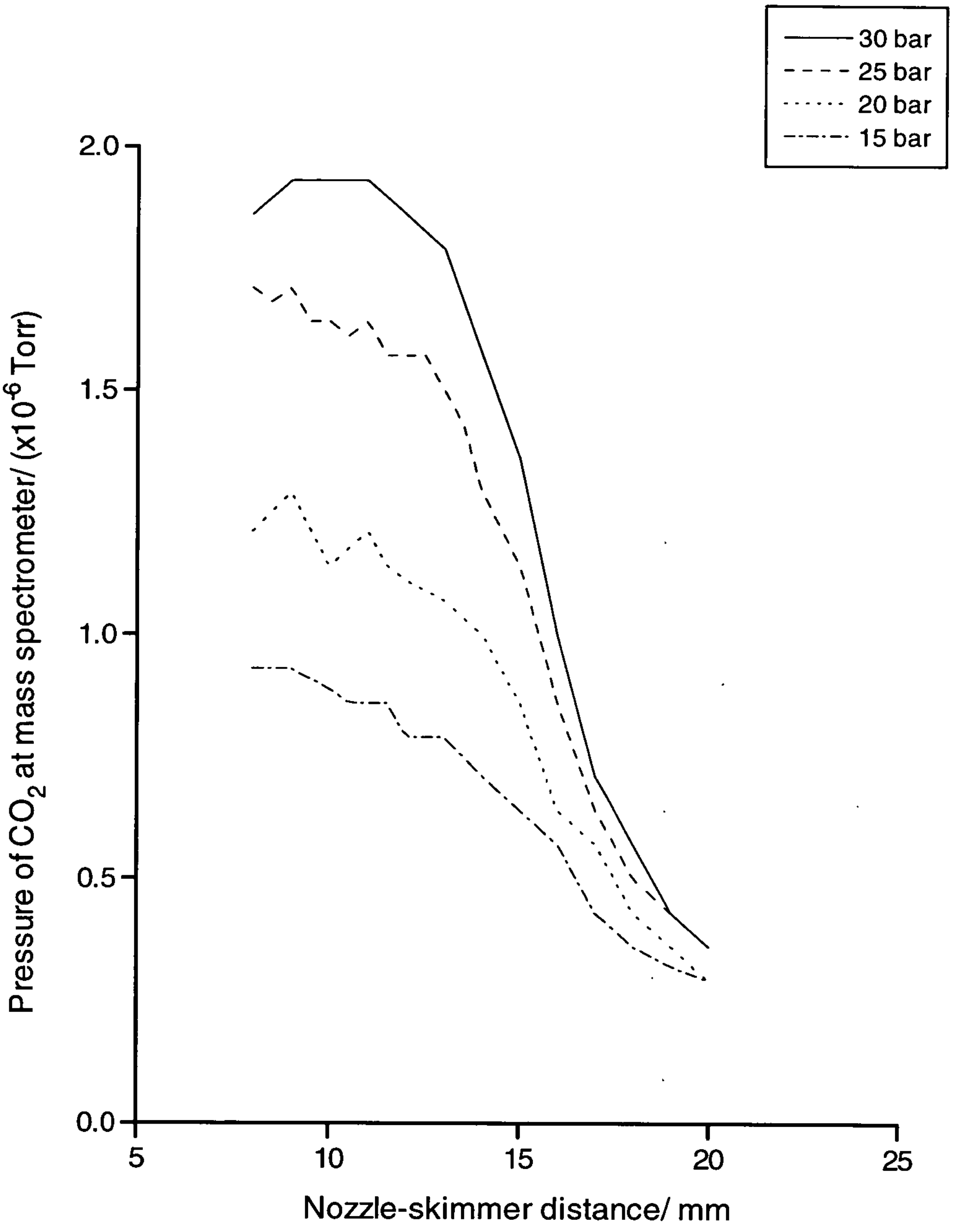

Figure 4.10 Plot showing CO_2 intensities at mass spectrometer versus nozzle-skimmer distance for four stagnation pressures of a He/CO_2 mixture.

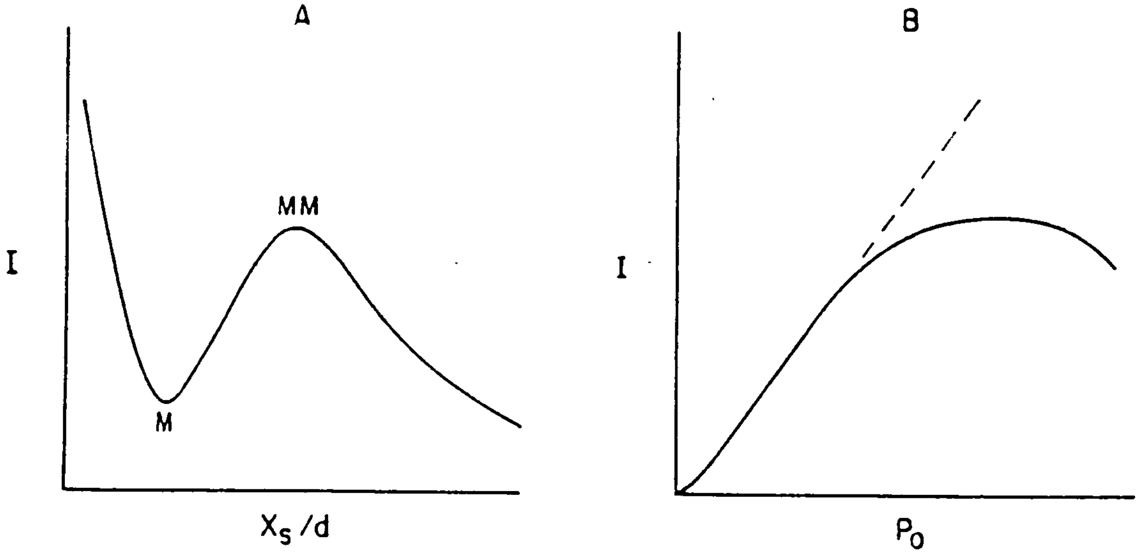

Figure 4.11 Typical beam intensity versus source skimmer distance (A) and versus source pressure (B). Taken from [7].

not observed as the smallest nozzle-skimmer distance possible was 6 mm. At distances less than the minimum it is thought that there is sufficient density inside the skimmer for a second expansion to occur causing the intensity to rise. **Figure 4.12** shows the centreline CO_2 pressures for a fixed nozzle-skimmer distance of 12 mm for a continuous beam of He/CO_2 at a range of stagnation pressures up to 45 bar. Also plotted are CO_2 pressures for a pulsed He/CO_2 beam with stagnation pressures ranging from 35-70 bar. The beam was pulsed on for 500 µs and off for 10 ms. The results for the continuous beam match those in **Figure 4.11b** apart from the point where the curve flattens and turns over. Stagnation pressures over 45 bar for a continuous beam were not used as the pressure in the nozzle chamber became very high. This P_o appeared to be the pumping limit for the Roots blower combination. **Figure 4.13** shows the results of **Figure 4.12** translated into CO_2 number densities at the collision zone.

Further measurements were taken using the same He/CO_2 mixture for another range of stagnation pressures. **Figure 4.14** shows the CO_2 intensities in the mass spectrometer versus the nozzle-skimmer distance for stagnation pressures of 10, 20, 30 and 40 bar. Comparing the maximum intensities measured at 20 and 30 bar with those for the same conditions in **Figure 4.10** it was observed that the CO_2 intensities were reduced by a factor of four. The reason for this reduction was unclear but could have been due to misalignment of the molecular beam axis or contamination of the ion source of the mass spectrometer. **Figures 4.15-4.18** display the variation of the CO_2 intensity and the pressure in the main chamber (surrounding the dump tank) versus the nozzle-skimmer distance. As expected the pressure in the main chamber is high at small distances and drops quickly to a constant value as the distance is increased. **Figure 4.19** illustrates the nearly linear increase in pressure in the nozzle chamber (P_b) versus stagnation pressure.

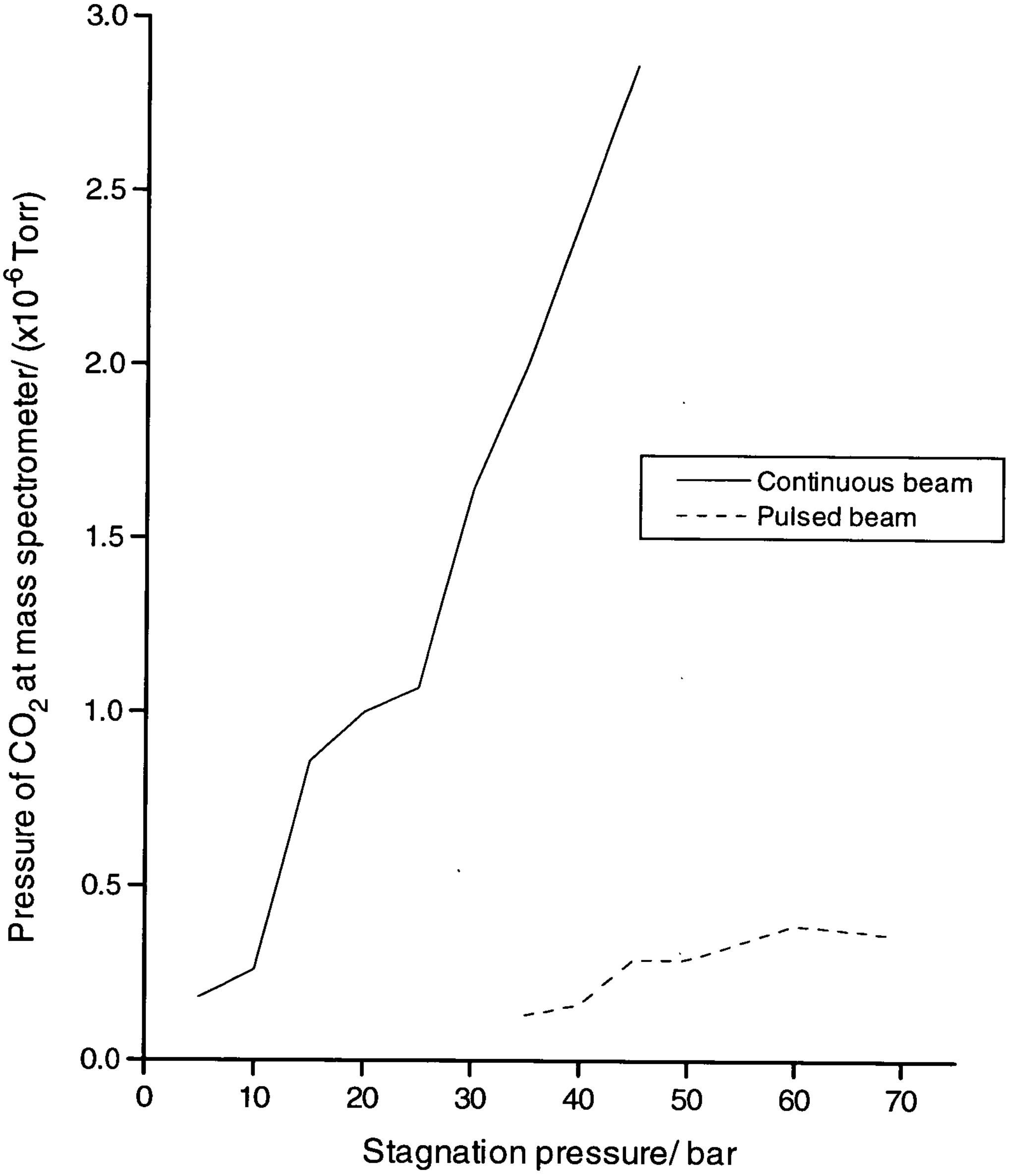

Figure 4.12 Plot showing CO_2 intensities at mass spectrometer versus stagnation pressure for a continuous and a pulsed molecular beam (500 μs on and 10 ms off).

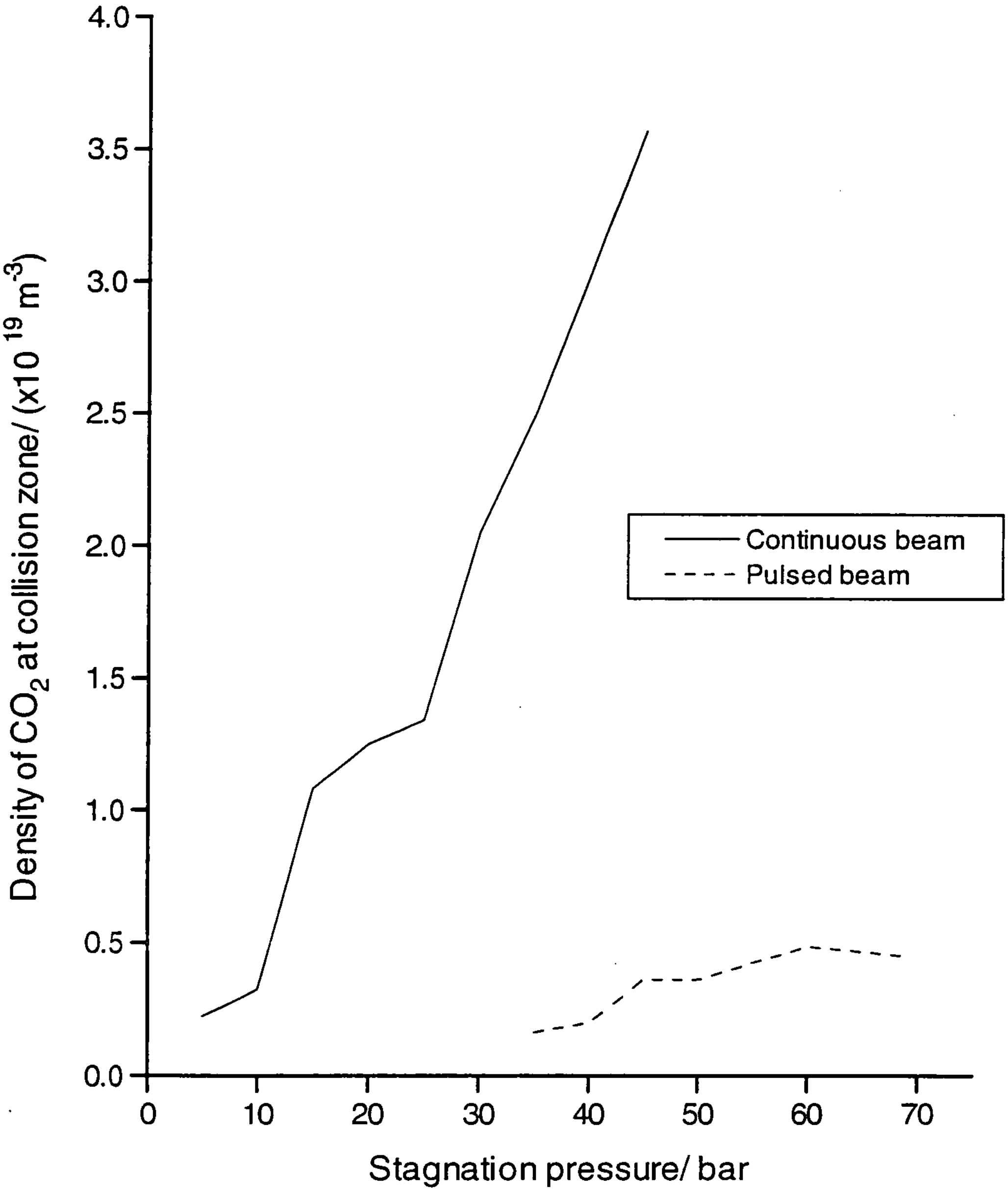

Figure 4.13 Plot showing the number density of CO_2 at the collision zone versus stagnation pressure for a continuous and a pulsed molecular beam (500 µs on and 10 ms off).

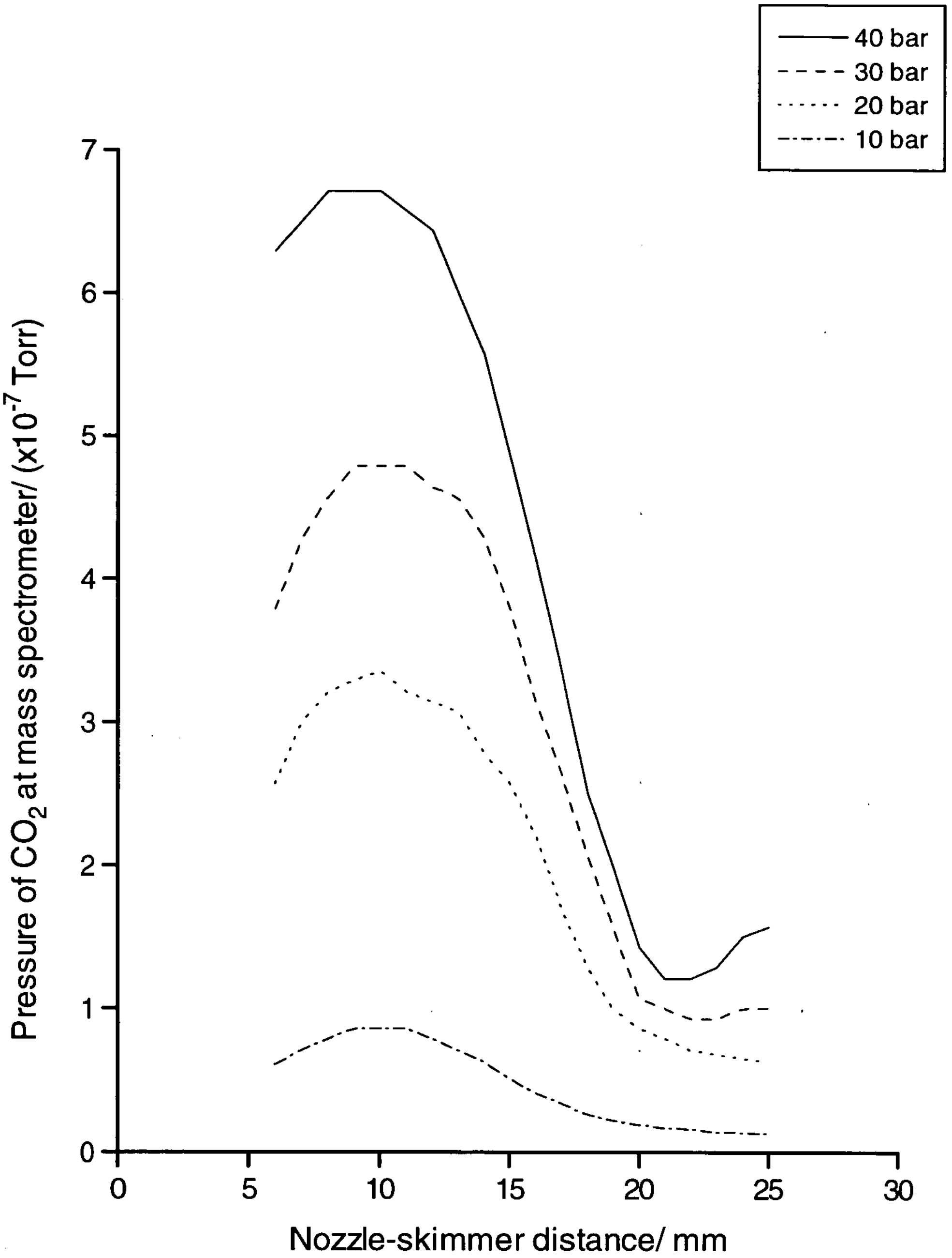

Figure 4.14 Plot showing CO_2 intensities at mass spectrometer versus nozzle-skimmer distance for four stagnation pressures of a He/CO_2 mixture.

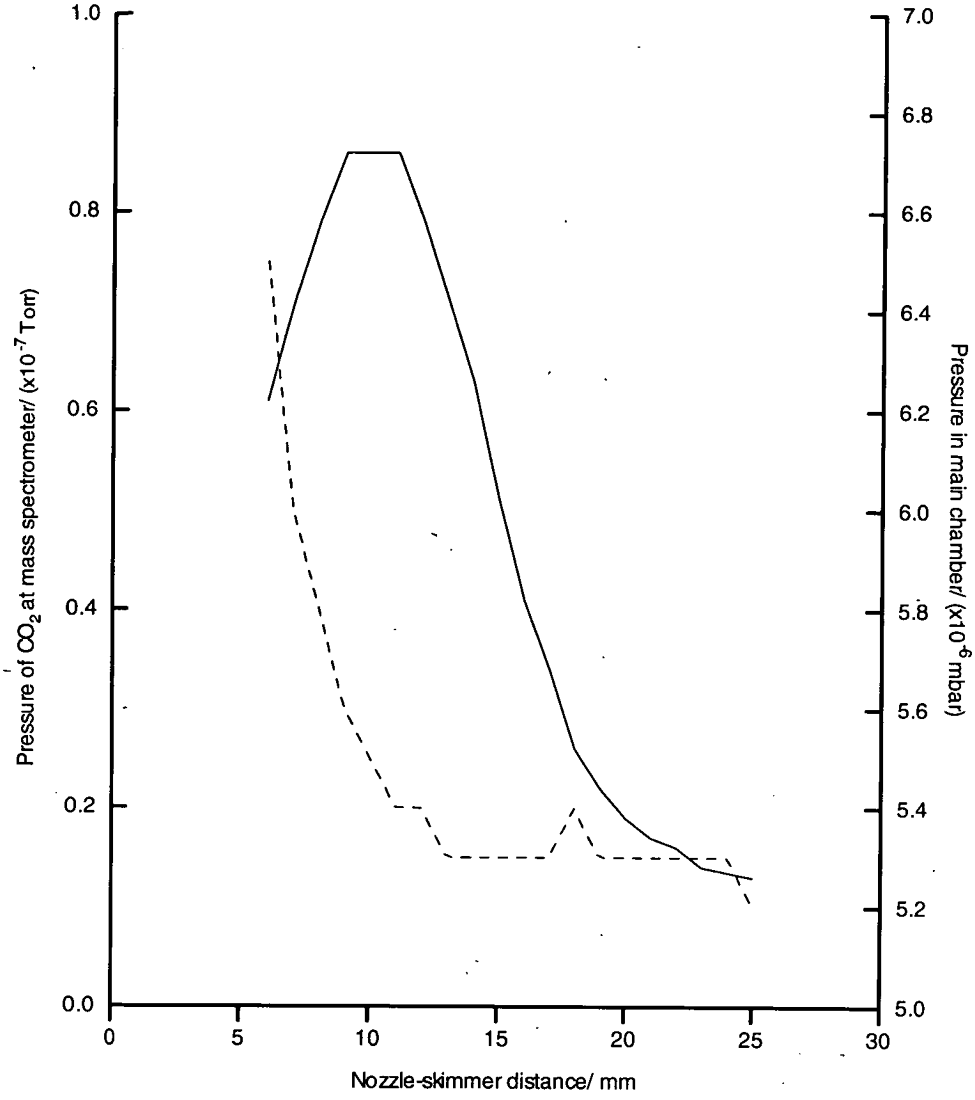

Figure 4.15 Plot showing CO_2 intensity at mass spectrometer (solid line) and pressure in main chamber (dashed line) versus nozzle-skimmer distance for a continuous molecular beam of a 10 bar He/CO_2 mixture

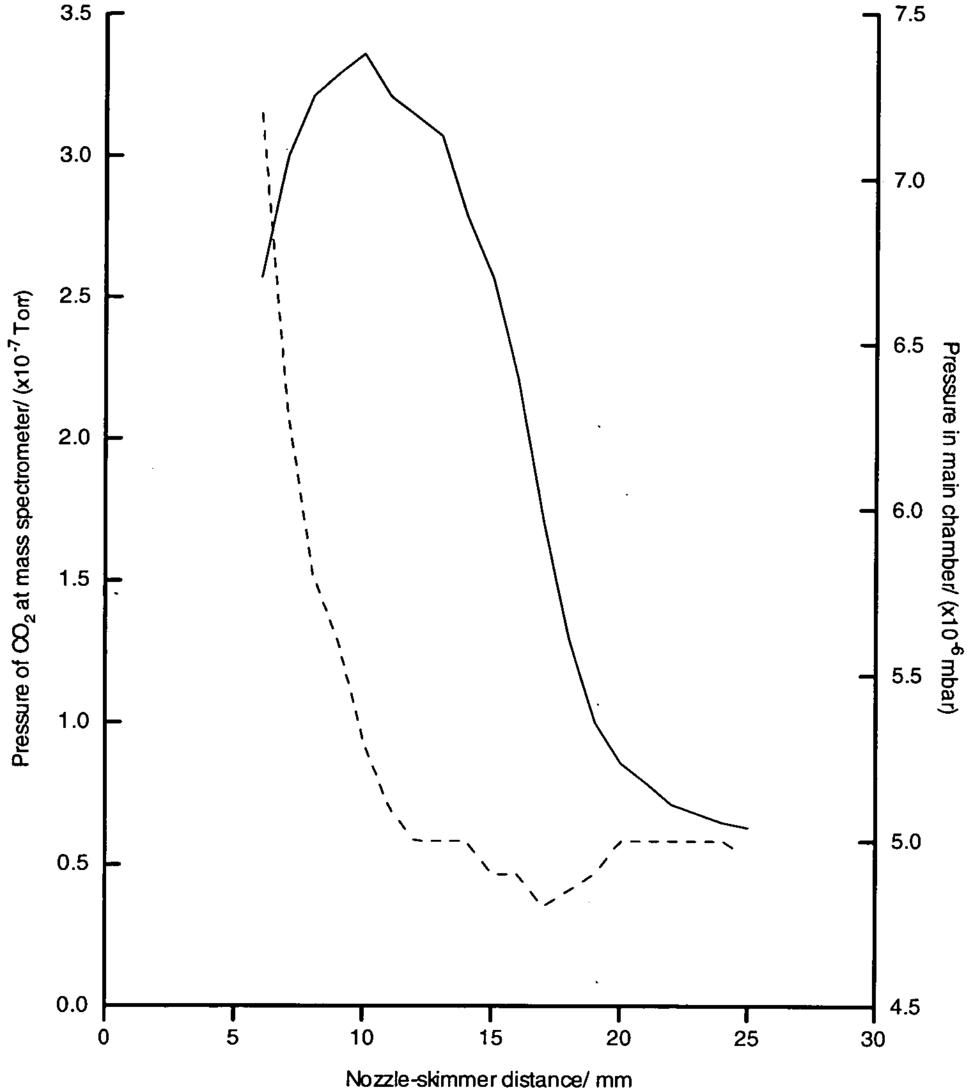

Figure 4.16 Plot showing CO_2 intensity at mass spectrometer (solid line) and pressure in main chamber (dashed line) versus nozzle-skimmer distance for a continuous molecular beam of a 20 bar He/CO_2 mixture.

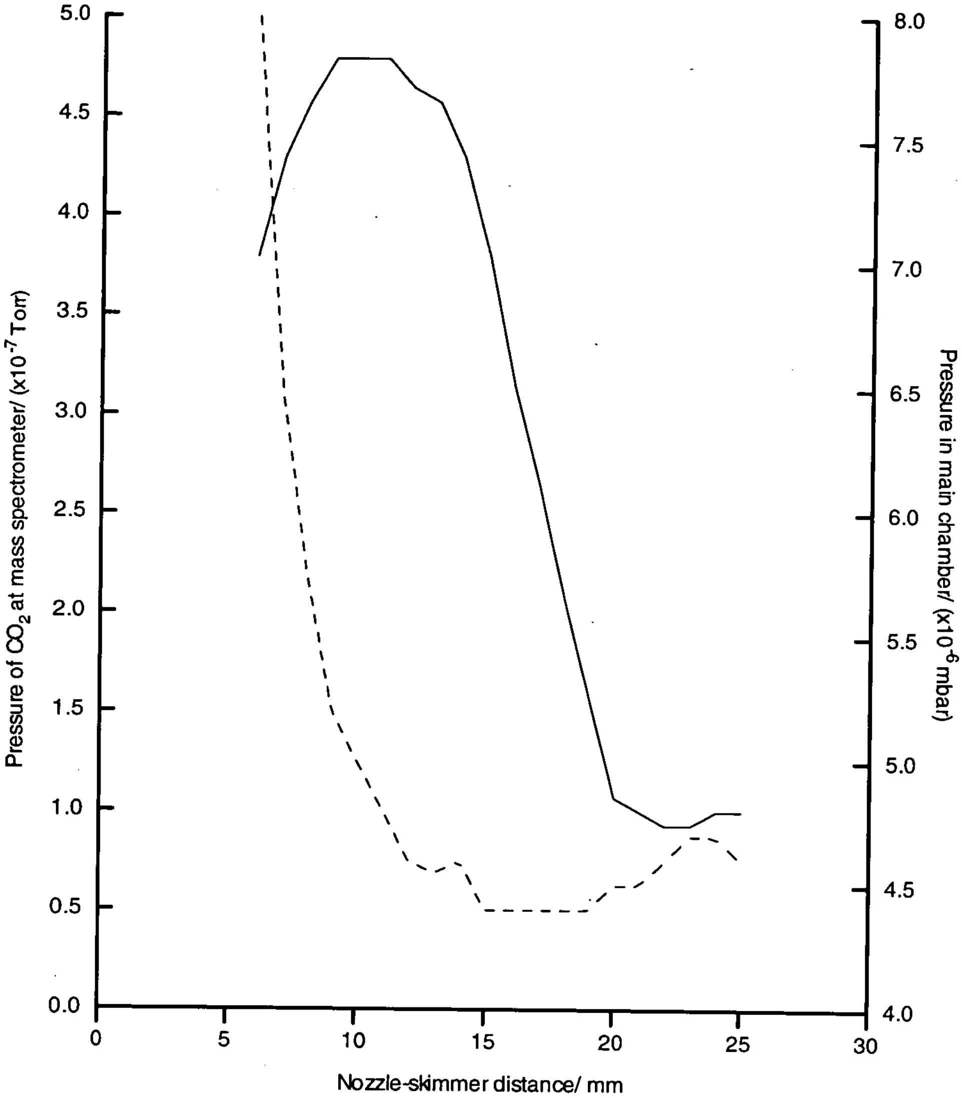

Figure 4.17 Plot showing CO_2 intensity at mass spectrometer (solid line) and pressure in main chamber (dashed line) versus nozzle-skimmer distance for a continuous molecular beam of a 30 bar He/CO_2 mixture.

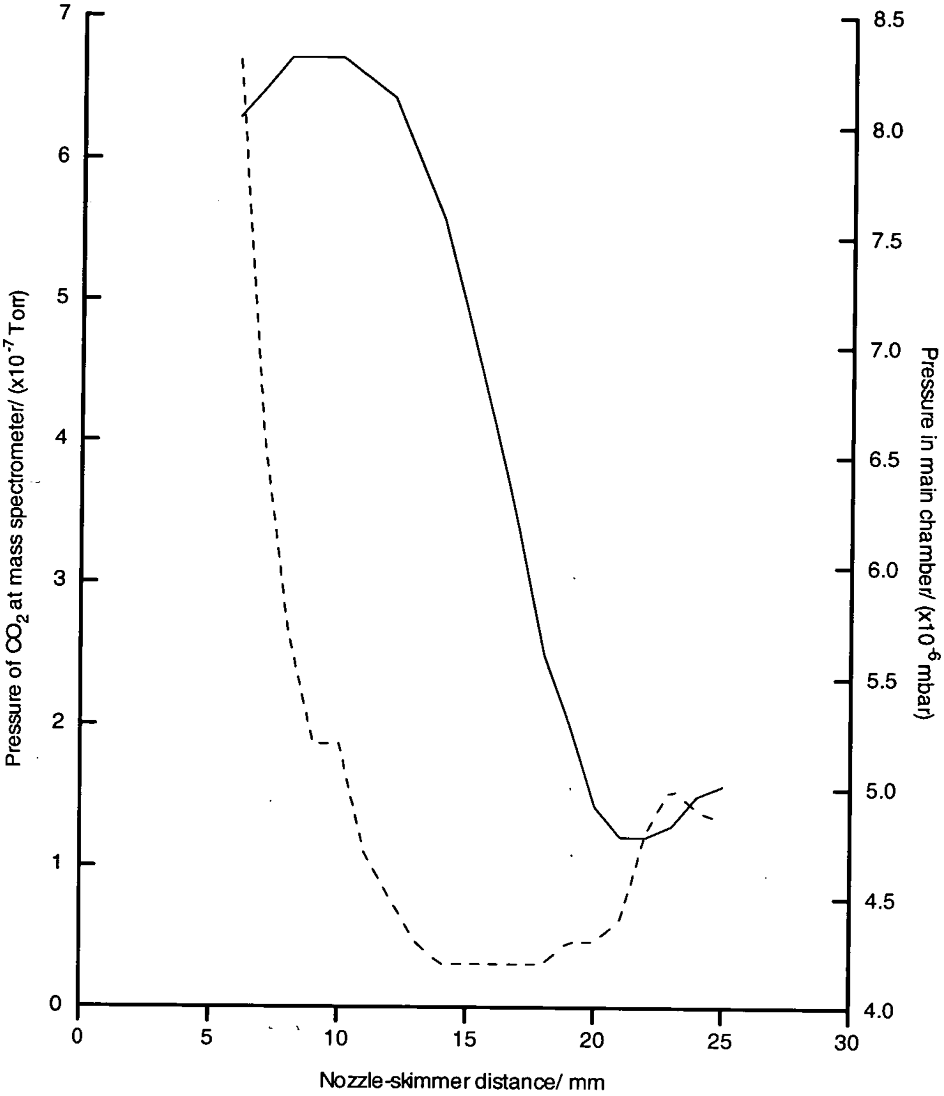

Figure 4.18 Plot showing CO_2 intensity at mass spectrometer (solid line) and pressure in main chamber (dashed line) versus nozzle-skimmer distance for a continuous molecular beam of a 40 bar He/CO_2 mixture.

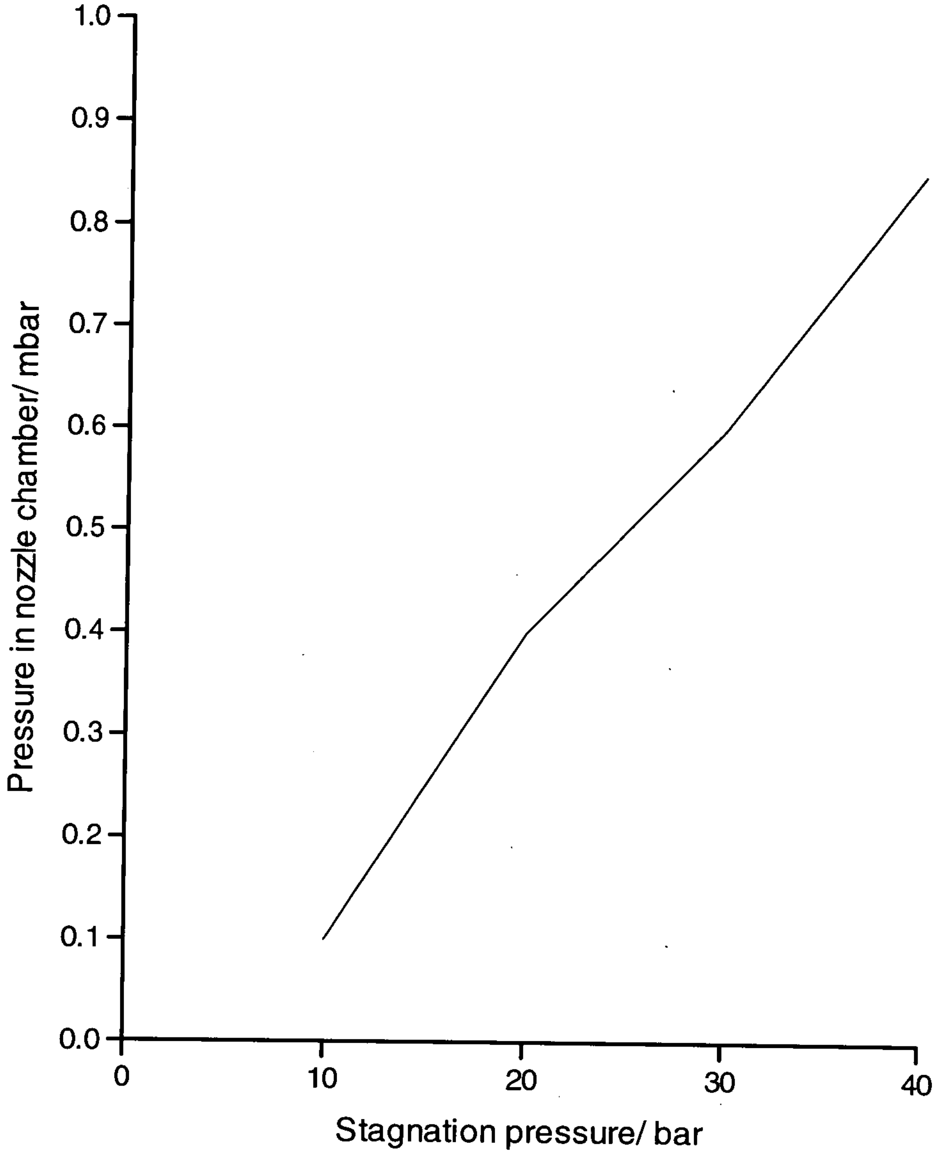

Figure 4.19 Plot showing pressure in nozzle chamber versus stagnation pressure.

At the same time as the CO_2 pressures were monitored the He pressures in the mass spectrometer were also measured for the four stagnation pressures. **Figures 4.20-4.23** show the plots of He versus nozzle-skimmer distance. The plots at 10 and 20 bar show very structured profiles with sharp peaks at around the same distance for CO_2 intensities. There are also pronounced minima at around 8 mm followed by the expected increase at lower distances (see **Fig. 4.11a**) due to re-expansion. As the stagnation pressure is increased (at 30 and 40 bar) the "peaks" at 12-13 mm are much reduced with the "peak" effectively sitting in a minimum. At 30 and 40 bar the overall He intensities are lower than at 20 bar. This loss of structure for the He profile at 30 and 40 bar (**Figs. 4.22** and **4.23**) could be due to the large gas density in the system. **Figure 4.24** shows the profile of a pure He beam with a stagnmation pressure of 10 bar. Comparing this to **Figure 4.20** (10 bar He/CO_2) it was observed that the He maximum of the pure beam (2.14×10^{-7} Torr) was around 30 times that of the He maximum for the 10 bar He/CO_2 mixture (7.50×10^{-9} Torr). The reason for this reduction in He along the beam centreline was thought to be efficient scattering of the He atoms by the CO_2 molecules. Indeed when the ratios of the corrected pressures at the mass spectrometer (P_{co2}/P_{He}) were plotted versus nozzle-skimmer distance for the four stagnation pressures (**Figs. 4.25-4.28**) an interesting structure was noted. At 10 and 20 bar the ratios of P_{CO2}/P_{He} show two distinct maxima with a minimum corresponding to the maxima in both the He and CO_2 intensities. This minimum is due to the large increase in CO_2 intensity at 12 mm. The ratios increase as the stagnation pressure increases reaching values of around 270 at 40 bar. As with the He profiles (**Figs. 4.22** and **4.23**) the structure begins to break down at 30 and 40 bar with the minimum becoming less distinct and the larger of the two peaks shifting to higher nozzle-skimmer distances. No reasonable explanation has been found to describe the double maximum structure in the ratio plots.

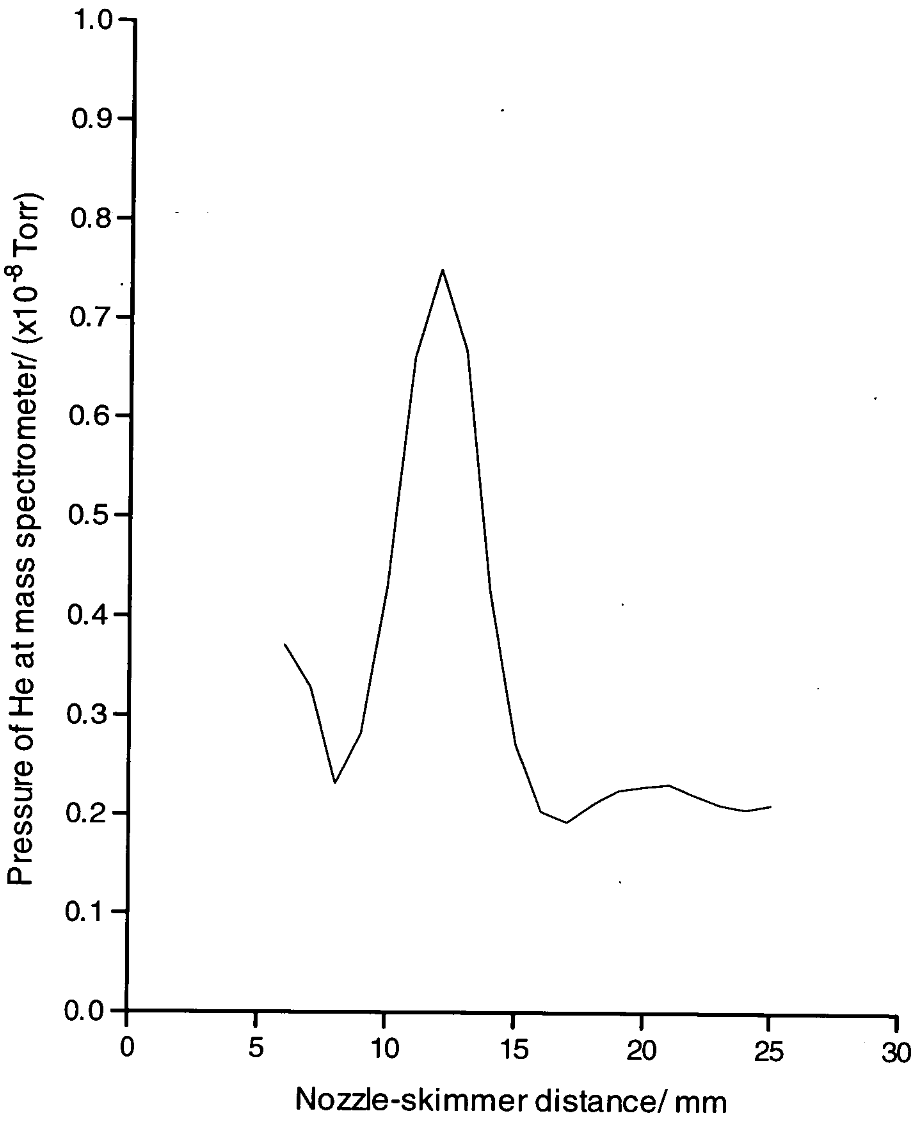

Figure 4.20 Plot showing He intensity at mass spectrometer versus nozzle-skimmer distance for a continuous molecular beam of a 10 bar He/CO_2 mixture.

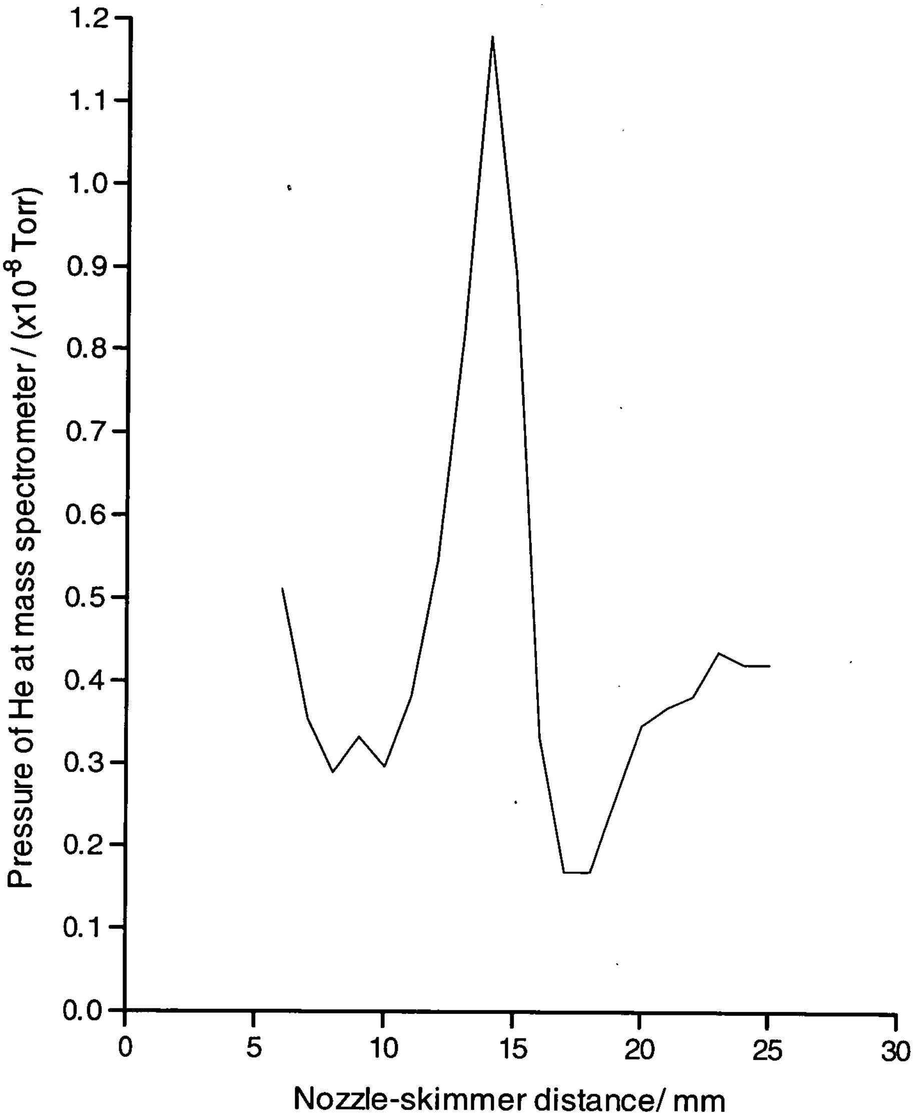

Figure 4.21 Plot showing He intensity at mass spectrometer versus nozzle-skimmer distance for a continuous molecular beam of a 20 bar He/CO_2 mixture.

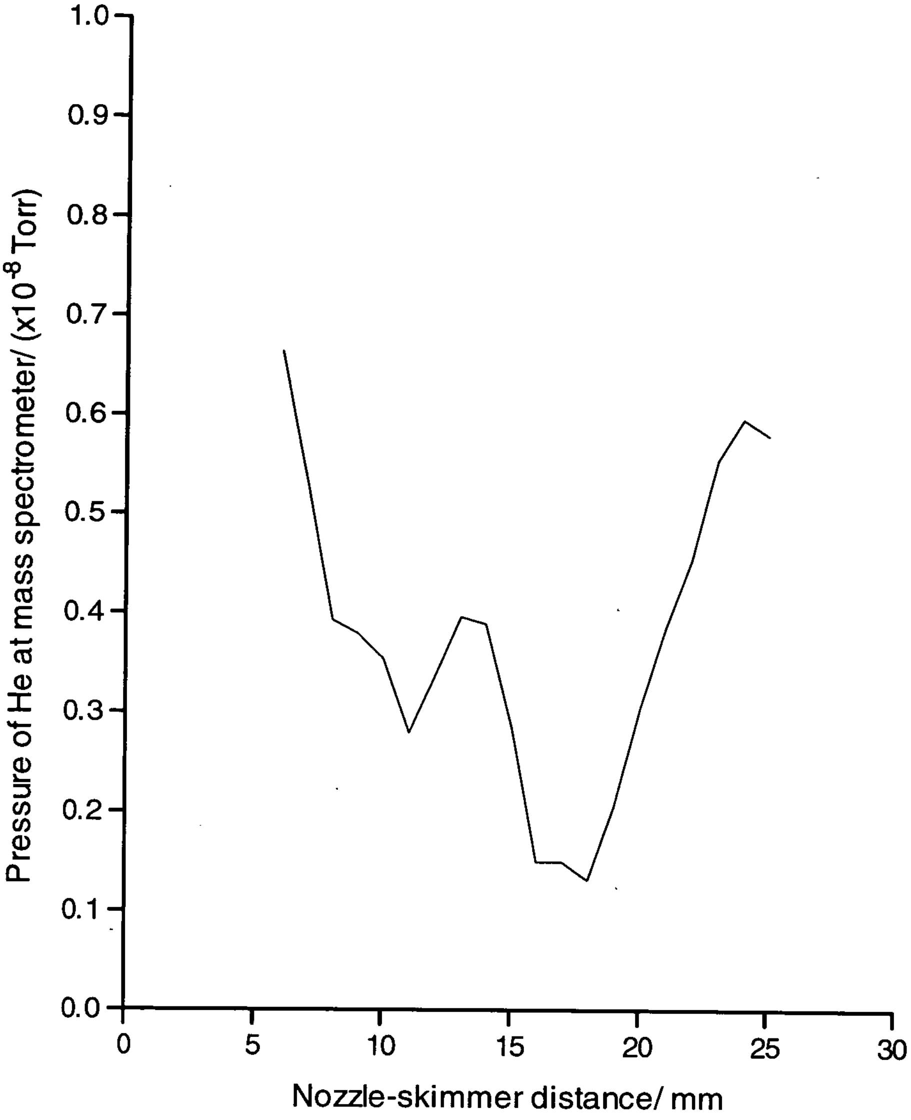

Figure 4.22 Plot showing He intensity at mass spectrometer versus nozzle-skimmer distance for a continuous molecular beam of a 30 bar He/CO_2 mixture.

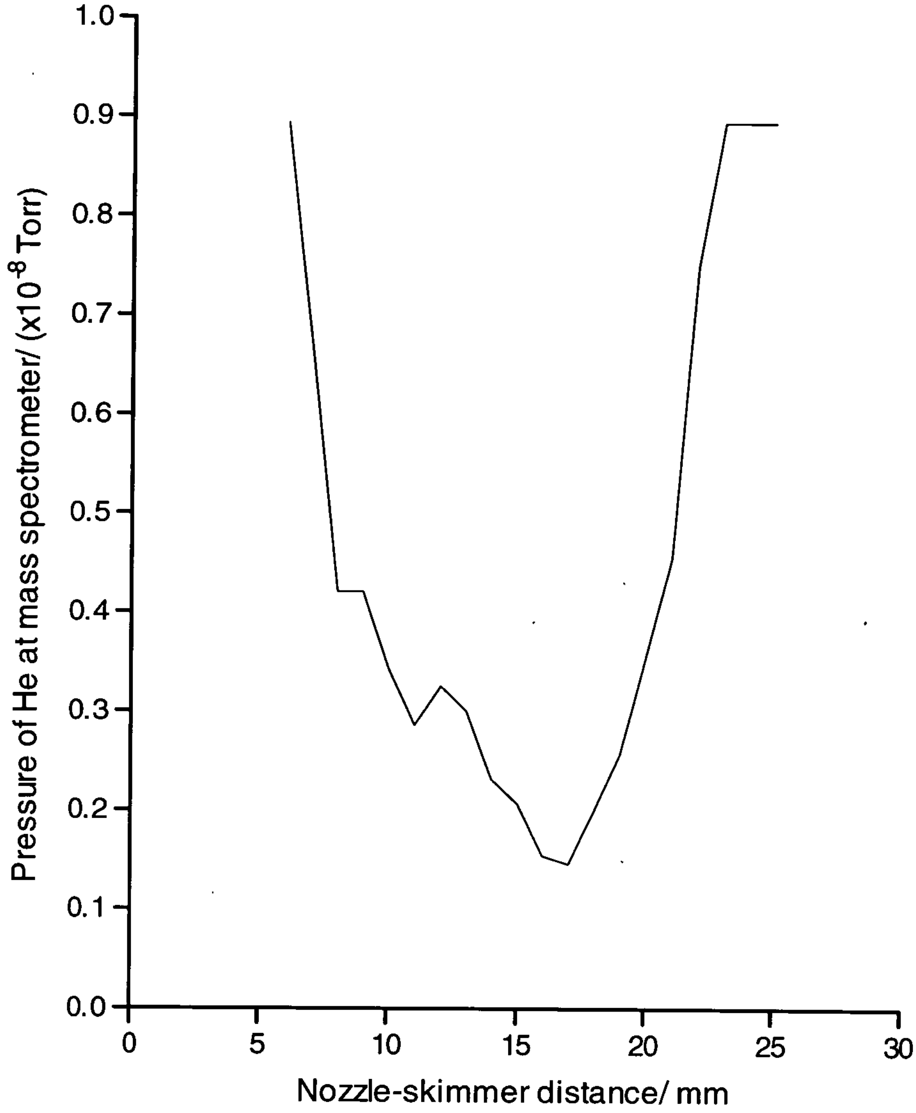

Figure 4.23 Plot showing He intensity at mass spectrometer versus nozzle-skimmer distance for a continuous molecular beam of a 40 bar He/CO_2 mixture.

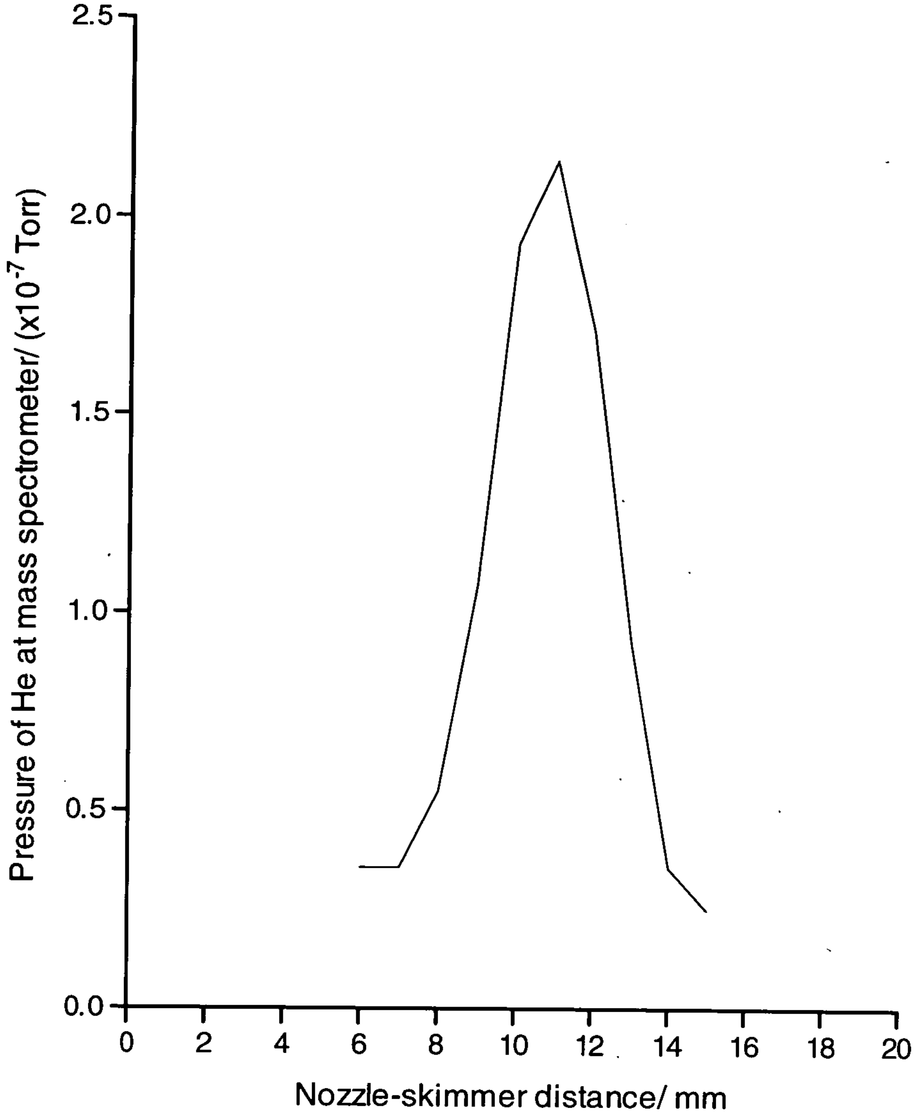

Figure 4.24 Plot showing He intensity at mass spectrometer versus nozzle-skimmer distance for a continuous molecular beam of 10 bar pure He.

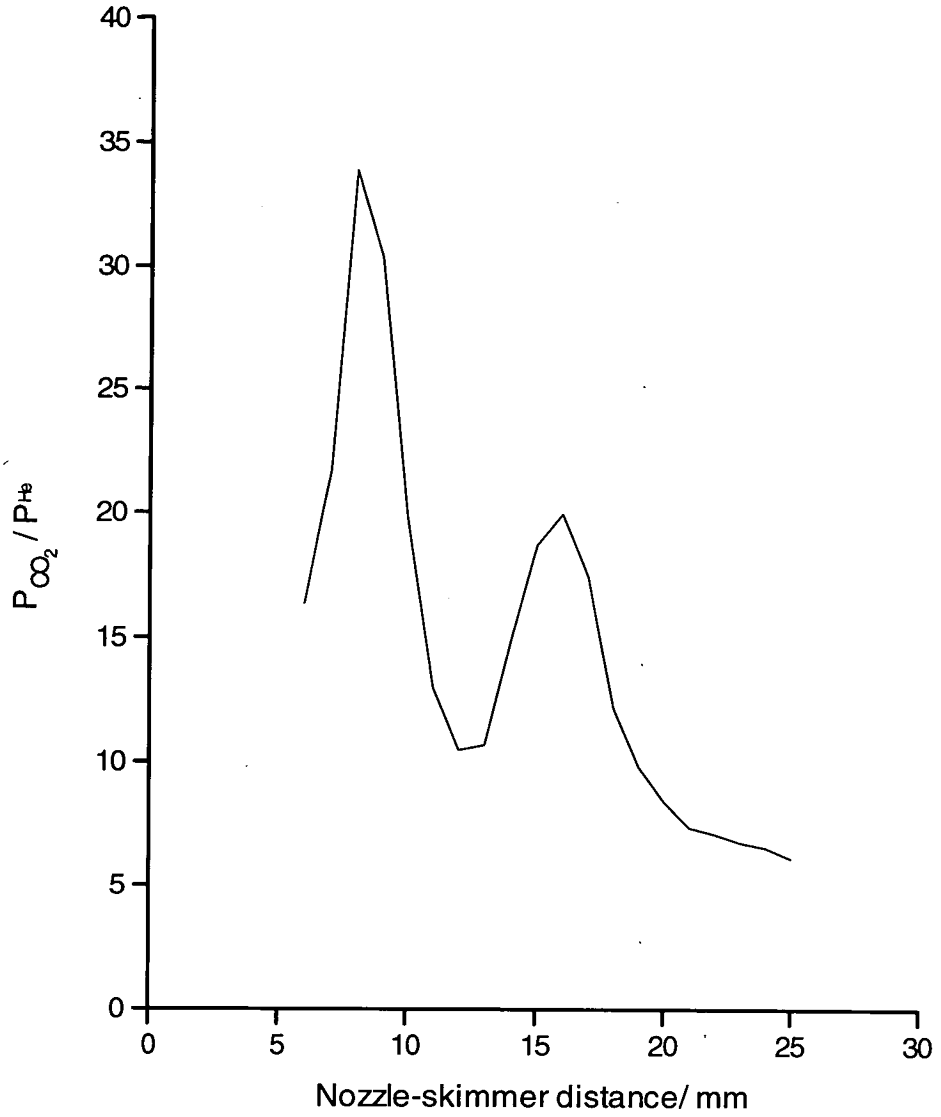

Figure 4.25 Plot showing the ratio of CO_2/He versus nozzle-skimmer distance for a 10 bar He/CO_2 mixture.

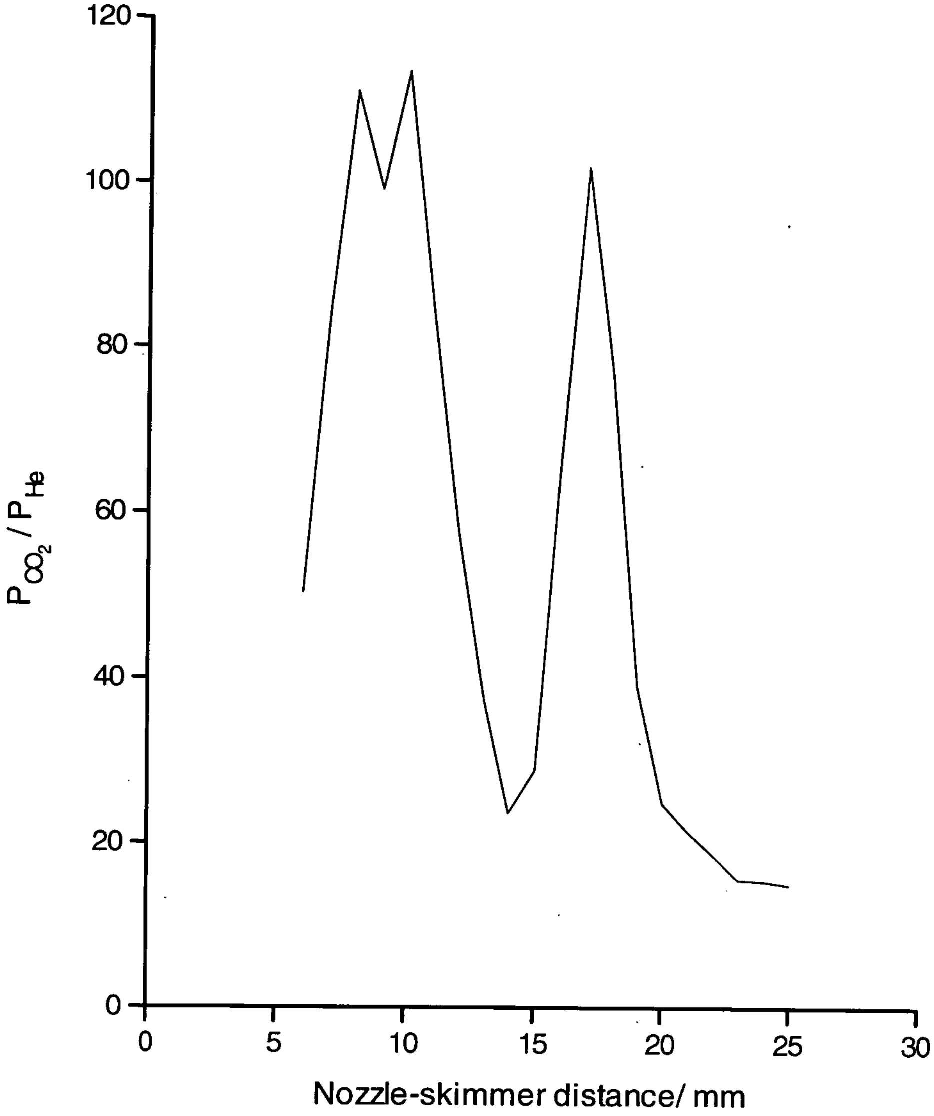

Figure 4.26 Plot showing the ratio of CO_2/He versus nozzle-skimmer distance for a 20 bar He/CO_2 mixture.

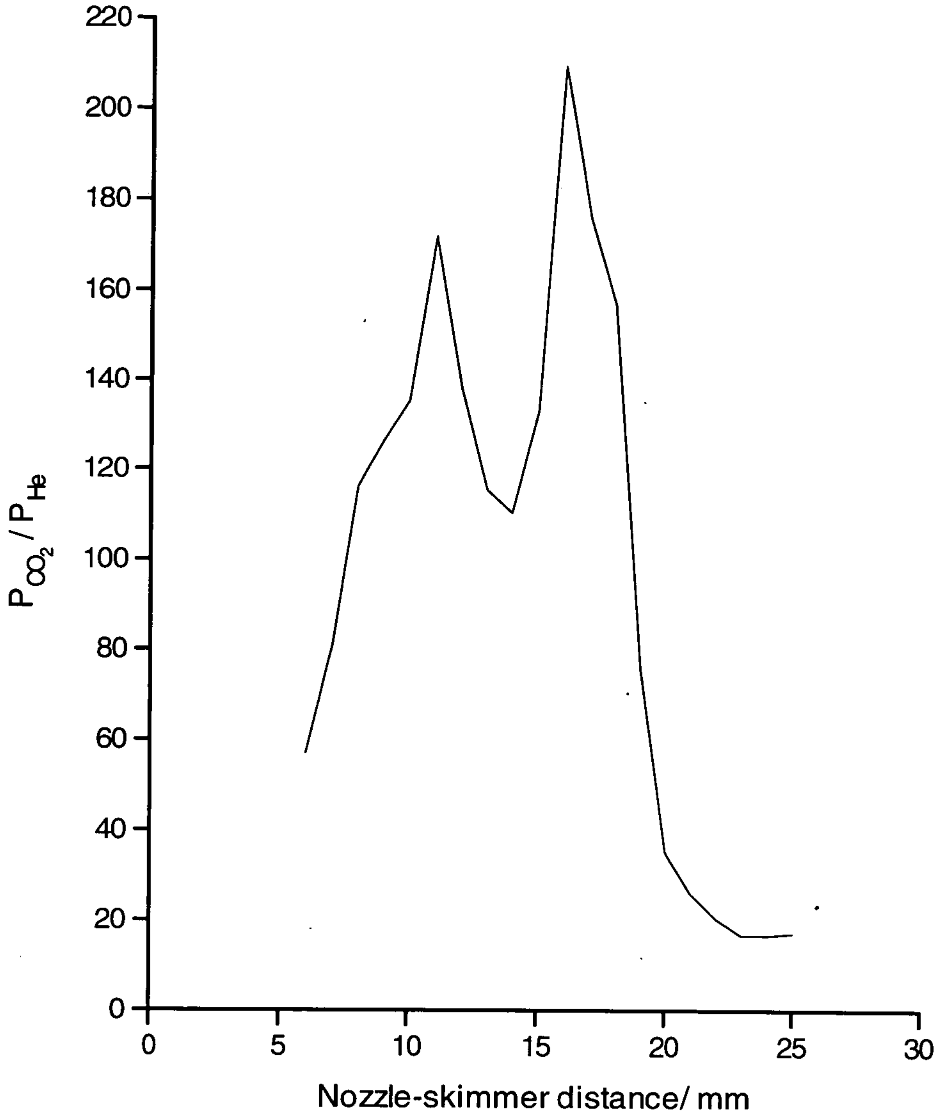

Figure 4.27 Plot showing the ratio of CO_2/He versus nozzle-skimmer distance for a 30 bar He/CO_2 mixture.

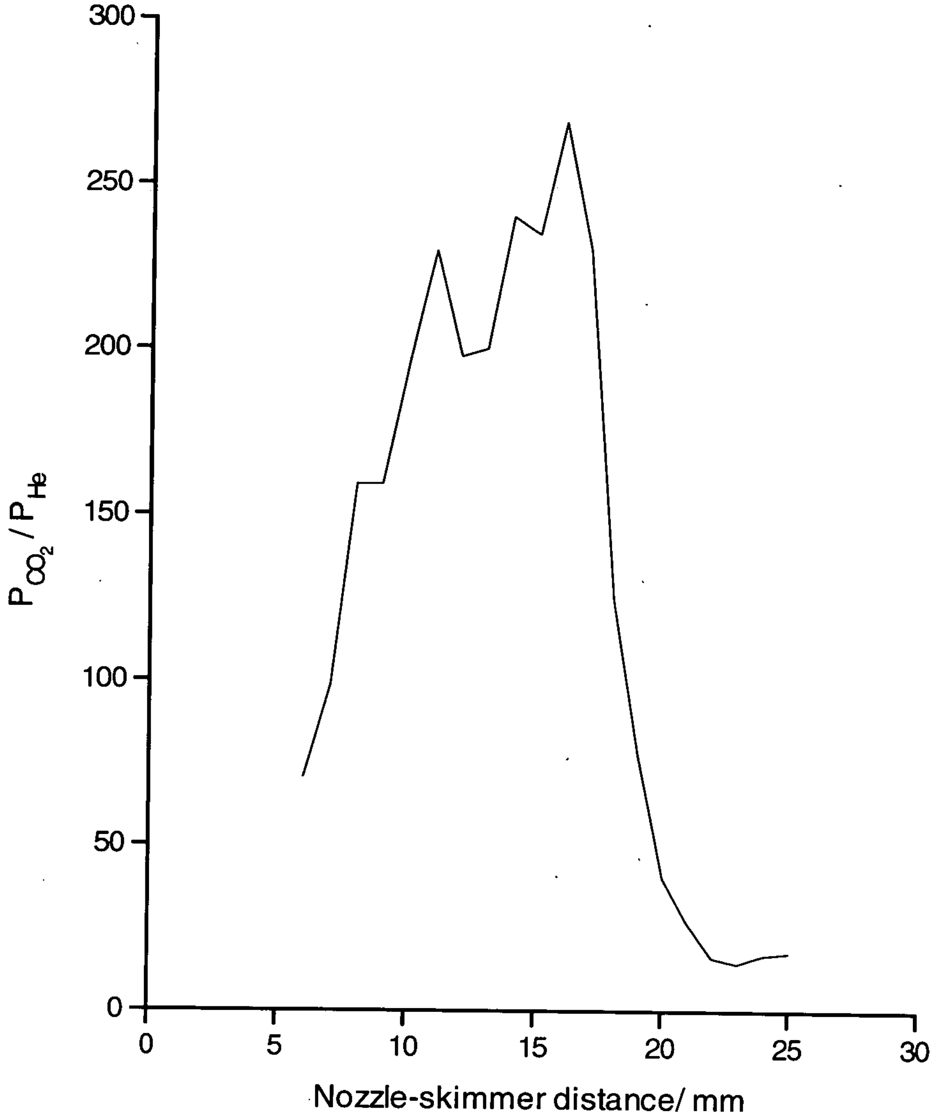

Figure 4.28 Plot showing the ratio of CO_2/He versus nozzle-skimmer distance for a 40 bar He/CO_2 mixture.

An attempt was also made to evaluate the rotational temperature of the molecular beam using a mixture of 5% NO seeded in He. Using an Nd-YAG pumped dye laser with wavelength extender (see **Fig. 3.2**) 1+1 multiphoton ionisation (MPI) of NO [20,21,22] was undertaken. Unfortunately these experiments proved unsuccessful due to an incorrectly made amplifier but beam profiles of NO pressures versus nozzle-skimmer distance were obtained. One such profile is illustrated in **Figure 4.29**. For a stagnation pressure of 23 bar He/NO a maximum NO pressure of 5.92×10^{-8} Torr was recorded at a nozzle-skimmer distance of 15 mm. Compared to **Figure 4.14** (20 bar He/CO_2) the maximum has shifted to a larger distance with the NO pressure much lower than the CO_2 pressure for a similar stagnation pressure. In **Figure 4.14** the CO_2 maximum of 3.36×10^{-7} Torr occurs at a nozzle-skimmer distance of 10 mm. A profile of a pure Ar beam was also recorded at a stagnation pressure of 40 bar (see **Fig. 4.30**) giving a maximum Ar pressure of 7.58×10^{-7} Torr at a nozzle-skimmer distance of 18 mm. Comparable CO_2 pressures were obtained for a 40 bar He/CO_2 mixture (see **Fig. 4.14**). A maximum CO_2 pressure of 6.71×10^{-7} Torr at a nozzle-skimmer distance of 8-10 mm was recorded. This lends further weight to the argument that the heavier species in a mixed free-jet expansion becomes enriched along the beam centreline. Although the CO_2 was diluted to a concentration of 5% in the He carrier gas CO_2 pressures of the same magnitude as the pure Ar expansion produced were recorded.

More recently some CO_2 profiles, in the He/CO_2 mixture, were recorded. In **Figure 4.31** shows the CO_2 intensities versus nozzle-skimmer distances for three stagnation pressures; 2, 4 and 6 bar. The maximum CO_2 pressure at 6 bar was 3.07×10^{-7} Torr. In **Figure 4.14** the CO_2 maxima were 8.57×10^{-8} Torr and 3.36×10^{-7} Torr at 10 bar and 20 bar He/CO_2 respectively. It was also noted the pressure in the main chamber was much higher than had previously been the case. Indeed the pumps could not handle a gas load greater than 10 bar perhaps indicating an increase in diameter of the nozzle source.

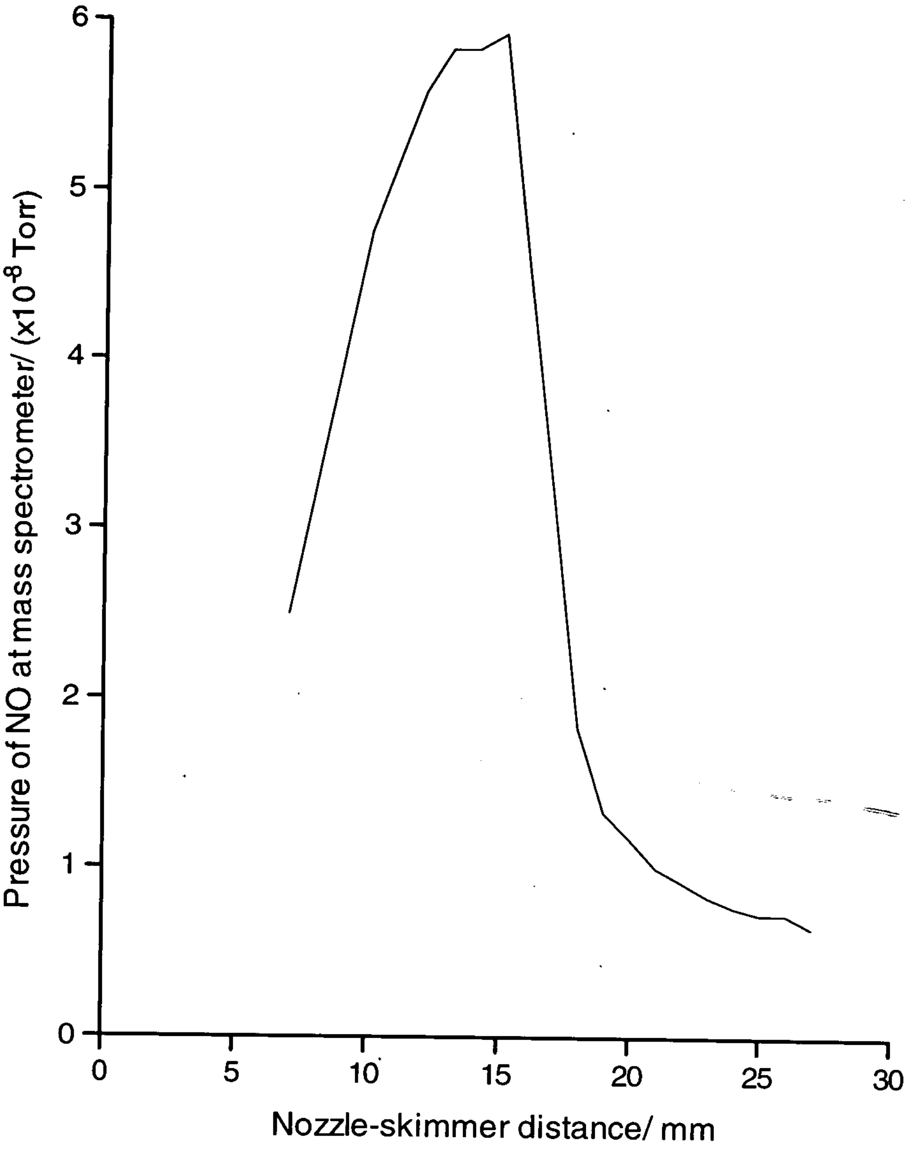

Figure 4.29 Plot showing NO intensity at mass spectrometer versus nozzle-skimmer distance for a continuous molecular beam of a 23 bar He/NO mixture.

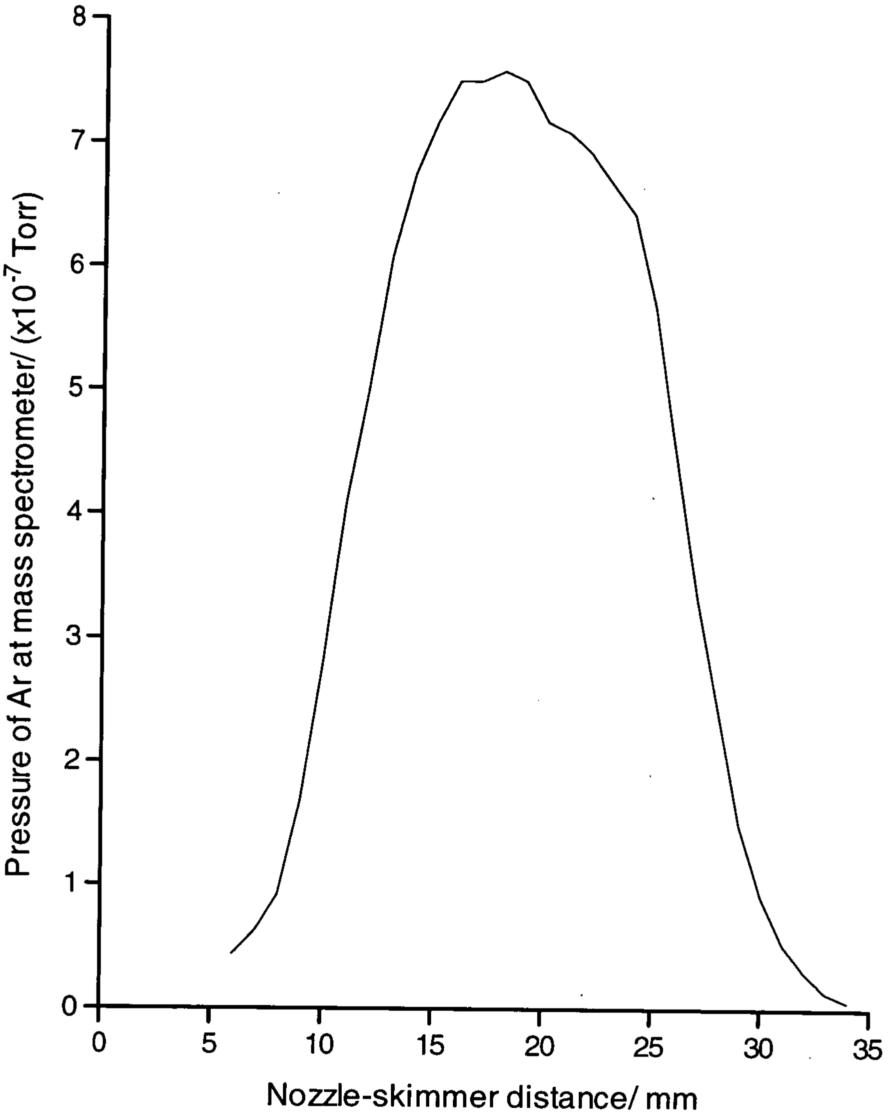

Figure 4.30 Plot showing Ar intensity at mass spectrometer versus nozzle-skimmer distance for a continuous molecular beam of 40 bar pure Ar.

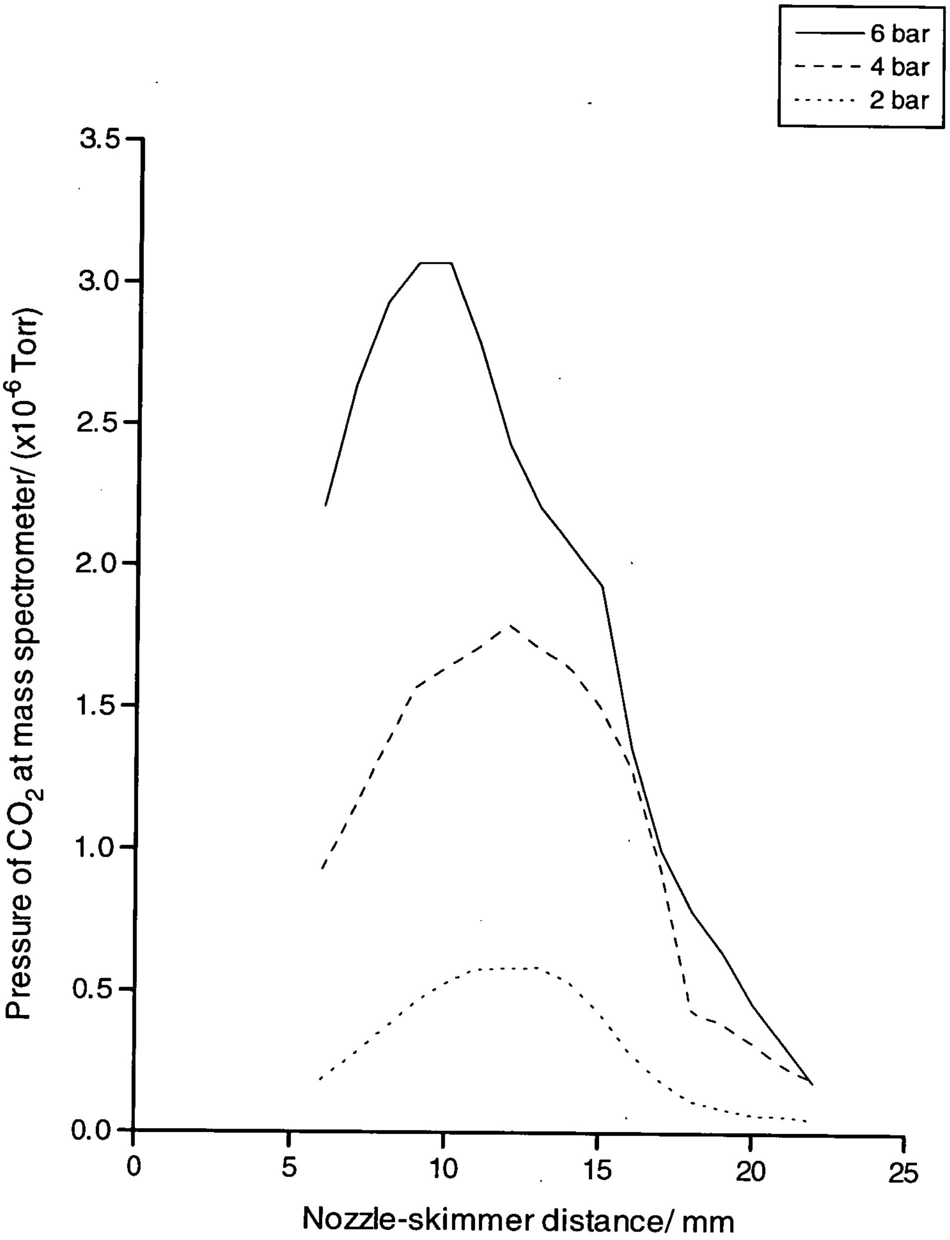

Figure 4.31 Plot Showing CO_2 intensities at mass spectrometer versus nozzle-skimmer distance for three stagnation pressures of a He/CO_2 mixture.

Bibliography

1 R. Campargue, J. Phys. Chem., 88 (1984) 4466 (and references therein)

2 J.B. Anderson and J.B. Fenn, Phys. Fluids, 8 (1965) 780

3 L.S. Bartell, Chem. Rev., 86 (1986) 780 (and references therein)

4 H.J. Neusser, Int. J. Mass Spec. Ion. Proc., 79 (1987) 141

5 A. Kantrowitz and J. Grey, Rev. Sci. Instrum., 22 (1951) 328

6 J.B. Anderson, R.P. Andres, and J.B. Fenn, in: Advances in atomic and molecular physics, Eds.: D.R. Bates and I. Estermann (Academic Press Inc., New York, 1965; and references therein)

7 D.R. Miller in: Atomic and molecular beam methods, Ed.: G. Scoles, (Oxford University Press, Oxford/New York, 1988) Ch.2, 14, (and references therein)

8 C.E. Klots, Chem. Phys. Lett., 137 (1987) 353

9 C.E. Klots, J. Chem. Phys., 72 (1980) 192

10 R.G. Gallagher and J.B. Fenn, J. Chem. Phys., 60 (1974) 3487

11 R.G. Gallagher and J.B. Fenn, J. Chem. Phys., 60 (1974) 3492

12 P.N. Bajaj and P.K. Chakraborti, Chem. Phys., 104 (1986) 41

13 H.R. Murphy and D.R. Miller, J. Phys. Chem., 88 (1984) 4474

14 M. Kappes and S. Leutwyler in: [7] Ch.15, 380, (and references therein)

15 T.A. Milne and F.T. Greene, J. Chem. Phys., 47 (1967) 4095

16 T.A. Milne, A.E. Vandegrift, and F.T. Greene, J. Chem. Phys., 52 (1970) 1552

17 D. Golomb, R.E. Good, and R.F. Brown, J. Chem. Phys., 52 (1970) 1545

18 R.J. Gordon, Y.T. Lee, and D.R. Herschbach, J. Chem. Phys., 54 (1971) 2393

19 M.P. Sinha, A. Schultz, and R.N. Zare, J. Chem. Phys., 58 (1973) 549

20 D.C. Jacobs, R.J. Madix, and R.N. Zare, J. Chem. Phys., 85 (1986) 5469

21 D.C. Jacobs and R.N. Zare, J. Chem. Phys., 85 (1986) 5457

22 H. Zacharias, M.M.T. Loy, P.A. Roland, and A.S. Sudbo, J. Chem. Phys., 81 (1984) 3148

Chapter 5

Telefocus Electron Gun

5.1 Introduction

A reliable electron beam is critical to the electron diffraction experiment. The electron beam used in a scattering experiment should be intense, but have a small diameter and opening angle. In most electron diffraction instruments a triode system with thermionic emission is used.

In this system the electrons are produced by thermionic emission from a tungsten cathode bent in a hairpin shape. A voltage is applied between anode and cathode leading to an electric field which penetrates the Wehnelt cylinder drawing the electrons from the tip of the wire. The Wehnelt cylinder is at a potential negative with respect to the cathode and this creates a space charge cloud in front of the cathode. This potential limits the cloud at the sides and by altering this potential the intensity of the electron beam can be controlled.

This triode system has one major disadvantage; the electric field close to the emitting wire is largely responsible for the electron beam's shape. The strength of the optical lens created by the electric field penetrating the Wehnelt is very high resulting in the electrons being focused on a small spot only a few microns in front of the filament. Thus the electron beam leaves the electron gun with a large angle of divergence. To overcome this problem beam limiting apertures can be used to produce a narrow beam. However this results in an electron beam of much reduced electron density by the time it reaches the scattering centre. In electron diffraction studies this may lead to longer recording times than normal, of the order of a few minutes. For many compounds of interest to the chemist the large amounts required to sustain the molecular beam are unavailable.

To overcome this problem the electron beam source chosen for this new instrument was a telefocus electron gun [1]. This electron gun can produce high beam currents that can be focused to a small spot size over a wide range of distances. The operation of the telefocus gun is discussed in **section 5.2**.

5.2 Telefocus Electron Gun

The telefocus gun (see **Fig. 5.1**), consisting of a hairpin cathode, a specially shaped Wehnelt cylinder and a flat anode diaphragm was first reported by Steigerwald [2]. This electron gun was capable of producing a fine focused electron beam over a variable range of distances from a gun without a previous cross-over.

This type of electron gun is ideal for various kinds of diffraction experiment as it can produce an intense electron beam of small angular divergence without the use of limiting apertures. The properties of the Steigerwald system were investigated in great detail by Braucks [3] and independently by Kamigaito [4]. Bas and Gaydou [5] investigated the telefocus system with a bolt cathode. Indeed, the Steigerwald system has been adapted for use in electron diffraction instruments using counting techniques [6,7,8]. The electron gun reported here was designed by Hermann Wellenstein of Brandeis University in Boston. He has experience in using the telefocus electron gun in diffraction experiments and published an excellent paper in which the mechanical parameters of this electron source were investigated [7]. The gun used in the Edinburgh apparatus was subsequently built by Chip Theusen at the University of Texas, Austin. Several views of the gun are shown in **Figures 5.2 - 5.4**.

In some telefocus systems [6,7,8], the relative positions of the two electrodes can be varied by the axial movement of the Wehnelt electrode inside the outer cylinder called the Trichter. More recently, Schiewe *et al.*

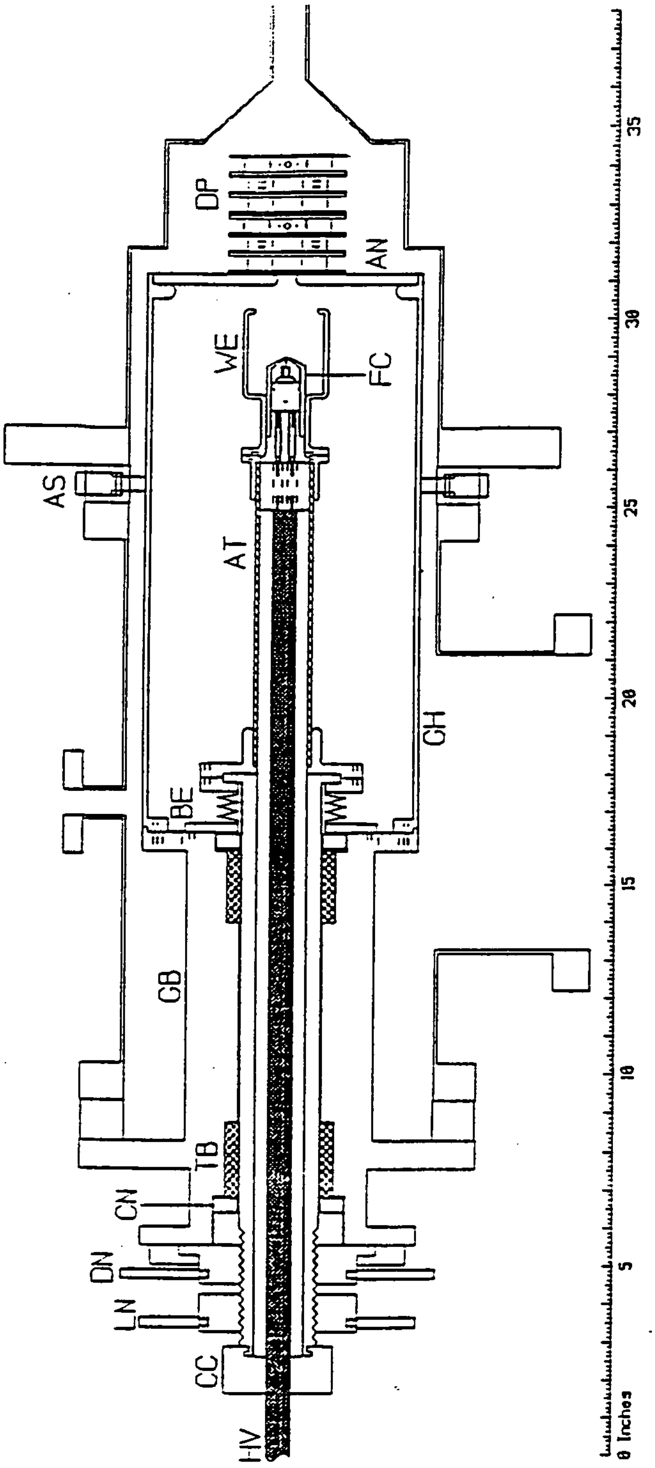

Figure 5.1 Schematic of telefocus electron gun.

AN - Anode
AS - Adjust/Support Screw
AT - Alumina Tube
BE - Bellows
CC - Cable Clamp
CN - Compression Nut
DN - Drive Nut
DP - Deflector Plate
FC - Filament Cup
GB - Guide Block
GH - Gun Housing
HV - High Voltage Cable
LN - Lock Nut
TB - Teflon Bearing
WE - Wehnelt

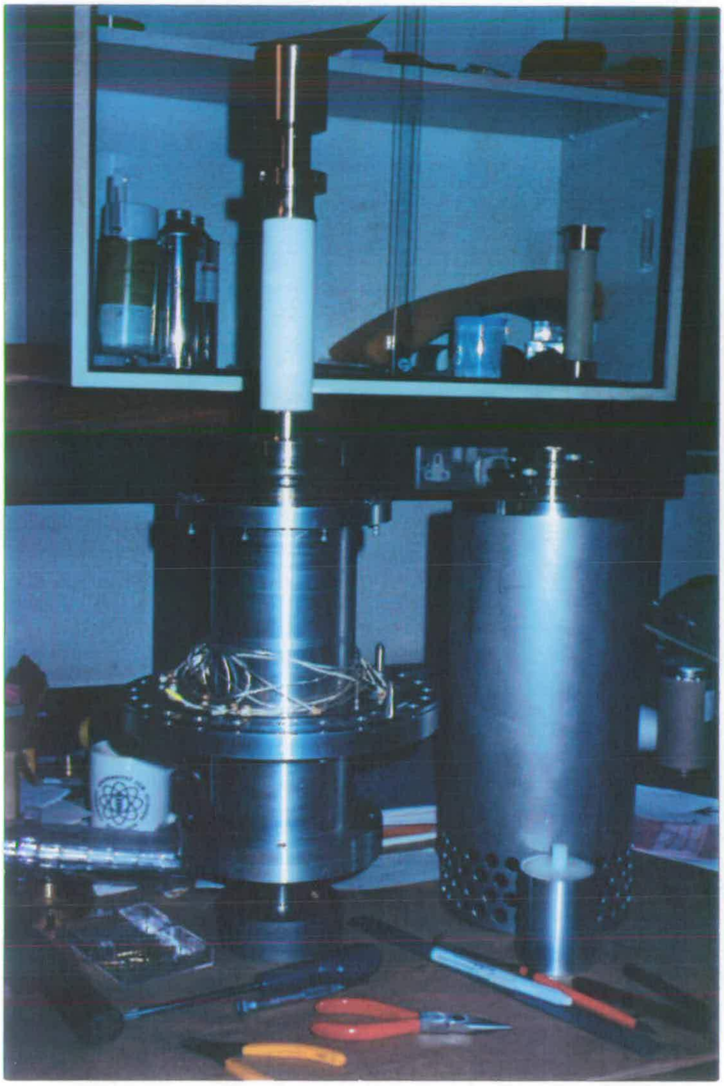

Figure 5.2 Picture of telefocus electron gun. On the right hand side is the gun housing with the anode and the deflector plates at the top. The gun optics including the outer Wehnelt can be clearly seen on the left hand side at the top of the ceramic feedthrough.

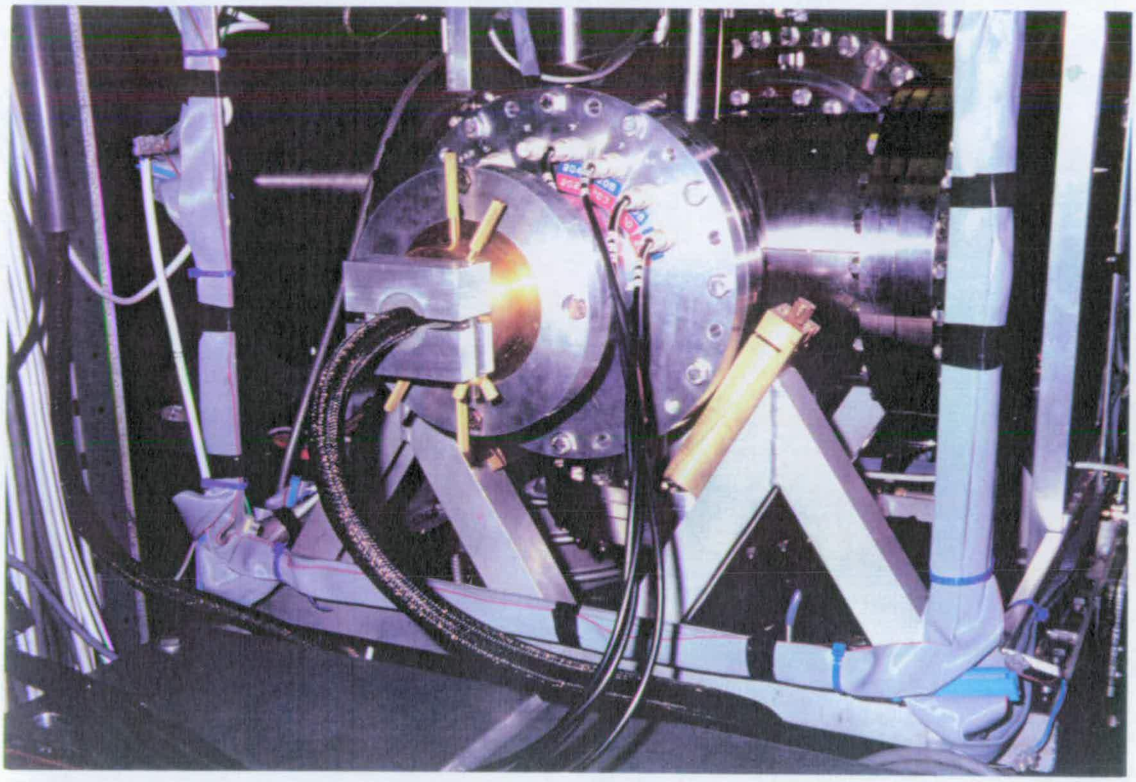

Figure 5.3 View of electron gun as seen from outside vacuum system. Note the E.H.T. cable and its clamp together with the B.N.C. connections for the deflector plate voltages. Also note the brass drive nut, lock nut and aluminium cable clamp.

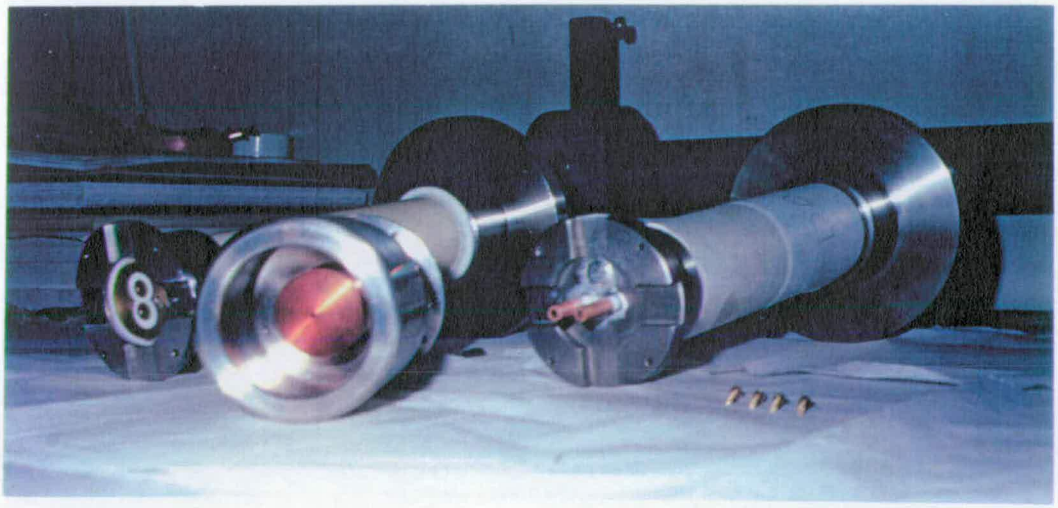

Figure 5.4 High voltage feedthrough and electron gun optics. On the left hand side of the picture the outer Wehnelt can be seen together with the angled copper Wehnelt which houses the filament.

constructed a Steigerwald system with an axially-movable anode [9]. The electron gun detailed in this thesis is of the latter type. Taguchi and Iijima [10] have also reported a telefocus electron gun for use in a gas electron diffraction unit [11], in which sheet films are used as detectors. In this telefocus system the distance between the inner cylinder and the exit of the outer Wehnelt is altered by changing the length of the Trichter. The height of the anode can also be changed to keep the distance between the Trichter and the anode constant.

In the Edinburgh telefocus gun a high voltage power supply built by Start Spellman is used to provide an E.H.T. of up to 50 kV to a Siemens cathode made of tungsten wire. The cathode or filament is bent in a hairpin shape to enhance the production of electrons through thermionic emission. The power supply feeds a current of up to 3 A to the filament. Generally a filament current of 2.3-2.4 A is used. The filament in this gun sits 0.006 inches (0.15 mm) behind the copper pointers which form the filament cup (see **Figs. 5.1** and **5.5**).

Voltage applied between the anode and the filament (see **Fig. 5.6**) creates an electric field which penetrates the large hole in the Wehnelt cylinder. A variable voltage V_g on this Wehnelt aperture, which is negative with respect to the cathode, causes a space charge cloud to form in front of the filament. By altering the Wehnelt voltage V_g the beam current can be changed.

Due to the cone-shaped copper electrode in whose centre the filament is mounted (see **Fig. 5.5**), the equipotential lines penetrating the large opening form a diverging lens which determines the trajectories of the slowly moving electrons near the filament. At the large opening near the end of the Wehnelt cylinder, the equipotential lines form a converging lens. The fact that the electrons have already been accelerated makes the action of the lens weaker. The Wehnelt voltage which controls the lenses can now be arranged so that

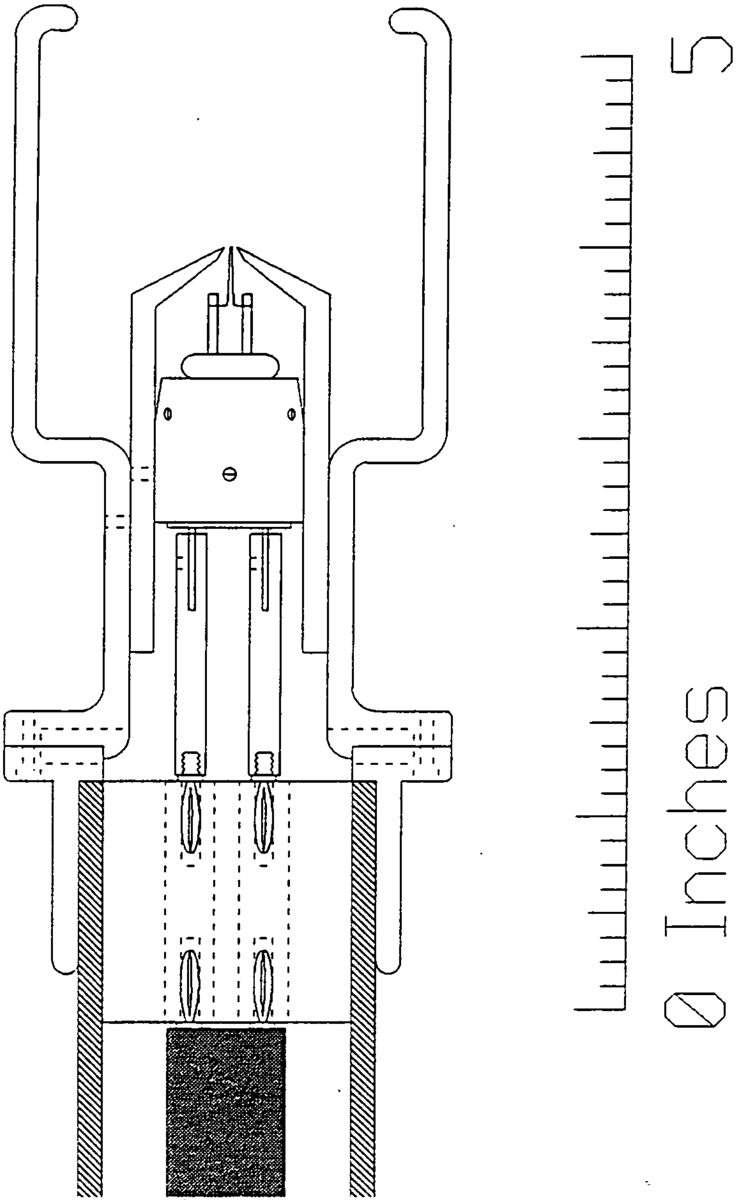

Figure 5.5 Detail of telefocus electron gun optics. In this diagram the filament appears to be flush with the copper pointers (inner Wehnelt). It actually sits 0.006 inches behind the pointers.

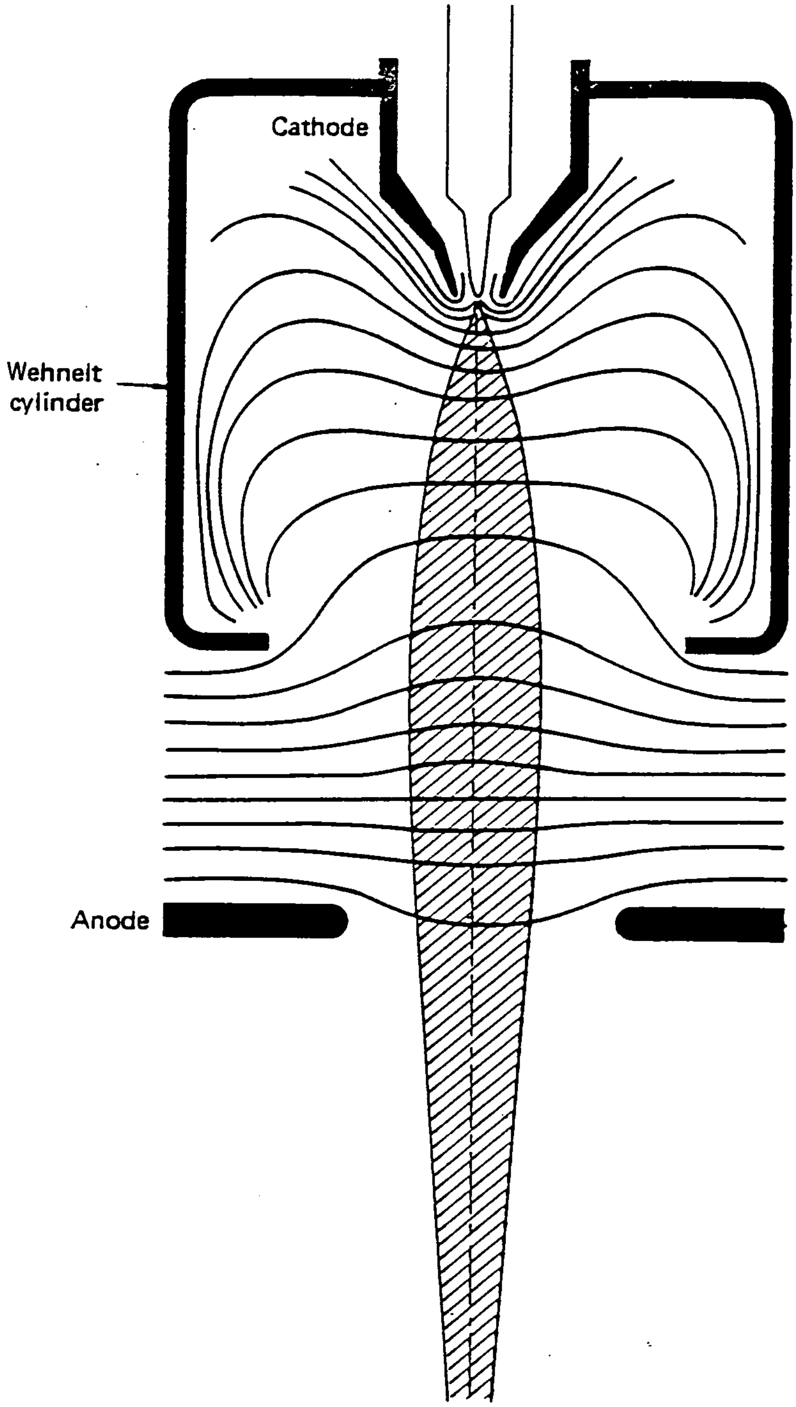

Figure 5.6 Diagram showing the equipotentials created by a telefocus system. There is a diverging lens close to the filament and a converging lens at the large opening near the end of the Wehnelt cylinder. Taken from [1].

the first cross-over of the electron beam can be set at nearly any desired distance.

In the Edinburgh telefocus electron gun the Wehnelt and filament cup (see **Fig. 5.1**) can be moved with respect to the anode. This should have allowed the beam to be focused at different points. No focussing effect has been observed although the electron beam was seen to have a FWHM of around 0.6 mm at all points along the scattering path.

Another method of altering the position of the cross-over is illustrated in **Figure** 5.7. By increasing the distance between the filament and the large opening in the Wehnelt cylinder it is possible to bring the electron beam cross-over closer to the filament. This is because the diverging field gets weaker and the converging field stronger.

As mentioned the Start Spellman supply feeds a voltage of up to -50 kV to the filament whilst the maximum voltage to the Wehnelt, V_g, is a further 167 Volts negative with respect to the cathode. When this maximum voltage is in place no beam current can flow.

A routine was developed to get good beam stability. Initially the filament would be run at 2.30 Amperes with no E.H.T. dialled up. This allowed the filament to warm up and assume its operating shape. This operation took around 40 minutes to 1 hour. The next step is to dial up the required high voltage; in the case of most of the work done on this machine this was 30.00 kV. The gun would be left for a further hour and then a beam current dialled up (on the 0-1000 nA scale). The bias voltage starts at the maximum difference of -167 volts and drops to a point known as the "pinch-off" where electrons in the charge cloud in front of the filament can leave the Wehnelt cylinder. It was noted that for a set beam current of around 500 nA (4.0 on dial) the bias voltage decreased with decreasing E.H.T. whereas the time it took for an emission current to flow (the time after being dialled up)

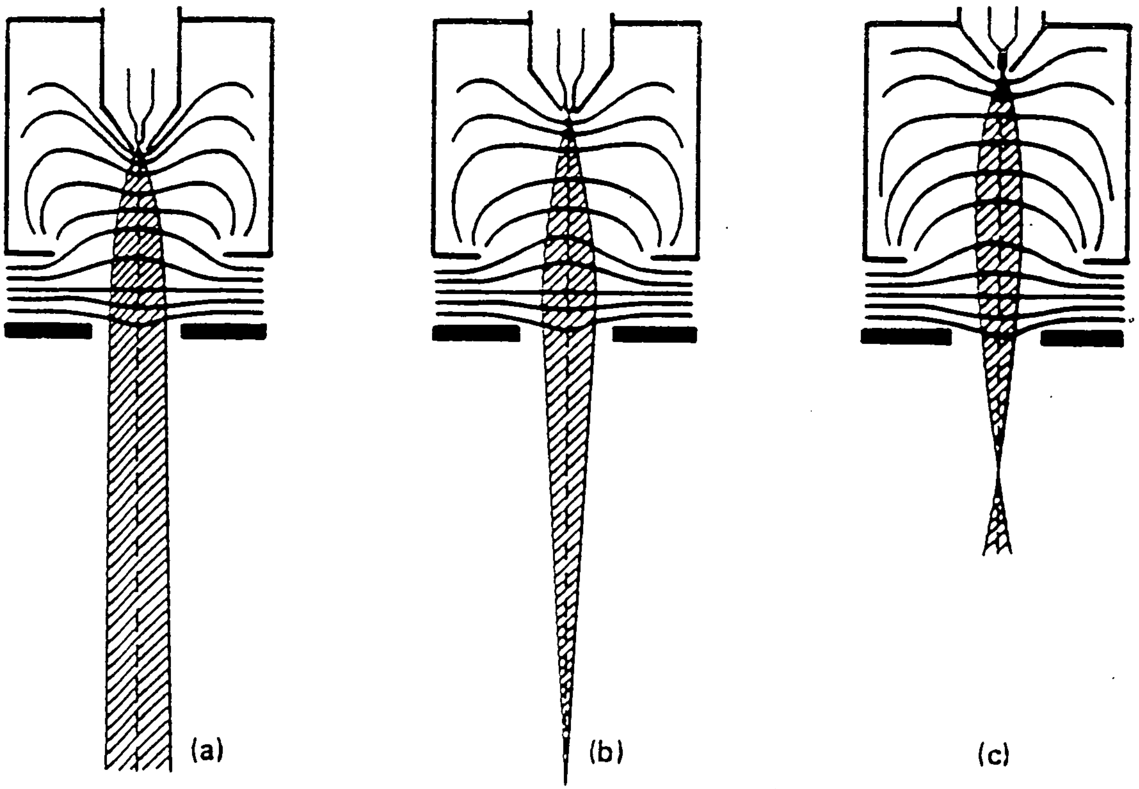

Figure 5.7 Diagram showing the effect of moving the filament further away from the anode whilst maintaining a fixed distance from the Wehnelt to the anode. The filament to anode distance increases from (a) to (c) bringing the cross-over closer to the filament due to the increased power of the converging field. Taken from [1].

increased with decreasing E.H.T.. These results on the performance of the power supply are displayed in **section 5.3**.

The control of the electron beam can be manual or automatic. Most work reported was carried out under manual control. As mentioned a beam current is dialled up and some time after this, depending on the E.H.T., a beam current begins to flow. If once the desired beam current is reached the current changes, the dial must be altered by hand in the manual mode. In the automatic mode, once a beam current has been dialled up a servo mechanism alters the Wehnelt bias internally to maintain the required beam current. A small switch inside the power supply is used to choose the mode of operation.

It has been found that the electron beam is stable over a period of several hours. However much of the work reported in the following section concerning beam profiles and cross-sections was undertaken when the E.H.T. was unstable. This was corrected and the E.H.T. is now accurate to within 0.01%. At this stage the original current scales 0-5 μA and 0-100 μA were reduced one hundred-fold to 0-50 nA and 0-1000 nA. All of the data collected on the operation of the power supply and gun presented in **section 5.3.2** were obtained on the 0-1000 nA scale. The 0-50 nA scale was found to be inoperable due to the combined high capacitance of the electron gun and high tension cable that supplies power to the gun. .

5.3 Experimental Details

5.3.1 Electron Beam Cross-Sections And Profiles

It was mentioned in **Chapter 3** that two pairs of deflector plates were used to steer the electron beam through the centre of the beam tube. Two copper collars, insulated from the beam tube, were used to collect the beam when it was deflected in order to establish the deflection voltages required in the horizontal and vertical dimensions (see **Fig. 5.8**). This ensured that the

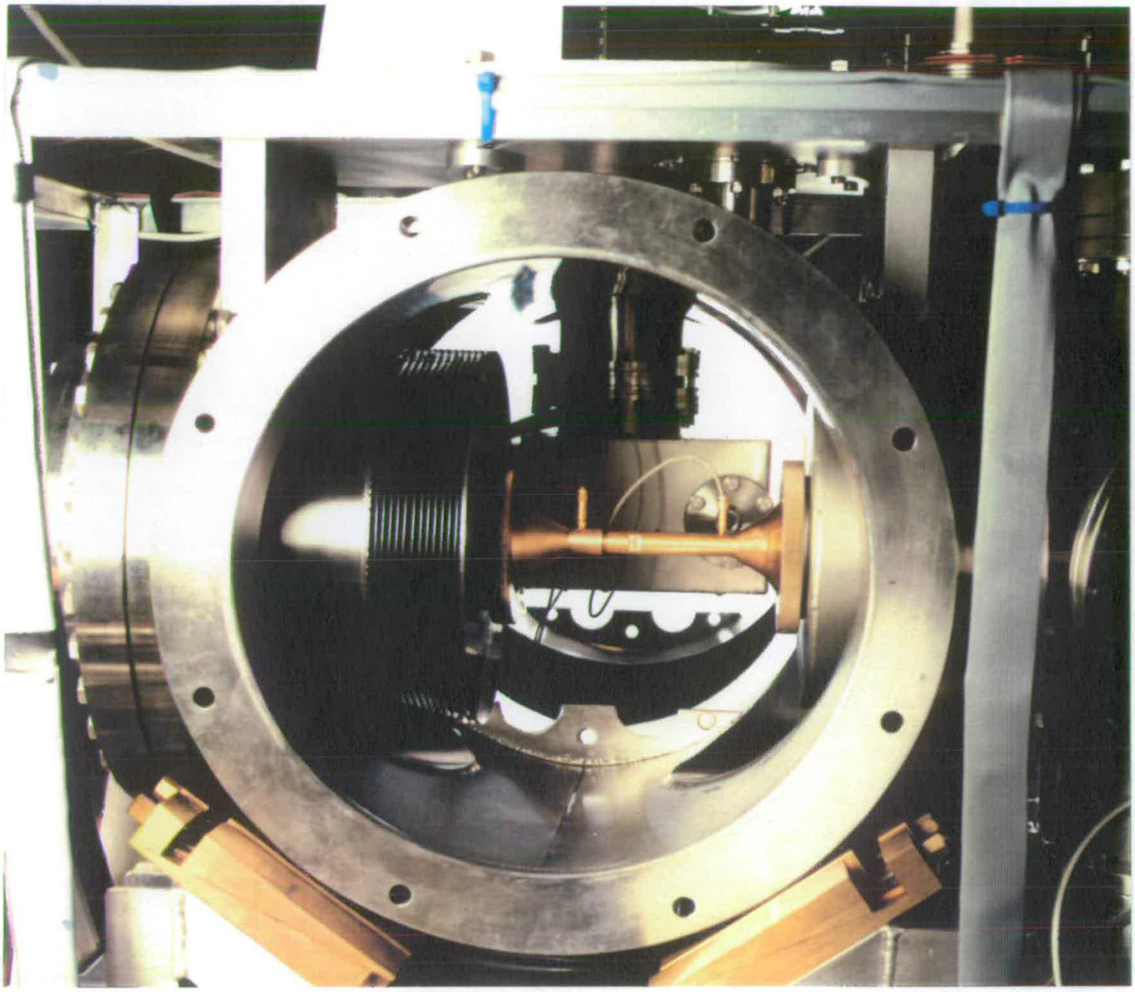

Figure 5.8 Picture of apparatus showing the original brass beam tube held in position by the two brass retaining rings. The two connectors to the copper collars inside the beam tube are pictured. These collars are used for centring the electron beam with the one on the right hand side situated just before the scattering centre.

electron beam passed directly through the molecular beam. As the majority of the electron beam remains undeflected after passing through the molecular target a collection system was needed for the primary electron beam. Holes of diameter 6 mm situated at the centres of the MCPs and the anode plate allowed the primary electron beam to pass into a collector. This was positioned about 40 mm behind the front of the MCPs. The main collector consisted of a copper Wood's horn situated behind a hole of diameter 0.85 mm in a circular piece of ceramic of diameter 25 mm. The front of the ceramic had a copper surface and four separate quadrants were etched to create four further collectors. The signals from all five collectors were amplified using a simple head amplifier. These currents could be monitored in the control program acting as a further aid to beam positioning.

Once suitable deflection voltages had been established the whole detector head , with the collector at its centre, was moved using the xyz translator. By moving the detector in the horizontal and vertical dimensions the maximum beam current captured in the Wood's horn was found. By then moving the detector head in a horizontal line at the height of the beam maximum, cross-sections of the electron beam were obtained. **Figures 5.9** and **5.10** show the cross-sections for electron beam intensities of 1.0 μA and 2.0 μA respectively. In **Figure 5.9** the beam maximum was 0.51 μA and the beam had a FWHM of 0.94/0.95 mm. The maximum current collected in **Figure 5.10** was 1.25 μA and had a FWHM of 0.76/77 mm. As expected both plots show the beam to have a Gaussian distribution.

Beam profiles were also obtained by systematically recording beam cross-sections at a range of detector heights. **Figure 5.11** shows an example of the raw data measured in the Wood's horn. At this point it was decided to deconvolute the beam profiles. This was done to remove the influence the shape of the hole in the ceramic (circular, diameter 0.85 mm) had on the recorded profile. A program called **decoke**, listed in **Appendix A**, was written by Dr. M.A.D. Fluendy to carry this out. The data was fitted using a

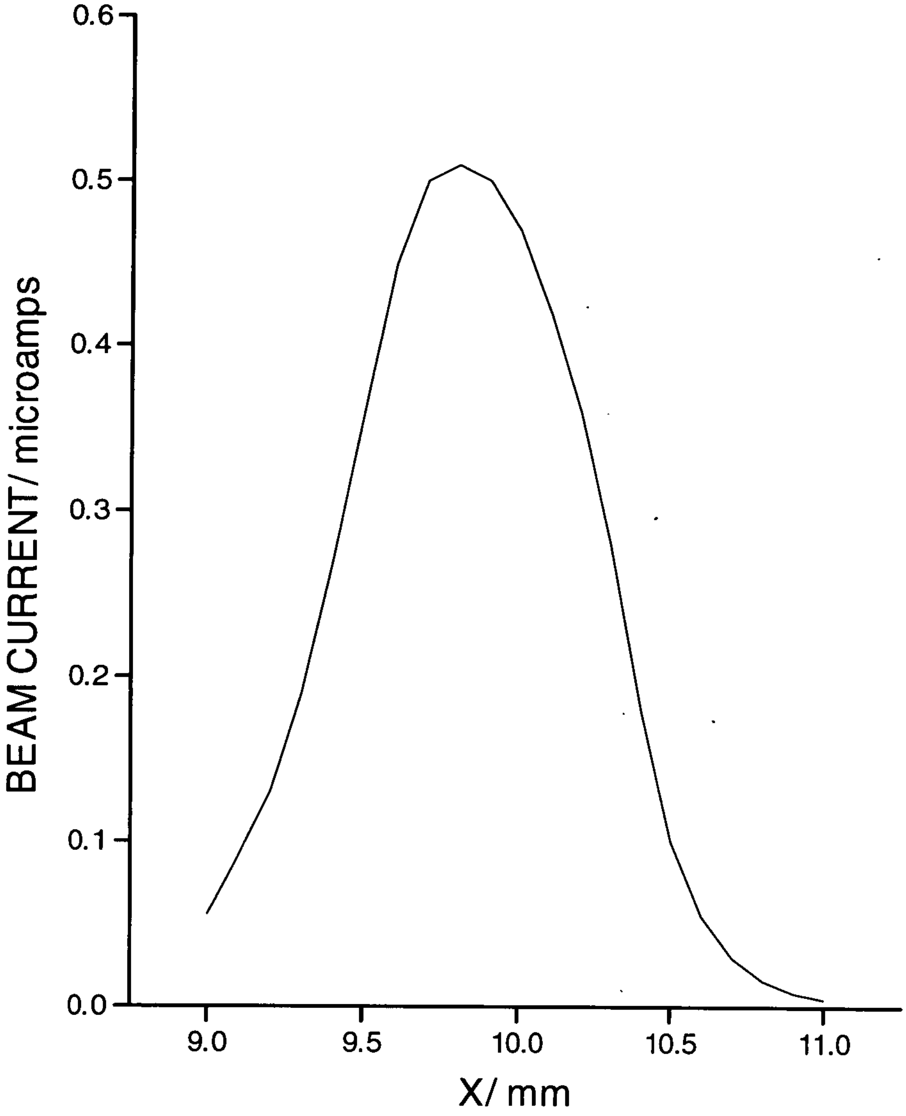

Figure 5.9 Cross-section through maximum of an electron beam of intensity 1.0 μA. The cross-section has a FWHM of 0.94/95 mm and a maximum collected current of 0.51 μA. The distance from the electron gun to the collector is 600 mm.

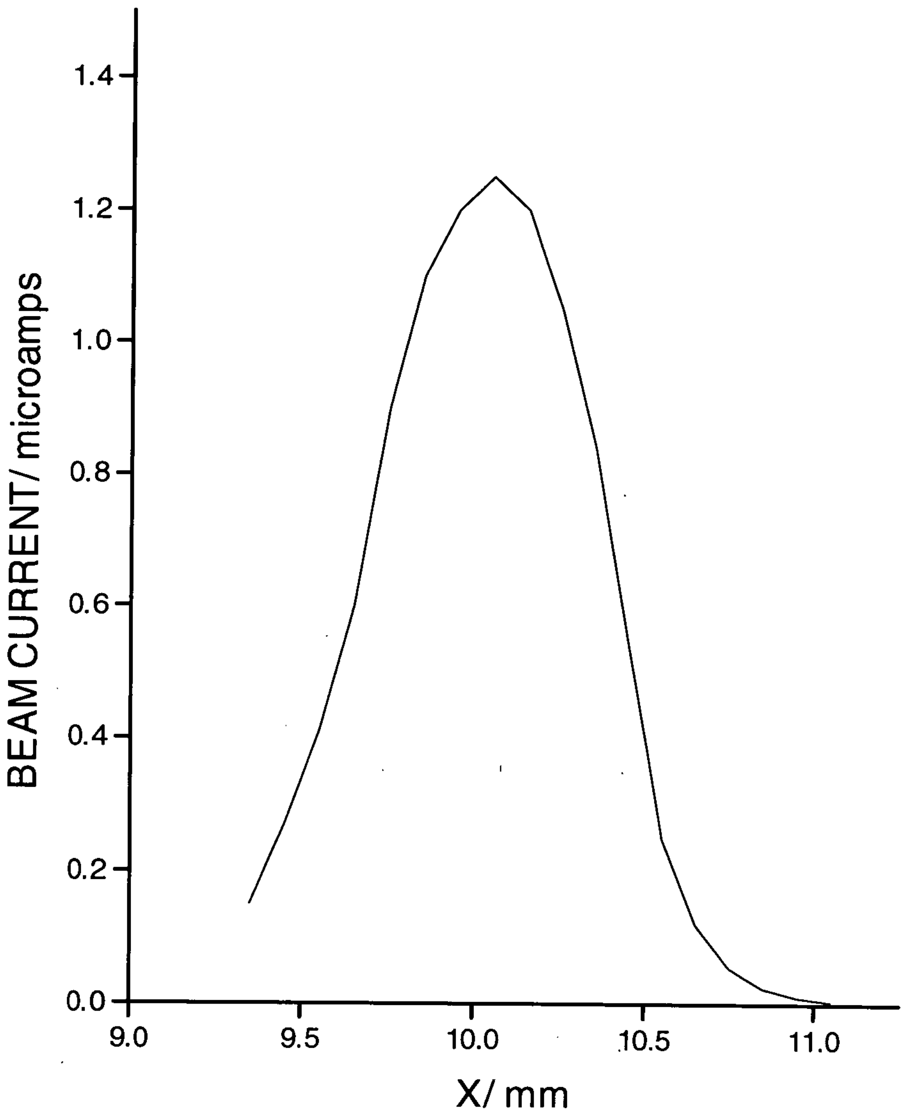

Figure 5.10 Cross-section through maximum of an electron beam of intensity 2.0 μA. The cross-section has a FWHM of 0.76/77 mm and a maximum collected current of 1.25 μA. The distance from the electron gun to the collector is 500 mm.

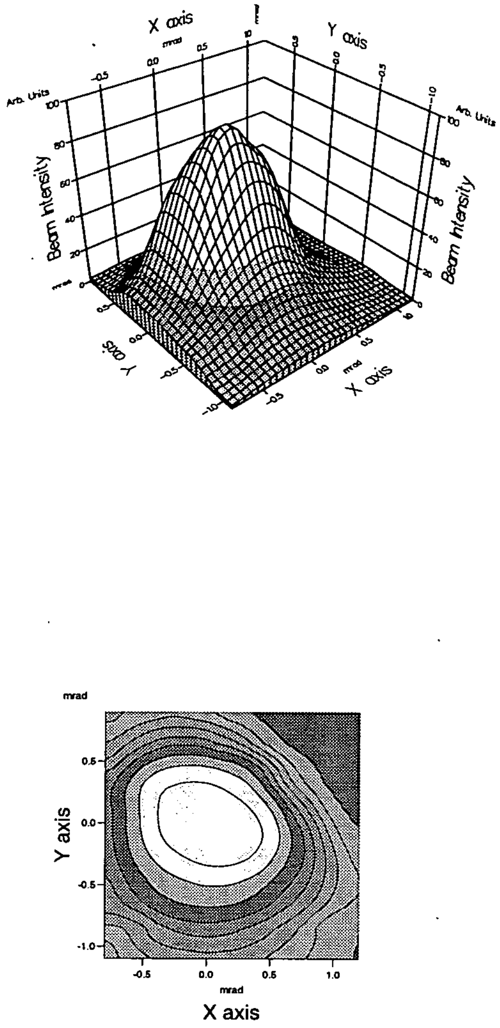

Figure 5.11 Contour plots of raw data for an electron beam collected in Wood's horn. The electron beam intensity is 1.0 μA and the maximum collected current is 0.51 μA. The FWHM is 0.94/95 mm and the distance from the electron gun to the collector is 600 mm. The plots are normalised to a maximum of 100.

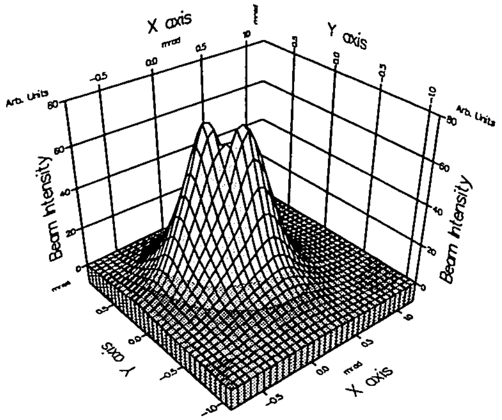

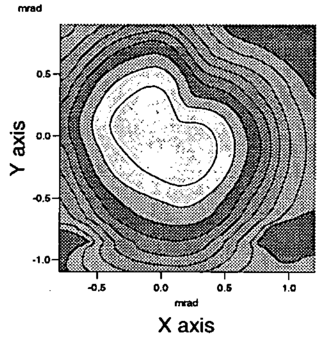

Figure 5.12 Contour plots of the deconvoluted electron beam. Note the double maximum, possibly caused by poor fitting of the data. The deconvoluted beam has a FWHM of around 0.6 mm.

circular function to fit radially whilst Legendre polynomials of up to order five fitted the angular part of the data. The deconvoluted profile appears in **Figure 5.12**. There appears to be two maxima after deconvolution and the FWHM was reduced from 0.94/0.95 mm to 0.6 mm. No explanation, apart from poor fitting, could be found to account for the double maximum as the input data set in **Figure 5.11** has a fairly symmetric Gaussian distribution.

5.3.2 Operational Details

In **section 5.2** it was mentioned that some work was done on the operational characteristics of the high voltage power supply and telefocus electron gun. The Start Spellman supply had an instability in its high voltage output when the work in **section 5.3.1** was carried out. On its return a small meter had been added allowing the Wehnelt bias voltage to be monitored. **Figures 5.13-5.20** show the bias voltage and beam current produced at different dial settings on the supply. This was done at four E.H.T.s; 30, 35, 40 and 45 kV. It was noted that as the E.H.T. was reduced the bias voltage needed for a set current was lower (see **Table 5.1**).

Further work was carried out where the bias voltage and the emission current were monitored for several minutes after a beam had been dialled up on the power supply. This work was done at the four E.H.T.s above for a set beam current of around 500 nA (4.0 on dial setting). These data are shown in **Figures 5.21-5.24**. It can be seen that the time it takes for a beam to flow after being dialled up takes longer the lower the E.H.T. is. These results are summarised in **Table 5.2**.

Table 5.1 Bias voltages and dial settings at three different beam currents for four high voltages.

High voltage/ kV	Beam current/ nA	Bias voltage/ V	Dial setting
30	500	94.7	3.80
30	250	95.8	2.50
30	100	96.8	1.70
35	500	107.4	3.85
35	250	109.1	2.50
35	100	110.3	1.70
40	500	122.5	3.80
40	250	123.9	2.45
40	100	125.3	1.70
45	500	137.5	3.85
45	250	139.3	2.50
45	100	141.4	1.65

Table 5.2 Bias voltage and emission time (time it takes for a beam current to flow after being dialled up) for a set beam current of around 500 nA at four different high voltages.

High voltage/ kV	Emission time/s	Bias voltage/ V
30	420	94.8
35	330	108.3
40	230	123.6
45	180	137.5

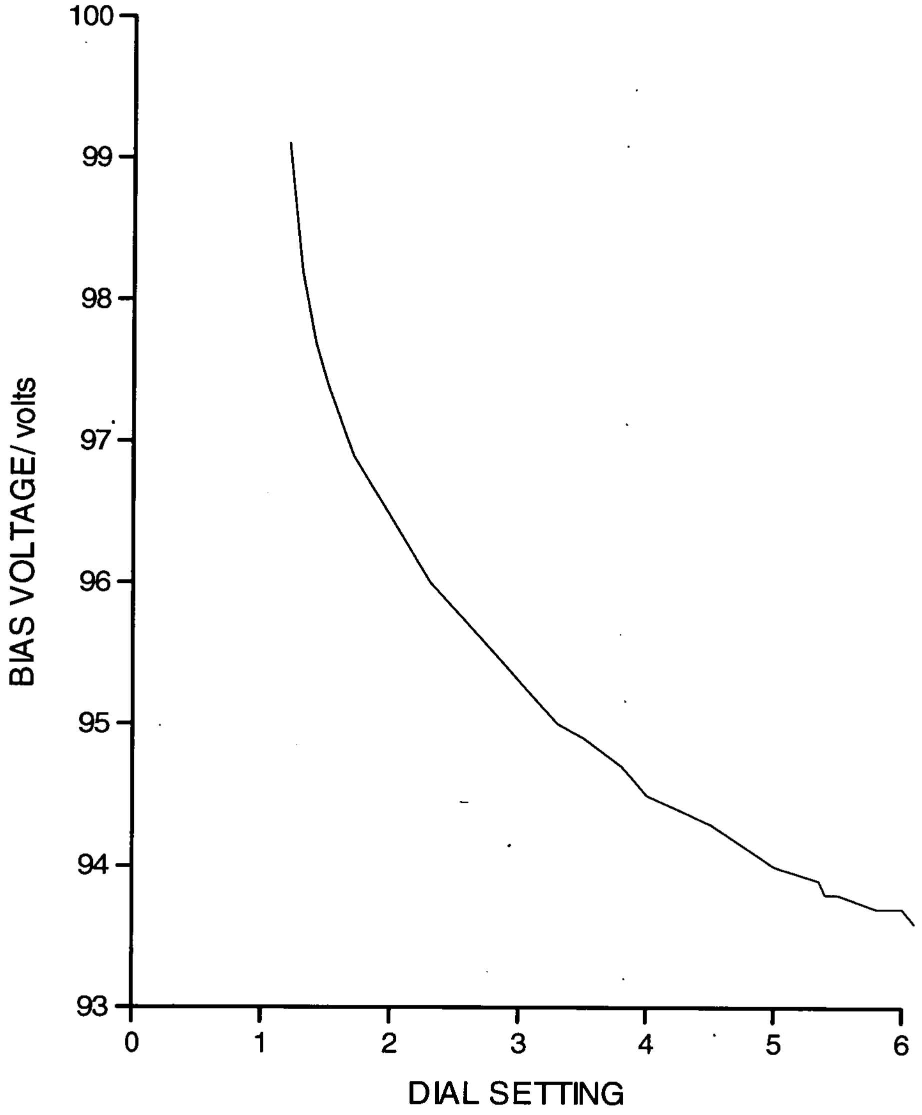

Figure 5.13 Plot of bias voltage versus dial setting at 30 kV.

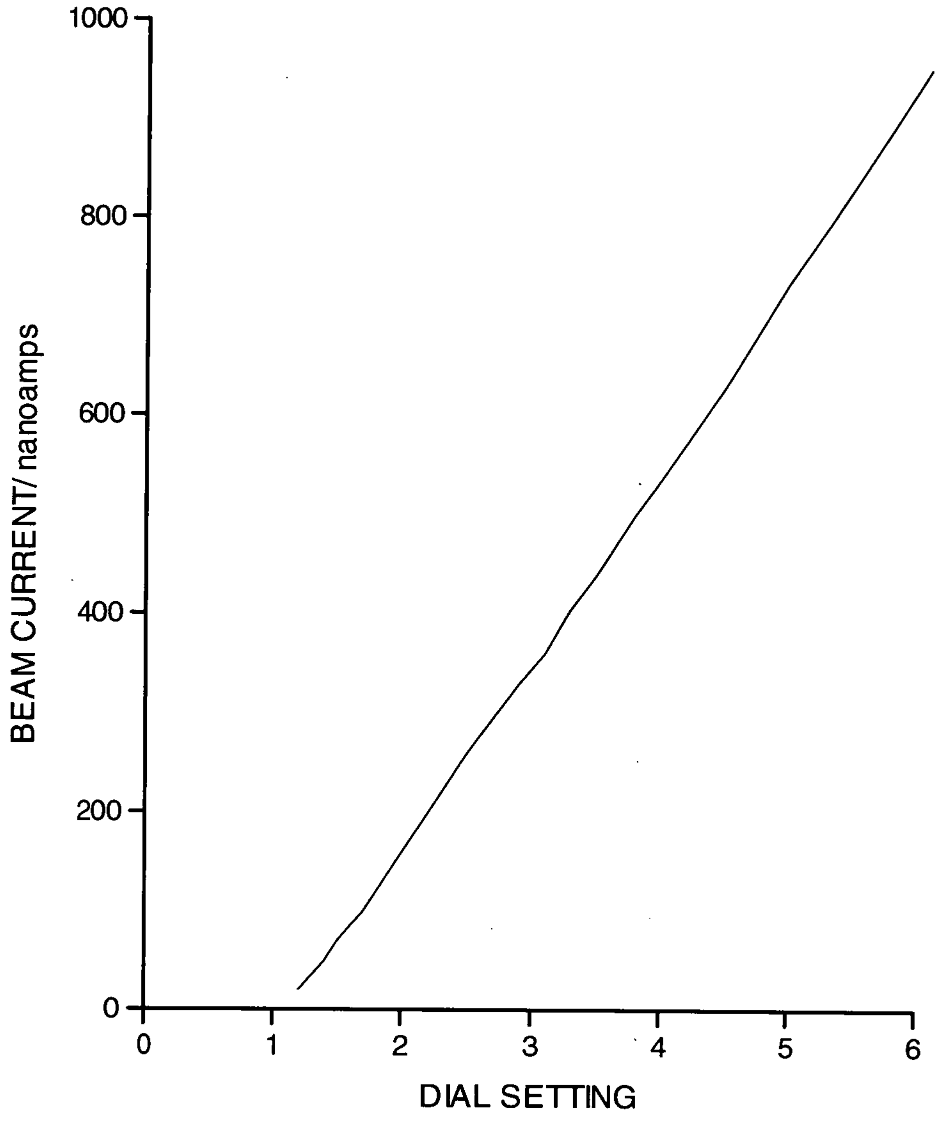

Figure 5.14 Plot of beam current versus dial setting at 30 kV.

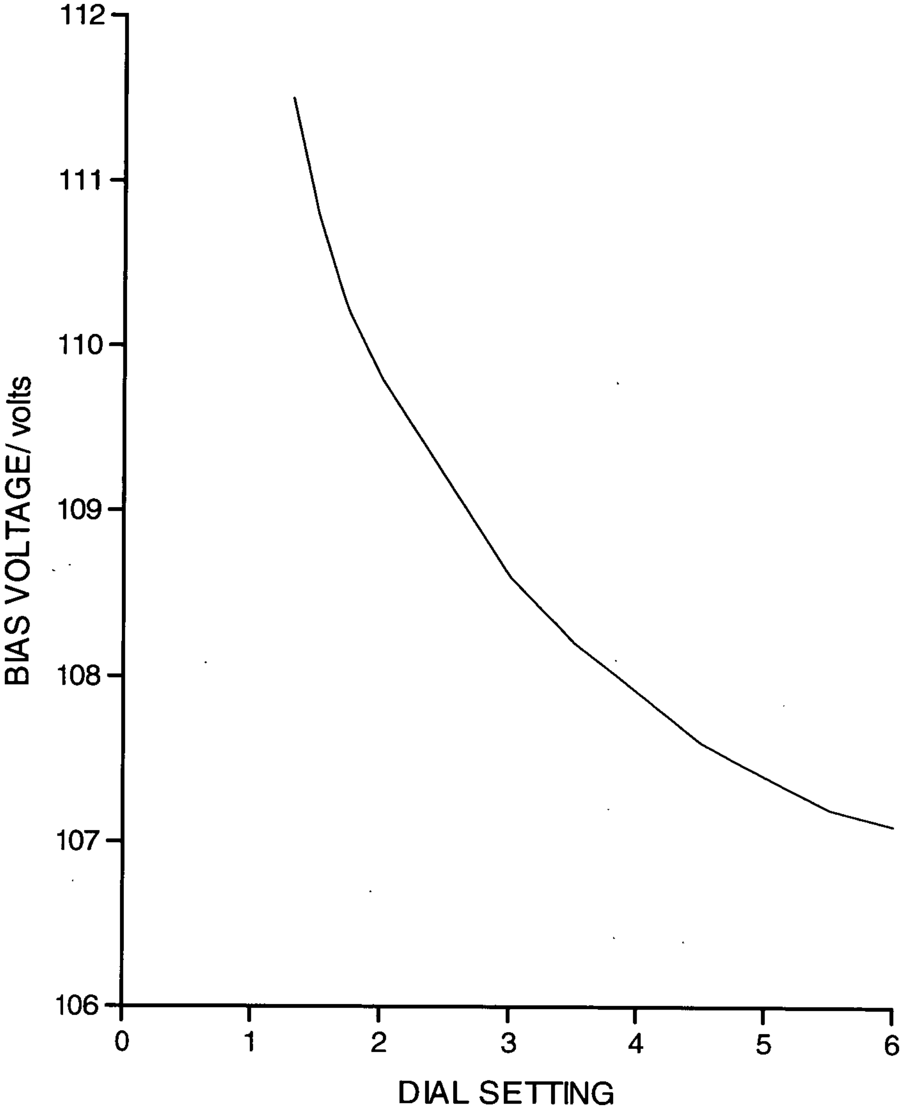

Figure 5.15 Plot of bias voltage versus dial setting at 35 kV.

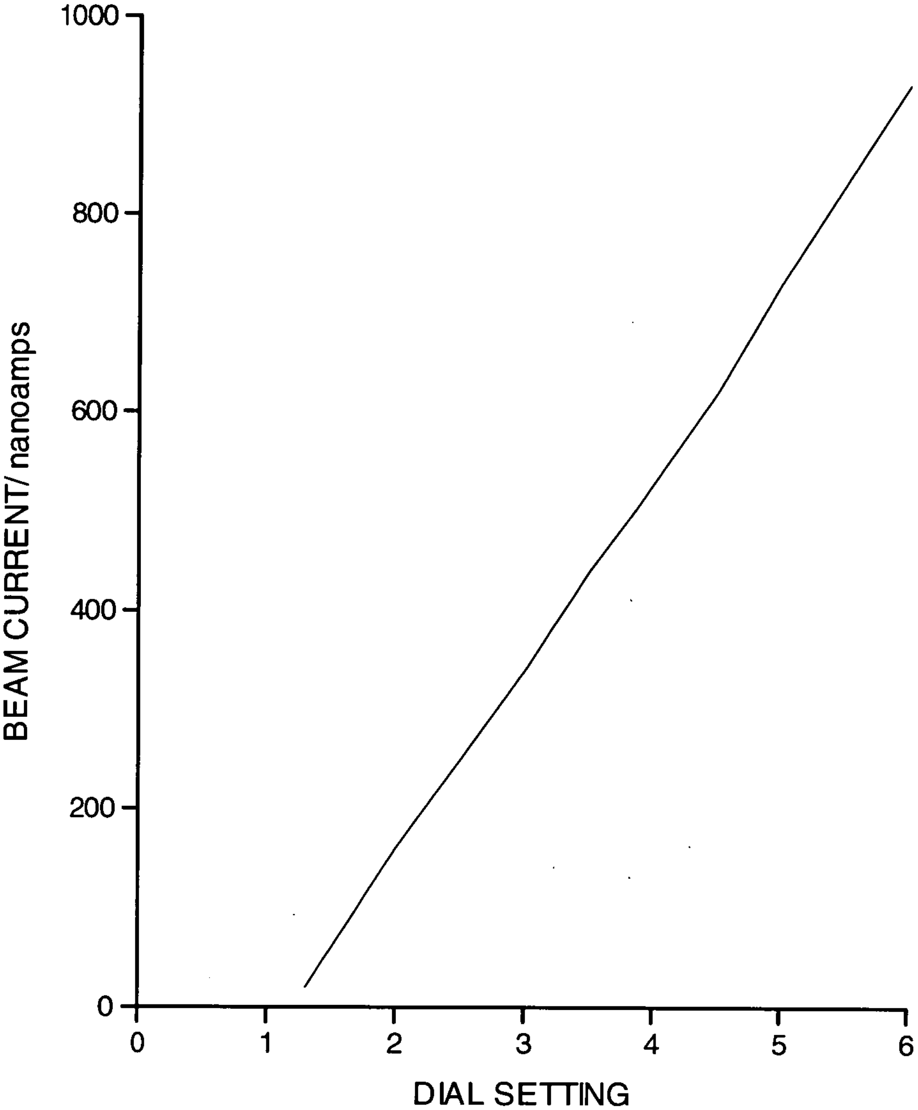

Figure 5.16 Plot of beam current versus dial setting at 35 kV.

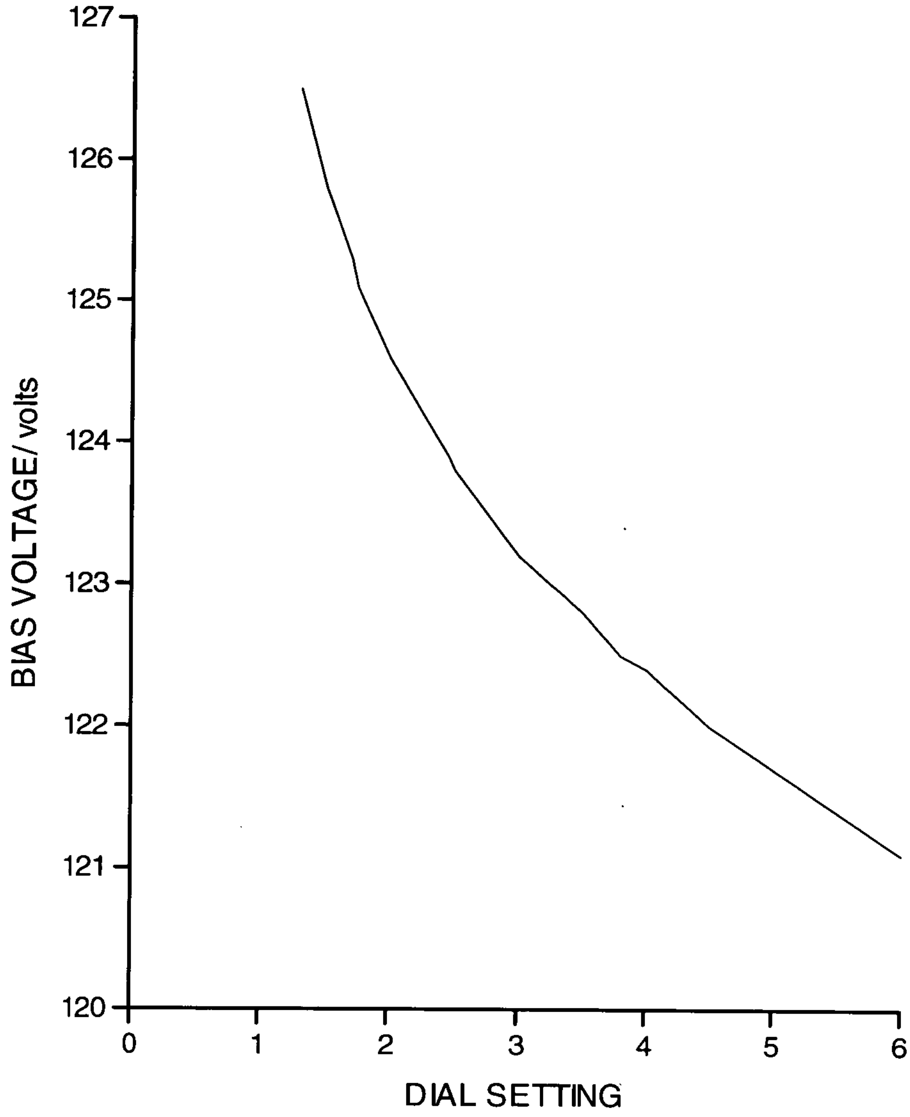

Figure 5.17 Plot of bias voltage versus dial setting at 40 kV.

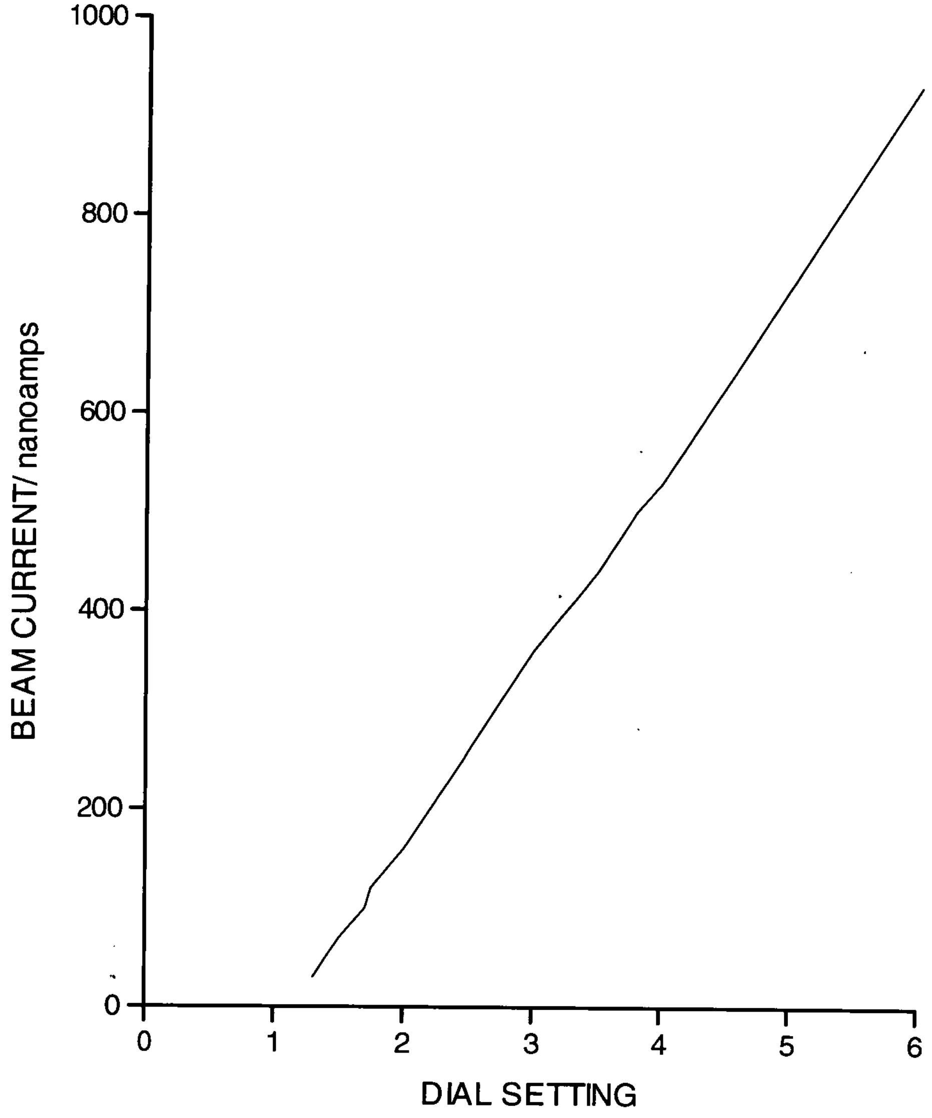

Figure 5.18 Plot of beam current versus dial setting at 40 kV.

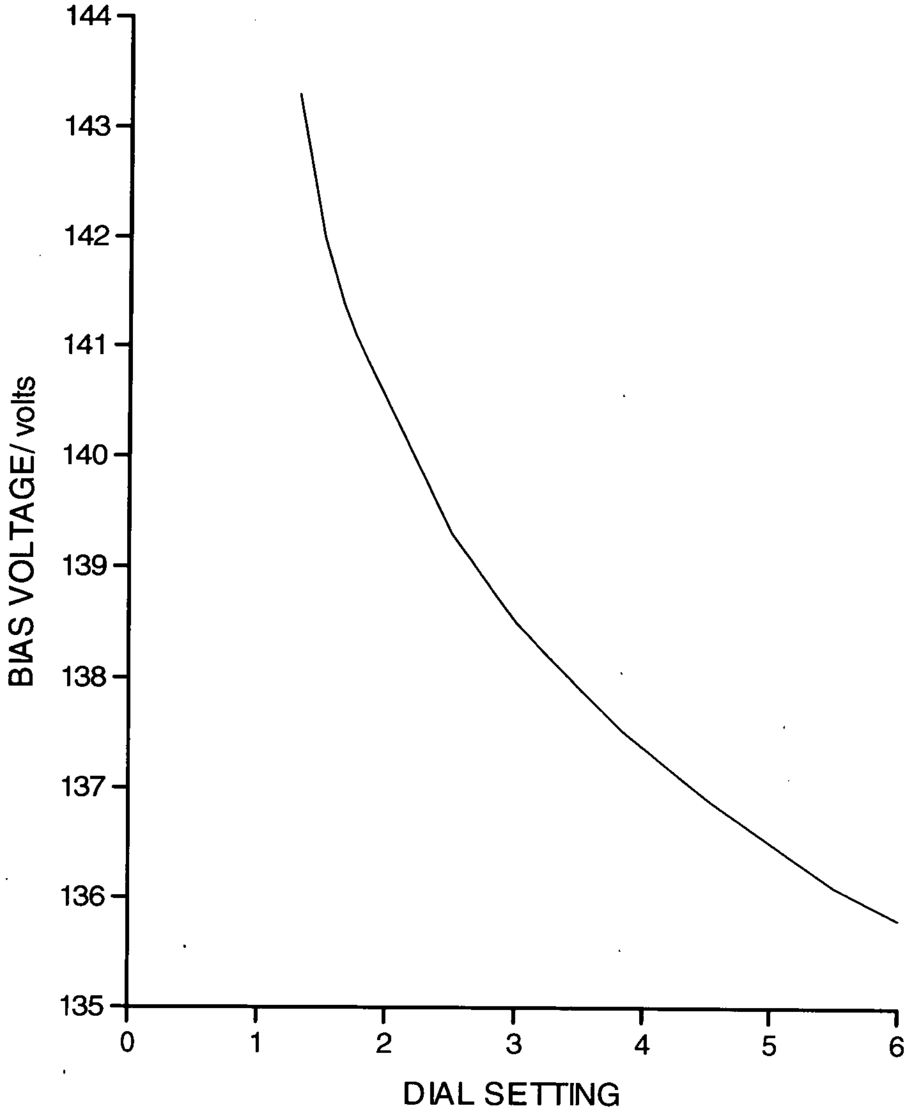

Figure 5.19 Plot of bias voltage versus dial setting at 45 kV.

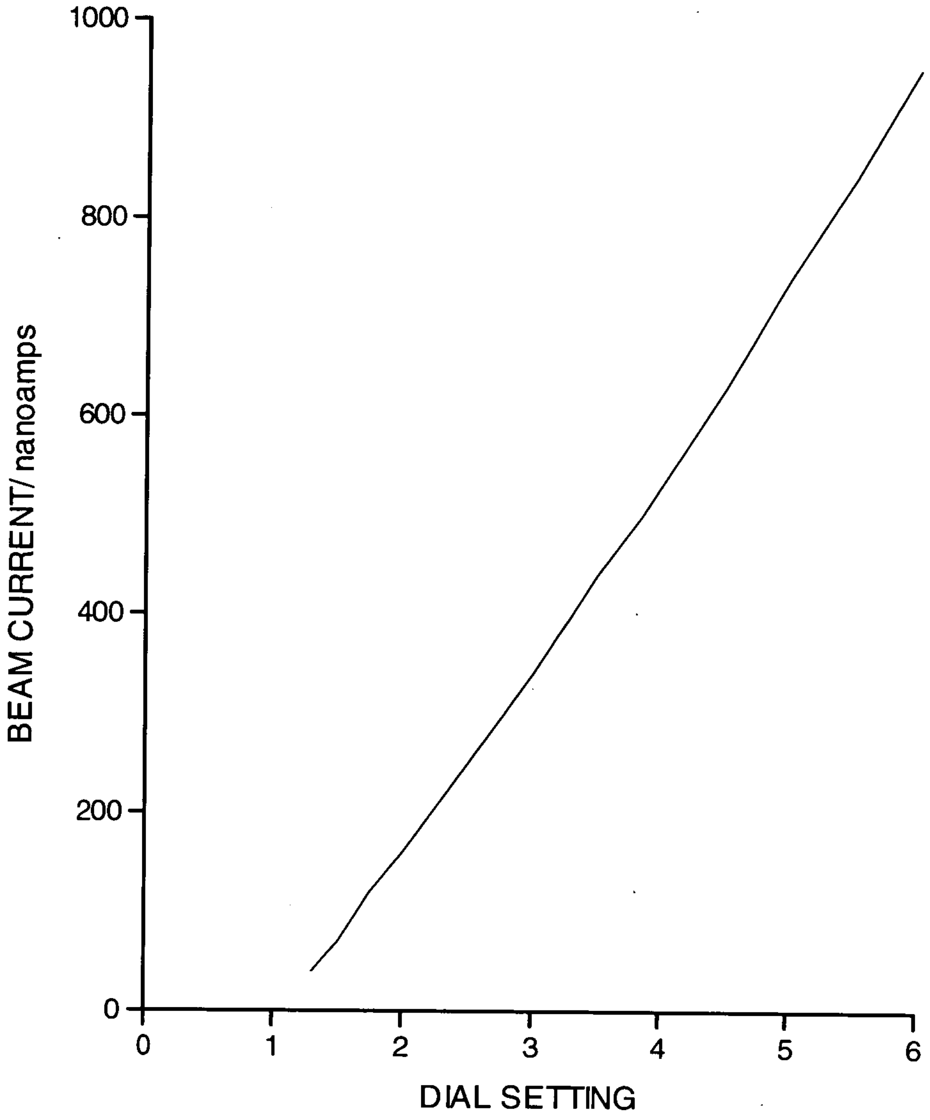

Figure 5.20 Plot of beam current versus dial setting at 45 kV.

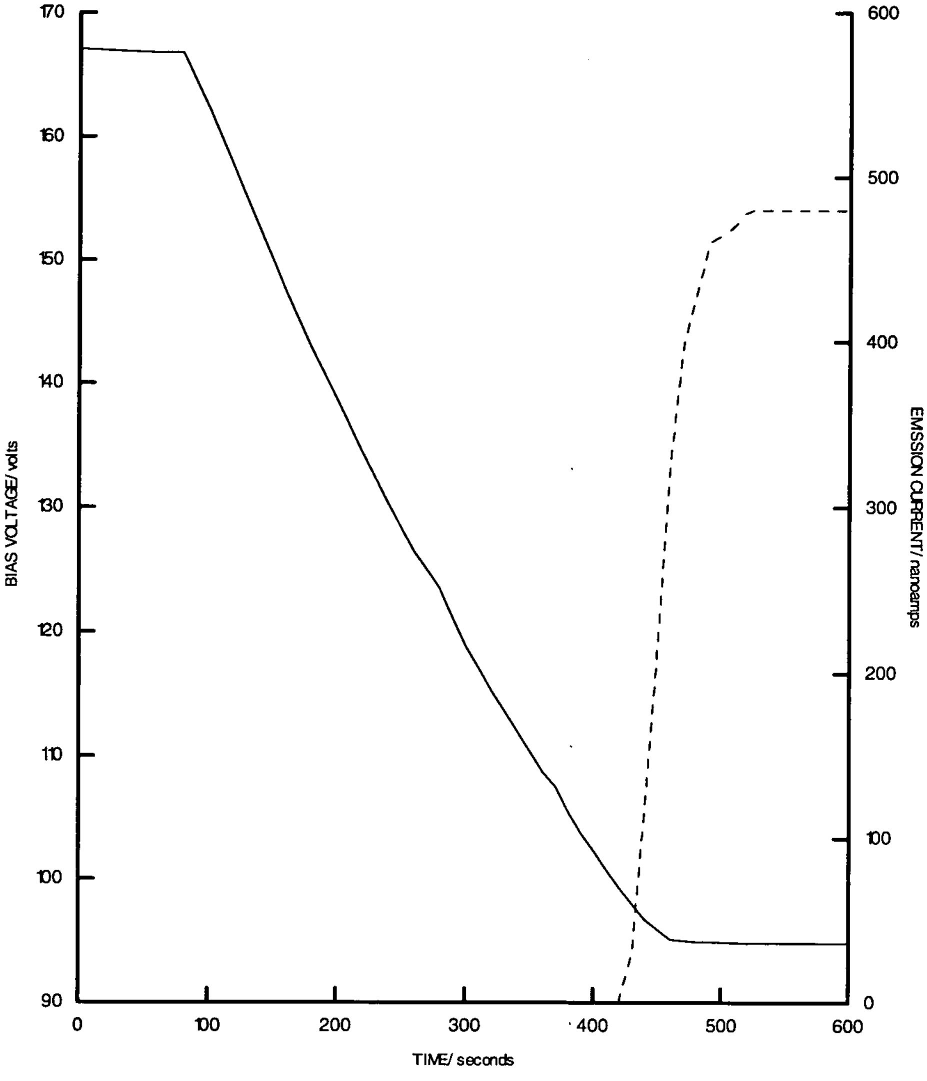

Figure 5.21 Plot of bias voltage (solid line) and emission current (dashed line) versus time for a set beam current of around 500 nA (4.0 on dial) at 30 kV.

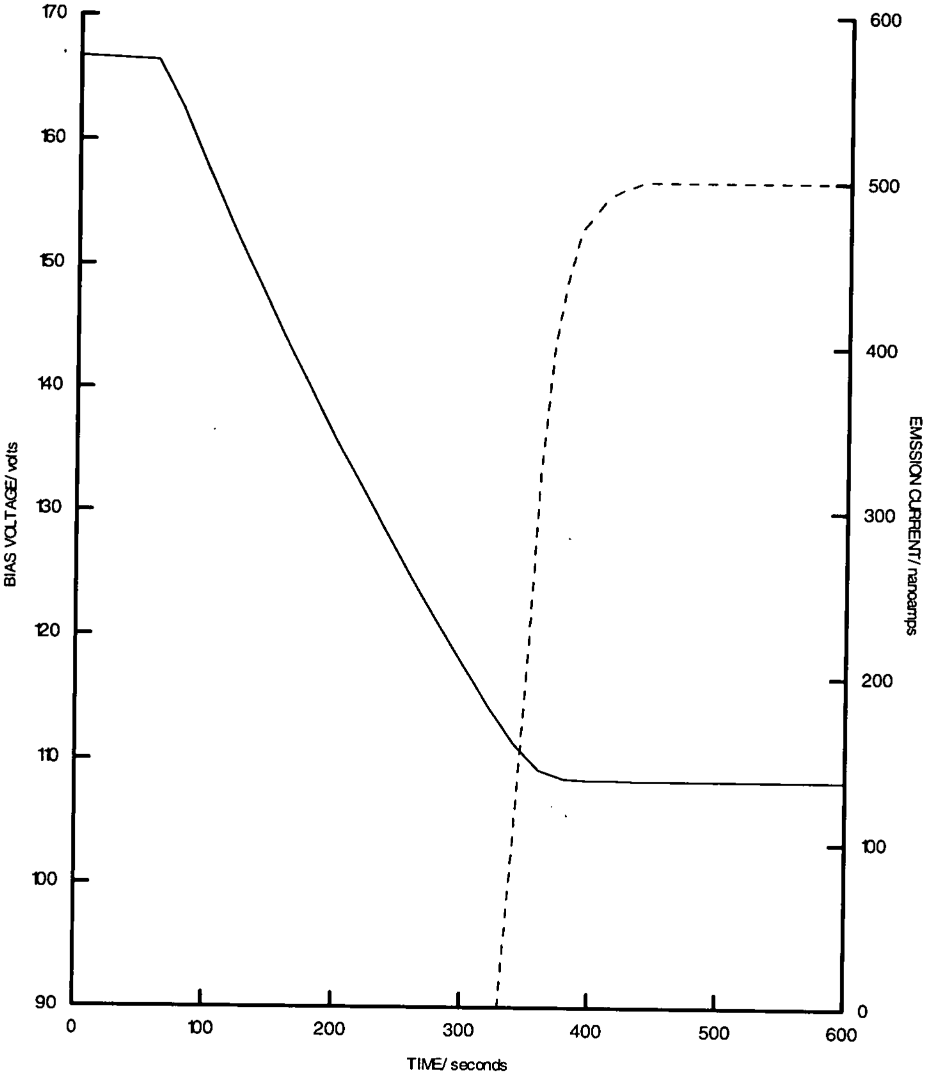

Figure 5.22 Plot of bias voltage (solid line) and emission current (dashed line) versus time for a set beam current of around 500 nA (4.0 on dial) at 35 kV.

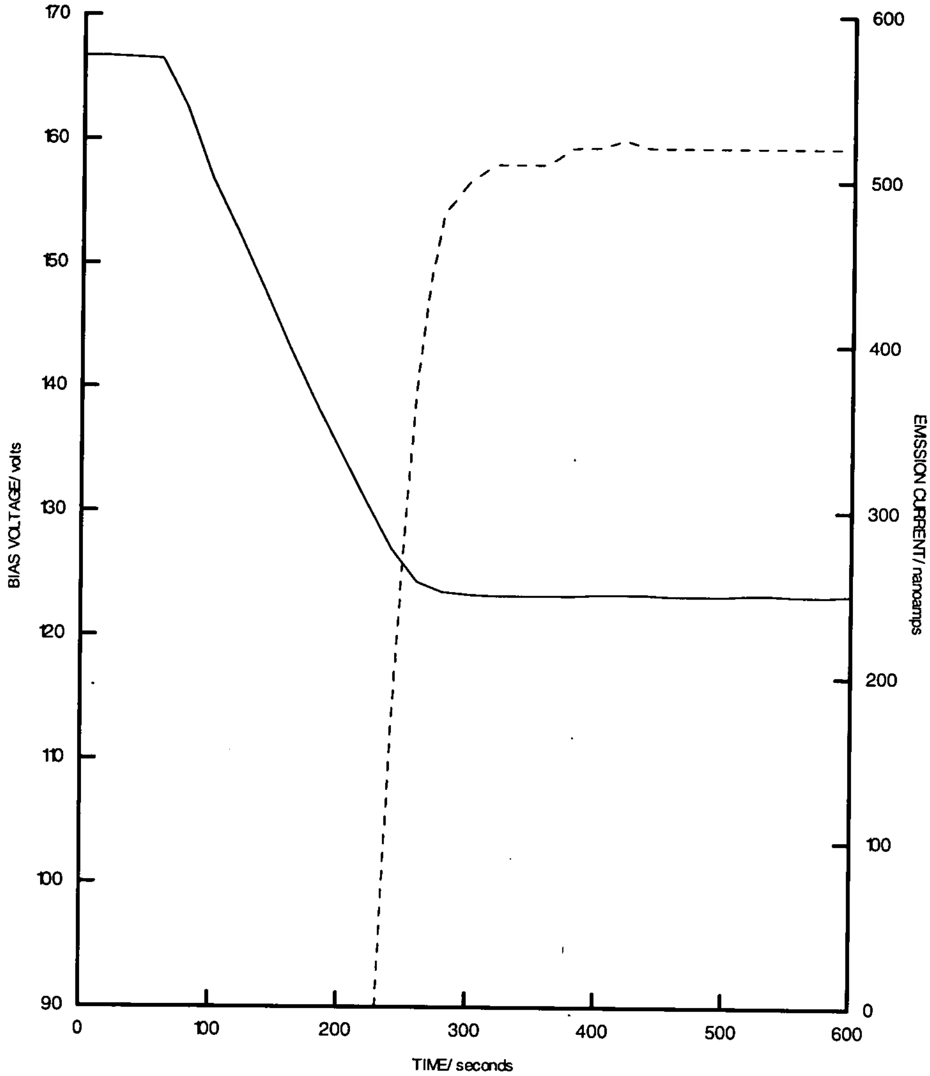

Figure 5.23 Plot of bias voltage (solid line) and emission current (dashed line) versus time for a set beam current of around 500 nA (4.0 on dial) at 40 kV.

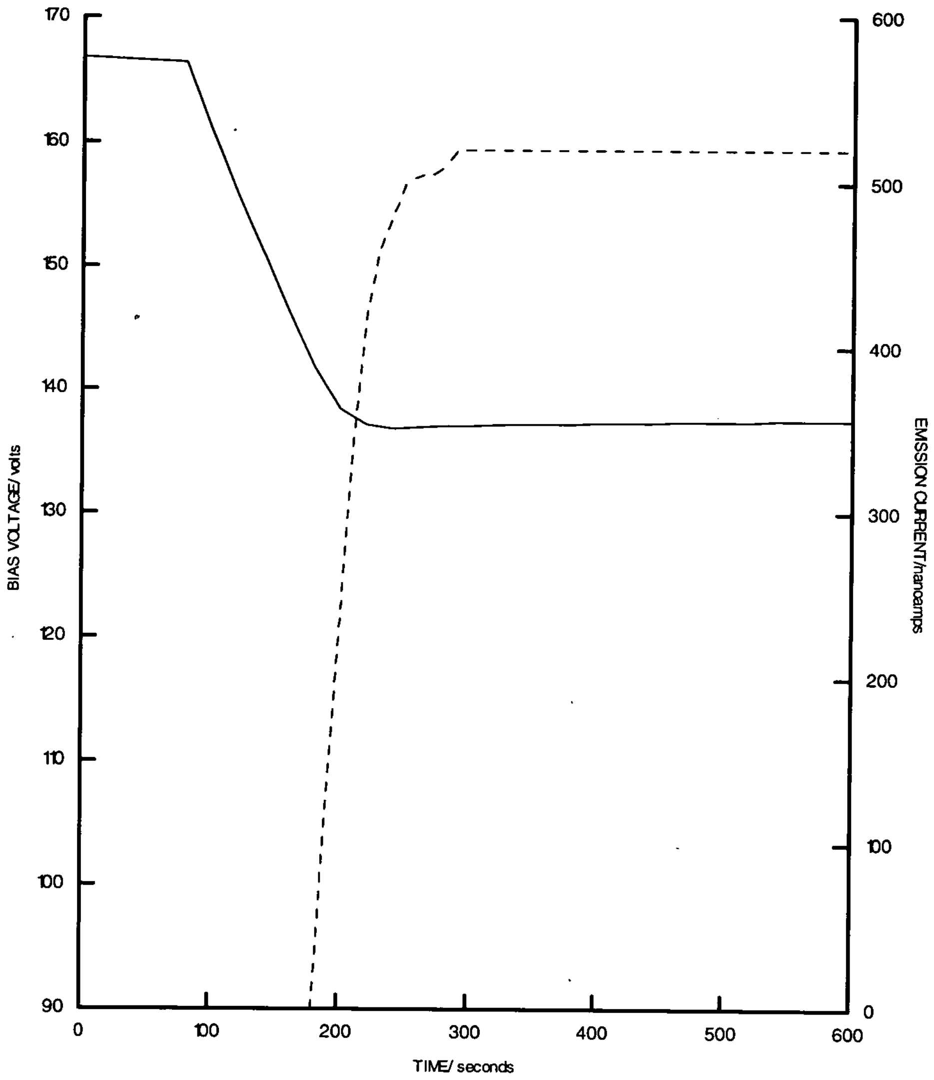

Figure 5.24 Plot of bias voltage (solid line) and emission current (dashed line) versus time for a set beam current of around 500 nA (4.0 on dial) at 45 kV.

Bibliography

1 High energy electron scattering, Eds.: R.A. Bonham and M. Fink, (Van Nostrand Reinhold Co., New York, 1974), ACS Monograph 169

2 K.H. Steigerwald, Optik, 5 (1949) 469

3 F.W. Braucks, Optik, 14 (1958) 242

4 O. Kamigaito, Oyo Buturi, 31 (1962) 984 [in Japanese]

5 E.B. Bas and F. Gaydou, Z. Angew. Phys., 11 (1959) 370

6 M. Fink, P.G. Moore, and D. Gregory, J. Chem. Phys., 71 (1979) 5227

7 H. Schmoranzer, H.F. Wellenstein, and R.A. Bonham, Rev. Sci. Instrum., 46 (1975) 89

8 M. Fink and R.A. Bonham, Rev. Sci. Instrum., 41 (1970) 389

9 B. Schiewe, H. Schmoranzer, and P. Wollenweber, Rev. Sci. Instrum., 48 (1977) 893

10 M. Taguchi and T. Iijima, Jpn. J. Appl. Phys., 23 (1984) 921

11 M. Taguchi and T. Iijima, Jpn. J. Appl. Phys., 23 (1984) 1509

Chapter 6

Position-Sensitive Detector

6.1 Introduction

When the decision was made to build this instrument a new type of detector was required to replace the photographic plate as the method of electron detection. Photographic plates have been used for 60 years and although they produce relatively accurate molecular parameters for stable, gas-phase molecules they are prone to several experimental drawbacks. The main aim of the new instrument was to extend the range of chemical systems studied by electron diffraction and this led to the choice of a detector capable of single electron counting.

The main problem with the photographic plate is its small dynamic range. This is the ratio of the largest recordable signal to the smallest recordable signal. As electron scattering falls off as the inverse of the fourth power of the scattering angle the integrating effect of the photographic plate leads to the plate becoming overexposed at small scattering angles before a reasonable signal is recorded at higher angles. To overcome this problem the rotating sector method [1,2] was introduced. The sector is simply a piece of metallic sheet cut into a specified mathematical form (generally a function of r^3 form) which increases the relative exposure time of the plate toward the larger scattering angles. Once the diffraction image has been recorded the plate must then be developed. After this the plates are optically scanned by a microdensitometer to produce a set of optical densities. In the case of the plates recorded in Edinburgh University this is done at Daresbury. The effect of the rotating sector is then removed during data analysis and this operation together with the errors associated with photographic plates such as non-uniform thickness of emulsion and blackness corrections introduce errors into the data set.

An electron detector which incorporated single electron counting together with time resolution and an increased dynamic range was a discrete channel detector [3,4,5]. The detector chosen was composed of two parts. A pair of stacked HOT (high optical technology) microchannel plates (MCPs) [6] amplified the electron image which was then counted by an anode device made up of a set of discrete electron-sensing electrodes. Each electrode has its own fast preamplifier, discriminator and 8-bit counter. This detector removed the need for a rotating sector as it possesses a greater dynamic range (10^6:1) than the photographic plate (10^2:1).

Such position-sensitive detectors (PSDs) have been employed in many areas of research such as high-energy particle physics, inelastic neutron scattering, photon spectroscopies (both UV visible and X-ray), mass spectrometry, and electron spectroscopies [both ultraviolet photoemission (UPS) and X-ray photoemission (XPS or ESCA)]. An excellent review of the main classes of PSDs and in particular their application to the detection of low energy electrons in electron energy loss spectroscopy (EELS) was published by Richter and Ho [7]. The four classes of PSD discussed are:

1. discrete anode
2. coincidence array
3. charge division
4. solid-state optical image detectors (OIDs)

These detectors are generally used in conjunction with microchannel plates (MCPs) as spatially imaging electron amplifiers. The detector chosen is in the first class of PSD above. There were several reasons for choosing this type of detector, the main one being that it could support the high count rates associated with the electron diffraction experiment. It obeys Poissonian counting statistics and has a good signal to noise ratio. Finally it is forgiving of MCP gain reduction at high local count rates. This is particularly useful at small scattering angles. In fact the detector developed for the new electron diffraction instrument was capable of counting rates of up to 4 MHz and with the planned gating system could have had a time resolution of around 20 nanoseconds.

The electron detector utilised in this machine has been adopted in various pieces of technical equipment [8] but has never been employed in the area of gas-phase electron diffraction. The physical form of the detector is a novel design. Normally the electron sensing electrodes are arranged in a rectangular array. However in this application they consist of a set of independent angularly and radially disposed electrodes to accommodate the diffracted electron image (see **Fig. 6.1**).

The detector was designed and built by Integrated Sensors Limited (I.S.L.) based at U.M.I.S.T. in Manchester. In the present design there are 168 electrodes arranged in 83 concentric annular rings as displayed in **Figure 6.1**. The 28th ring from the centre is split into four quadrants while all other rings are split into two equal semicircular areas. Each electrode has a width of 0.3 mm with an inter electrode spacing of 0.1 mm. Currently only 128 channels are operational and they are controlled by four microchips mounted on the reverse of the ceramic wafer (32 channels per chip). There is a hole in the centre of the detector of diameter 6.0 mm to allow the passage of the primary electron beam.

The electrodes are made of gold and are fabricated on an alumina ceramic substrate. This discrete anode is processed on both sides of the wafer with through-plated holes connecting to hybrid integrated devices mounted on the reverse side as in **Figure 6.2**. The detector chips are mounted on the substrate with tracking fabricated in pure gold over a copper base. The chips are electrically connected to the substrate by gold wire bonds. Also mounted on the ceramic substrate is a control chip known as a Xilinx [9,10] device used to supply control signals to the detector chips and to arbitrate and strobe the output data to a remote processing unit.

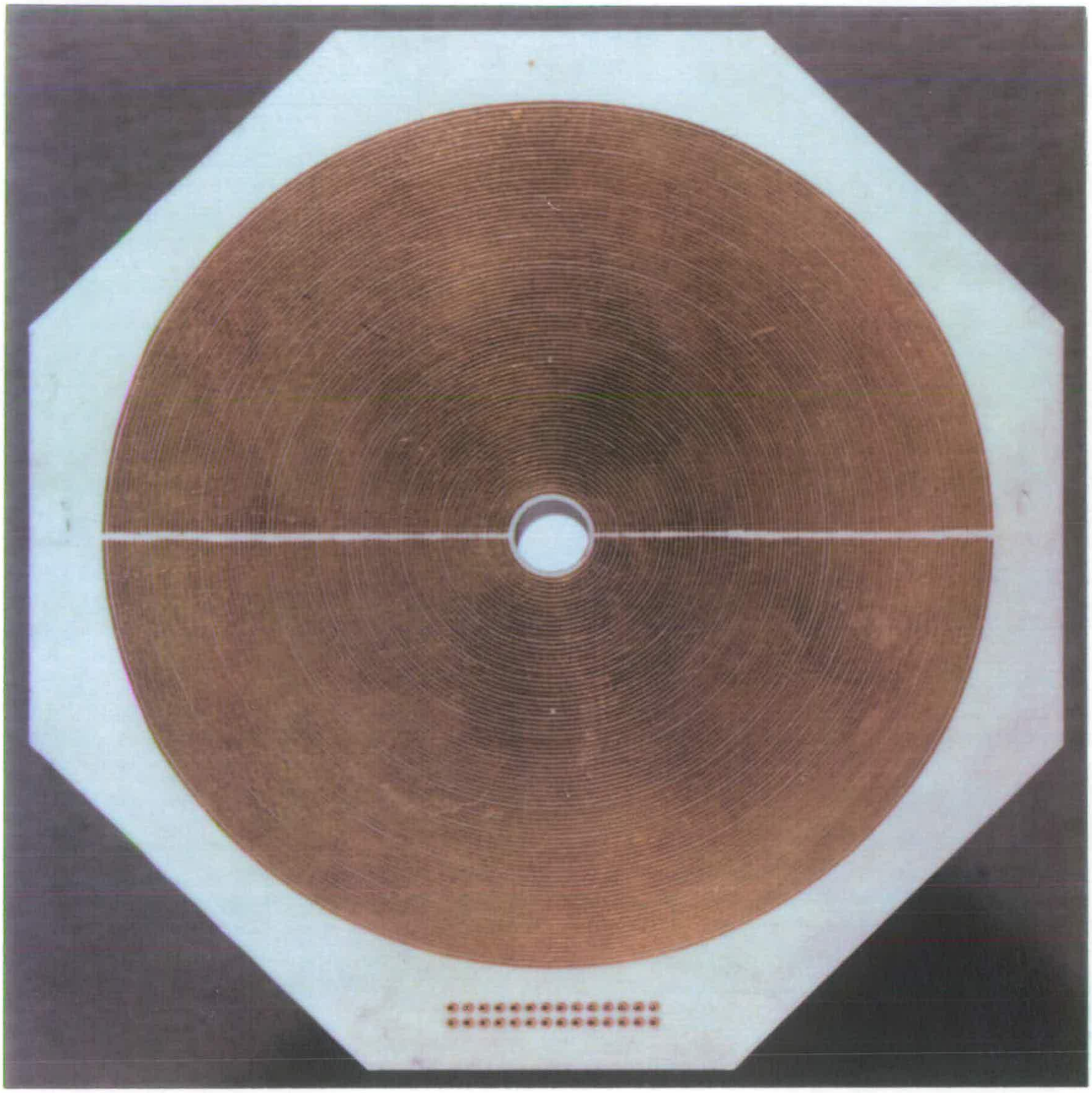

Figure 6.1 Photograph showing the front of a dummy version of the anode device. In this picture the device has been enlarged slightly. In reality the diameter of the active area is 7.3 mm and the ceramic measures 9.5 mm from side to side (left to right above). Note the 6 mm hole to allow for the passage of the primary electron beam and ring number 28 which is split into four quadrants.

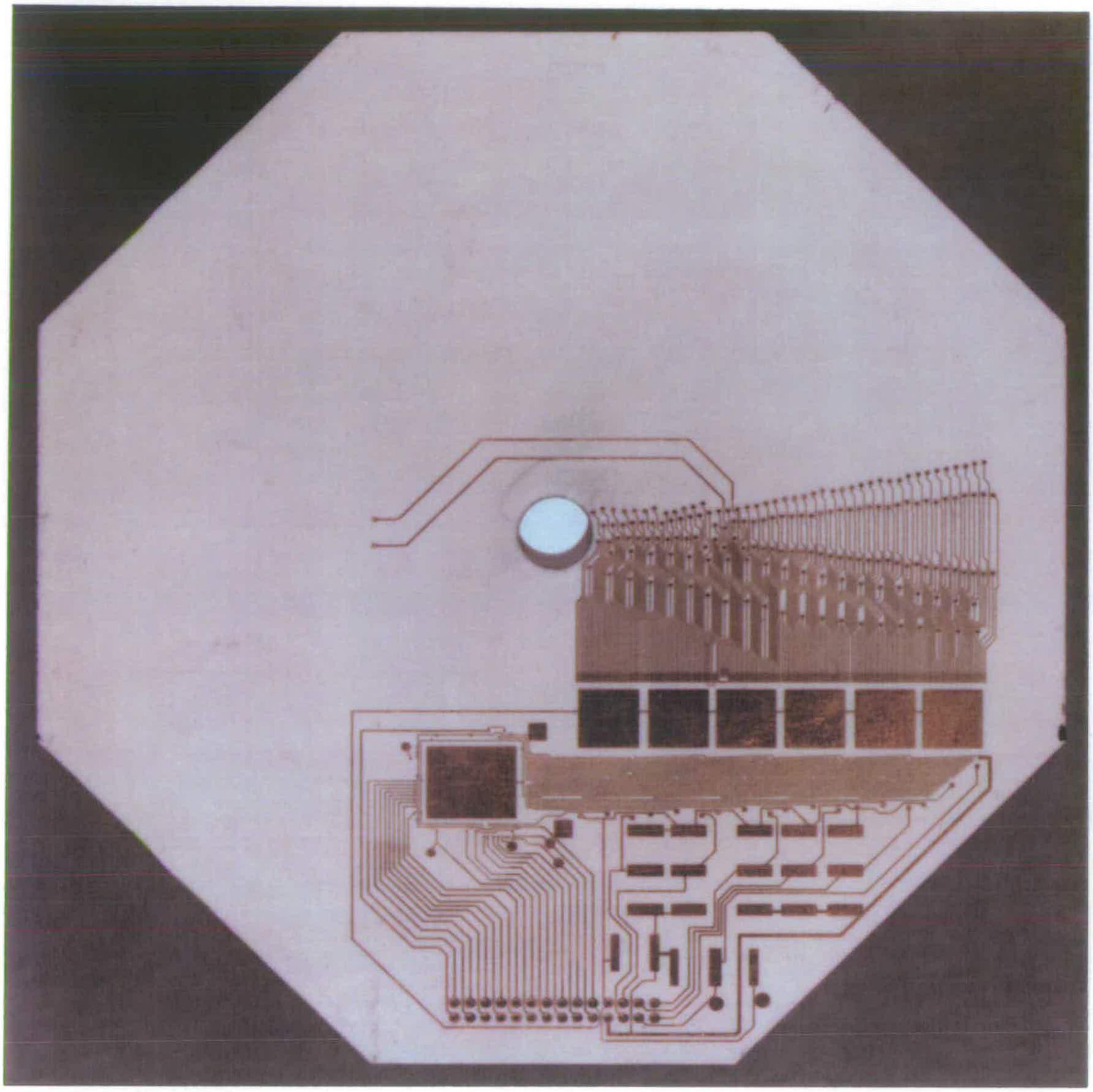

Figure 6.2 Photograph showing the back surface of a dummy version of the anode device (slightly enlarged). Note the tracking connecting the electrodes to microchips (not attached) on the centre right of the picture.

The set of stacked HOT microchannel plates that amplify the electron image can be seen in **Figure 6.3**. They have an active diameter of 75 mm and also have a central hole of diameter 6.0 mm. The MCPs are composed of semiconducting metallised glass with small microscopic pores. When an electron enters one of these channels and strikes the wall secondary electrons are released. For each electron incident on a pore approximately 10^6 electrons are produced.

This circular detector thus allows the whole diffraction pattern to be collected simultaneously. The use of microchannel plates to amplify the diffracted electron pattern coupled with the set of independent electrodes allows single electrons to be detected at a wide range of angles. The detector can be moved from a distance of 200 mm away from the collision zone to 600 mm giving an s range of 2.4 $Å^{-1}$ to 36.0 $Å^{-1}$ with a resolution of 0.2 $Å^{-1}$. This is done with the xyz translator pictured in **Figure 6.4**.

Electron-counting devices have rarely been used in electron diffraction and so far have been unable to deal satisfactorily with the wide dynamic range and precise counting requirements. In 1970 Bonham and Fink [11] reported an apparatus with an electron counter composed of a scintillator mounted on a photomultiplier. This machine could handle low target gas densities but was inefficient, taking many hours to collect a data set, instead of a few seconds with photographic methods. This machine required monitoring of the target molecular beam and primary electron beam to eliminate the effects of intensity variations. A similar apparatus was built by Konaka [12] to look at small angle scattering. Stein [13] also produced an apparatus to study the electron diffraction scattering produced by cluster beams of, for example, SF_6, Ar, Kr and Xe. This machine used a detection system identical to that of Bonham and Fink.

In 1983 Ischenko and co-workers [14] reported an apparatus to look at the time-resolved changes in molecular structure of short-lived molecular

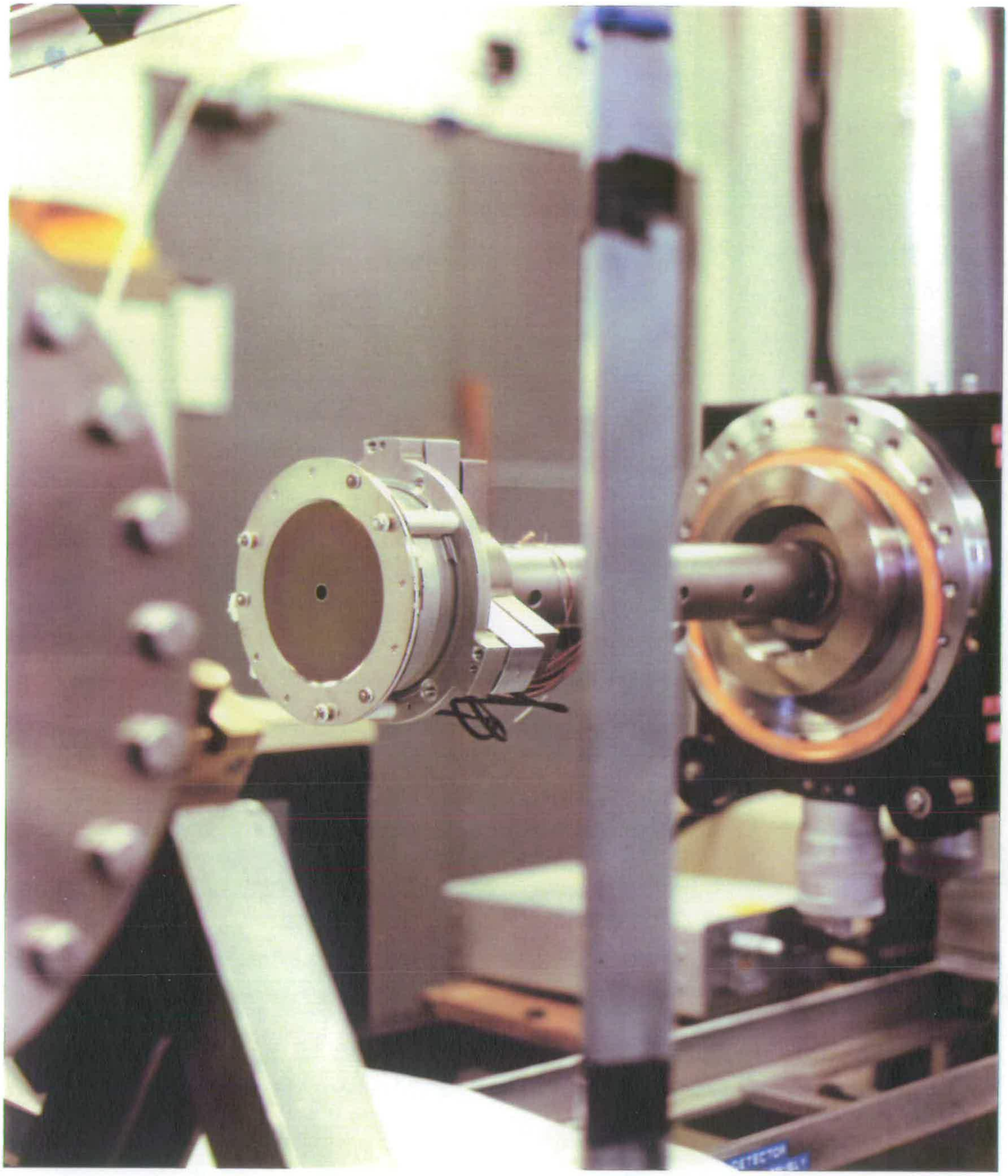

Figure 6.3 Photograph of detector connected to xyz translator before installation into vacuum system. Note the reflective surface of the MCPs with the hole of diameter 6 mm at the centre. Also pictured are three black wires; two of which are connected to the front and back of the MCPs, the third one being attached to the body of the aluminium holder on which the detector sits.

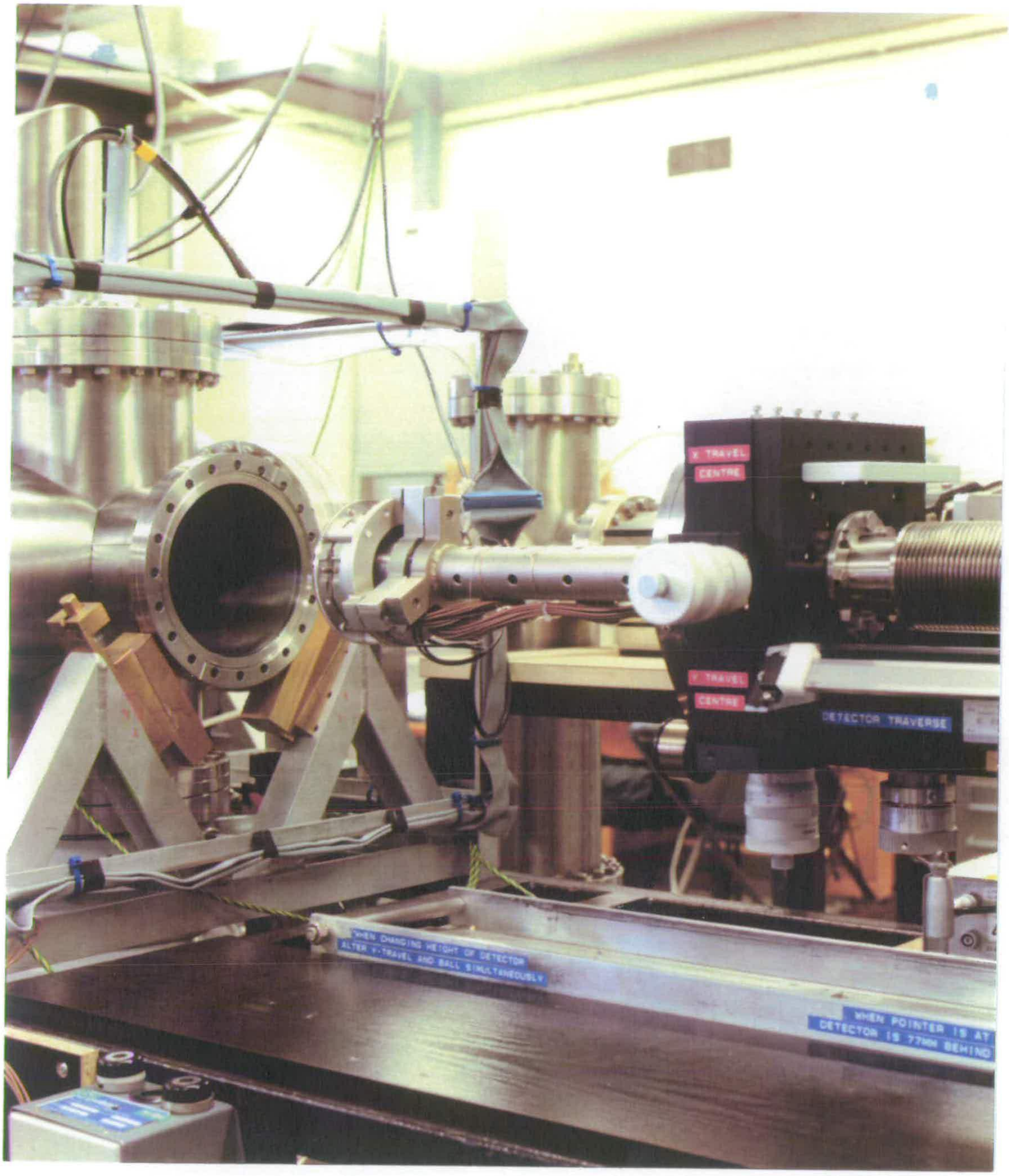

Figure 6.4 Photograph of detector connected to xyz translator before installation into vacuum system. Note the brown wires, beneath the aluminium arm, that carry the detector signals away from the detector head.

species such as free radicals and vibrationally and/or electronically excited molecules in the gas phase. The technique was known as "stroboscopic" electron diffraction and results were presented of the diffraction study of the multiphoton dissociation of the CF_3I molecule by IR-laser irradiation with a tuneable CO_2 laser.

Ewbank and co-workers [15,16,17] subsequently produced an apparatus incorporating a photodiode array to collect the diffracted electrons. This machine was designed to look at real-time gas electron diffraction but the detector used was not strictly an electron counting device. Scattered electrons are incident on a phosphor screen. The light from this screen is then imaged by a fibre-optic coupling onto the linear photodiode array. The photodiode array consists of a series of semiconducting cells onto which the resulting photons fall. The photodiode cells respond by producing an analogue signal proportional to the intensity of the electron signal. This analogue signal must then be digitised and this process limits the rate at which data can read out. They have studied several systems to varying degrees of success.

Using a pair of linear CCD imagers Monot and co-workers [18] have studied the structures of large metallic clusters, in particular those of silver. In an attempt to increase the range of chemical systems studied by electron diffraction Zewail and co-workers [19] have utilised a CCD based system. With a 2-D CCD camera they hope to look at time-dependent molecular phenomena including transition states.

Thus much effort has been put into the task of extending the capabilities of the electron diffraction technique. The advent of single electron counting machines has facilitated an increased signal-to-noise ratio for lower target densities than are commonly used in the photographic method. Early counting instruments and those used solely for cluster studies tend to have a small angular range below that routinely used in structural studies and this new detector will extend the angular range available.

The increased sensitivity of this detector together with its time resolution capabilities should allow the elucidation of the structures of many exotic chemical species. It is hoped to study molecules with low vapour pressures, floppy molecules, unstable molecules and clusters or van der Waals molecules. With laser excitation the structures of molecular ions and molecular excited states and time-dependent phenomena may be investigated.

6.2 Position-Sensitive Detector

In **section 6.1** it was mentioned that the new electron detector consisted of two components. The first component is a set of stacked HOT MCPs arranged in a chevron configuration. This is a commercial device purchased from Galileo and amplifies the scattered electron signal. The discrete anode device then counts the charge pulses produced by the MCPs.

This position-sensitive detector consists of a set of 168 angularly and radially disposed electron sensing electrodes arranged in a series of 83 concentric annular rings (see **Fig. 6.1**). Each of these electrodes has its own fast preamplifier, pulse discriminator and 8-bit counter. Currently 128 channels are operational and are controlled by four microchips mounted on the reverse of the ceramic wafer (see **Fig. 6.2**). Each chip controls 32 counting channels, 3 of which produce zero counts to aid interchip spacing.

Each detector chip has 29 electrodes fabricated on the top surface of the detector chip. In order to extend the detector area of the chips, the method chosen is to abut chips side by side, until the desired area is covered. There are several mechanical and electrical considerations to be borne in mind when choosing this method. The first concerns the design rules that must be adhered to in the design of a full custom chip. These dictate that a certain minimum distance must be left between the edge of circuitry within a chip and the line between chips on a wafer (the scribe line) that is used when cutting up a wafer into single chips. This minimum distance is actually only just less than the pitch of the electrodes on the chip surface.

The second consideration is that in cutting up wafers into chips a diamond tipped saw is used with a blade width of some 100 μm and it is not possible to guarantee that the saw will cut directly down the centre line of a row of chips for every single row on the wafer.

The result of these considerations is that when chips are placed together to increase the detector area, they cannot be abutted close enough to allow the gap between the edges of electrodes on adjacent chips to equal the gap between the edges of adjacent electrodes on a chip.

The method used to overcome this problem is to add three virtual electrodes to each detector chip. Detector chips therefore have a total of 32 electrodes per chip made of 29 real electrodes and 3 virtual electrodes. These virtual electrodes are not actually fabricated on the chip but exist as part of the read-out mechanism. They are read in exactly the same way as the normal electrodes, but always read zero counts. The read-out mechanism is arranged so that one of these virtual electrodes appears as the first electrode on a chip and the other two appear at the end of a chip. Thus when detector chips are butted together, three virtual channels appear next to each other. The area that these three virtual electrodes would cover is then used to space apart the detector chips on the ceramic substrate so that an integer gap equal to three electrodes spacings is left between adjacent chips. Thus, as far as the user is concerned, all electrodes in a multi-chip system are placed exactly the same distance apart, with three null electrodes between each chip. Simple scanning algorithms can be used to mask out the effect of the null channels.

The operations of the detector chips are monitored by a programmable logic device known as a Xilinx chip [9,10]. This device controls the timing sequences of the anode including the sampling rates at the electrodes. The 8-bit counters are continuously read out on a cyclic basis and the data driven off the detector head and through a 25-way vacuum feed-through to the control unit mounted outside of the vacuum system. As the microchannel plates only operate when there is a potential difference of approximately 1800 volts across them, and as the faces of the detector chips are also at a high voltage, the data leaving the detector head will be raised by approximately 1800 volts with respect to real ground. To be of practical use, the signals have to be isolated (see **Fig. 6.5**). This is done by a set of optoisolators situated in the multidetector control unit, which is mounted to the airside of the vacuum feed-through using a polarised connector with a lock-ring. The isolated digital signals are then buffered to a P.C. via a 15-way D-type connector. Inside the P.C. a Frame Grabber card passes the data into two 16-bit stores. While one of these stores is being filled the other is emptied to a suitable data file.

In this current application the front face of the first MCP sits at a potential of +8-10 volts and is earthed through a 10 kΩ resistor. By measuring the voltage across this resistor it is possible to monitor the current flowing in the MCPs. The back of the second plate sits at a potential of +1850 volts (see **Figs. 6.6** and **6.7**).

The microchannel plates act to amplify the scattered electron image produced by the electron diffraction experiment. The MCP is a device made of metallised glass, in particular lead. The surface of the plate is permeated by many microscopic, parallel pores each with an internal resistive (semiconducting) surface designed to have a high secondary electron emission coefficient (see **Fig. 6.8**). A potential difference is applied between the ends of each pore. An electron entering the tube at the low potential end collides with the wall and produces several secondary electrons as in **Figure**

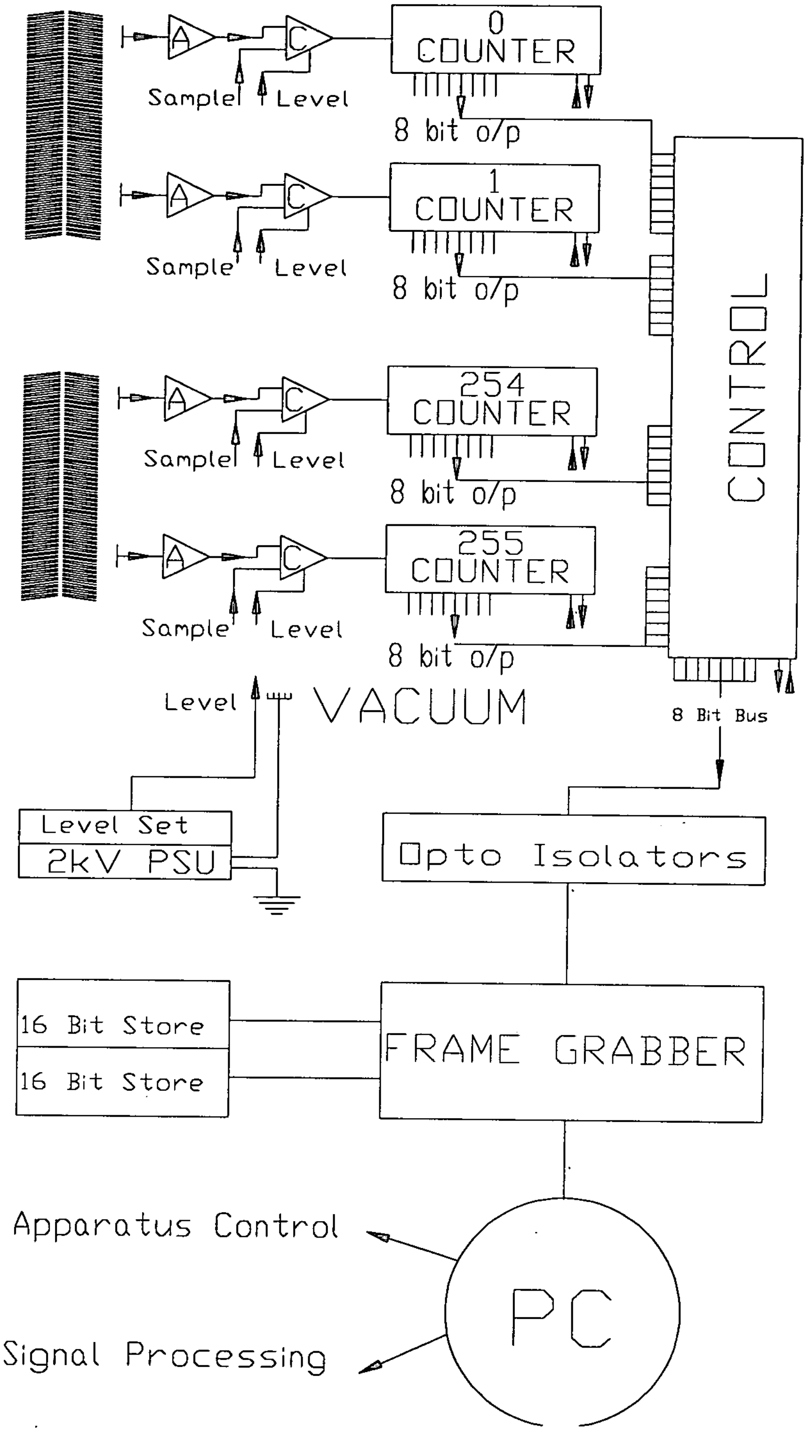

Figure 6.5 Schematic showing the read-out mechanism of the position-sensitive anode detector.

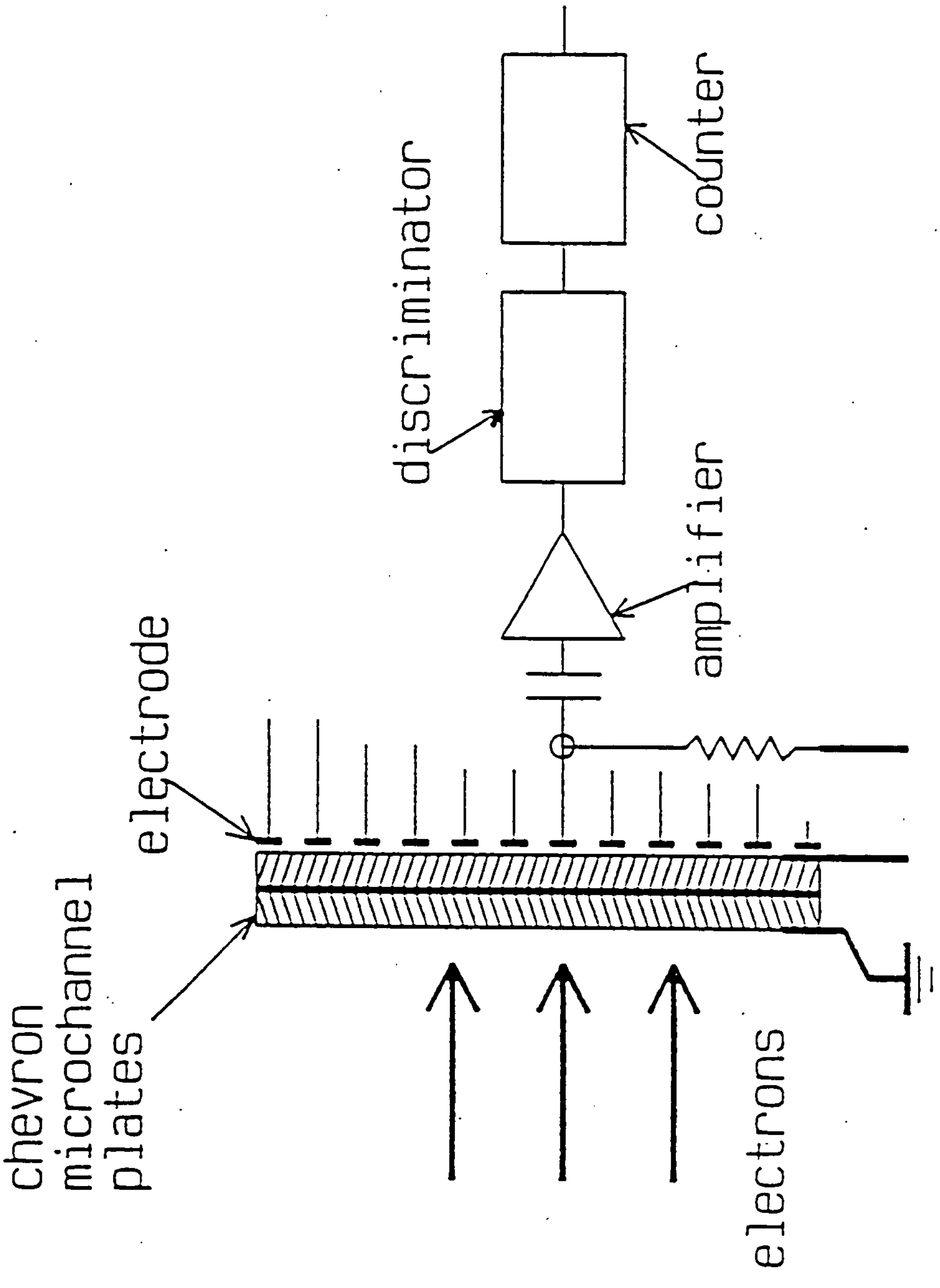

Figure 6.6 Diagram showing a single element of the anode device. Taken from [4].

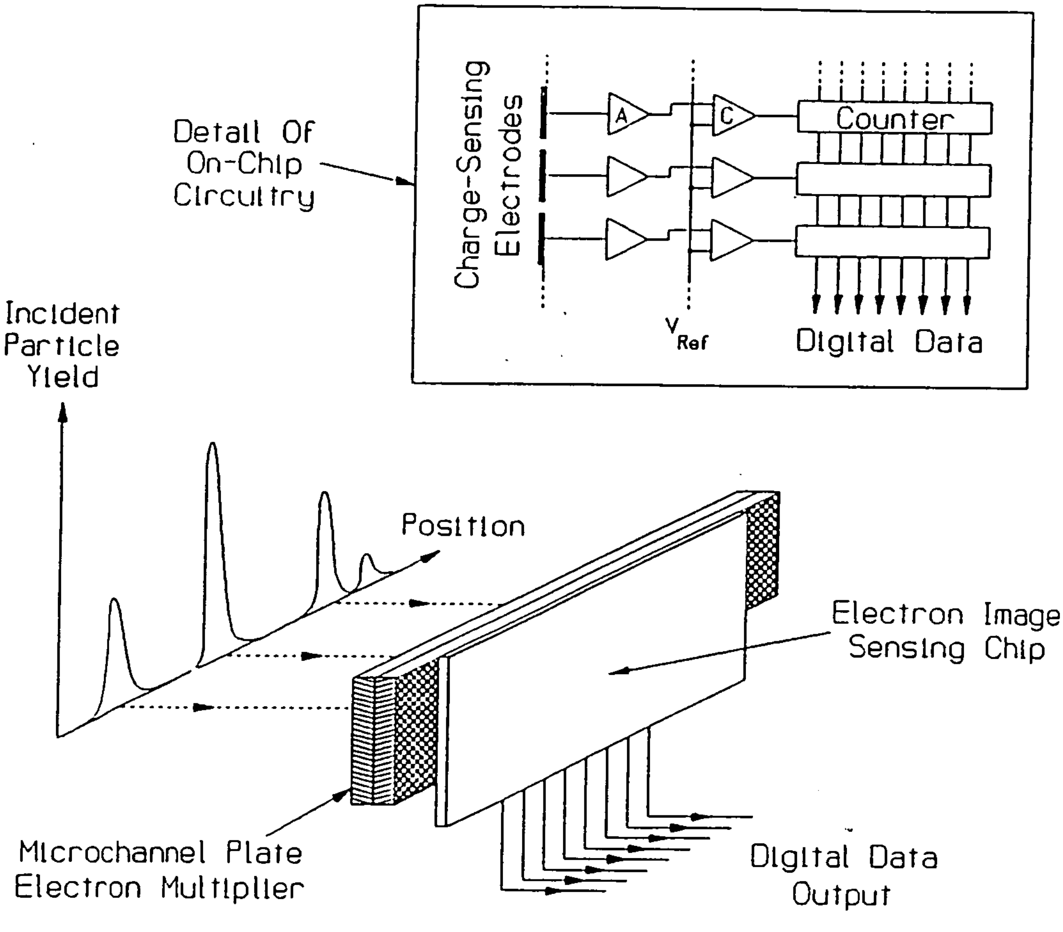

Figure 6.7 Diagram illustrating the position-sensitivity of the anode/MCP arrangement. Taken from [4].

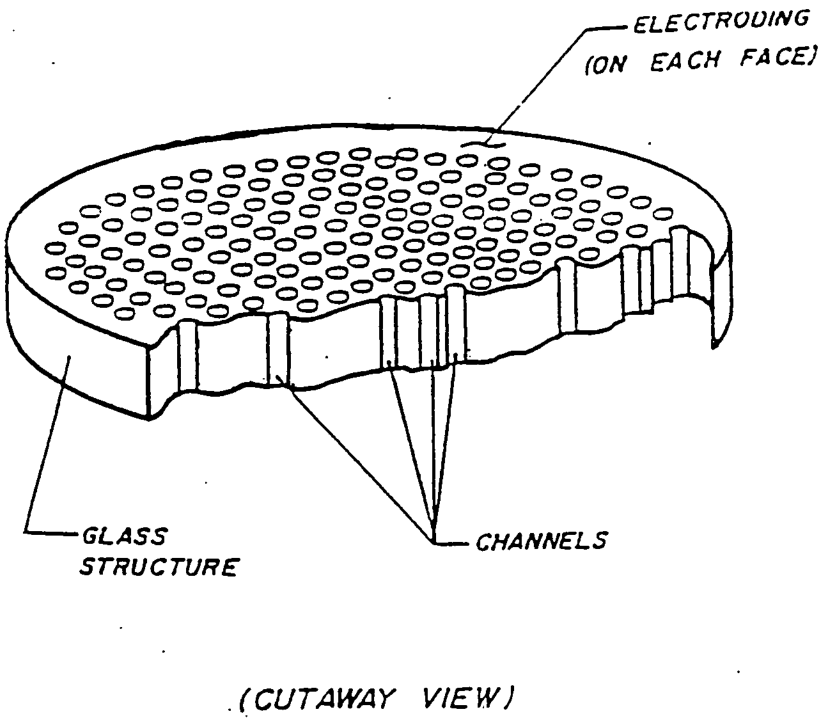

Figure 6.8 Cutaway view of a single MCP. Taken from [6].

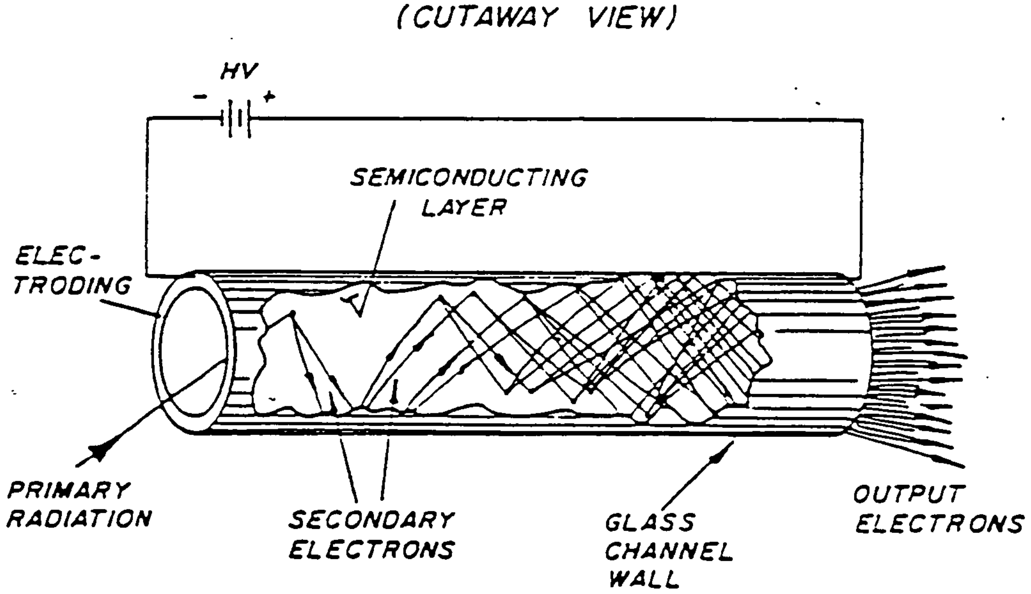

Figure 6.9 A single pore of a typical microchannel plate. Taken from [6].

6.9. After further accelerations by the fields, these electrons again collide with the wall but further down the tube, producing more secondary electrons. The gain of the device is determined by the length-to-diameter ratio of the channels. An MCP is made up of a parallel array of 10^4 -10^7 single-channel multipliers each with a gain of around 10^4. It is therefore capable of amplifying an electron image whilst preserving spatial resolution (see **Fig. 6.10**). The MCPs used in this instrument have a pore diameter of 25 μm and centre-to-centre spacings of 32 μm. As each channel operates essentially independently of its neighbours such an array can resolve events that are spatially separated by distances of the order of the channel size.

Charge replenishment, from an external voltage source, is through parallel contacts on the front and rear surfaces of the MCP. These are provided by the deposition of a metallic alloy such as Nichrome or Inconel. The channel axes are biased at about 8 degrees to the MCP input surface. By mounting channel plates back-to-back the chevron configuration of **Figure 6.10** is achieved and this has two advantages. The bias angles of the channels provide enough directional change to prevent positive ions produced at the output of the rear plate from reaching the input to the front plate, an effect known as ion feedback. The other advantage is that the peak gain of the chevron stack is of the order 10^6-10^7. There is a pulse height distribution which is approximately Gaussian.

The MCP used is a set of two stacked HOT microchannel plates with an active diameter of 75 mm. The front input surface has been metallised to optimise the response to keV electrons and to be unresponsive to X-ray and VUV photons generated by the inevitable keV electron/surface collisions. When such an MCP is operated in the pulse counting (saturated) mode it yields a constant amplitude output pulse regardless of input event rate. This charge pulse is produced in around 5 nanoseconds. When an incoming electron triggers the channel of an MCP array, the resulting cascade multiplication of electrons leaves the channel temporarily incapable of

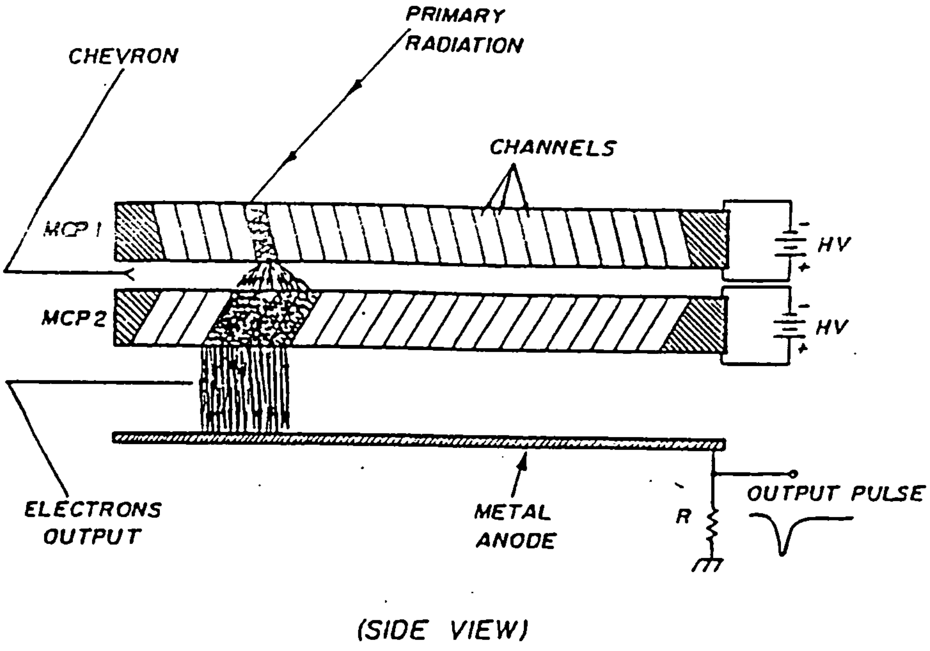

Figure 6.10 Diagram showing the arrangement of the MCPs and anode detector. Taken from [6].

processing subsequent incoming electrons. The time required to bring the channel back to readiness is called the dead time and is of the order of 10^{-2} seconds per channel. The dead time can be roughly equated to the resistance/capacitance time constant of the MCP and by decreasing resistance the response of the MCP can be improved. However the effective dead time of the MCP is much lower than 10^{-2} seconds as there many essentially independent channels on each plate.

Thus for each electron incident on a pore a charge pulse of around 10^6 electrons is created in 5 ns. The electron image leaving the back of the MCP is then accelerated over a gap of around 1 mm to the electrodes of the anode. These electrodes were initially set at a potential of +2150 volts giving an accelerating field of +300 volts but this accelerating field was subsequently reduced to +45 volts.

At the beginning of a detection cycle (see **Fig. 6.5**), the chip electrodes are charged to approximately half the supply voltage by briefly shorting the outputs of the input amplifiers to the inputs. An amplified electron pulse falls on the electrode causing a drop in potential. This drop is inverted and amplified by the electrode input amplifier. A comparison is then made between the voltage on the output of the electrode input amplifier and a user -adjustable threshold voltage common to each of the electrodes associated with a particular detector chip.

As the radius of each element increases the area of the element increases correspondingly (see **Fig. 6.1**). This means that the outer electrodes have larger capacitances as the capacity is proportional to the area of the element. The result of this is that a unit charge pulse of Q (equivalent to a single electron event) impinging on an element of larger capacitance C, will undergo a smaller drop in potential by the relationship Q=CV.

To compensate for this each of the four chips has a different discriminator level for its associated electrodes. As the electrode radii increase the chip discriminator voltages decrease. The detector is designed to have user adjustable discriminator voltages. Ideally the detector would have many more electrodes (of the same width and separation) of equal capacitance giving identical discriminator levels.

If the threshold voltage is less than the output voltage of the input amplifiers, then an electron event is registered and the 8-bit counter for a particular electrode incremented by one. The electrodes are then recharged to approximately 2.5 volts and the detection cycle repeats. The detection cycle is currently limited to 0.25 μs as the electrode sampling rate is 4 MHz.

Also, as the threshold voltage can be adjusted to set the point at which an electron event is considered detected, the setting of this adjustment automatically masks out virtually all background noise effects.

The 8-bit counters are capable of holding up to 255 counts and are interrogated asynchronously and sequentially read out on a data bus. The read-out mechanism for data stored on these counters has been designed to operate independently of the electrode sampling circuitry. In addition, the circuitry has been designed so that while a counter is being read, only the electrode associated with that counter is disabled and cannot register any events. The advantage of this is that as one counter is being read out, all other counters can continue collecting data. Thus the minimum read-out time is 0.5 μs for each counter.

The read-out circuitry operates within each chip by passing a token down a 29 stage shift register, with the shift register being the 29 separate 8-bit counters on the detector chip. The token is initialised by a chip select signal to the detector chip going low. When the token appears at a particular counter it causes that counter to be enabled, thereby transferring the stored data onto an internal bus common to all the counter outputs, and resetting the contents of the accessed counter to zero. The data on the common bus is then driven off the chip. As this particular detector has several chips, the external programmable control chip controls the chip select lines to the chips, ensuring that each is selected in turn, and that only one is selected at any one time.

This detector overcomes the disadvantages normally associated with discrete channel devices, namely the large amount of external processing electronics and interchannel cross coupling, by integrating the amplifiers and counters onto the detector chips. Cross coupling is of far less significance because only digital signals, rather than low-level analogue signals, need to be taken via long wires out of the vacuum system housing the instrument.

Interchannel cross coupling is potentially a severe problem with discrete anode detectors. This is a consequence of the wide pulse height distribution (PHD) from channel plates. This is a serious problem if there is only about an order of magnitude difference between a cross-coupled pulse and a signal pulse. This implies that a discriminator threshold that rejects all cross-coupled pulses will be within the PHD of the channel plates, and therefore, will reject the low amplitude pulses. However, cross-coupling is negligible in integrated devices.

To increase the time response of the detector electronic gating could be utilised. Gates of around 20 ns are currently available and with suitable time delays and modulation the structures of many unexplored chemical systems, including time-dependent changes resulting from laser irradiation, could be investigated. By measuring background scattering (from residual gas or from the walls of the chamber) between pulses of target gas and subtracting them from recorded intensities a more accurate total electron scattering pattern can be obtained, i.e. the true experimental background can be measured.

The detector used was only a prototype and the planned anode device could have sampling rates of up to 10 MHz. The final detector was to consist of 256 separate electrodes spread over the 83 annular rings with 32 channels on each of 8 detector chips

6.3 Experimental Details

Although this detector looked to be capable of improving upon the results obtained with photographic plates several difficulties were experienced when we tried to install and run it. The position-sensitive anode appeared not to be robust enough to cope with the conditions in the new instrument and consequently we failed to observe any definite counting with this device.

The first problem encountered was static. Initially the detector ran using a counting simulation program called **FRAME**. The detector worked well on the bench but after installation in the vacuum system it quickly ceased working and the chips became latched. This prevented us from rebooting the detector and all channels appeared to be counting (in a high state). This latching was attributed to static damage which probably occurred during installation. A possible source of static was from soldering, as several of the pins that connected the signal lines to the vacuum side of the detector feedthrough fell off.

I.S.L. subsequently made the device more static resistant and further attempts were made to observe counting. The next step taken was to ramp up the MCPs and once there was around 1000 volts across the plates the anode device was turned on. The idea was that as the MCPs warmed up they may emit charged particles and cause counting events in the anode. Upon turning off the MCPs the same "counting" rates were observed, indicating no real counting. Eventually the detector stalled after a few days and was sent back to Manchester.

When the detector was returned the same method for observing counts was used initially. The MCPs were ramped up slowly with the detector on. No counting was recorded and we noticed that the MCPs crashed several times when operating at over 2 kV leaving the anode device running. It was then decided to expose the detector to an electron beam. With the MCPs ramped up fully and the anode device operating an attempt was made to centre an electron beam of 30 keV electrons of intensity 0.5 μA in the centre of the detector. We expected to see counts in the anode device produced by rest gas scattering. However, the electron beam appeared to clip the inner edge of the MCPs resulting in the MCPs crashing. The effect on the anode device was to produce counting in dummy channels (where zero counts were expected) and all the chips were latched high. The electron beam caused permanent static damage to several inner elements on the anode. Once again the anode was returned to I.S.L.

Upon its return the anode operated well under no signal and no MCP voltage conditions, although 2 or 3 channels on chip 1 (controlling the innermost channels) counted continuously and the threshold discrimination was rather uneven between the four chips. An improvement made at this stage was to use a small battery to float the anode and its electronics 45 volts above the back of the MCP. A multiway connector was also added (see **Fig. 6.4**) to expedite installation of the detector head in the vacuum system.

When the MCP was slowly ramped up (with no input signal) it was noted that one or two additional channels in chip 1 now also counted continuously. Repeating this operation (with the device remaining under vacuum) produced additional changes and this extra damage was assumed to be associated with the initial degassing of the MCPs. At this point damage was also caused to the channels on chip 1 by the electron beam. With both anode and MCPs off an electron beam of around 1 μA was centred in the collector at the middle of the detector. Centring proved successful but the beam did clip the inner part of the detector and probably caused further damage.

Experiments were then conducted using an electron beam of 2 μA at around 30 keV, and some signs of electron counting in the anode device were observed. The MCPs were ramped up to an operating voltage of +1850 volts and the detector turned on and floated at a further 45 volts. Both MCP and detector were operated under a vacuum of around 5×10^{-8} mbar behind the gate valve. At the same time the main part of the apparatus was under high vacuum and the electron gun was running. The counting pattern with the gate valve closed was noted and the gate valve was then opened and the electron beam guided into the central collector cup (in the centre of the detector head). This produced very rapid counting in all channels. Closing the gate valve returned the detector to a very low counting state - essentially only the channels previously noted as defective remained active. These were rather uniformly spread across the detector area, although a very rapid fall off to larger radii elements was expected. This could have been associated with poor setting of the discriminator levels, which had been turned down to just stop counting. These results seemed to suggest some electron counting in many channels of the anode device. An attempt was immediately made to repeat the measurements by turning the electron beam on and off with the gate valve remaining open. In retrospect this may not have been the best strategy since it is possible that the electron beam had moved slightly under this operation leading to larger signals into the detector. The same counting pattern was seen before the beam current reached 2 μA but the detector quickly crashed and could not be restarted. Two loud cracks were heard from the power supply.

The symptoms seemed exactly the same as on all previous occasions, suggesting that the control logic arrays had been damaged. It was concluded that at least two damage mechanisms operated under large signal conditions:

1. through the input element with large signals destroying individual channels,

2. major system damage to control logic, probably associated with large signals in many channels.

The overall conclusion was that the device was not robust enough to operate under our experimental conditions.

Calculations were done to evaluate the worst case scenario if all the channels in the MCP counted simultaneously. The gain of the MCPs is roughly $5\text{x}10^6$ and there are $2.5\text{x}10^3$ channels mm^{-2}. If all channels counted at the same time a charge of ($2.5\text{x}10^3 \text{ x } 5\text{x}10^6 \text{ x } 1.6\text{x}10^{-19}$) = $2.0\text{x}10^{-9}$ C could be delivered per mm^2. The detector elements vary in area from 2-40 mm^2 so that the charge delivered to a single detector channel could be $4\text{x}10^{-9}$ C to $8\text{x}10^{-8}$ C. The typical pulse duration is around $5\text{x}10^{-9}$ s and if these charge pulses were passed across an impedance of 50 ohms voltages of between 40 volts and 800 volts may be experienced at the input to the comparator.

This worst case signal should be compared with a normal counting event delivering a charge of between 1 and $8\text{x}10^{-13}$ C providing about 8 mV at the channel input. The signal input conditions to produce this worst case situation - a count in every pore of the MCP - is ($2.5\text{x}10^3 \text{ x} 1.6\text{x}10^{-19}$) / $5\text{x}10^{-9}$ = $8\text{x}10^{-8}$ A mm^{-2}. This is not an inconceivable situation, particularly under transient conditions. The likelihood of this situation occurring at several channels simultaneously is very small. However, it is likely that several of these large transients could damage single channels and subsequently affect the control arrays, in particular the Xilinx device.

As a precautionary method the power supply for the electron gun was then returned to Start Spellman in order that the two existing current scales of 0-5 μA and 0-100μA could be reduced one hundred fold to 0-50 nA and 0-1 μA. The idea was that by operating at lower beam currents the count rates would be reduced to a level that the detector could cope with. At the same time the instability in the E.H.T. that we were experiencing was to be corrected.

The detector was despatched to Manchester at the end of September 1994. Unfortunately it did not return until late in July 1995, a considerable delay. This was due partly to the fact that the ceramic was broken in half during repair, necessitating the complete building of a new ceramic. This was done but the workers at I.S.L. found that their last Xilinx device had sustained damage during fabrication. This was due to a static problem akin to those we experienced. They then had the problem of replacing the Xilinx die and found that the minimum order quantity had increased threefold. To overcome this hurdle took a considerable amount of time but a device was obtained. However, we felt that I.S.L. were particularly evasive at times and this also led to the substantial delays with the detector.

The detector was received for the final time in July 1995 with a warning about the amount of insulating tape and PTFE tape that we had used to insulate several exposed pieces of metal at different voltages (see **Fig. 6.11**). I.S.L. informed us that the damage to the previous sensors was caused by spikes on the supply and/or data lines. The spikes were sufficient to have damaged the i/o ports of the programmable logic device used on the detector, and they were almost certainly caused by momentary breakdown of the channel plates. This could have been due to particulate contamination of the plates or operation of the plates at too high a pressure. The gas pressure is very important; Galileo recommend the pressure should be $1x10^{-6}$ Torr or lower and the plates were always operated at around $5x10^{-7}$ to $5x10^{-8}$ mbar. As mentioned we had placed quite a lot of insulating tape and PTFE tape on the arm holding the detector head and on the head itself. This was done because several pieces of metal, including the exposed braids of the detector data lines, were at slightly different high voltages and we wished to prevent arcing between components on the detector head. However, under

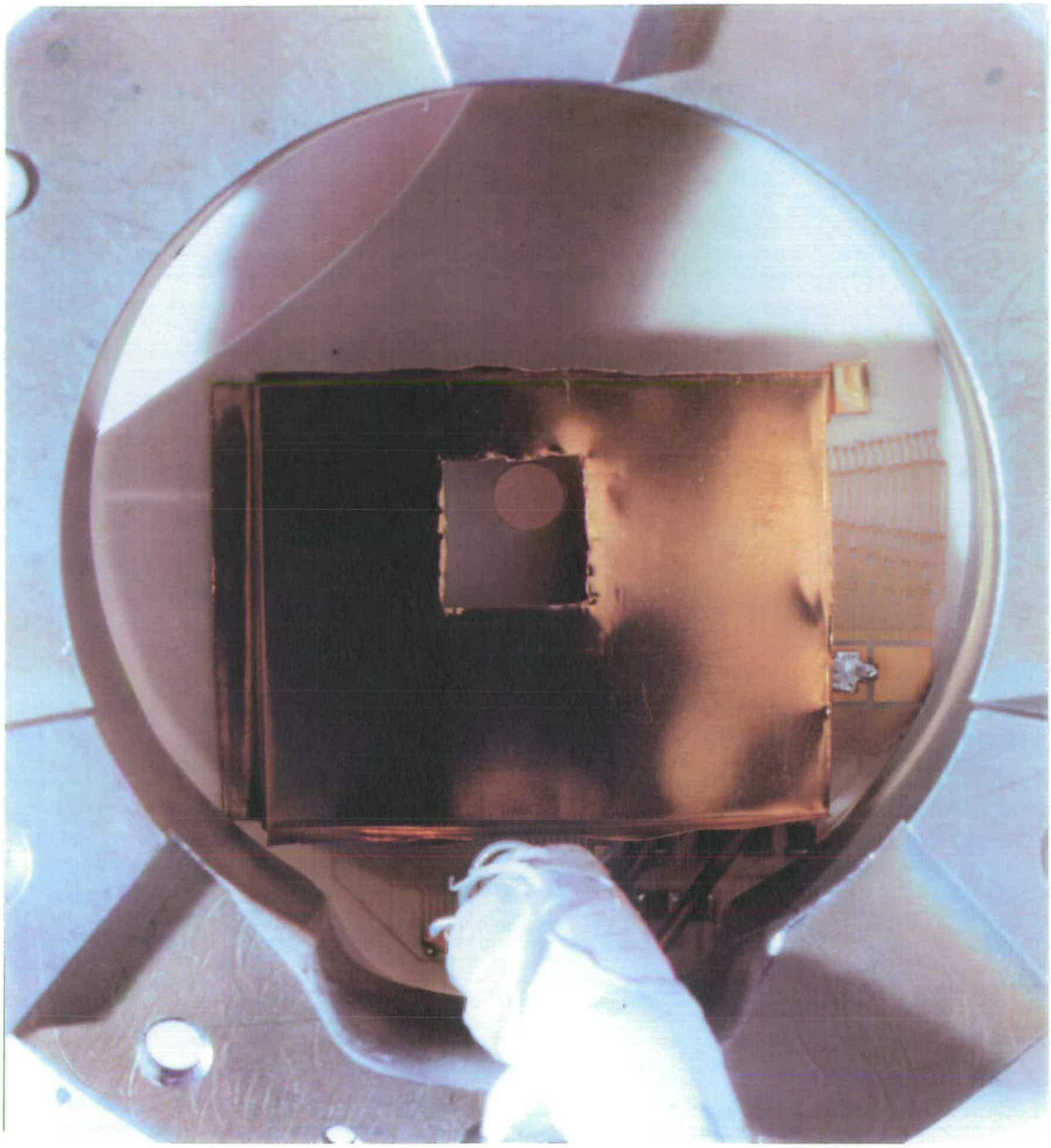

Figure 6.11 Photograph showing the back of the last version of the actual experimental anode device. In the top left of the picture the broken ceramic can be seen. Note also the white P.T.F.E. tape used to insulate the braids of the signal wires and the copper shield used to protect the electronics on the reverse of the ceramic.

vacuum this tape outgases extensively causing temporary pockets of high gas pressure near the plates.

To overcome the problem of spikes on the detector lines the detector was run from a separate power supply from the MCPs with mains filtering to prevent any spikes from coupling through from the mains. A substantial amount of tape was removed although some PTFE tape was needed to isolate the supply lines.

Unfortunately I.S.L. sent the detector plate upside down in the aluminium holder. When rectifying this mistake the plate was broken as pictured in **Figure 6.11** by Dr. M.A.D. Fluendy. When the detector was turned on we found that chip 2 did not work at all and all the dummy channels were counting high. We decided to test the detector under vacuum anyway. With the MCPs and detector powered by separate supplies with the appropriate filtering we left the detector on and ramped up the MCPs slowly. When the MCPs reached a voltage of +1600 volts a crackling sound from the back of the power supplies was heard. The voltage on the detector supply then dropped whilst the MCP voltage was maintained. It was suspected that there had been a short. Indeed, when the detector was removed from the vacuum system it was noted that there was a very small black charred spot on the white PTFE tape in **Figure 6.11**. There must have been an arc through the tape between the braids of the detector supply lines and the aluminium plate holder.

6.4 Further Work

As a result of the difficulties experienced with the anode device, work has ceased with this detector. To replace it a CCD (Charge Coupled Device) camera-based system has recently been purchased and installed by a new research student, Paul Papathomas. The operation of the CCD is considerably different from that of the discrete anode detector. In the new system scattered electrons strike a scintillating screen and the resulting photons are collected by the CCD camera.

A CCD consists of a two-dimensional array of square potential wells (typically 512 x 512 or more, not necessarily in a square array) made of silicon or another semi-conducting material. Incident photons (or electrons) create electron-hole pairs and the resulting electrons can be accumulated in each of the cells. The contents of these wells can be individually read out to produce a two-dimensional image of the light intensity (or electron intensity) incident on the CCD in the previous exposure. This read-out is accomplished by shifting the charge in each potential well to an output amplifier, digitising the output voltage with an analogue-to-digital converter and finally storing the digitised data in computer memory. This is the major difference between the CCD and the discrete anode device. The CCD is an analogue device which requires A→D conversion before signals can be stored whereas the anode counter, despite its technical drawbacks, was capable of much higher read-out rates. As electron events were recorded digitally they needed no conversion before read-out. These lower read-out rates for the CCD limit the range of experiments that can be carried out. However, use of a gated MCP and modulation of the CCD could allow nanosecond detection rates, opening up the way for time-resolved studies.

Like the MCP/anode device, the CCD camera has a wide dynamic range (65,000:1). This means that a rotating sector is not required although a graded optical filter could be used if problems were encountered. CCDs also have two main sources of unwanted noise. The first is due to what is known as dark charge. Even without a light signal being incident on the CCD charge is produced in each pixel through thermal energy. This dark charge pattern, for a particular temperature and exposure length, can be subtracted as a background. However, it still causes problems by reducing the dynamic range and producing dark charge noise. By cooling the CCD to -40° C this effect can be reduced. The second source of noise is the output preamplifier of the CCD. This noise is influenced by temperature and read-out rate. It is greatly reduced at temperatures below -60° C, and decreases as the read-out rate is reduced.

The actual CCD used in our apparatus is a Scientific Grade 1 CCD made by SITe (TEA/CCD-512SB), which has 512 x 512 pixels, each 24 μm square. The analogue-to-digital conversion operates at 16-bit resolution, and the read-out rate is 50 kHz, to minimise read-out noise. To reduce dark charge to acceptable levels, the CCD is operated at temperatures of -40° C or lower. Down to -40° C heat is removed by thermoelectric Peltier effect cooling using forced air flow. At lower temperatures, down to -50° C, water cooling is needed. To prevent condensation forming on the chip and leaving harmful deposits the CCD enclosure is evacuated down to 2×10^{-2} mbar.

Physically the CCD sits outside the vacuum system. The scintillator is mounted on a quartz viewport at the end of a re-entrant tube. The scintillator sits inside the vacuum system with the viewport and tube forming the vacuum seal. The CCD sits on an xyz translator about 60 cms behind the scintillator covered in black cloth to reduce the signal from stray light. A collector cup at the centre of the scintillator is used to monitor beam current and to collect the primary electron beam.

Initial work by Paul Papathomas has shown some evidence of scattered electron signal. By looking at the scattered signal with and without the molecular beam a difference was observed, although as yet it has not been firmly attributed to scattering from the He/CO_2 molecular beam and much of it could be due to rest gas scattering.

As mentioned it appears that the anode device provided by I.S.L. will no longer be used. In retrospect it may have been wiser to have purchased the CCD at an earlier date given the ten month delay with the anode device during my final year and the lack of co-operation and evasiveness from I.S.L.

During the period when the detector was away I suggested the use of a photographic plate or a series of concentric, annular split collectors as a means of detecting any scattering, but both ideas were rejected. With hindsight, it appears that too much trust was put in to a novel detector that was fragile and prone to failure.

Bibliography

1 C. Finbak, Avh. Norsk Vidensk.-Akad. Oslo, (1937) 13

2 P.P. Debye, Phys. Z., 80 (1939) 404

3 J.V. Hatfield, S.A. Burke, J. Comer, F. Currell, J. Goldfinch, T.A. York, and P.J. Hicks, Rev. Sci. Instrum., 63 (1992) 235

4 J.V. Hatfield, J. Comer, T.A. York, and P.J. Hicks, Rev. Sci. Instrum., 63 (1992) 792

5 J.V. Hatfield, Sensors and Actuators A, 41-42 (1994) 256

6 J. Wiza, Nucl. Instrum. and Meth., 162 (1979) 587

7 L.J. Richter and W. Ho, Rev. Sci. Instrum., 57 (1986) 1469

8 J.V. Hatfield, J. Comer, T.A. York, and P.J. Hicks, I.E.E.E. J. Solid-State circuits, SC-24 (1984) 704

9 B.C. Cole, Electronics, (Sept. 1987) 61

10 J. Mcleod, Electronics, 65 (1992) 7

11 M. Fink and R.A. Bonham, Rev. Sci. Instrum., 41 (1970) 389

12 S. Komaka, Jpn. Appl. Phys., 11 (1972) 1199

13 S.S. Kim and G.D. Stein, Rev. Sci. Instrum., 53 (1982) 838

14 A.A. Ischenko, V.V. Golubkov, V.P. Spiridonov, A.V. Zgurskii, A.S. Akhmanov, M.G. Vabischevich, and V.N. Bagratashvili, Appl. Phys., B32 (1983) 161

15 J.D. Ewbank, L. Schäfer, D.W. Paul, O.J. Benston, and J.C. Lennox, Rev. Sci. Instrum., 55 (1984) 1598

16 J.D. Ewbank, L. Schäfer, D.W. Paul, and D.L. Monts, Rev. Sci. Instrum., 57 (1986) 967

17 J.D. Ewbank, W.L. Faust, J.Y. Luo, J.T. English, D.L. Monts, D.W. Paul, Q. Dou, and L. Schäfer, Rev. Sci. Instrum., 63 (1992) 3352

18 B.D. Hall, M. Flüeli, D. Reinhard, J.-P. Borel, and R. Monot, Rev. Sci. Instrum., 62 (1991) 1481

19 J.C. Williamson, M. Dantus, S.B. Kim, and A.H. Zewail, Chem. Phys. Lett., 196 (1992) 529

Chapter 7

G.E.D. Structures

7.1 Introduction

Previously it has been mentioned that there already exists an electron diffraction apparatus within the chemistry department of Edinburgh University. This apparatus incorporates the standard rotating sector and photographic plate as the method of recording the diffracted electron image. This apparatus is used solely for structural studies. In the apparatus data are recorded at two camera distances. Gaseous samples enter the system via a metal or glass nozzle with an opening of 300 μm. Solid or liquid samples are held in glass or metal containers and if necessary volatilised by a set of heaters. Three data sets and two benzene calibration data sets are recorded at each distance. The benzene sample is used to calibrate the camera distance and the electron wavelength.

Once these diffraction images have been exposed and developed the photographic plates are sent to Daresbury, where they are optically scanned using a microdensitometer to give the total electron scattering intensity. This total scattering is composed of molecular, atomic and extraneous scattering contributions modulated by the rotating sector function. The data from these scans are then transferred to datafiles compatible with the local **tattoo** server which runs under the UNIX operating system. This allows structure refinement and solution to be carried out.

The structural analysis is done using a program called **ed92,** mounted on the **tattoo** processes available to the electron diffraction group. This FORTRAN program together with several other files can be used to solve molecular geometries from the total electron scattering intensities. Initially a geometrical model of the molecule to be studied is written. This too takes the form of a FORTRAN file and it uses bond lengths, bond angles and internal angles of rotation to produce a set of internal co-ordinates. These allow all the positions of the nuclei relative to each other to be calculated with one position in the molecule taken to be the origin of a global co-ordinate system. To do this the model is compiled with **ed92**.

Two other files known as the **input** file and the **distu** file must also be created. In the model file each of the atoms is numbered systematically. For a molecule containing N atoms there are N(N-1)/2 scattering pairs. This gives N(N-1)/2 distances which may reduce in number to give fewer distinct distances. This is because scattering from like pairs of atoms, the same distance apart, may occur through local or overall symmetry. The **input** file thus contains up to 100 distinct distances together with their multiplicities.

The **input** file includes the distances and amplitudes of vibration for bonded atoms together with non-bonded pairs of atoms which make the biggest contribution to the molecular scattering, i.e. atom pairs containing heavy atoms or those separated by short distances. This file also contains the numbered parameters used to specify the molecular structure. It is important to start off with a good model of the molecule as this is an integral part of the refinement process. If the starting model is too different from the true geometry the structure may never be refined properly. Getting sensible initial values for refinable parameters is also crucial and often quantum mechanical calculations are used to provide them otherwise they are taken from published data for related molecules. The **distu** file is only required when more than 100 distances are needed to describe the molecule; it contains any extra non-bonded distances.

Once a satisfactory model has been created and the distance files written the procedure for solving and refining a structure then consists of four main parts. The scattering raw data are comprised of two parts. As mentioned in **Chapter 2** they are the atomic and molecular scattering. The atomic scattering takes the form of a monotonically decreasing curve as the scattering from atoms falls off as $1/s^4$ with increasing s. These data are then treated using three parts of the **ed92** program to produce the molecular intensities. These are composed of a set of superimposed sinusoidal functions. In the total scattering intensity they appear as small bumps on the decreasing atomic or theoretical background. The molecular intensities are then subsequently used in the refinement process and Fourier transformation of these data produces the radial distribution curve displaying the atomic distribution within the molecule.

The **'a' job** creates a set of scattering factors for each of the atoms in the molecule at a particular electron beam energy. The accelerating voltage currently used in structural studies at Edinburgh University is 44.5 keV. In the **'b' job** the effect of the rotating sector is removed and corrections are made for the flatness of the photographic plate and plate blackness saturation. The total intensity after these operations is then multiplied by s^4 to produce uphill curves. The data are made apparatus independent by this treatment and can now be analysed by any electron diffraction group in the world. In the uphill curves the molecular scattering manifests itself as small oscillations on a rising curve. If data from any one plate appear incongruous they can be removed at this stage.

Finally the **'c' job** reduces the uphill curves to molecular intensity curves and averages them. The atomic background (i.e. atomic scattering times s^4) is removed and the first estimate of the experimental background is calculated and displayed. The experimental background results from extraneous scattering and is evaluated by fitting a cubic function.

The **ed92** refinement consists of a least-squares refinement during which the experimental intensities are fitted to the theoretical intensities with subsequent improvement of the background as refinement progresses. The theoretical intensities are derived from the molecular model. This is only done for Fourier transformation to give the radial distribution curve and as experimental data are unavailable below a certain *s* value due to the electron collector the theoretical intensities are used to fill this gap in the data. The refinement consists of allowing certain parameters (distances and angles) together with some associated amplitudes of vibration to become part of the refining scheme whilst fixing others. Care must be taken that the parameters, distances and amplitudes do not become unrealistic whilst trying to reduce the R-factor or goodness of fit. This R-factor is an mathematical function which gives an idea of how good the fit is between the experimental and theoretical data.

The output from the **ed92** program consists of a refinement list which shows the current state of the parameters; the radial distribution and intensity curves can also be plotted. In **section 2.2.4** an explanation is given as to how the radial distribution curve is derived. It is composed of a series of nearly Gaussian peaks corresponding to the internuclear distances within a molecule. Although it offers a pictorial description of the refinement it is not normally used for reading molecular distances directly. Only for relatively small symmetrical molecules can the radial distribution curve be used to infer anything about the molecular geometry. However, for large, complicated molecules with many distances the near Gaussian distributions begin to overlap and information is lost. A rough rule of thumb is that for each peak in the radial distribution curve one geometrical parameter or distance and one vibrational parameter can be refined. The area under each peak is proportional to the quantity $n_{ij}Z_iZ_j/r_{ij}$ where Z_i and Z_j are the atomic numbers of a pair, r_{ij} the distance between the pair and n_{ij} the multiplicity of that distance.

The two molecules discussed in the rest of this chapter are 1,2-di-*tert*-butyldisilane and 1,2-dicarbapentaborane(7).

7.2 Structure Of 1,2-di-*tert*-butyldisilane

7.2.1 GED Measurements

Using the Edinburgh gas diffraction apparatus [1] the electron scattering intensities for a sample of $(CH_3)_3CSiH_2SiH_2C(CH_3)_3$ were recorded on Kodak Electron Image photographic plates. The operational voltage used was approximately 44.5 kV whilst the sample and nozzle were kept at 333 and 382 K respectively during the experiments. Calibration of the electron wavelength and nozzle-to-plate distances were facilitated by recording scattering data for benzene. Two plates were recorded at each distance (259.47 and 93.50 mm) and were optically scanned using a computer-controlled Joyce-Loebl Microdensitometer 6 at the S.E.R.C. Daresbury Laboratory [2]. These data, in digital form, were subsequently analysed using established data-reduction [2] and least-squares refinement programs [3] incorporating complex scattering factors [4]. The weighting points used in setting up the off-diagonal weight matrix, *s* ranges, scale factors, correlation parameters, and electron wavelengths are all displayed in **Table 7.1.**

7.2.2 Molecular Model And Structure Determination From GED Data

To simplify the least-squares refinement it was assumed that the CH_3 groups had local C_{3v} symmetry and that the $C(CH_3)_3$ groups had local C_3 symmetry. An overall symmetry of C_2 was adopted for the $(CH_3)_3CSiH_2SiH_2C(CH_3)_3$ molecule although a model with an overall symmetry of C_i was also examined. This latter model proved to give much poorer fits than the C_2 structure and was not considered to be a satisfactory representation of the experimental geometry. The molecular geometry (see **Fig. 7.1**) was then defined by the five bond lengths (*r*(Si-Si), *r*(Si-C), *r*(C-C), *r*(C-H), *r*(Si-H)), the five angles (SiSiC, CCC, CCH, SiSiH, HSiH) and three twist angles. The first of these, around the Si(1)-Si(2) bond, had positive values for a clockwise rotation from the eclipsed C(21)-Si(2)-Si(1)-C(11) form

Table 7.1 Nozzle-plate distances, weighting functions, correlation parameters, scale factors, and electron wavelengths.

Nozzle to plate distance (mm)	259.47	93.50
Δs (nm^{-1})	2	4
s_{min} (nm^{-1})	30	88
sw_1 (nm^{-1})	50	108
sw_2 (nm^{-1})	140	384
s_{max} (nm^{-1})	164	336
Correlation parameter p/h	0.1096	-0.0907
Scale factor k[a]	0.713(7)	0.577(9)
Electron wavelength[b] (pm)	5.686	5.689

[a] Figures in parentheses are the estimated standard deviations of the last digits.

[b] Determined by reference to the scattering pattern of benzene vapour.

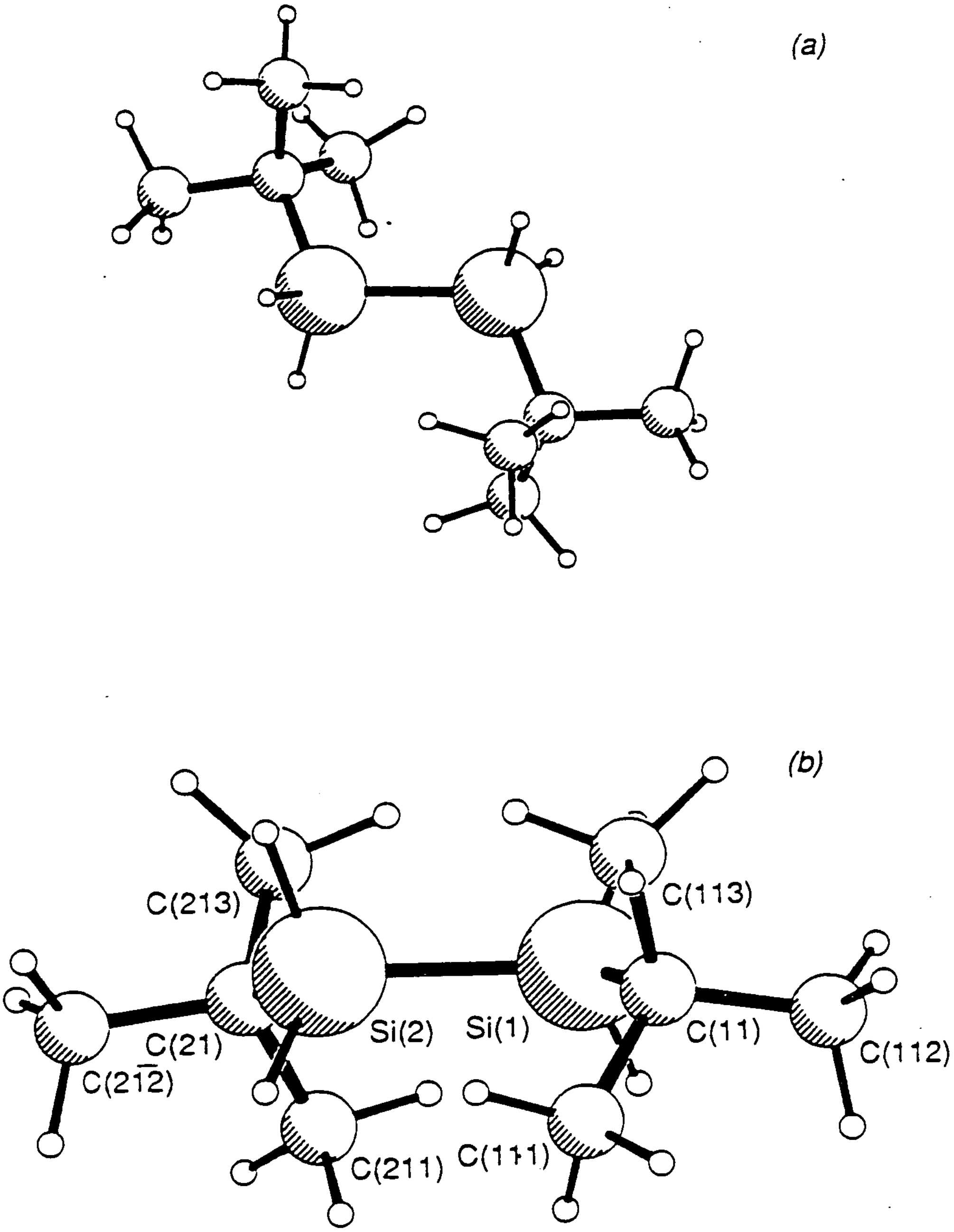

Figure 7.1 The $(CH_3)_3CSiH_2C(CH_3)_3$ molecule in the optimum refinement of the electron diffraction data, also showing the atomic numbering of the $C_3CSiH_2SiH_2CC_3$ skeleton: (a) a perspective view; (b) a view showing the molecular C_2 symmetry.

(0° and 180° for the mutual *syn* and *anti* arrangements of the Si-C bonds, respectively). Twists were also included for the CH_3 and $C(CH_3)_3$ groups, and were taken to be positive for clockwise rotations from the eclipsed (*syn*) H-C(111)-C(11)-Si(1) and C(111)-C(11)-Si(1)-Si(2) positions, respectively. A further addition was to allow the local C_3 axes of the $C(CH_3)_3$ group to deviate from the lines of the Si-C bonds, a positive tilt representing a movement of the CH_3 groups away from the other silicon. The 14 molecular parameters that describe the molecular geometry are listed in **Table 7.2.** These are the final parameters (C_2) which gave an R_G value of 0.044 (R_D=0.041).

Most of the refinement of the GED data for this structure was carried out by Dr. D. Hnyk and the results reported have been published [5] along with *ab initio* calculations and vibrational spectroscopy studies (**Appendix B**). Details of the refinement procedure are described here. The main problem encountered during the analysis was the magnitude of the SiSiC angle. Initially, simultaneous refinement of the geometrical and vibrational parameters associated with the heavy-atom skeleton, together with some relating to hydrogen atom positions, led to a false minimum characterised by an unrealistically wide SiSiC bond angle of about 127°. This model also gave other unrealistic parameters and although it produced an R_G factor of 0.044 it was rejected. Many refinements, still in C_2 symmetry, were then carried out with the SiSiC angle and Si-Si distance kept fixed at 115° and 234 pm respectively, i.e. close to the *ab initio* values computed for this molecule [5]. The number of refined parameters was gradually increased, until eventually the SiSiC angle, the Si-Si bond length and the Si-Si vibrational amplitude were included in the refinement scheme. This procedure led to a more reasonable structure, in which the SiSiC angle was 113.7°. The R_G factor arrived at under these refinement conditions (0.044) was identical to that obtained with the structure having an extremely wide SiSiC angle. Further refinements, starting with SiSiC angles in the range 109-127°, always led to one of the two structures already described, and angles between 113.7 and 127° never fitted the data satisfactorily.

An attempt was made to investigate the relative amounts of the *anti* and *gauche* forms within the refinement scheme. It was not possible to determine from the GED data how much of the *gauche* conformer was present, although it was reckoned to be quite small, certainly less than 20%.

The interatomic distances and the corresponding amplitudes of vibration are listed in **Table 7.3**. **Table 7.4** shows the least-squares correlation matrix. The atomic coordinates are listed in **Table 7.5**, from which interatomic distances, bond angles, and dihedral angles may be computed. **Figures 7.2** and **7.3** show the molecular scattering intensity curves and the radial distribution curve, respectively.

7.3 Structure Of 1,2-dicarbapentaborane(7)

7.3.1 GED Measurements

Using the Edinburgh gas diffraction apparatus [1] the electron scattering intensities for a sample of the carborane $B_3C_2H_7$ were recorded on Kodak Electron Image photographic plates. The operational voltage used was approximately 44.5 kV whilst the sample and nozzle were held at around 293 K during the experiments. Calibration of the electron wavelength and nozzle-to-plate distance were facilitated by recording scattering data for benzene. Two plates were recorded at a single distance (~201 mm) giving a limited data set in the *s* range 4-22.4 $Å^{-1}$. The plates were optically scanned using a computer-controlled Joyce-Loebl Microdensitometer 6 at the S.E.R.C. Daresbury Laboratory [2]. These data, in digital form, were subsequently analysed using established data-reduction [2] and least-squares programs [3] incorporating complex scattering factors [4]. The weighting points used in setting up the off-diagonal weight matrix, *s* ranges, scale factors, correlation parameters, and electron wavelengths are all displayed in **Table 7.6**.

Table 7.2 Geometrical parameters for $(CH_3)_3CSiH_2SiH_2C(CH_3)_3$ (distances in pm, angles in deg)[a]

	Molecular symmetry
	C_2
p_1 r(Si-Si)	234.8(3)
p_2 r(Si-C)	190.1(1)
p_3 r(C-C)	154.1(1)
p_4 r(C-H)	112.0(1)
p_5 r(Si-H)	149.8(8)
p_6 $\angle$SiSiC	113.7(3)
p_7 $\angle$CCC	109.2(1)
p_8 $\angle$CCH	110.0[b]
p_9 $\angle$SiSiH	107.1(15)
p_{10} $\angle$HSiH	109.0[b]
p_{11} $\angle$(CH_3 twist)	36.8(25)
p_{12} $\angle$(Me_3C twist)	49.8(4)
p_{13} $\angle$(Si-Si twist)	195.5(12)
p_{14} $\angle$(C_3C-Si tilt)	2.1(5)
R_G	0.044

[a] Figures in parentheses are the estimated standard deviations of the last digits.

[b] Fixed in the final refinement.

Table 7.3 Interatomic distances (r_a in pm)[a] and mean amplitudes of vibration (u in pm) for $(CH_3)_3CSiH_2SiH_2C(CH_3)_3$

Atomic Pair	r_a[b]		u[b]
Si-Si	234.8(3)	u_1	6.8(4)
Si-C	190.1(1)	u_2	5.1(2)
C-C	154.1(1)	u_3	5.4(1)
Si-H	149.7(8)		8.0[c]
C-H	112.0(1)	u_4	6.8(2)
Si(1)...C(11N)[d]	279-285	u_5	9.3(3)
Si(1)...C(21)	356.6(5)	u_6	9.6(8)
Si(1)...C(211)	378.4(14)		11.3[e]
Si(1)...C(212)	489.7(6)	u_7	12.3(6)
Si(1)...C(213)	401.6(11)	u_8	15.1(10)
Si(1)...$H_{(1)}$}	275-284		11.0[c]
Si(1)...$H_{(2)}$}-C(11N)[d]	320-328		16.0[c]
Si(1)...$H_{(3)}$}	376-381		18.0[c]
Si(1)...$H_{(1)}$}	362.6(29)		14.0[c]
Si(1)...$H_{(2)}$}-C(211)	490.3(15)		20.0[c]
Si(1)...$H_{(3)}$}	353.4(55)		14.0[c]
Si(1)...$H_{(1)}$}	505.9(17)		20.0[c]
Si(1)...$H_{(2)}$}-C(212)	573.8(4)		23.0[c]
Si(1)...$H_{(3)}$}	523.0(23)		20.0[c]
Si(1)...$H_{(1)}$}	337.1(15)		18.0[c]
Si(1)...$H_{(2)}$}-C(213)	479.6(26)		20.0[c]
Si(1)...$H_{(3)}$}	470.7(33)		20.0[c]
Si(1)...H-Si(2)	313.4(27)	u_9	12.1(19)
C(111)...C(112)	251.2(2)	u_{10}	7.5(3)
(C...C)[g]	(519-579)[f]	u_{11}	[12.3-13.7](17)
(C...C)[h]	(630-678)[f]	u_{12}	28.3(20)
C(113)...C(213)	621.5(30)[f]		25.0[c]
C(112)...C(212)	755.7(15)[f]		30.0[c]

C(11)...H[C(111)]	219.3(1)	u_{13}	9.9(6)

---

[a] Other C...H and all the H...H nonbonded distances were included in the refinement, but are not listed here. Their vibrational amplitudes were within the range 12-35 pm.

[b] Least-squares standard deviations in the last digit are given in parentheses.

[c] Fixed.

[d] N = 1, 2, 3: for the numbering scheme see Fig. 1.

[e] Tied to u_6.

[f] Dependent on the Si-Si twist angle.

[g] Six distances arising from the contact of the two *t*-Bu groups.

[h] Eight distances arising from the contact of the two *t*-Bu groups.

Table 7.4 Portion of the least-squares correlation matrix for $(CH_3)C_3SiH_2SiH_2C(CH_3)_3$ showing all elements ≥ 50% (k_1 and k_2 are scale factors).

p_5	p_6	p_7	p_9	p_{11}	p_{12}	p_{13}	u_1	u_5	u_6	u_8	u_9	u_{10}	u_{13}	k_1	k_2	
	-59												-72			p_1
-84																p_3
		-50		-58												p_6
				65			-77				52	-68	-61			p_7
									-71							p_9
			71		-55	-57			-62	-56	66					p_{11}
			-53													p_{12}
								-81								p_{14}
												81	75			u_1
														57		u_3
														51		u_4
											-50					u_6
													53			u_{10}
															54	k_1

Table 7.5 Atomic coordinates (pm) for $(CH_3)_3CSiH_2SiH_2C(CH_3)_3$

Atom	*x*	*y*	*z*
Si(1)	0.0	234.8	0.0
C(11)	167.7	311.2	-46.6
C(111)	222.4	249.8	-176.9
$H_{(1)}$}	138.0	226.9	-246.9
$H_{(2)}$}-C(111)	292.5	321.6	-226.7
$H_{(3)}$}	277.6	154.9	-154.3
C(112)	146.2	462.5	-67.2
$H_{(1)}$}	71.0	500.8	6.4
$H_{(2)}$}-C(112)	242.8	517.2	-52.4
$H_{(3)}$}	108.8	482.1	-171.0
C(113)	270.1	289.6	66.4
$H_{(1)}$}	257.2	187.6	110.8
$H_{(2)}$}-C(113)	374.2	298.8	26.1
$H_{(3)}$}	255.3	366.3	146.7
$H_{(1)}$}-Si(1)	-105.0	278.8	-97.4
$H_{(2)}$}-Si(1)	-39.7	278.8	137.6
Si(2)	0.0	0.0	0.0
C(21)	-174.1	-76.4	0.0
C(211)	-261.7	-14.9	-110.8
$H_{(1)}$}	-199.1	-8.0	-200.9
$H_{(2)}$}-C(211)	-342.5	-86.8	-140.1
$H_{(3)}$}	-308.8	79.9	-74.3
C(212)	-158.9	-227.6	-25.6
$H_{(1)}$}	-66.7	-266.0	25.2
$H_{(2)}$}-C(212)	-248.0	-282.4	15.0
$H_{(3)}$}	-150.7	-247.3	-135.5
C(213)	-242.4	-54.8	136.4
$H_{(1)}$}	-218.1	47.3	175.7
$H_{(2)}$}-C(213)	-353.5	-64.0	125.5

$H_{(3)}$}	-206.7	-131.5	209.8
$H_{(1)}$}-Si(2)	75.1	-43.9	-122.0
$H_{(2)}$}-Si(2)	75.1	-43.9	122.0

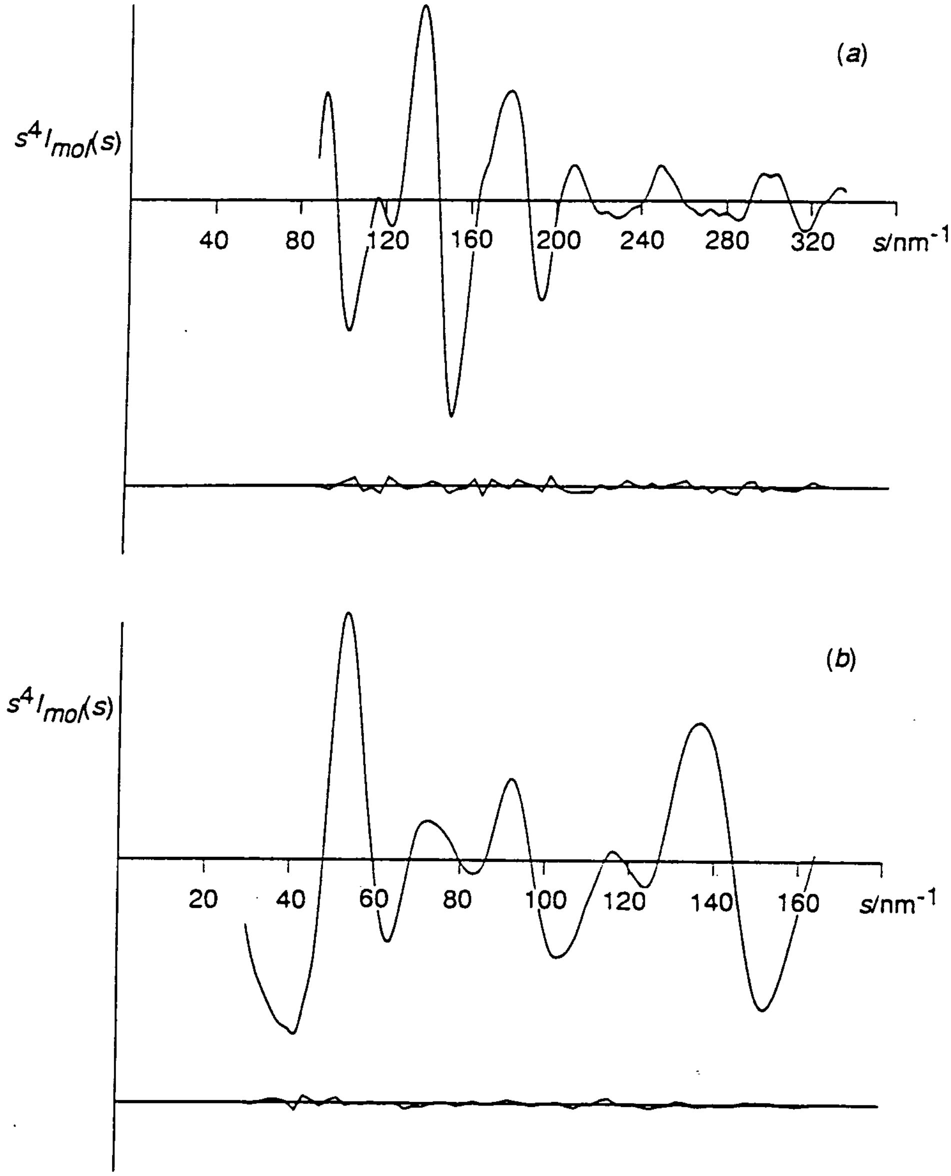

Figure 7.2 Experimental and final difference (experimental minus theoretical) molecular-scattering intensities for $(CH_3)_3CSiH_2SiH_2C(CH_3)_3$ at nozzle-to-plate distances of (a) 94 mm and (b) 259 mm.

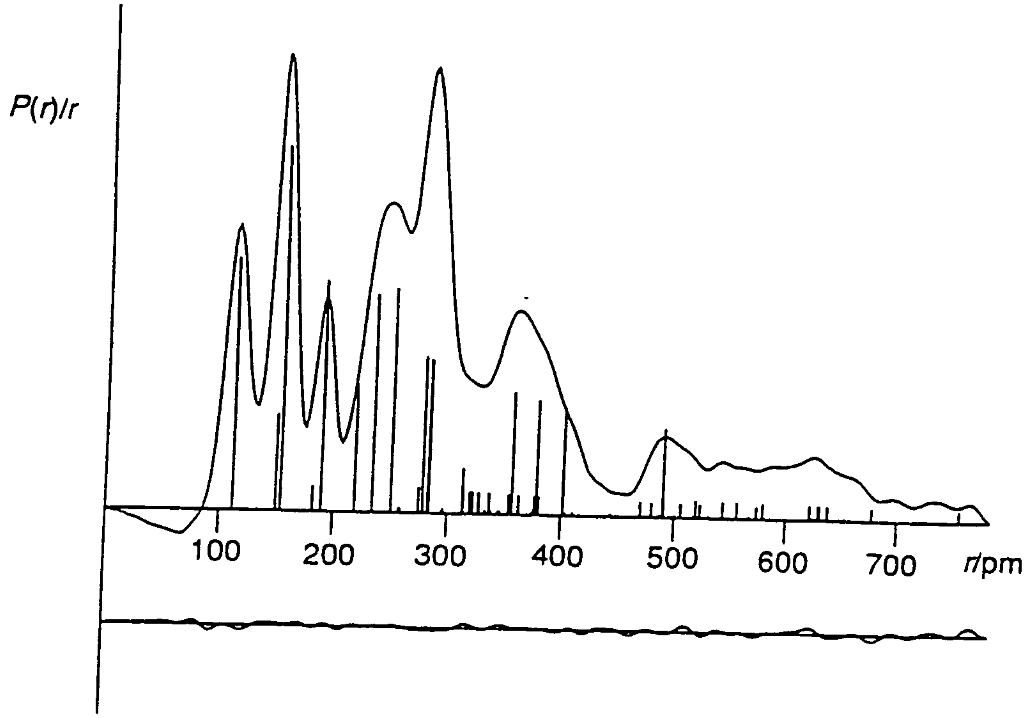

Figure 7.3 Experimental and difference (experimental minus theoretical) radial-distribution curves, *P(r)/r*, for $(CH_3)_3CSiH_2C(CH_3)_3$ vapour; before Fourier inversion, the data were multiplied by $s.\exp(-0.00002s^2)/(Z_{Si} - f_{Si})(Z_c - f_c)$.

Table 7.6 Nozzle-plate distances, weighting functions, correlation parameters, scale, factors, and electron wavelengths.

Nozzle to plate distance (mm)	200.89
Δs (nm^{-1})	4
s_{min} (nm^{-1})	40
sw_1 (nm^{-1})	60
sw_2 (nm^{-1})	192
s_{max} (nm^{-1})	224
Correlation parameter p/h	-0.254
Scale factor k[a]	0.728(10)
Electron wavelength[b] (pm)	5.681

[a] Figures in parentheses are the estimated standard deviations of the last digits.

[b] Determined by reference to the scattering pattern of benzene vapour.

7.3.2 Molecular Model And Structure Determination From GED Data

On the basis of *ab initio* calculations a model was formulated to describe the atomic coordinates of the molecule $B_3C_2H_7$ in terms of sixteen parameters. The final refined parameters are listed in **Table 7.7**. The proposed structure was that of a nido-carborane, 1,2-dicarbapentaborane(7) (see **Fig. 7.4**). The molecule has overall C_s symmetry.

The three boron atoms were defined in the xy plane in the model. Atoms B(3) and B(4) lay on the x-axis and B(5) on the y-axis. One of the carbon atoms, C(2), sat below the xy plane in the yz plane (the mirror plane). Parameter 4, a dip angle, defined the position of C(2). The heavy atom framework was completed by the second carbon atom, C(1), which was defined as the apex of the B_3C_2 structure. The description of this B_3C_2 structure required six parameters (1-6 in **Table 7.7**).

The molecule also contained seven hydrogen atoms; five terminal hydrogens and two bridging hydrogens. Three of the terminal H atoms, H(6), H(9) and H(10) lay in the mirror plane. The position of H(10) was defined by the position of C(2), the angle C(1)C(2)H(10) (parameter 11) and the average C-H distance (parameter 9). Similarly H(9) was defined by the position of C(1), the C-H distance and parameter 10, the angle between C(1)-H(9) and the xy plane. The coordinates of H(6) were defined by the position of B(5), the average terminal B-H distance (parameter 7) and the angle C(1)B(5)H(6) (parameter 8). The equivalent hydrogen atoms H(7) and H(8) were defined by the positions of B(3) and B(4) respectively, along with the average bridging B-H distance (parameter 12) and the angle B(4)B(3)H(7) (parameter 15) together with a twist angle of the bond B(3)-H(7) away from the xy plane (parameter 16). Parameter 13, the difference between the two bridging distances, was not refined but was fixed in the refinement scheme.

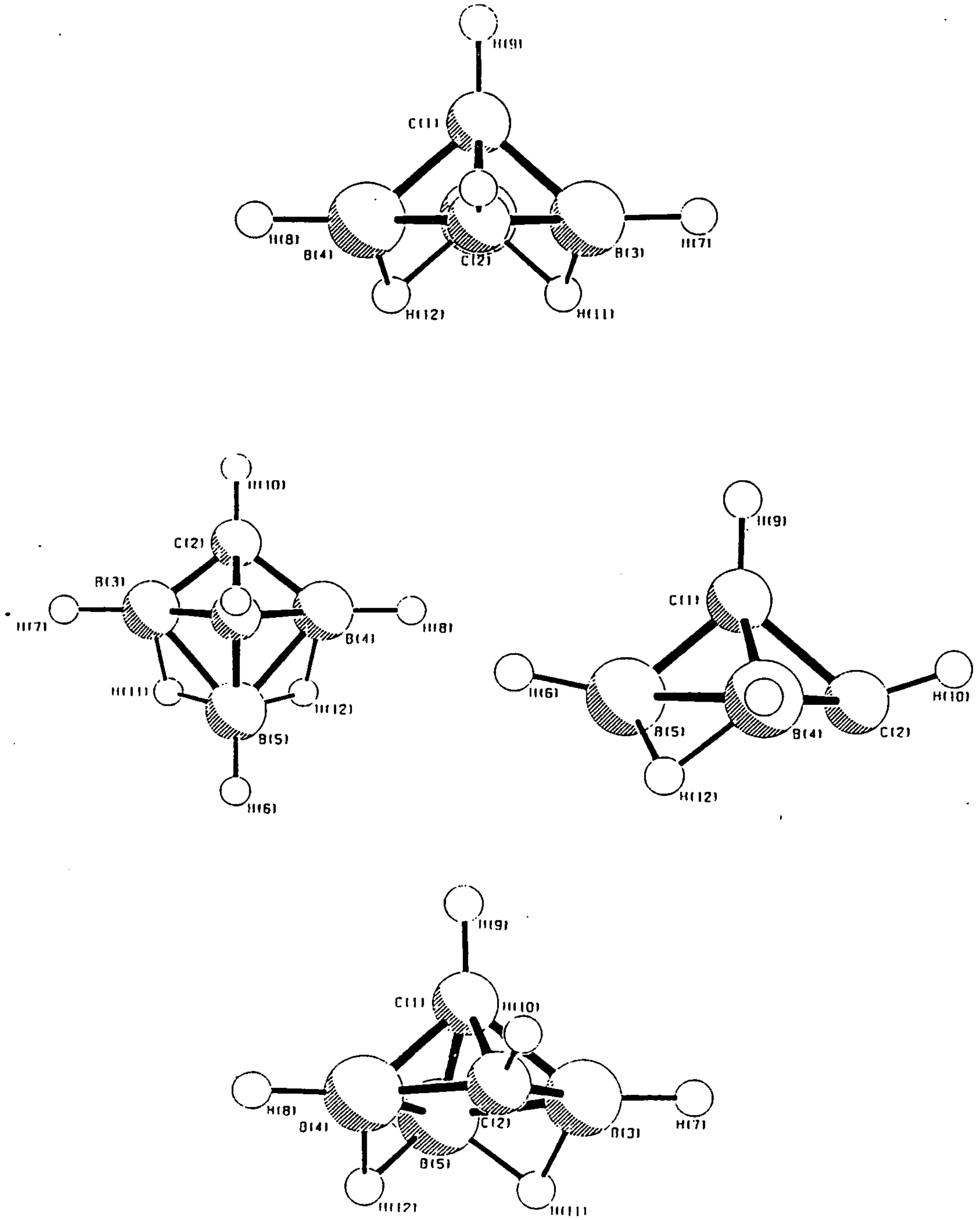

Figure 7.4 The $B_3C_2H_7$ molecule in the optimum refinement of the electron diffraction data.

Table 7.7 Geometrical parameters for $B_3C_2H_7$ (distances in pm, angles in deg)[a].

p_1	B(3)-B(5) distance	186.9(3)
p_2	angle B(4)B(5)B(3)	79.0(2)
p_3	average B-C distance[b]	157.3(1)
p_4	dip angle of C(2) below heavy atom plane containing the three boron atoms	120[c]
p_5	[R31-(2xR23+R51)/3][d]	6.0(1)
p_6	[R51-R23][e]	2.7[c]
p_7	average terminal B-H distance	121.5(6)
p_8	angle C(1)B(5)H(6)	126.6[c]
p_9	average C-H distance	108.5[c]
p_{10}	angle between C(1)-H(9) distance and xy plane[f]	91.1[c]
p_{11}	angle C(1)C(2)H(10)	119.8[c]
p_{12}	average bridging B-H distance	133.6(4)
p_{13}	difference between bridging B-H distances	2.5[c]
p_{14}	dip angle of bridging H atom[g]	62.12[c]
p_{15}	angle B(4)B(3)H(7)[h]	0.9[c]
p_{16}	twist angle B(4)B(3)H(7)[i]	95.0[c]
	R_G	0.01825

---

[a] Figures in parentheses are the estimated standard deviations of the last digits.

[b] Average B-C distance defined as [(2xR31+2xR23+R51)/5], where R13 is the distance between atoms 1 and 3, R23 is the distance between atoms 2 and 3 with R51 being the distance between atoms 5 and 1.

[c] Fixed in the final refinement.

[d] Difference between largest B-C distance and the average of the other three.

[e] Smallest difference between B-C distances; second longest minus shortest.

[f] The xy plane defined as heavy atom plane containing all three boron atoms.

[g] Dip of plane B(3)B(5)H(11) below heavy atom plane B(3)B(4)B(5).

[h] Rotation angle of distance B(3)-H(7) in xy plane.

[i] Twist angle of distance B(3)-H(7) away from xy plane.

The bridging hydrogen atoms H(11) and H(12) were defined in planes with B(3)&B(5) and B(4)&B(5) respectively. Four parameters were needed to calculate their coordinates; an average bridging B-H distance (parameter 12), a difference between the bridging B-H distances, B(3)-H(11) and B(5)-H(11) (parameter 13), the B(3)-B(5) distance and the dip angle of the plane containing H(11) below B(3) and B(5) (parameter 14).

Even though there was a limited data set six parameters and four amplitudes refined satisfactorily. Initially the B-B distance, the angle B(4)B(5)B(3), the average B-H distance, the average terminal B-H distance and the mean bridging B-H distance refined well. The R_G at this point was 0.02045. When the C-H distance was introduced the R_G factor dropped but this must have been a false minimum. The C-H distance refined to an unrealistic value of 1.0584 Å and as a result this parameter was removed from the refinement scheme and it was fixed at a value of 1.085 Å. The next step was to refine some amplitudes. The amplitude u_1 (see **Table 7.8** for interatomic distances and amplitudes) was then included in the refinement as part of a group with u_2, u_3 and u_5. These were the amplitudes of the distances making up the heavy atom framework and were eventually fixed once they had reached a reasonable value. Four further amplitudes were included in the refinement scheme; u_7 [B(3)-B(5)], u_9 tied to u_{11} [B(3)-H911) and B(5)-H(11)] the bridging B-H distances, u_{16} tied to u_{21} [C(2)...B(5) and B(3)...B(4) respectively] and u_{13} tied to u_{12}, u_{14}, u_{15}, u_{18}, u_{19} and u_{20} (all of the two-bond C...H distances). Finally parameter 5 was allowed to refine. This parameter was the difference between the largest and smallest B-C distances. The final R_G value was 0.01825 (R_D = 0.02301) for the model defined by the parameters in **Table 7.7**. **Table 7.9** shows the least-squares correlation matrix. The atomic coordinates are listed in **Table 7.10**, from which interatomic distances, bond angles and dip angles may computed. **Figures 7.5** and **7.6** show the molecular scattering intensity and radial distribution curves respectively.

Table 7.8 Interatomic distances (r_a in pm) and mean amplitudes of vibration (u in pm) for $B_3C_2H_7$.

		Distance/(r_a in pm)	Amplitude/(u in pm)
d1	C1-C2	164.9(4)	5.7 (fixed)
d2	C1-B3	161.0(3)	5.7 (fixed)
d3	C1-B5	156.7(2)	5.7 (fixed)
d4	C1-H9	108.5	7.6 (fixed)
d5	C2-B3	154.0(2)	5.7 (fixed)
d6	C2-H10	108.5	7.7 (fixed)
d7	B3-B5	186.9(3)	6.4 (2)
d8	B3-H7	121.5(5)	8.3 (fixed)
d9	B3-H11	134.9(4)	10.5(7)
d10	B5-H6	121.5(5)	8.3 (fixed)
d11	B5-H11	132.4(4)	10.5 (tied to u_9)
d12	C1...H6	249.1(5)	10.4 (tied to u_{13})
d13	C1...H7	263.0(5)	10.4(8)
d14	C1...H10	238.2(4)	10.4 (tied to u_{13})
d15	C1...H11	223.5(7)	10.4 (tied to u_{13})
d16	C2...B5	242.0(5)	5.3(3)
d17	C2...H6	362.1(9)	9.9 (fixed)
d18	C2...H7	259.6(5)	10.4 (tied to u_{13})
d19	C2...H9	248.2(3)	10.4 (tied to u_{13})
d20	C2...H11	235.1(5)	10.4 (tied to u_{13})
d21	B3...B4	237.9(6)	5.3 (tied to u_{16})
d22	B3...H6	289.9(7)	11.7 (fixed)
d23	B3...H8	359.4(6)	9.9 (fixed)
d24	B3...H9	245.6(3)	11.1 (fixed)
d25	B3...H10	235.2(3)	10.8 (fixed)
d26	B3...H12	249.7(6)	12.3 (fixed)
d27	B5...H7	280.4(5)	12.0 (fixed)
d28	B5...H9	244.1(7)	10.6 (fixed)
d29	B5...H10	345.9(5)	9.5 (fixed)

d30	H6...H7	357.4(9)	18.3 (fixed)
d31	H6...H9	303.9(3)	18.6 (fixed)
d32	H6...H10	463.4(8)	12.6 (fixed)
d33	H6...H11	215.5(5)	15.0 (fixed)
d34	H7...H8	480.9(10)	12.8 (fixed)
d35	H7...H9	321.2(4)	19.6 (fixed)
d36	H7...H10	314.3(4)	17.5 (fixed)
d37	H7...H11	199.2(4)	15.0 (fixed)
d38	H7...H12	359.0(5)	14.8 (fixed)
d39	H9...H10	287.7(3)	18.4 (fixed)
d40	H9...H11	321.0(6)	13.1 (fixed)
d41	H10...H11	337.5(5)	14.3 (fixed)
d42	H11...H12	185.6(5)	15.8 (fixed)

Table 7.9 Portion of the least-squares correlation matrix for $B_3C_2H_7$ showing all elements ≥ 50% (k_1 is a scale factor)

p_1	p_2	p_3	p_5	p_7	p_{12}	u_9	u_{13}	u_{16}	k_1	
									73	p_1
		89		-53	57					p_2
	89				52					p_3
83								64	73	p_5
	-53					85	57			p_7
	57	52							-56	p_{12}
							-59			u_9
				-57		-59				u_{13}
			64							u_{16}
73			73		-56					k_1

Table 7.10 Atomic coordinates (pm) for $B_3C_2H_7$.

Atom	x	y	z
1 (C)	0.0	27.6	104.8
2 (C)	0.0	-97.8	-2.0
3 (B)	118.9	0.0	0.0
4 (B)	-118.9	0.0	0.0
5 (B)	0.0	144.1	0.0
6 (H)	0.0	263.2	24.0
7 (H)	240.4	-0.2	1.9
8 (H)	-240.4	-0.2	1.9
9 (H)	0.0	25.6	213.3
10 (H)	0.0	-199.9	34.6
11 (H)	92.7	101.8	-84.4
12 (H)	92.7	101.8	-84.4

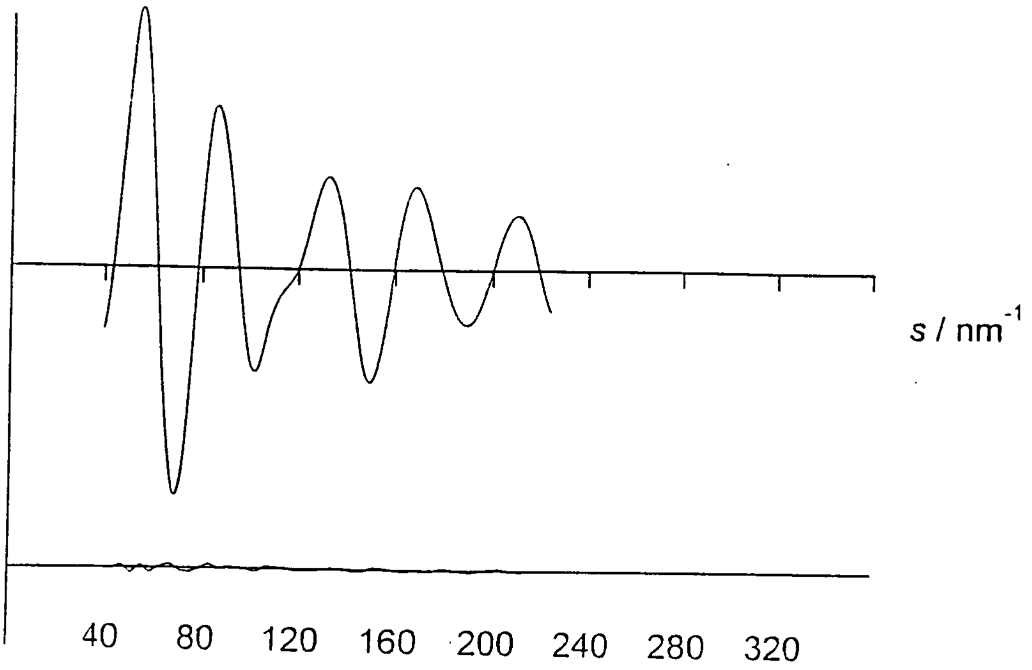

Figure 7.5 Experimental and final difference (experimental minus theoretical) molecular-scattering intensities for $B_3C_2H_7$ at a nozzle-to-plate distance of 200.89 mm.

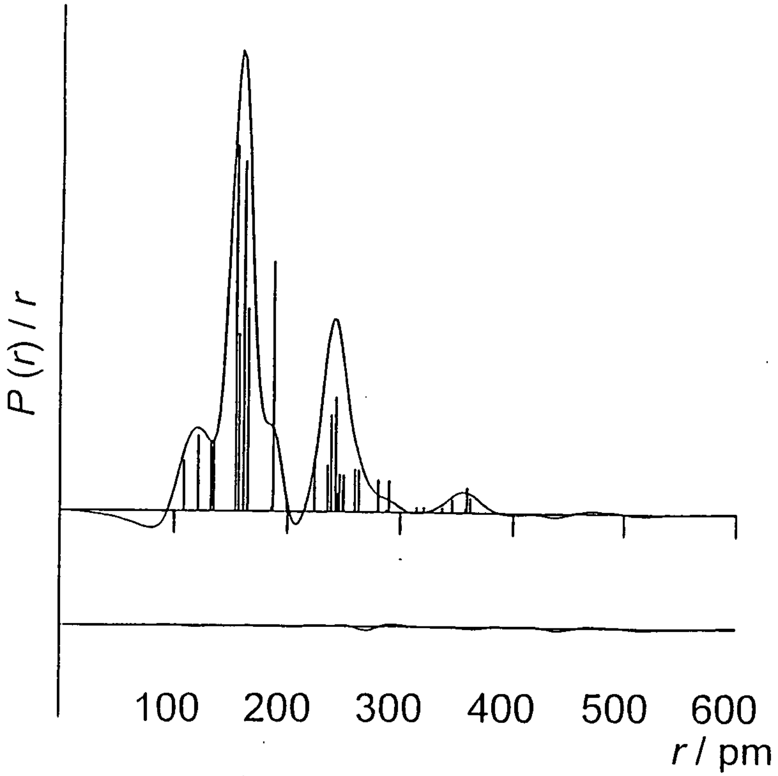

Figure 7.6 Experimental and difference (experimental minus theoretical) radial-distribution curves, P(r)/r, for $B_3C_2H_7$.

Bibliography

1 C.M. Huntley, G.S. Laurenson, and D.W.H. Rankin, J. Chem. Soc., Dalton Trans., (1980) 954

2 S. Cradock, J. Koprowski, and D.W.H. Rankin, J. Mol. Struct., 77 (1981) 113

3 A.S.F. Boyd, G.S. Laurenson, and D.W.H. Rankin, J. Mol. Struct., 71 (1981) 113

4 A.W. Ross, M. Fink and R. Hilderbrandt, in A.J.C. Wilson (Ed.), International Tables for Crystallography, Vol. C, Kluwer Academic, Dordrecht/Boston/London, 1992, p.245

5 D. Hnyk, R.S. Fender, H.E. Robertson, D.W.H. Rankin, M. Bühl, K. Hassler, and K. Schenzel, J. Mol. Struct., 346 (1995) 215

Chapter 8

Conclusion

The work carried out so far has been unsuccessful in producing any firm evidence of electron scattering and has yielded no results useful for structural studies. This has been due to the problems experienced with the new position-sensitive electron detector. The detector, in conjunction with the microchannel plates, was capable of single electron counting at count rates of up to 4 MHz at small scattering angles. The expected time resolution of the detector was around 1 ns as the time resolution was dependent only on the dead-time of the microchannel plates. This should have led to an increased signal-to-noise ratio allowing electron diffraction studies to be carried out at much lower target densities than are used in standard machines. Modulation of the detector could have allowed the evaluation of a true background scattering count rate and studies of ions, excited states and time-resolved phenomena. A simulation program has shown that bond lengths could have been determined with a precision of 0.0001 Å with this class of detector.

The over-riding problem with the anode device was that it did not seem robust enough for the conditions in our apparatus. Initially problems were experienced with static. The detector was then made more static resistant and further tests were undertaken. The next difficulty was that both the MCPs and anode plate were powered by a common power supply. This led to spiking when charge was drawn from the MCPs and the solution was to connect the anode and the MCPs to separate power supplies. Despite this some counting elements had suffered permanent static damage although the detector did appear to count briefly. A further attempt was made with separate supplies for the two elements of the detector. This too proved unsuccessful and work then ceased with the position-sensitive anode plate.

Over the course of 26 months the detector was sent back to I.S.L. in Manchester six times, each time a problem occurred. This led to considerable delays and the detector was used in the lab for a total period of only 2 or 3 months. Indeed the detector was kept in Manchester for 10 months during my final year and it was these delays as much as anything else that have led to the anode device being abandoned.

A 2-D CCD camera based system has recently been installed. In this set-up scattered electrons impinge upon a scintillator screen and the resulting fluorescence is collected by the CCD array. Preliminary results with this device have shown some evidence of electron scattering. However, as yet the scattering has not been firmly attributed to the molecular beam and may consist mainly of rest gas scattering. Work is continuing with the CCD. Although the anode device was capable of higher counting rates this detector has been effectively abandoned. The ultimate design for the anode device was to have 256 counting elements arranged on 8 microchips capable of count rates of up to 10 MHz.

Apart from the setbacks suffered with the anode detector the other elements of the apparatus appear to be working at or above expected capabilities. Measurements of the molecular beam using 5% CO_2 by volume in a He carrier have given estimated CO_2 target densities of around 10^{19} molecules m^{-3} at the scattering centre. Also, very little helium reaches the mass-spectrometer used to monitor beam intensity. This has been attributed to efficient scattering of the helium by the heavier carbon dioxide, the target molecule. This low helium pressure leads to a lower contribution to the background scattering than expected giving a reduced noise signal.

The telefocus electron gun produces a high energy electron beam which is stable over a period of several hours. The high voltage output of the power supply has an accuracy of 0.01%. A beam current of 1 μA at

29.96/97 keV has an observed FWHM of 0.94/95 mm. Deconvolution of this profile to remove the effects of the collector aperture give a FWHM of around 0.6 mm.

The width of the molecular beam at the scattering centre is around 1 mm. The finite widths of the two intersecting beams are small enough so as to make their effects negligible.

It appears that the only thing this apparatus lacks is a reliable detection system. Hopefully the CCD will provide some data on molecular scattering worthy of analysis. If so a comparison can be made with the accuracy of parameters currently obtained with the photographic plates in the existing electron diffraction apparatus.

Acknowledgements

There are many people who have supported me over the past four years. Firstly, I must thank my supervisors, Dr. Malcolm Fluendy and Prof. David Rankin for their guidance and encouragement. Parviz Ardebili and Richard Mawhorter instructed me in the operation of the apparatus and their advice proved invaluable. I would also like to thank Paul Brain and Drahomir Hnyk for their help with the structure refinements reported in this thesis. I am also grateful to Graeme Maitland who I worked with for 18 months. Many thanks must also go to the technical and electronics workshops in the Chemistry department, in particular Davy Paden. The help given by the Physics technical workshop was also greatly appreciated. Financial support for this work was provided by the SERC/EPSRC.

Finally I would like to thank all members of the laser group, past and present, and all my friends (you know who you are !) for cheering me up when I was down.

Appendix A

Electron Beam Deconvolution Program Listing

This appendix contains a listing of the electron beam deconvolution program **decoke** written by Dr. M.A.D. Fluendy. The program takes the raw electron beam profile, works out the position of the maximum and calculates the first moment of the distribution. It then normalises the maximum to 100. The raw data is deconvoluted using a radial function (RPT), and an angular function (ANGPT) which uses Legendre polynomials up to order five.

```
      program DECOKE
C     THIS PROGRAM DECONVOLUTES AN ELECTRON BEAM PROFILES USING
C     A CIRCULAR APERTURE COLLECTOR
      IMPLICIT DOUBLE PRECISION(A-H,O-Z)
      DIMENSION X(200),Y(200),Z(200),A(20),temp(200)
      COMMON X,Y,Z,A,XF,YF,XMAX,XMIN,YMAX,YMIN,AD
      DIMENSION IWORK(3000),WORK(3000),ZFVECC(200),ZF(200),ZD(200)
      DIMENSION XP(20),ZDC(200)
      EXTERNAL E04FDF
      EXTERNAL D01DAF
      EXTERNAL LSFUN1,PHI1,PHI2,FIT,APERTURE,CONVOLVE




C     READ IN DATA FILE
      OPEN (1,FILE=’ebeaminput’)
C     OUTPUT FILE
      OPEN (2,FILE=’ebeamoutput’)
      ZMAX=0.0
      XSUM=0.0D00
      YSUM=0.0D00
      ZSUM=0.0D00


      READ(1,*) RDIST
C     COLLISION DISTANCE IN MM
      print*,’RDIST= ’,RDIST
C     NOTE MUST EDIT DATA FILE TO HAVE RDIST AT TOP
C     AND END WITH 3 -VE NUMBERS XYZ AT BOTTOM OF FILE
      DO 100 J=1,200
      READ(1,*)X(J), Y(J),Z(J)
      IF(X(J).LT.-1) THEN
      JMAX=J-1
      GO TO 120
      ENDIF
      XSUM=Z(J)**4*X(J)+XSUM
      YSUM=Z(J)**4*Y(J)+YSUM
      ZSUM=Z(J)**4+ZSUM
      IF(Z(J).GT.ZMAX) THEN
      ZMAX=Z(J)
      XMID=X(J)
      YMID=Y(J)
      ENDIF
 100  CONTINUE
 120  CONTINUE
      XMEAN=XSUM/ZSUM
      YMEAN=YSUM/ZSUM
C      print*,’xmid/ymid/zmax=’,xmid,ymid,zmax
C     NORMALISE ZMAX TO 100 AND X,Y TO MAX POINT
      DO 200 J=1,JMAX
      Z(J)=1.0*Z(J)/ZMAX
      X(J)=X(J)-XMEAN
      Y(J)=Y(J)-YMEAN
```

```
 200    CONTINUE
        PRINT*,'BEAM CENTRE XMEAN/XPK=',XMEAN,XMID,'YS=',YMEAN,YMID
        DO 220 J=1,JMAX
        IF(X(J).GT.XMAX) THEN
        XMAX=X(J)
        ENDIF
        IF(Y(J).GT.YMAX) THEN
        YMAX=Y(J)
        ENDIF
        IF(X(J).LT.XMIN) THEN
        XMIN=X(J)
        ENDIF
        IF(Y(J).LT.YMIN) THEN
        YMIN=Y(J)
        ENDIF
 220    CONTINUE
        PRINT*,'READ IN OF DATA FINISHED,POINT= ',JMAX,ZMAX,XMAX,XMIN,
     1  YMAX,YMIN



C       USES FITTING TECHNIQUE TO FIT A DECON RESULT AFTER
C       CONVOLUTING WITH FILTER TO DATA
C       SET UP FITTING ROUTINE
        INPTS=JMAX
        PRINT*,'NUMBER OF PARMS(8 MAX)='
        READ*,NFITS
        IFAIL=1
C       PEAK IS APPROX CENTERED
        DO 250 I=1,NFITS
        XP(I)=0.0
        PRINT*,'INPUT STARTING VALUES FOR',NFITS,' PARMS'
        PRINT*,'        X3=X1;    Y3=Y1'
        PRINT*,' R1=X3**2+Y3**2; R2=R2**2;R0=SQRT(R1)'
        PRINT*,' THETA=ATAN(Y3/X3)'
        PRINT*,' RPT=A(1)*EXP(-A(2)*R1-A(3)*R2-A(6)*R0-A(7)*R0*R1)'
        PRINT*,' P0 + A(4)*P1 + A(5)*P2 + A(8)*P4'
        PRINT*,' FIT=RPT*ANGPT'
        PRINT*,' I = ',I,'  PARM = '
        READ*,XP(I)
 250    CONTINUE



        PRINT*,'DIAMETER OF APERTURE(MM)= '
        READ*,AD
        FSUMSQ=0.0
C       RADIUS SQUARED OF APERTURE USED IN APERTURE FN
        AD=(AD/2)**2
c        print*,'before eo4fdf'
        CALL E04FDF(INPTS,NFITS,XP,FSUMSQ,IWORK,3000,WORK,3000,IFAIL)
```

```
      IF (IFAIL.GT.0) THEN
      PRINT*,'ERROR IN FITTING ROUTINE,IFAIL=',IFAIL
      ENDIF
      PRINT*,'FINISHED FITTING,SUM SQS=',FSUMSQ
 777  WRITE(2,*) 'FITTED PARAMETERS'
      DO 20 I=1,NFITS
      XP(I)=A(I)
      WRITE(2,1000) I,XP(I)
 1000 FORMAT (I5,3X,E12.6)
 20   CONTINUE
      WRITE(2,*) 'DIAMETER OF APERTURE=', 2.0*SQRT(AD)
      WRITE(2,*) 'FIT OF DATA TO CONVOLUTED FUNCTION '
      WRITE(2,*) 'X,Y,ZDATA,ZFITTED,ZDIFF,ZDECON'



      CALL  LSFUN1(INPTS,NFITS,XP,ZFVECC)
      ZDMAX=0.0
      ZDCMAX=0.0
      DO 500 J=1,INPTS
C     ZF IS FITTED TO DATA
      ZF(J)=ZFVECC(J)+Z(J)
C     ZD IS DECONVOLUTED RESULT
      ZD(J)=FIT(X(J),Y(J))
      ZDC(J)=FITC(X(J),Y(J))
      IF(ZD(J).GT.ZDMAX) THEN
      ZDMAX=ZD(J)
      ENDIF
      IF(ZDC(J).GT.ZDCMAX) THEN
      ZDCMAX=ZDC(J)
      ENDIF
 1001 FORMAT(7F11.3)
 500  CONTINUE



C     NORMAISE TO PEAK OF 100.0 FOR DECON PROFILE
      RDN=1000./RDIST
      DO 510 J=1,INPTS
      ZD(J)=100.0*ZD(J)/ZDMAX
      ZDC(J)=100.0*ZDC(J)/ZDCMAX
      Z(J)=100.0*Z(J)
      ZF(J)=100.0*ZF(J)
      ZDIF=(ZF(J)-Z(J))
C     POSITION IN MRAD DIFF IS ABSOLUTE VALUE WITH PEAK AT 100
      WRITE(2,1001)  RDN*X(J),RDN*Y(J),Z(J),ZF(J),ZDIF,ZD(J),ZDC(J)
 510  CONTINUE
      END
```

```
      FUNCTION CONVOLVE(X1,Y1)
C     FUNCTION TO CONVOLUTE FITTING FORM WITH APERTURE FUNCTION
C     CONVOLVES TO YIELD VALUE AT POINT X,Y IN ARRAY MAX SIZE IMAX
      IMPLICIT DOUBLE PRECISION(A-H,O-Z)
      COMMON X(200),Y(200),Z(200),A(20),XF,YF,XMAX,XMIN,YMAX,YMIN,AD
      EXTERNAL FIT,APERTURE
      X2=X1-XF
      Y2=Y1-YF
      TEMP=FIT(X1,Y1)*APERTURE(X2,Y2)
C      print*,'FIT/APERTURE= ',FIT(X1,Y1),APERTURE(X2,Y2)
C      print*,'leaving convolve,convolve= ',temp
      CONVOLVE=TEMP
      END




      FUNCTION FIT(X1,Y1)
C     FUNCTION TO BE FITTED TO DECONVOLUTED SIGNAL
      IMPLICIT DOUBLE PRECISION(A-H,O-Z)
      COMMON X(200),Y(200),Z(200),A(20),XF,YF,XMAX,XMIN,YMAX,YMIN,AD
      X3=X1
      Y3=Y1
       R1=X3**2+Y3**2
       R2=R1**2
       if(x3.lt.1.0d-30) then
       x3=1.0d-20
       endif
       THETA=ATAN(Y3/X3)
       THETA=THETA+(A(4)+.376)
       XR=COS(THETA)
       PO = 1.0
       P1 = XR
       P2 = 0.5*(3.0*XR**2-1.0)
       P3 = 0.5*(5.0*XR**3-3.0*XR)
       P4 = 0.125*(35.0*XR**4-30.0*XR**2+3.0)
       P5 = 0.125*(63.0*XR**5-70.0*XR**3
     1 +15.0*XR)
       P6 = XR*1.857143*P5-0.857143*P4

c     ARG=(-6.6+A(2))*R1+(1.63-A(3))*R2
        ARG=(-6.6*R1)+1.63*R2

      IF (ARG.GT.70) THEN
      ARG=70
      ENDIF
      IF(ARG.LT.-70) THEN
      ARG=-70
      ENDIF
      RPT=EXP(ARG)

      ANGPT = A(1)**2 + (A(5)+3.666)*P1 + (A(6)-5.236)*P2
```

```
     1  + (A(7)+9.6939)*P3
C         ANGPT=ANGPT+(A(2)-9.579)*P4+(A(3)+6.619)*P5
C         ANGPT=A(1)**2+3.672*P1+4.528*P2+.4256*P3-2.914*P4+3.617*P5
C         ANGPT=ANGPT-0.273*P6
         FIT=RPT*ANGPT
C       FITTING FORM
C        print*,'leaving fit/rpt/angpt,fit=',FIT,rpt,angpt
        END




        FUNCTION FITC(X1,Y1)
C       FUNCTION TO BE FITTED TO DECONVOLUTED SIGNAL FORCING SYMMETRY
        IMPLICIT DOUBLE PRECISION(A-H,O-Z)
        COMMON X(200),Y(200),Z(200),A(20),XF,YF,XMAX,XMIN,YMAX,YMIN,AD
        X3=X1
        Y3=Y1
         R1=X3**2+Y3**2
         R2=R1**2
         if(x3.lt.1.0d-30) then
         x3=1.0d-20
         endif
         ARG=(-6.6+A(2))*R1+(1.63-A(3))*R2
         IF (ARG.GT.70) THEN
         ARG=70
         ENDIF
         IF(ARG.LT.-70) THEN
         ARG=-70
         ENDIF
         RPT=EXP(ARG)
         FITC=RPT
C       FITTING FORM
C        print*,'leaving fit/rpt/angpt,fit=',FIT,rpt,angpt
        END




        FUNCTION APERTURE(XA,YA)
C       RETURNS APERTURE FN 0 OR 1
C       APERTURE IS CIRCULAR WITH DIA 0.087MM
C       FN IS =1 IF XA**2+YA**2<0.087**2
        IMPLICIT DOUBLE PRECISION(A-H,O-Z)
        COMMON X(200),Y(200),Z(200),A(20),XF,YF,XMAX,XMIN,YMAX,YMIN,AD
        R=XA**2+YA**2
        IF(R.LE.AD) THEN
        APX=1.0
        ELSE
        APX=0.0
        END IF
        APERTURE=APX
```

```
C        print*,'leaving aperture,aperture= ',APX
         END




         SUBROUTINE LSFUN1(M,N,XC,FVECC)
C        COMPUTES DIFF BETWEEN DATA AT X,Y SEQ NO J
C        AND CONVOLUTION OF APERTURE FN WITH FITTING FORM
         IMPLICIT DOUBLE PRECISION(A-H,O-Z)
         COMMON X(200),Y(200),Z(200),A(20),XF,YF,XMAX,XMIN,YMAX,YMIN,AD
         DIMENSION FVECC(M),XC(N)
         EXTERNAL PHI1,PHI2,CONVOLVE
C        PUT XC (THE PARMS) INTO COMMON
         SUMS=0.0
         DO 10 J=1,N
         A(J)=XC(J)
 10      CONTINUE
         DO 100 I=1,M
C        X AND Y AT POINT I PUT INTO COMMON
         XF=X(I)
         YF=Y(I)
         ADR=SQRT(AD)
         YMI=YF-ADR
         YMA=YF+ADR
         ABSACC=1.0D-01
         IFAIL=1
         CALL D01DAF(YMI,YMA,PHI1,PHI2,CONVOLVE,ABSACC,ANS,NEVS,IFAIL)
C         PRINT*,'NUMBER OF FUN EVALUATIONS/ans/z= ',NEVS,ANS,z(i)
         IF (IFAIL.GT.0) THEN
         PRINT*,'FAIL IN CONVOLUTION,IFAIL=',IFAIL
         ENDIF
         FVECC(I)=ANS-Z(I)
         SUMS=SUMS+FVECC(I)**2
 100     CONTINUE
         PRINT*,'STEP WITH PARMS AS:'
         DO 11 J=1,N
         PRINT*,XC(J)
 11      CONTINUE
         PRINT*,'SUM OF SQD= ',SUMS
         END




         FUNCTION PHI1(Y1)
         IMPLICIT DOUBLE PRECISION(A-H,O-Z)
         COMMON X(200),Y(200),Z(200),A(20),XF,YF,XMAX,XMIN,YMAX,YMIN,AD
         PHI1=XF-SQRT(AD)
         END
```

```
FUNCTION PHI2(Y1)
IMPLICIT DOUBLE PRECISION(A-H,O-Z)
COMMON X(200),Y(200),Z(200),A(20),XF,YF,XMAX,XMIN,YMAX,YMIN,AD
PHI2=XF+SQRT(AD)
END
```

Appendix B

Publication

D. Hnyk, R.S. Fender, H.E. Robertson, D.W.H. Rankin, M. Bühl, K. Hassler, and K. Schenzel, J. Mol. Struct., 346 (1995) 215

Reprinted from

Journal of
MOLECULAR
STRUCTURE

Journal of Molecular Structure 346 (1995) 215–229

An electron diffraction, ab initio and vibrational spectroscopic study of 1,2-di-*tert*-butyldisilane☆

Drahomír Hnyk[a,1], Robert S. Fender[a], Heather E. Robertson[a], David W.H. Rankin[a,*],
Michael Bühl[b], Karl Hassler[c], Karla Schenzel[d]

[a]*Department of Chemistry, University of Edinburgh, West Mains Road, Edinburgh, EH9 3JJ, UK*
[b]*Institut für Organische Chemie, Universität Zürich, Winterthurerstrasse 190, CH-8057 Zürich, Switzerland*
[c]*Institut für Anorganische Chemie, Technische Universität Graz, Stremayrgasse 16, A-8010 Graz, Austria*
[d]*Institut für Analytische Chemie, Martin-Luther-Universität, Weinbergweg 16, D-06120 Halle, Germany*

ELSEVIER

ELSEVIER

Journal of Molecular Structure 346 (1995) 215–229

Journal of
MOLECULAR
STRUCTURE

An electron diffraction, ab initio and vibrational spectroscopic study of 1,2-di-*tert*-butyldisilane☆

Drahomír Hnyk[a,1], Robert S. Fender[a], Heather E. Robertson[a], David W.H. Rankin[a,*], Michael Bühl[b], Karl Hassler[c], Karla Schenzel[d]

[a] *Department of Chemistry, University of Edinburgh, West Mains Road, Edinburgh, EH9 3JJ, UK*
[b] *Institut für Organische Chemie, Universität Zürich, Winterthurerstrasse 190, CH-8057 Zürich, Switzerland*
[c] *Institut für Anorganische Chemie, Technische Universität Graz, Stremayrgasse 16, A-8010 Graz, Austria*
[d] *Institut für Analytische Chemie, Martin-Luther-Universität, Weinbergweg 16, D-06120 Halle, Germany*

Received 12 September 1994

Abstract

The molecular structure of 1,2-di-*tert*-butyldisilane has been accurately determined by gas-phase electron diffraction (GED) and ab initio calculations. These techniques show that the large majority of molecules at room temperature have the anti conformation with overall symmetry C_2, and vibrational spectra confirm this conclusion. Infrared spectra of the gas and liquid phases, and Raman spectra of the liquid and solid phases, have been recorded for $(CH_3)_3CSiH_2SiH_2C(CH_3)_3$ and $(CH_3)_3CSiD_2SiD_2C(CH_3)_3$.

The most striking feature of this structure (r_a) is a relatively large deviation of the SiSiC angle from the parent tetrahedral angle 109.5° (113.7(3)°, GED; 114.4°, SCF/6-31G* as calculated for the anti form). That the Si–Si bond length does not show any substantial deviation from its usual value (234.8(3) pm, GED; 236.8 pm, SCF/6-31G* computed for the anti form) is also substantiated by the value of the SiSi valence force constant (169 N m^{-1}) given by normal coordinate analysis. The *t*-butyl groups are tilted so that the Si–C bonds (GED (SCF/6-31G*): 190.1(1) (191.9) pm) do not coincide with the local C_3 axes of the $C(CH_3)_3$ groups in which the C–C bond length is 154.1(1) (GED); 154.0 (SCF/6-31G*) pm. The conformations along all the single bonds are more or less staggered.

1. Introduction

The structures of several disilanes of the general formula Si_2X_6 (X = H, F, Cl, CH_3) have been mentioned in Ref. [1]. In addition to these simple examples, the molecular structures of more complex systems have been recently elucidated. Thus, 1,1,2,2-tetrabromodisilane [2], 1,2-diododisilane [3] and 1,1,2,2-tetraiododisilane [3] have been structurally characterised using gas-phase electron diffraction (GED) data. Although the vibrational spectra of 1,2-dimethyldisilane have been reported [4], no accurate experimental structural data for alkyl-substituted disilanes containing less than six alkyl groups have been reported so far.

In this paper we report the determination of the molecular structure and conformational properties

---

☆ Dedicated to Professor Kenneth Hedberg on the occasion of his 75th birthday.

* Corresponding author.

[1] On leave from the Institute of Inorganic Chemistry of the Academy of Sciences of the Czech Republic, 250 68 Řež near Prague, Czech Republic.

SSDI 0022-2860(94)09019-X

Table 1
Nozzle-to-plate distances, weighting functions, correlation parameters, scale factors, and electron wavelengths

Nozzle-to-plate distance (mm)	Δs (nm^{-1})	$s_{\min}$ (nm^{-1})	sw_1 (nm^{-1})	sw_2 (nm^{-1})	$s_{\max}$ (nm^{-1})	Correlation parameter p/h	Scale factor k[a]	Electron wavelength[b] (pm)
259.47	2	30	50	140	164	0.1096	0.713(7)	5.686
93.50	4	88	108	384	336	−0.0907	0.577(9)	5.689

[a] Figures in parentheses are the estimated standard deviations of the last digits.

[b] Determined by reference to the scattering pattern of benzene vapour.

of 1,2-di-*tert*-butyl-disilane, the first 1,2-dialkyldisilane to be investigated in the gas phase, by the concerted use of GED, ab initio calculations and vibrational spectroscopy.

2. Experimental

2.1. Synthesis and characterisation

A sample of $(CH_3)_3CSiI_2SiI_2C(CH_3)_3$ (5.5 g, 11.5 mmol) [5] was dissolved in 50 ml of dry di-ethyl ether, and a solution of 0.87 g (23 mmol) of $LiAlH_4$ in 20 ml of Et_2O was added dropwise at 0°C. After refluxing for two hours, the reaction mixture was slowly hydrolysed with 2N aqueous H_2SO_4. The organic layer was separated and dried over Na_2SO_4 and the solvent was removed on a Rotavapor. The remaining oil was purified by fractionation, giving 1.7 g (85%) of $(CH_3)_3CSiH_2SiH_2C(CH_3)_3$ as a colourless liquid (b.p. 90°C/75 Torr). $(CH_3)_3CSiD_2SiD_2C(CH_3)_3$ was prepared by the same method. $C_8H_{22}Si_2$ (174.44), anal. (calc./exp.): C, 55.08/54.84%; H, 12.71/12.75%. ^{29}Si NMR: −45.2 ppm (TMS), ^1J(SiH) = 179.4, ^2J(SiSiH) = 6.7, ^3J(SiCCH) = 7.0 Hz.

2.2. Infrared and Raman spectra

Infrared spectra were measured with a Perkin Elmer 883 spectrometer as films between CsBr disks, and Raman spectra with a Bruker IFS 66 spectrometer (Nd: YAG Laser, 300 mW) in sealed 1 mm capillary glass tubes.

2.3. GED measurements

The electron scattering intensities for a sample of $(CH_3)_3CSiH_2SiH_2C(CH_3)_3$ were recorded on Kodak Electron Image photographic plates using Edinburgh gas diffraction apparatus [6] operating at approximately 44.5 kV. The sample and nozzle were kept at 333 and 382 K respectively during the experiments. The electron wavelength and nozzle-to-plate distances were calibrated using scattering data for benzene as reference. Data from two plates for each distance were obtained in digital form using a computer-controlled Joyce–Loebl Microdensitometer 6 at the S.E.R.C. Daresbury Laboratory [7]. In the subsequent analysis of the data, established data-reduction [7] and least-squares refinement programs [8], and complex scattering factors were employed [9]. The weighting points used in setting up the off-diagonal weight matrix, s ranges, scale factors, correlation parameters, and electron wavelengths are all presented in Table 1.

3. Ab initio calculations of geometries, energy and frequencies

The geometries of *anti*- and *gauche*-$(CH_3)_3CSiH_2SiH_2C(CH_3)_3$ have been fully optimised at the SCF level employing standard methods, 3-21G(*) and 6-31G* basis sets [10], and the TURBOMOLE program [11]. The SCF/6-31G* geometrical parameters are reported in Table 2. Single-point energy calculations at the MP2(fc)/6-31G* level have been performed for the 6-31G* geometries (notation MP2/6-31G*//SCF/6-31G*).

Table 2
Ab initio optimised geometry of $(CH_3)_3CSiH_2SiH_2C(CH_3)_3$ at the 6-31G* level

(a) Bond lengths (pm)

	Si-Si	Si–C	C–C	C–H	Si–H
anti	236.8	191.9	154.0[a]	108.7[a]	148.4[a]
gauche	237.0	192.1	153.9[a]	108.7[a]	148.5[a]
anti (GED)	*234.8*	*190.1*	*154.1*	*112.0*	*149.8*

(b) Bond angles (deg)

	SiSiC		SiCC		CCH	SiSiH		HSiH
anti	114.4	110.4	108.6	110.4	111.4[a]	109.3	108.9	106.8
gauche	120.1	110.8	108.0	111.0	111.5[a]	109.1	103.9	106.8
anti (GED)	*113.7*	*111.1*	*107.7*	*110.5*	*110.0*[b]	*107.1*		*109.0*[b]

(c) Dihedral angles (deg)[c]

	CSiSiC		SiSiCC	
anti	176.8	59.4	178.8	−61.8
gauche	69.0	44.5	163.7	−77.4
anti (GED)	*195.5*	*50.5*	*170.0*	*−70.9*

[a] Only the mean value is listed.

[b] Fixed.

[c] There are nine (3 × 3) different dihedral SiCCH angles; the electron diffraction (6-31G*) mean values for the anti form are 36.9 (60.3), 156.9 (178.5), −83.2 (−60.6).

Analytical harmonic frequencies have been computed at the SCF/6-31G* level, for both the parent and deuterated species (Tables 3 and 4). MP2 and frequency calculations employed the GAUSSIAN92 program [12].

4. Molecular model and structure determination from GED data

For the purpose of the least-squares refinements it was assumed that the CH_3 groups had local C_{3v} symmetry and that the $C(CH_3)_3$ groups had local C_3 symmetry. The molecular geometry of the $(CH_3)_3CSiH_2SiH_2C(CH_3)_3$ molecule (**1**, Fig. 1), for which an overall symmetry of C_2 was adopted, was then defined by the five bond lengths (*r*(Si–Si), *r*(Si–C), *r*(C–C), *r*(C–H), *r*(Si–H)), the five angles (SiSiC, CCC, CCH, SiSiH, HSiH) and three twist angles. The first of these, around the Si(1)–Si(2) bond, had positive values for a clockwise rotation from the eclipsed C(21)–Si(2)–Si(1)–C(11) form (0° and 180° for the mutual syn and anti arrangements of the Si–C bonds, respectively). Twists of the CH_3 and $C(CH_3)_3$ groups were also considered, and were taken to be positive for clockwise rotations from the eclipsed (syn) H–C(111)–C(11)–Si(1) and C(111)–C(11)–Si(1)–Si(2) positions, respectively. Finally, the local C_3 axes of the $C(CH_3)$ groups were also allowed to deviate from the lines of the Si–C bonds, a positive tilt representing a movement of the CH_3 groups away from the other silicon. The molecular geometry thus depended on 14 molecular parameters, as listed in Table 5.

At first, simultaneous refinement of the geometrical and vibrational parameters associated with the heavy-atom skeleton, together with some relating to hydrogen atom positions, led to a false minimum characterised by an unrealistically wide SiSiC bond angle of about 127°. Including the tilt angle in the refinement did not reduce the value of the SiSiC

Table 3
Observed and calculated frequencies (ν_i) (cm^{-1}) and potential energy distributions (PED) (> 15%) of the normal modes of species A_g for $(CH_3)_3CSiH_2SiH_2C(CH_3)_3$ and $(CH_3)_3CSiD_2SiD_2C(CH_3)_3$

i	$(CH_3)_3CSiH_2SiH_2C(CH_3)_3$				$(CH_3)_3CSiD_2SiD_2C(CH_3)_3$			
	Exp.	Ab initio[a]	NCA[b]	PED[c]	Exp.	Ab initio[a]	NCA[b]	PED[c]
1	2123	2144	2126	100(1)	1542	1540	1540	100(1)
2	2115	2131	2111	100(2)	1531	1536	1514	100(2)
3	1186	1220	1200	48(3), 24(7)	1187	1223	1200	48(3), 23(7)
4	1014	1040	1011	50(4), 29(5)	1013	1041	1011	50(4), 29(5)
5	945	951	930	29(5), 41(9), 20(6)	945	945	929	30(5), 42(9), 20(8)
6	1014	1044	1001	50(6), 26(8)	1013	1041	1001	50(6), 26(8)
7	1014	1043	1022	64(7), 33(3)	1013	1042	1022	64(7), 33(3)
8	928	943	918	37(8), 44(10)	937	943	918	37(8), 44(10)
9	1200	1226	1242	50(9), 25(5)	1200	1225	1246	50(9), 25(5)
10	1200	1224	1215	46(10), 23(8)	1200	1224	1214	47(10), 23(8)
11	824	818	821	59(11), 27(15)	825	820	820	64(11), 27(15)
12	945	945	946	97(12)	680	699	691	82(12)
13	728	746	733	68(13), 18(11)	569	558	534	30(13), 15(15), 18(17)
14	695	697	688	98(14)	529	537	492	97(14)
15	596	581	595	46(15), 16(9), 17(13)	661	670	659	30(15), 18(11), 22(14), 15(17)
16	431	395	435	59(16), 15(21)	360	355	351	31(16), 32(18), 19(21)
17	479	461	480	55(17), 20(23)	436	433	434	22(17), 25(23), 20(13)
18	383	363	376	31(18), 23(19), 16(20)	387	380	408	45(18), 17(16)
19	383	384	385	41(19), 16(20)	387	381	372	50(19)
20	349	341	352	31(20), 49(19)	343	336	340	40(20), 26(19)
21	277	278	275	73(21), 18(16)	264	278	243	52(21), 43(16)
22	220	212	219	67(22), 17(17)	215	212	218	67(22), 17(17)
23	134	199	132	58(23)	122	118	131	58(23)

[a] Scaled by 0.92, anti form.
[b] From normal coordinate analysis.
[c] Potential energy distributions in %.

angle at all, as the refined tilt values were very close to zero. In addition to this pronounced deviation from the regular tetrahedral arrangement at silicon, the amplitude of vibration of the Si–Si bond was unrealistically large (≈ 10 pm) when compared with, for example, the calculated and experimental values of 5.5 and 6.8 pm, respectively, for 1,2-diiododisilane [3]. Moreover, the refined SiSiH bond angle values were smaller than 100°. This model, for which the *R* factor, R_G, was 0.044, was therefore rejected.

Many refinements, still in C_2 symmetry, were then carried out with the SiSiC angle and Si–Si distance kept fixed at 115° and 234 pm respectively, i.e. close to the ab initio calculated values (Table 2). The number of refined parameters was gradually increased, until eventually the SiSiC angle, the Si–Si bond length and the Si–Si vibrational amplitude were included in the refinement scheme. This procedure led to a much more reasonable structure, in which the SiSiC angle was 113.7° (Table 5). The R_G factor arrived at under these refinement conditions (0.044) was identical to that obtained with the structure having an extremely wide SiSiC angle. Further refinements, starting with SiSiC angles in the range 109–127°, always led to one of the two structures already described, and angles between 113.7 and 127° never fitted the data satisfactorily.

The tilt of the *t*-butyl groups was easily refined to give a tilt of 2.1(5)° away from the other silicon atom. Refinement without the tilt gave rise to an R_G value of 0.052, but with only marginal changes in the molecular geometry. The CCH and HSiH angles could not be determined, and both of them increased to implausibly large values. They had to

Table 4
Observed and calculated frequencies (ν_i) (cm^{-1}) and potential energy distributions (PED) (> 15%) of the normal modes of species A_u for $(CH_3)_3CSiH_2SiH_2C(CH_3)_3$ and $(CH_3)_3CSiD_2SiD_2C(CH_3)_3$

i	$(CH_3)_3CSiH_2SiH_2C(CH_3)_3$				$(CH_3)_3CSiD_2SiD_2C(CH_3)_3$			
	Exp.	Ab initio[a]	NCA[b]	PED[c]	Exp.	Ab initio[a]	NCA[b]	PED[c]
24	2130	2140	2129	100(24)	1547	1547	1541	100(24)
25	2112	2136	2110	100(25)	1527	1531	1511	100(25)
26	1011	1043	1013	35(26), 35(28), 22(30)	1009	1038	1013	35(26), 36(28), 22(30)
27	1011	1044	1014	62(27), 32(29)	1009	1041	1014	62(27), 32(29)
28	940	940	927	29(28), 39(32)	939	945	928	30(28), 43(32)
29	1188	1220	1196	48(29), 24(27)	1185	1221	1185	49(29), 24(27)
30	1011	1040	1006	37(30), 33(31), 22(26)	1009	1041	1006	37(30), 33(31), 23(26)
31	940	939	918	37(31), 39(33)	939	942	917	37(31), 42(33)
32	1200	1241	1236	47(32), 26(28)	1199	1241	1236	48(32), 26(28)
33	1200	1225	1228	49(33), 23(31)	1199	1225	1227	49(33), 24(31)
34	824	818	820	72(34)	823	818	820	73(34), 18(38)
35	940	951	949	89(35)	670	688	690	90(35)
36	726	758	728	90(36)	546	552	519	71(36)
37	690	697	691	97(37)	496	527	499	93(36)
38	590	576	590	56(38), 19(32), 15(34)	597	592	613	44(38), 20(36)
39	428	395	430	70(39)	336	334	327	49(39), 19(41), 23(44)
40	398	384	399	72(40)	375	372	399	71(40)
41	368	374	376	69(41)	375	366	391	64(41)
42	342	355	341	70(42)	336	334	333	62(42), 16(38)
43	308	339	301	70(43)	290	291	295	65(43)
44	277	279	275	78(44)	264	247	247	52(44), 40(39)
45	85	68	80	86(45)	80	67	79	87(45)

[a] Scaled by 0.92, anti form.
[b] From normal coordinate analysis.
[c] Potential energy distributions in %.

be fixed in subsequent refinements. The three dihedral angles were easily refined.

As 1,2-diiododisilane [3], 1,1,2,2-tetrabromodisilane [2], and 1,1,2,2-tetraiododisilane [3], were found to be mixtures of the anti and gauche forms, we also tried a series of refinements which allowed for the presence of a mixture of gauche and anti conformers of the present molecule. The lowest R factor was obtained with a dihedral angle of 50° for the gauche form, which accounted for 11% of the molecules present. The 75% confidence limits [13] for the percentage composition (corresponding approximately to one standard deviation) were +4 and −6%, and the 97.5% confidence limits spanned the composition range 0 to 18%. When the gauche dihedral angle was fixed at 60°, the R factor minimum corresponded to only 6% abundance, with the 75% confidence limit covering the whole range up to 18%; however, even the R factor minimum was significantly higher, at the 90% level, for the refinement with a dihedral angle of 50°. When the dihedral angle was set at 69°, as calculated ab initio at the 6-31G* level, the minimum R factor corresponded to 100% anti conformer. It is clearly not possible to determine from the GED data how much of the gauche conformer is present, although it is clear that the amount is small, and certainly less than 20%. Consequently, it has little effect on the other parameters, and the results in Tables 2–4 are for 100% anti conformer.

Apart from the C_2 model, a model with an overall symmetry of C_i was also examined. The resulting refinements similarly led to two minima that also differed in the magnitudes of the SiSiC angle (113.7° and 126°) and were characterised by almost identical R factor values (0.051 and 0.052 for R_G, respectively). As the fits were much poorer than

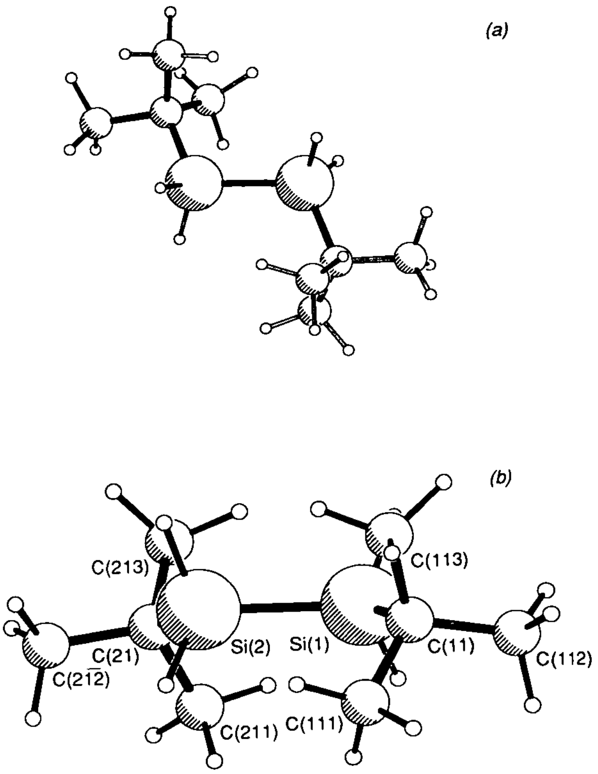

Fig. 1. The $(CH_3)_3CSiH_2SiH_2C(CH_3)_3$ molecule in the optimum refinement of the electron diffraction data, also showing the atomic numbering of the $C_3CSiH_2SiH_2CC_3$ skeleton: (a) a perspective view; (b) a view showing the molecular C_2 symmetry.

those obtained with the C_2 structure, this model was not considered to be a satisfactory representation of the experimental geometry. Nevertheless, the C_1 parameters were used in the subsequent normal coordinate analysis for the reasons given below.

The final parameters (C_2), for which R_G was 0.044 ($R_D = 0.041$), are given in Table 5. The parameters for the C_i model are also shown in this table for comparison. Interatomic distances and the corresponding amplitudes of vibration are listed in Table 6, whilst the least-squares correlation matrix is shown in Table 7. Table 8 provides the atomic coordinates, from which interatomic distances, bond angles, and dihedral angles of interest may be computed. Figs. 2 and 3 show the molecular scattering intensity curves and the radial distribution curve, respectively.

Table 5
Geometrical parameters for $(CH_3)_3CSiH_2SiH_2C(CH_3)_3$ (distances in pm, angles in deg)[a]

		Molecular symmetry	
		C_2	C_i
p_1	r(Si–Si)	234.8(3)	234.8(3)
p_2	r(Si–C)	190.1(1)	190.1(1)
p_3	r(C–C)	154.1(1)	154.1(1)
p_4	r(C–H)	112.0(1)	112.0(1)
p_5	r(Si–H)	149.8(8)	149.7(8)
p_6	∠SiSiC	113.7(3)	113.7(4)
p_7	∠CCC	109.2(1)	109.1(1)
p_8	∠CCH	110.0[b]	110.0[b]
p_9	∠SiSiH	107.1(15)	108.1(13)
p_{10}	∠HSiH	109.0[b]	109.0[b]
p_{11}	∠(CH_3 twist)	36.8(25)	37.9(22)
p_{12}	∠(Me_3C twist)	49.8(4)	49.3(5)
p_{13}	∠(Si–Si twist)	195.5(12)	180.0[b,c]
p_{14}	∠(C_3C–Si tilt)	2.1(5)	2.1(6)
R_G		0.044	0.051

[a] Figures in parentheses are the estimated standard deviations of the last digits.
[b] Fixed in the final refinement.
[c] Attempts to refine this parameter led to 187(5)° in a rather unstable minimum.

5. Vibrational spectra and their assignment

Table 9 summarises the infrared and Raman vibrational spectra of liquid $(CH_3)_3CSiH_2SiH_2C(CH_3)_3$ and $(CH_3)_3CSiD_2SiD_2C(CH_3)_3$, as well as the Raman spectra of the solids recorded at 140 K. Gas-phase IR spectra were also measured, but are not included in Table 9.

90 vibrations of 1 (32 atoms) are divided into 41 A_g and 40 A_u species for the point group C_i (twist angle around the Si(1)–Si(2) bond 180°), obeying the rule of mutual exclusion. The point group C_2 (Si(1)–Si(2) twist: 195.5(12), GED; 176.8° 6-31G*) allows all 90 modes to become infrared and Raman active. The selection rules of C_2 also hold for the gauche rotamer.

The number of internal vibrations of a $C(CH_3)_3$ group is calculated as $6A_1 + 5A_2 + 12E$ if local C_{3v} symmetry is assumed (this reduces to $11A + 12E$ for C_3 symmetry). Lowering the symmetry of the molecule removes the twofold degeneracy of the E vibrations and allows the A_2 vibrations to become

Table 6
Interatomic distances (r_a in pm)[a] and mean amplitudes of vibration (u in pm) for $(CH_3)_3CSiH_2SiH_2C(CH_3)_3$

Atomic pair		r_a[b]	u[b]	
Si–Si		234.8(3)	u_1	6.8(4)
Si–C		190.1(1)	u_2	5.1(2)
C–C		154.1(1)	u_3	5.4(1)
Si–H		149.7(8)		8.0[c]
C–H		112.0(1)	u_4	6.8(2)
Si(1)···C(11N)[d]		279–285	u_5	9.3(3)
Si1)···C(21)		356.6(5)	u_6	9.6(8)
Si(1)···C(211)		378.4(14)		11.3[e]
Si(1)···C(212)		489.7(6)	u_7	12.3(6)
Si(1)···C(213)		401.6(11)	u_8	15.1 (10)
Si(1)···H(1)	–C(11N)[d]	275–284		11.0[c]
Si(1)···H(2)		320–328		16.0[c]
Si(1)···H(3)		376–381		18.0[c]
Si(1)···H(1)	–C(211)	362.6(29)		14.0[c]
Si(1)···H(2)		490.3(15)		20.0[c]
Si(1)···H(3)		353.4(55)		14.0[c]
Si(1)···H(1)	–C(212)	505.9(17)		20.0[c]
Si(1)···H(2)		573.8(4)		23.0[c]
Si(1)···H(3)		523.0(23)		20.0[c]
Si(1)···H(1)	–C(213)	337.1(15)		18.0[c]
Si(1)···H(2)		479.6(26)		20.0[c]
Si(1)···H(3)		470.7(33)		20.0[c]
Si(1)···H–Si(2)		313.4(27)	u_9	12.1(19)
C(111)···C(112)		251.2(2)	u_{10}	7.5(3)
(C···C)[g]		(519–579)[f]	u_{11}	[12.3–13.7](17)
(C···C)[h]		(630–678)[f]	u_{12}	28.3(20)
C(113)···C(213)		621.5(30)[f]		25.0[c]
C(112)···C(212)		755.7(15)[f]		30.0[c]
C(11)···H[C(111)]		219.3(1)	u_{13}	9.9(6)

[a] Other C···H and all the H···H nonbonded distances were included in the refinement, but are not listed here. Their vibrational amplitudes were within the range 12–35 pm.

[b] Least-squares standard deviations in the last digit are given in parentheses.

[c] Fixed.

[d] $N = 1, 2, 3$: for the numbering scheme see Fig. 1.

[e] Tied to u_6.

[f] Dependent on the Si–Si twist angle.

[g] Six distances arising from the contact of the two *t*-Bu groups.

[h] Eight distances arising from the contact of the two *t*-Bu groups.

IR and Raman active, giving rise to 35 vibrations. These can be described as ν_{as}, ν_s, δ_{as}, δ_s, ρ and τCH_3, as well as ν_{as}, ν_s, δ_{as}, δ_s, ρ and τCC_3. Of these, only δ_{as}, δ_s and ρCC_3 are sensitive to the remaining substituents on the Si silicon atoms, and their frequencies are shifted upon deuteration. Torsional vibrations, in general, give rise to only weak Raman bands.

The SiSi stretching vibrations of disilane [14] and 1,2-dimethyldisilane [4] have been reported to give intense Raman bands at 423 cm^{-1} (Si_2H_6), 424 cm^{-1} (*anti*-$CH_3SiH_2SiH_2CH_3$) and 413 cm^{-1} (*gauche*-$CH_3SiH_2SiH_2CH_3$). For **1**, the intense liquid Raman band at 479 cm^{-1} is assigned to the SiSi stretching vibration. The SiC stretching modes are located at 593 (Raman) and 590 cm^{-1} (IR). Upon deuteration these vibrations are shifted to 436 cm^{-1} (νSiSi), and 661 and 597 cm^{-1} (SiC vibrations), respectively. These rather unexpected shifts can be attributed to strong coupling with SiD_2 deformations (see Tables 3 and 4).

The stretching, scissors (δ_s), wagging (γ), twisting (τ) and rocking (ρ) modes for the (C)SiH_2(Si) group are expected around 2100–2130, 930–950, 700–800, 550–700 and 430–550 cm^{-1}, respectively. Their exact frequencies depend on the masses and the nature (electronegativity) of the two remaining substituents at the silicon atom, and on coupling interactions with other vibrations (see Section 6). $\delta_s SiH_2$ and γSiH_2 usually have strong IR absorptions and medium Raman intensities, with τ and ρSiH_2 being much weaker. The vibrations are observed in the expected regions (Table 9), but coupling of γ, τ, and $\rho SiH_2/SiD_2$ with νSiC, νSiSi and CC_3 deformations does occur.

6. Normal coordinate analysis (NCA)

The NCA for *anti*-$(CH_3)_3CSiH_2SiH_2C(CH_3)_3$ and $(CH_3)_3CSiD_2SiD_2C(CH_3)_3$ was performed using the FG method of Wilson et al. [15]. ***G***-matrices were computed using the C_i geometrical parameters obtained by GED (Table 5). By using the point group C_i instead of the effective C_2, the dimensions of the ***G*** and ***F*** matrices involved were reduced to more easily manageable sizes without a significant reduction in accuracy, as the rule of mutual exclusion is largely obeyed.

Symmetry coordinates were calculated using local C_{3v} symmetry for the methyl groups and also for the CC_3 skeleton, as described elsewhere [16,17]. Because the calculation of CH force constants was not within the scope of this work, ν_{as}, ν_s, δ_{as} and $\delta_s CH_3$ coordinates were removed from the *G*-matrices using a method described by Wilson

Table 7
Portion of the least-squares correlation matrix for $(CH_3)_3CSiH_2SiH_2C(CH_3)_3$ showing all elements ⩾ 50% (k_1 and k_2 are scale factors)

p_5	p_6	p_7	p_9	p_{11}	p_{12}	p_{13}	u_1	u_5	u_6	u_8	u_9	u_{10}	u_{13}	k_1	k_2	
	−59												−72			p_1
−84																p_3
		−50		−58												p_6
				65			−77				52	−68	−61			p_7
									−71							p_9
			71		−55	−57			−62	−56	66					p_{11}
			−53													p_{12}
								−81								p_{14}
												81	75			u_1
														57		u_3
														51		u_4
											−50					u_6
													53			u_{10}
															54	k_1

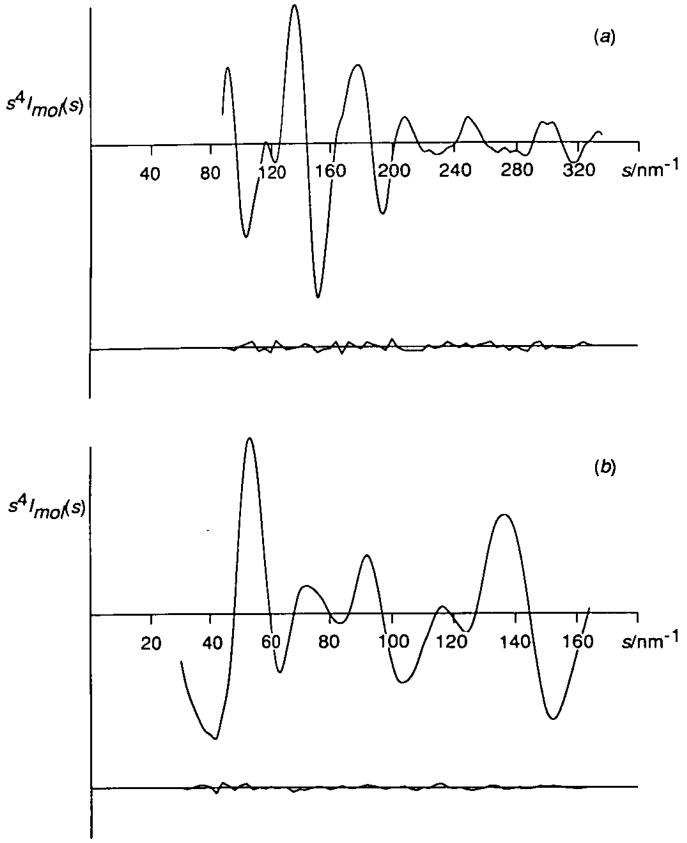

Fig. 2. Experimental and final difference (experimental minus theoretical) molecular-scattering intensities for $(CH_3)_3CSiH_2SiH_2C(CH_3)_3$ at nozzle-to-plate distances of (a) 94 mm and (b) 259 mm.

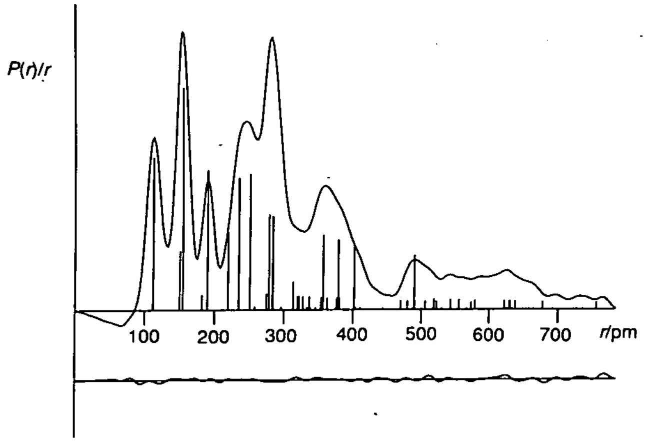

Fig. 3. Experimental and difference (experimental minus theoretical) radial-distribution curves, $P(r)/r$, for $(CH_3)_3CSiH_2SiH_2C(CH_3)_3$ vapour; before Fourier inversion, the data were multiplied by $s.\exp(-0.00002s^2)/(Z_{Si}-f_{Si})(Z_C-f_C)$.

Table 8
Atomic coordinates (pm) for $(CH_3)_3CSiH_2SiH_2C(CH_3)_3$

Atom		x	y	z
Si(1)		0.0	234.8	0.0
C(11)		167.7	311.2	−46.6
C(111)		222.4	249.8	−176.9
H(1)	−C(111)	138.0	226.9	−246.9
H(2)		292.5	321.6	−226.7
H(3)		277.6	154.9	−154.3
C112		146.2	462.5	−67.2
H(1)	−C(112)	71.0	500.8	6.4
H(2)		242.8	517.2	−52.4
H(3)		108.8	482.1	−171.0
C113		270.1	289.6	66.4
H(1)	−C(113)	257.2	187.6	110.8
H(2)		374.2	298.8	26.1
H(3)		255.3	366.3	146.7
H(1)	−Si(1)	−105.0	278.8	−97.4
H(2)		−39.7	278.8	137.6
Si(2)		0.0	0.0	0.0
C(21)		−174.1	−76.4	0.0
C(211)		−261.7	−14.9	−110.8
H(1)	−C(211)	−199.1	−8.0	−200.9
H(2)		−342.5	−86.8	−140.1
H(3)		−308.8	79.9	−74.3
C(212)		−158.9	−227.6	−25.6
H(1)	−C(212)	−66.7	−266.0	25.2
H(2)		−248.0	−282.4	15.0
H(3)		−150.7	−247.3	−135.5
C(213)		−242.4	−54.8	136.4
H(1	−C(213)	−218.1	47.3	175.7
H(2)		−353.5	−64.0	125.5
H(3)		−206.7	−131.5	209.8
H(1)	−Si(2)	75.1	−43.9	−122.0
H(2)		75.1	−43.9	122.0

et al. [15]. ρCH_3 coordinates were retained as they are strongly coupled with CC-stretching vibrations. If torsional coordinates are also neglected, the vibrational problem reduces to $\Gamma_{vib} = 23A_g(\text{Raman}) + 22A_u(\text{IR})$. Table 10 gives the notation and numbering of the modes, and Tables 3 and 4 summarise the results of the computations, including ab initio frequencies, and the assignments based on the predominant potential energy distributions.

Force constants of the *t*-butyl groups were initially taken from Schachtschneider and Snyder [18], and data for $(CH_3)_3CSiX_3$ [16]. Both CC and ρCH_3 force constants had to be slightly reduced to fit the experimental frequencies, but no further refinement was attempted. The force constants of the $CSiH_2SiH_2C$ moiety were taken from related molecules such as $CH_3SiH_2SiH_2CH_3$ [4] or $(CH_3)_2SiH_2$ [19], and were iterated until reasonable agreement between calculated and observed frequencies was achieved. As is indicated by the calculated potential energy distributions (Tables 3 and 4), strong mixing between SiH_2/SiD_2 and CC_3 deformation modes occurs.

7. Results and discussion

7.1. Geometry

The GED geometrical parameters refined in C_2

Table 9
Infrared and Raman spectra ($<2200\,cm^{-1}$) of $(CH_3)_3CSiH_2SiH_2C(CH_3)_3$ and $(CH_3)_3CSiD_2SiD_2C(CH_3)_3$

$(CH_3)_3CSiH_2SiH_2C(CH_3)_3$			$(CH_3)_3CSiD_2SiD_2C(CH_3)_3$			Assignment
IR(1)	Ra(1)	Ra(s) (140 K)	IR(1)	Ra(1)	Ra(s) (140 K)	
2130 sh		2123 vs	1547 vs	1542 sh, p	1547 s	$\nu_{as}SiH_3/SiD_3$
2112 vs	2113 vs, b, p	2115 s	1527 vs	1531 vs, p	1535 vs	$\nu_{s}SiH_3/SiD_3$
1468 ms		1471 w	1468 sh		1465 vw	$\delta_{as}CH_3$
1461 ms	1462 ms	1466 m	1460 s	1460 mw	1456 m	
		1458 s				
1445 sh	1445 ms	1443 s		1443 mw	1443 m	
1391 w		1386 vvw	1390 w			$\delta_{s}CH_3$
1363 ms	1364 vw	1364 vw	1364 s		1364 w	
1261 w			1260 vw			
		1218 w				
1200 w	1200 s	1203 s	1199 m	1200 s	1202 m	$\nu_{as}CC_3$
1188 mw	1186 sh	1181 s	1185 mw	1187 sh	1190 mw	
1124 m			1124 m			
1075 w			1076 w			ρCH_3
1011 s	1014 mw	1019 m	1009 s	1013 w	1013 w	
940 sh	945 s	939 s	939 ms	945 s	944 ms	δ_{sSiH_2}, ρCH_3
				937 sh	939 s	
921 vs	928 s	926 s				
		831 w				
824 m	824 s	824 s	823 vs	825 s	825 s	$\nu_{s}CC_3$
	794 w					
770 sh			760 vw			
750 sh			725 vw			
726 vs	728 mw, b	728 m				γSiH_2
690 sh	695 vw					τSiH_2
			670 vs	680 w, dp	683 m	$\delta_{s}SiD_2$
			660 sh	661 m, p	663 s	νSiC
			597 vs			νSiC
				569 vs, p	567 vs	τSiD_2
590 m	596 vs, p	596 s				νSiC
			546 vs		543 vvw	γSiD_2
	558 vw	558 vw				
500 mw, b			522 mw	529 w, dp	529 s	
				465 vw	469 mw	
			496 m			τSiD_2
	466 ms, p	466 ms	435 vw	436 m, p	436 s	$\nu SiSi$
	431 ms, p					
428 vw						ρSiH_2
398 w	383 mw, b, p	390 w	375 m	387 mw, p	387 m	$\delta_{as}CC_3$
368 vw		369 w				
				360 vvw	360 m	ρSiD_2
360 w						$\delta_{s}CC_3$
342 m	349 vw	345 mw	336 m	343 w	339 s	
				311 w, p		
			290 w			
	277 w	275 w		264 vvw	275 w	ρCC_3
	235 vw, sh	230 mw				
	220 ms, p	220 m		215 ms, p	223 s	
				205 sh	207 vw	
	124 m, p	134 m		122 ms, p	133 s	$\delta SiSiC$
	115 sh	125 w		115 sh	124 m	
	84 m	85 w		84 m	80 w	

Table 10
Numbering of the normal vibrations of $(CH_3)_3CSiH_2SiH_2C(CH_3)_3$

Mode	A_g	A_u
$\nu_{as}SiH_2$	ν_1	ν_{24}
ν_sSiH_2	ν_2	ν_{25}
ρCH_3	$\nu_3, \nu_4, \nu_5, \nu_6, \nu_7, \nu_8$	$\nu_{26}, \nu_{27}, \nu_{28}, \nu_{29}, \nu_{30}, \nu_{31}$
$\nu_{as}CC_3$	ν_9, ν_{10}	ν_{32}, ν_{33}
ν_sCC_3	ν_{11}	ν_{34}
δ_sSiH_2	ν_{12}	ν_{35}
γSiH_2	ν_{13}	ν_{36}
τSiH_2	ν_{14}	ν_{37}
νSiC	ν_{15}	ν_{38}
ρSiH_2	ν_{16}	ν_{39}
$\nu SiSi$	ν_{17}	
$\delta_{as}CC_3$	ν_{18}, ν_{19}	ν_{40}, ν_{41}
δ_sCC_3	ν_{20}	ν_{42}
ρCC_3	ν_{21}, ν_{22}	ν_{43}, ν_{44}
$\delta SiSiC$	ν_{23}	ν_{45}

Table 11
Important symmetry force constants F^a_{ii} ($N m^{-1}$) of $(CH_3)_3CSiH_2SiH_2C(CH_3)_3$

Force constant	Value[b]	Force constant	Value[b]
$F(\nu_sSiH_2)$	265.5	$F(\rho CH_3)$	55
$F(\nu_{as}SiH_2)$	258	$F(\nu_{as}CC_3)$	437
$F(\delta_sSiH_2)$	21	$F(\nu_sCC_3)$	382
$F(\gamma SiH_2)$	17	$F(\delta_sCC_3)$	37
$F(\tau SiH_2)$	18	$F(\delta_{as}CC_3)$	43
$F(\rho SiH_2)$	17.5	$F(\rho CC_3)$	36
$F(SiC)$	279		
$F(SiSi)$	169		

[a] $F(\delta_s, \gamma, \tau, \rho SiH_2)$ scaled by r(Si–Si), $F(\rho CH_3)$, by r(C–H) and $F(\delta_{as}, \delta_s, \rho CC_3)$ by r(C–C).

[b] Mean values of species A_g and A_u.

symmetry are superior to the C_i ones in terms of the corresponding R factors (0.044 and 0.051, respectively). No symmetry constraints were applied in the ab initio optimisations; however, the resulting geometries also possess effective C_2 symmetry, and are quite close to C_{2h}: the deviation of the CSiSiC unit from planarity is only 3.2° at the SCF/6-31G* level.

The most striking feature of the structural analysis is a significant deviation of the SiSiC bond angle from the angle in "pure" sp^3 silicon (109.5°) towards to a higher value of 113.7°, which compares well with the theoretical value of 114.4°, computed using a 6-31G* basis set for the anti form. The 6-31G* value of this angle in the gauche form, 120.1°, exhibits an even more pronounced distortion from the parent angle of 109.5°. In contrast, the SiSiX angles (X = Br, I) in 1,2-diiodosilane [3], 1,1,2,2-tetraiodosilane [3], and 1,1,2,2-tetrabromodisilane [2] show the opposite trend, and were all refined to approximately 107°. Note that these angles were assumed to be identical in the anti and gauche forms of each of these compounds.

The experimental Si–Si bond length of 235 pm is shorter than those reported for 1,2-diiododisilane and 1,1,2,2-tetraiododisilane (238.0(34) and 238.9(37) pm, respectively), and is in a reasonable agreement with the r_e value of 236.8 pm found using the 6-31G* optimisation. The Si–Si amplitude of vibration was refined to the same value, 6.8 pm, as reported for 1,2-diiododisilane, which has the most similar structure to **1**.

The Si–C and C–C bond lengths are well-determined parameters (190.1(1) and 154.1(1) pm respectively) and are in agreement with the theoretical values, $r_e = 191.9$ and 154.0 pm. The Si–C distance is somewhat longer than normally found for compounds which are not sterically crowded. The normal value of this bond length for such compounds is 187 pm [20].

As the $C(CH_3)_3$ groups are tilted from the local C_3 axes, the SiCC angles are not equal: the individual Si(1)C(11)C(11N) angles are 111.1, 107.7 and 110.5° for $N = 1, 2, 3$ respectively (see Fig. 1 for numbering). The refinement of the GED data and the 6-31G* optimisation both indicate more or less staggered conformations along all the single bonds; the corresponding GED (6-31G*) Si(2)Si(1)C(11)C(11N) dihedral angles are approximately 51° (59°), 170° (179°), and −71°(−62°), for $N = 1, 2, 3$ respectively.

7.2. Force constants

The calculated force constants for the $CSiH_2SiH_2C$ part of **1** compare well with those for related molecules. No significant deviation in the SiSi valence force constant of 169 $N m^{-1}$ from previously published values ($Si_2(CH_3)_6$, 165 $N m^{-1}$

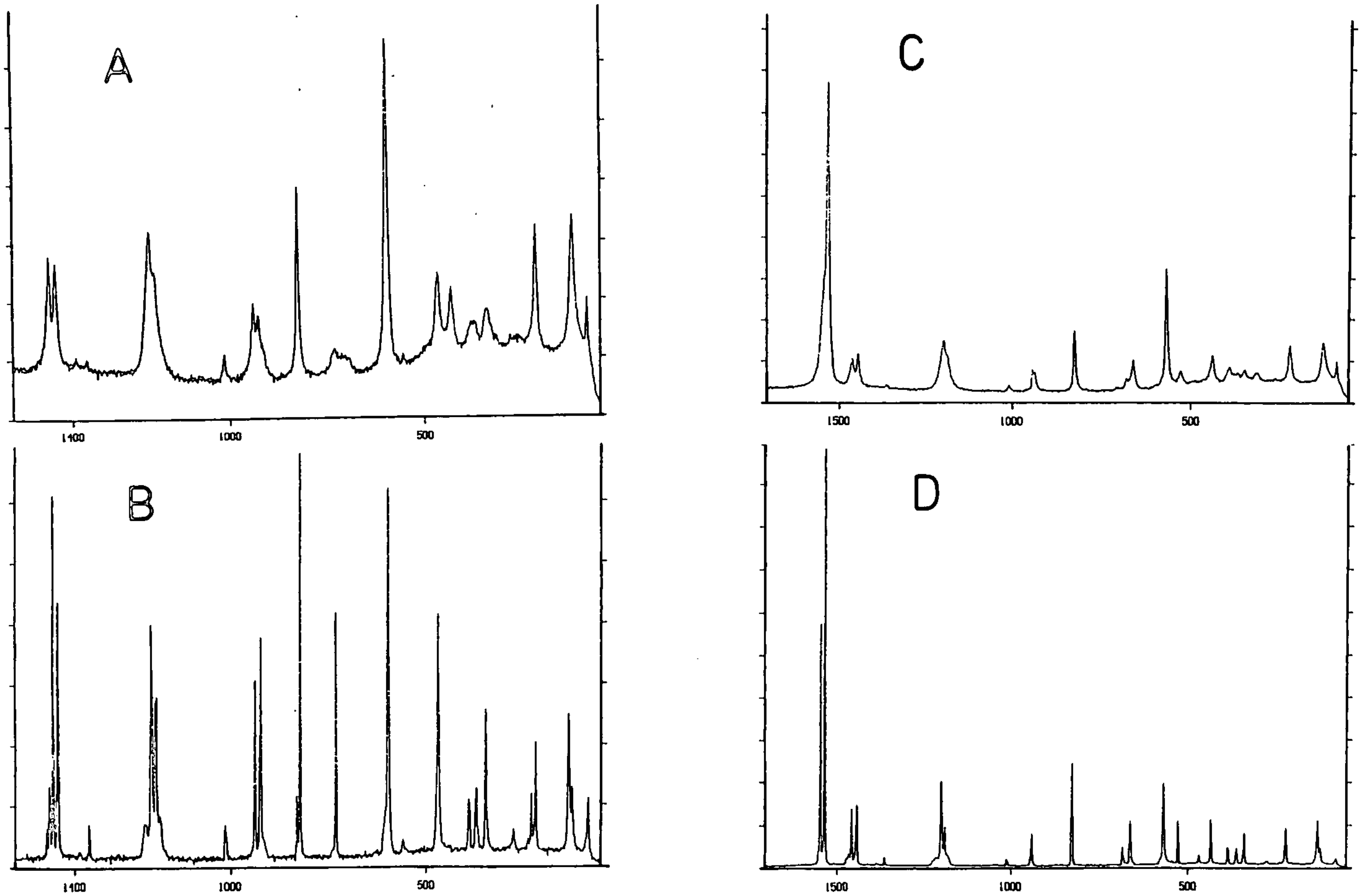

Fig. 4. Raman spectra of (A) liquid and (B) solid $(CH_3)_3CSiH_2SiH_2C(CH_3)_3$, and (C) liquid and (D) solid $(CH_3)_3CSiD_2SiD_2C(CH_3)_3$.

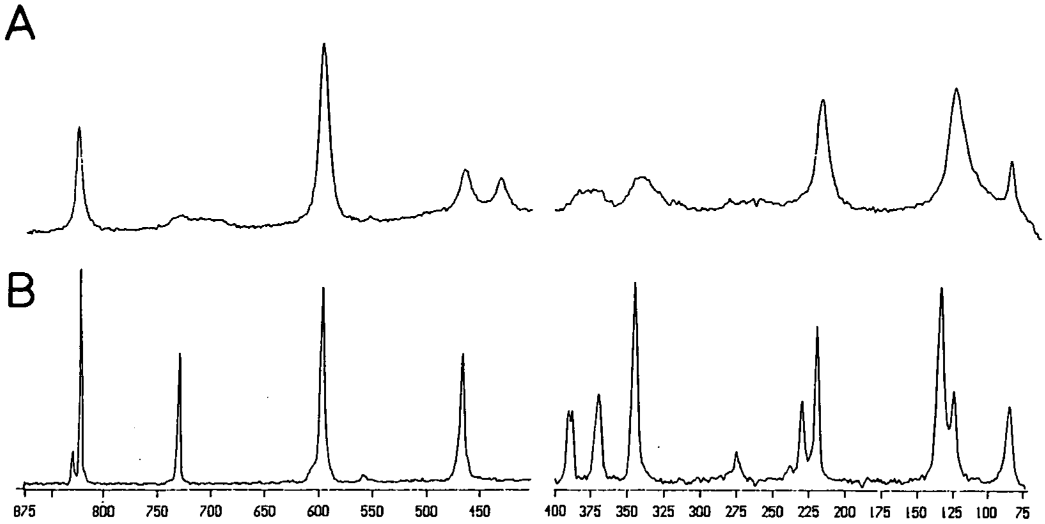

Fig. 5. Expanded Raman spectra of (A) liquid and (B) solid $(CH_3)_3CSiH_2SiH_2C(CH_3)_3$.

[21]; Si_2H_6; 173 N m^{-1} [22]) was observed, indicating a normal Si–Si bond. The CC valence force constants of *t*-butyl-substituted disilanes (calculated from Table 11; 400 N m^{-1}) seem to be somewhat (6%) smaller than those for *t*-butyl-substituted monosilanes, which are calculated to be 425 N m^{-1} [16]. However, the capability of the NCA to elucidate such small changes should not be stressed too much.

7.3. Rotational isomerism

According to infrared and Raman spectra and NCA calculations for $CH_3SiH_2SiH_2CH_3$ and $CH_3SiD_2SiD_2CH_3$ [4], $Br_2SiHSiHBr_2$, $I_2SiHSiHI_2$, $ISiH_2SiH_2I$ [23], $BrSiH_2SiH_2Br$ and $BrSiD_2SiD_2Br$ [24], and $Cl_2SiHSiHCl_2$ and $Cl_2SiDSiDCl_2$ [25], the SiSi and SiX stretching and SiH/SiD deformation modes, as well as the skeletal deformations, are sensitive to molecular conformations. As seen from Figs. 4–6, two liquid Raman bands of $(CH_3)_3CSiH_2SiH_2C(CH_3)_3$ (695 and 431 cm^{-1}) and one liquid Raman band of $(CH_3)_3CSiD_2SiD_2C(CH_3)_3$ (311 cm^{-1}) disappear in the solid state. One should, however, resist the temptation to assign these bands to the gauche conformers for several reasons.

As can be seen from Figs. 4–6, rather drastic changes in the relative band intensities occur upon solidification. Further, the GED data give no support to the existence of appreciable amounts of the gauche conformer. According to the ab initio calculations, the SiSi stretching vibrations of gauche- and anti-$(CH_3)_3CSiH_2SiH_2C(CH_3)_3$ should differ by 30 cm^{-1}, with $\nu(SiSi)_g$ being lower in energy. The scaled frequencies are 461 and 431 cm^{-1}. If the Raman band at 431 cm^{-1} (which disappears in the solid) is assigned to the gauche rotamer, the anti to gauche ratio must be roughly 2 : 1, taking into account the calculated Raman intensities. This certaintly contradicts the GED experiments. Further, the ab initio calculations predict the strong IR band at 726 cm^{-1} (γSiH_2, anti) to shift to 780 cm^{-1} for the gauche rotamer with almost identical infrared intensities of both bands. In the spectrum of the liquid, there is in fact a shoulder at 770 cm^{-1}, and the bands are clearly separated in the gas phase (735 and 780 cm^{-1}). However, the intensity of the 780 cm^{-1} gas band is very low, indicating a very large anti to gauche ratio. The Raman peak at 431 cm^{-1} thus cannot be assigned to the gauche rotamer, and its origin remains unexplained. Additional evidence against the existence of appreciable amounts of the gauche conformer at room temperature is provided by the Raman spectrum of $(CH_3)_3CSiD_2SiD_2C(CH_3)_3$, for which $\nu(SiSi)_g$ is missing in the liquid state. The whole spectrum

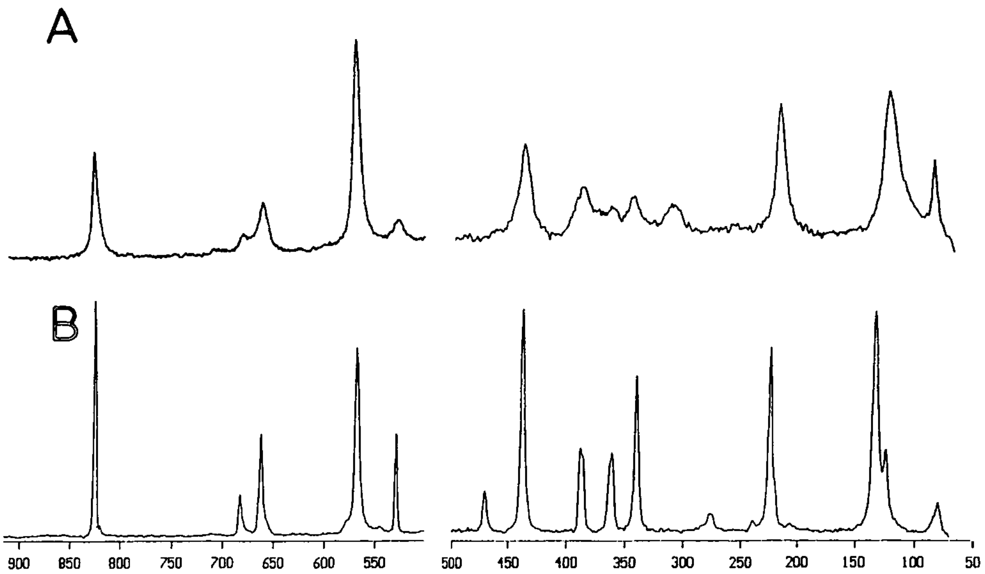

Fig. 6. Expanded Raman spectrum of (A) liquid and (B) solid $(CH_3)_3CSiD_2SiD_2C(CH_3)_3$.

hardly changes on passing from the liquid to the solid state, apart from the disappearance of the weak signal at 311 cm^{-1}.

In conclusion, the vibrational spectra give no evidence for the existence of appreciable amounts of the gauche rotamer in the liquid phase at room temperature. Observed intensity changes on cooling are obviously caused by solid state effects and not by changes in the anti to gauche ratio. No evidence for the presence of the gauche rotamer could be found in the GED data either, as pointed out above.

Moreover, at the 6-31G* level, the gauche isomer was computed to lie 7.11 kJ mol^{-1} above the most favoured anti form. The more refined MP2 single-point energy calculations at the MP2/6-31G*//SCF/6-31G* level reduced the energy difference to 5.02 kJ mol^{-1}. The SCF/6-31G* zero-point correction (ZPE) is small, favouring the anti form by less than 0.42 kJ mol^{-1}. Our final estimate for the energy difference between the gauche and anti forms is 5.44 kJ mol^{-1} (MP2/6-31G*//SCF/6-31G* + ZPE(6-31G*) level),[a] which corresponds to the presence of approximately 10% of the gauche form (weighted composition) in the mixture at room temperature. It is, however, possible that the energetic separation of the conformers will increase at higher levels of theory.

Acknowledgements

We are grateful to the SERC for support of the Edinburgh Electron-Diffraction Service, including provision of microdensitometer facilities at the Daresbury Laboratory and research fellowships for D.H. and H.E.R.

M.B. thanks Professor W. Thiel and the Alfried Krupp-Stiftung for support.

References

[1] V.S. Mastryukov, in I. Hargittai and M. Hargittai (Eds.), Stereochemical Applications of Gas-Phase Electron Diffraction, Part B, VCH, Weinheim, Germany, 1990, p. 1.

[2] H. Thomassen, K. Hagen, R. Stølevik and K. Hassler, J. Mol. Struct., 147 (1986) 331.

[3] E. Røhmen, K. Hagen, R. Stølevik, K. Hassler and M. Pöschl, J. Mol. Struct., 244 (1991) 41.

[4] K. Ohno, M. Hayashi and H. Murata, Spectrochim. Acta, Part A, 39 (1983) 373.

[5] K. Hassler and B. Reiter, J. Organomet. Chem., 467 (1994) 21.

---

[a] The zero-point energies have been scaled by 0.9 as recommended in Ref. [11].

[6] C.M. Huntley, G.S. Laurenson and D.W.H. Rankin, J. Chem. Soc., Dalton Trans., (1980) 954.

[7] S. Cradock, J. Koprowski and D.W.H. Rankin, J. Mol. Struct., 77 (1981) 113.

[8] A.S.F. Boyd, G.S. Laurenson and D.W.H. Rankin, J. Mol. Struct., 71 (1981) 217.

[9] A.W. Ross, M. Fink and R. Hilderbrandt, in A.J.C. Wilson (Ed.), International Tables for Crystallography, Vol. C, Kluwer Academic, Dordrecht/Boston/London, 1992, p. 245.

[10] W.J. Hehre, L. Radom, P.v.R. Schleyer and J.A. Pople, Ab Initio Molecular Orbital Theory, Wiley, New York, 1986.

[11] R. Ahlrichs, M. Bär, M. Häser, H. Horn and C. Kölmel, TURBOMOLE, Chem. Phys. Lett., 154 (1989) 165.

[12] M.J. Frisch, G.W. Trucks, M. Head-Gordon, P.M.W. Gill, M.W. Wong, J.B. Foresman, B.G. Johnson, H.B. Schlegel, M.A. Robb, E.S. Replogle, R. Gomperts, J.L. Andres, K. Raghavachari, J.S. Binkley, C. Gonzalez, R.L. Martin, D.J. Fox, D.J. DeFrees, J. Baker, J.J.P. Stewart and J.A. Pople, GAUSSIAN 92, Revision B, Gaussian Inc., Pittsburgh, PA, 1992.

[13] W.C. Hamilton, Acta Crystallogr., 18 (1965) 502.

[14] J.R. Durig and J.S. Church, J. Chem. Phys., 73 (1980) 4784.

[15] E.B. Wilson, J.C. Decius and P.C. Cross, Molecular Vibrations, McGraw-Hill, New York, 1955.

[16] K. Hassler and M. Weidenbruch, J. Organomet. Chem., 465 (1994) 127.

[17] K. Hassler and M. Weidenbruch, J. Organomet. Chem., 465 (1994) 137.

[18] J.H. Schachtschneider and R.G. Snyder, Spectrochim. Acta, 19 (1963) 117.

[19] K. Hassler, Spectrochim. Acta, Part A, 37 (1981) 511.

[20] L.E. Sutton (Ed.), Special Publication No. 18, The Chemical Society, London, 1965, Table S.

[21] F. Höfler, Monatsh. Chem., 107 (1976) 893.

[22] J.L. Duncan, Spectrochim. Acta, 20 (1964) 1807.

[23] K. Hassler and M. Pöschl, Spectrochim. Acta, Part A, 47 (1991) 439.

[24] K. Schenzel and K. Hassler, in preparation.

[25] K. Hassler, W. Köll and M. Ernst, in preparation.